UNIVERSITY OF SOUTHAMPTON

FACULTY OF PHYSICAL SCIENCES AND ENGINEERING

Physics & Astronomy

A Mode-Locked diode laser frequency comb for ultracold atomic physics experiments

by

Jonathan R. C. Woods

Thesis for the degree of Doctor of Philosophy

January 2016

UNIVERSITY OF SOUTHAMPTON

ABSTRACT

FACULTY OF PHYSICAL SCIENCES AND ENGINEERING

Physics & Astronomy

Doctor of Philosophy

A MODE-LOCKED DIODE LASER FREQUENCY COMB FOR ULTRACOLD ATOMIC PHYSICS EXPERIMENTS

by Jonathan R. C. Woods

This thesis is concerned with the development and characterisation of an actively mode-locked diode laser system for the provision of a stable optical frequency comb spanning approximately 1 nm around the D_2 spectroscopic line of Rubidium. Through large signal sinusoidal modulation of the laser DC injection current at around 3 GHz, Gaussian pulses of 21 ps are achieved with an associated spectral bandwidth in excess of 1 nm, generating pulses of optimal time-bandwidth product $\sim$13. An in-house built air-bearing Michelson interferometer is used to confirm the comb-like structure of the optical emission and a modulation frequency detuning range of 10 MHz is determined.

Through a proof of principle investigation of CW injection locking of the frequency comb, phase coherence of the CW master laser with the modes of the frequency comb is demonstrated over at least 36 GHz. Via CW injection locking, sidemode suppression of 20.6 dB is achieved resulting in an 18% rise in the pulse temporal width and a concomitant reduction in the time-bandwidth product to 1.44, as well as a power dependant phase locking detuning range of up to 370 MHz. In the closing chapters, two CW lasers are shown to be stabilised to the frequency comb via Optical Phase-Locked Loops, a temperature stabilised fibre Mach-Zehnder interferometer is demonstrated for carrier frequency removal from a phase modulated laser, and a novel intra-cavity trace water vapour detection method is introduced.

Contents

List of Figures

List of Tables

Declaration of Authorship

I, Jonathan R. C. Woods , declare that the thesis entitled *A Mode-Locked diode laser frequency comb for ultracold atomic physics experiments* and the work presented in the thesis are both my own, and have been generated by me as the result of my own original research. I confirm that:

- this work was done wholly or mainly while in candidature for a research degree at this University;
- where any part of this thesis has previously been submitted for a degree or any other qualification at this University or any other institution, this has been clearly stated;
- where I have consulted the published work of others, this is always clearly attributed;
- where I have quoted from the work of others, the source is always given. With the exception of such quotations, this thesis is entirely my own work;
- I have acknowledged all main sources of help;
- where the thesis is based on work done by myself jointly with others, I have made clear exactly what was done by others and what I have contributed myself;
- parts of this work have been published as: [1]

Signed:...

Date:...

Acknowledgements

Writing acknowledgements is a great experience, spoiled only by the sense of trepidation one gets at the thought of missing someone off! Firstly I would like to extend the utmost gratitude to my supervisor, Tim Freegarde, for providing the opportunity for me to strive towards a Ph.D and the endless support, guidance and calming perspective that went with it. I would also like to express my deepest thanks to Matthew Himsworth, without whose help, guidance and patience the project simply wouldn't have gone ahead. For their direct input, support and friendship, I'd like to thank Nathan Cooper, James Bateman and Andrew Chapman, whose help in the early and latter stages of the PhD respectively was invaluable.

I am hugely indebted to Anne Tropper for her belief in me, and her group for allowing me to use their lab space and equipment. Specifically I'd like to thank Keith Wilcox, Rob Head, Andrew Turnbull for their help and support and to Ed Shaw and Theo Chen Sverre for making the lab a better place. I would like to thank the staff of the department mechanical workshop, specifically Mark Bampton and Mark Scully for their time, patience and incredible expertise. In the same capacity, I'd like to thank Gareth Savage and Garry Taylor. I am incredibly thankful to James Gates for his support, excellent humour and for letting me camp out in his lab for a few months to use some vital equipment. I would also like to extend my thanks to Matthew Proctor, Rachel Gregory, Jo Rushton, Alex Dunning, Duncan McBryde Alan Forrester, Matt Aldous, Ned Hawes and Sakellaris Mailis for their friendship and support.

It is an absolute certainty in my mind that I'd not have completed this PhD and thesis without the endless support of my partner, Nichola Shaw. Her kindness, thoughtfulness and patience knows no bounds. Lastly, I'd like to thank Jan Woods, Justin Woods, Yen and Kev Cairney, and Joan, Phil and Nathan Shaw for all their support.

Nomenclature

α	The linewidth enhancement factor
α_i	Internal / Background losses
α_{ic}	Intra-cavity absorption losses
α_{il}	Insertion losses through coupling to the external cavity
α_{min}	Minimum detectable absorption coefficient
c	Vacuum velocity of light
B	Photodetector bandwidth
β	Modulation index
d	Diode laser waveguide thickness (semiconductor active region layer separation)
δ	Generic absorption function
E	Electric field
$\boldsymbol{\mathcal{E}}$	Generic vector electric field
E_0	Electric field peak amplitude
E_{sp}	Electric field contribution from spontaneous emission
e	Electron unit charge
F	Cavity finesse
F_t	Number of fringes recorded in an interferogram
G_N	Carrier density dependent Differential Gain
g	Gain factor
Γ	Optical confinement factor
γ_c	Optical cavity photon loss rate
h	Planks constant (6.63×10^{-34} kg m^2 s^{-1})
I	Laser diode DC injection current

I_{th}	Laser diode threshold current
J	Injection current density
$J_x(\beta)$	Bessel function of the first kind, or order x
L	Cavity mirror separation distance
λ	Wavelength
M	Amplitude modulation index
N	Charge carrier density
N_l	Number of diffraction grating lines illuminated by an incident beam
N_{th}	Semiconductor threshold carrier density
N_{tr}	Semiconductor transparency carrier density
n	Refractive index (Real part)
η	Detector electronic response
η_{ext}	External differential quantum efficiency
P_0	Power incident on a photodetector
P_{cw}	Laser optical power
$\boldsymbol{\mathcal{P}}$	Macroscopic material polarisation vector
ϕ	Generic term for phase
ψ	Generic term for phase
r	Generic term for mirror amplitude reflectivity
R_{AR}	Power reflectivity of the laser diode anti-reflection coated facet
R_b	Power reflectivity of the laser diode back facet
R_{eff}	Effective reflectivity of the external cavity
R_{ext}	Power reflectivity of the output coupler mirror which forms the external laser cavity
T_{eff}	$(1 - R_{eff})$
t	Time
τ_1	Upper laser level spontaneous lifetime
τ_{acq}	Interferogram acquisition time
τ_{ph}	Photon lifetime
τ_{ib}	Semiconductor inter-band carrier relaxation time
υ_{gr}	Group velocity
ω_0	Carrier frequency

ω_m	Modulation frequency
ω_{RO}	Relaxation oscillation frequency
$\Delta\omega$	Peak shift in frequency observed through modulation

Chapter 1

Introduction and Background

1.1 Introduction, Motivation and Thesis Structure

This thesis is concerned with the provision of closely spaced, regular optical frequency references around the D_2 spectroscopic line of Rubidium. These frequency references, which shall be derived from a commercially available diode laser, are required for the purpose of laser stabilisation and light generation for ultracold atom experiments. The diode laser is a small, cost effective laser source, whose principle of operation naturally lends itself to the generation of a uniformly distributed comb of phase coherent frequency components via a process called mode-locking. To achieve mode-locking in diode lasers, a common method is to modulate the DC drive current with a large sinusoidal waveform at a frequency matched to the laser cavity inverse round trip time. The result is optical pulses in the time domain and a frequency comb in the frequency domain. It is this frequency comb that we intend to build, characterise, stabilise, and ultimately use to lock subsequent continuous wave lasers by way of optical phase locking.

Atomic physics experiments use lasers to transfer atoms between states by exciting different radiative transitions. The laser sources therefore need to be spectrally narrow enough to address a desired transition and indeed often a specific Doppler shifted velocity class within it. Because the wavelength-determining mechanisms within lasers such as mechanical vibration, bias current and junction temperature are prone to drift, the laser wavelengths have to be stabilised to an absolute reference. Typically this reference is a spectral feature of the atomic species itself. This frequency reference can also take the form of an already spectroscopically stabilised laser which provides a fixed optical frequency that can be compared against the laser which is to be stabilised. This is a process known as offset locking and works by beating the two lasers on a photodiode, comparing the beat frequency to a known, electronically derived, stable oscillator, and using this comparison to correct the frequency of the unstable laser. Where the frequency offset between the two lasers is limited by the frequency response of the detector, the cost associated with achieving a frequency offset lock at more than approximately a few tens of GHz becomes prohibitive. In terms of the laser linewidth and stability, two conditions should be met. Firstly the linewidth is required to be less than the natural linewidth of the hyperfine level being addressed, and secondly the laser drift must be less than that same natural linewidth. For Rubidium, the FWHM natural linewidth of the cooling transition is approximately 5.7 MHz, and commonly accepted parameters for the laser are $\leq$1 MHz linewidth and $\leq$1 MHz drift over the period of the experiment.

The D_2 line in Rubidium shown in figure 1.1 contains the spectroscopic features of use for the main experiments conducted within the Quantum Control group. These experiments, which we shall summarise shortly, are spread across multiple laboratories and require multiple stabilised CW laser sources. The lasers close to the optical resonances of Rubidium that need wavelength stabilisation require their own discrete Rubidium spectroscopy experiment in order to generate the appropriate information used in stabilising the laser. These individual spectroscopy setups are both expensive and, when repeated for each laser, take up considerable optical bench 'real estate'. It is desirable therefore to have a collection of uniformly spaced, stable optical frequency references in the vicinity of the D_2 line, onto which the lasers for the atomic physics experiments may be easily phase-locked.

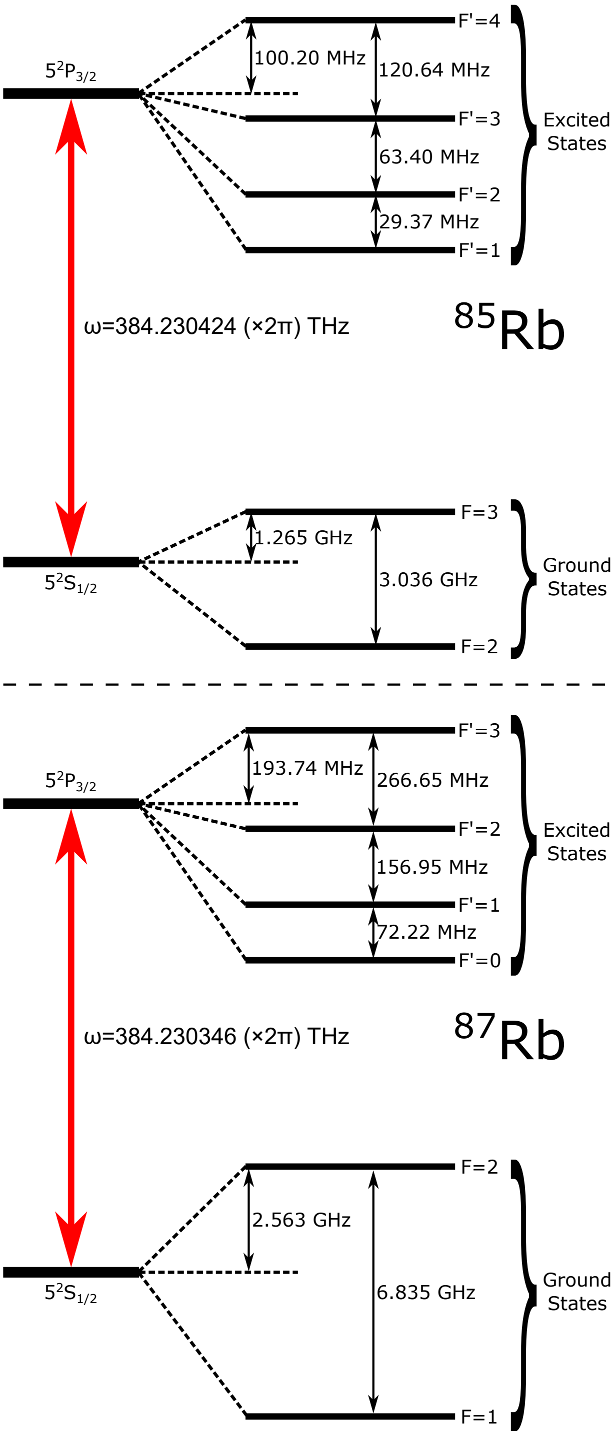

Figure 1.1: Schematic diagram showing the hyperfine splitting of the D_2 line for ^{85}Rb (top) and ^{87}Rb (bottom). The two $5^2P_{3/2}$ states are split by approximately 78 MHz, where ^{85}Rb is the higher frequency transition. The energy level splitting values were found in reference [2].

On the other hand, in certain situations it is required that the lasers be detuned from a specific resonance by potentially many tens of GHz for the specific purpose of avoiding a single photon transition. Without a fully stabilised, octave spanning frequency comb, how are the laser frequencies to be accurately stabilised when far beyond the limits of frequency offset locking? By way of active mode-locking of a laser diode, we wish to demonstrate a spectroscopically referenced optical frequency comb spanning approximately 1 nanometre, onto which the multiple CW lasers used in the atomic physics experiments may be stabilised. By setting the mode spacing frequency of the frequency comb to approximately a few GHz, which is well within easily achievable optical phase locking bandwidths, CW lasers may be accurately stabilised to the comb at arbitrary positions potentially hundreds of GHz away from the nearest atomic spectral line. Further, by removing the requirement of a spectroscopy experiment for the stabilisation of a single laser, the cost, complexity and size of the experimental laser stabilisation method may be drastically reduced. This aspect is also of specific interest to researchers in the field of ultracold atoms whose drive is to miniaturise the total experiment to lab-on-a-chip size [3].

A common problem with frequency combs in the context of the stabilisation of lasers to the frequency comb is that while the quality of the lock may be perfectly sufficient, the ability to precisely identify exactly which comb mode the laser is locked to is non-trivial. In an attempt to solve this problem, we propose a mode identification principle which employs two frequency combs which have a common comb mode each referenced to a spectroscopic feature but where each comb possesses a fractionally different mode spacing. As such, when a CW laser is beat against one comb at a known frequency, the precise mode number may be determined by identification of the unique beat frequency of the same CW laser with the second comb. This will in effect produce a frequency comb 'Vernier' scale, which could easily find use among automated locking systems.

More generally, the ability to arbitrarily lock a large number of CW lasers to a spectroscopically stable reference of this bandwidth naturally makes possible the cost effective generation of customisable beat frequencies for arbitrary function generation [4]. Also there are a number of spectral features of interest around 780 nm including the 2S-8S/D two-photon transition (777.79 nm) in Hydrogen [5–7], the 2S-3P two-photon transition

(777.94 nm) in Helium [8] and the two-photon (777.87 nm, Rubidium frequency standard) transition $5S_{1/2}$ — $5D_{5/2}$ [9]. All of these spectroscopic features could be probed with laser stabilised to a frequency comb spanning only 0.2 nm. Furthermore, with a stabilised frequency comb spanning just 2.5 nm, these could all be cross-referenced against the D2 line single photon resonances of Rubidium.

The experiments conducted in the Quantum Control group are multifaceted, but all stem from the preparation of small clouds of ultracold ^{85}Rubidium. These clouds are generated in a Magneto-Optical Trap (MOT), whereby a combination of magnetic fields and laser beams are applied in an appropriate configuration to spatially confine on the order of a few million rubidium atoms at a specific position and cool them to the microkelvin range [10]. In terms of the lasers, a total of 6 beams, comprised of the light from two separate lasers (a 'cooling' laser and a 'repump' laser) are used in such a way that a 'trap site' is formed when the beams all overlap. Initially the two laser beams are combined spatially before being split equally into three. These three beams are then directed into the MOT chamber along the three mutually orthogonal Cartesian axes. After exiting the MOT chamber at the other side, they are retro-reflected so as to be coaxial but counter propagating. The result is effectively 6 beams which all overlap at a specific location. The optical frequency of the cooling laser is then red-detuned from from the $5S_{1/2}$, F=3 — $5P_{3/2}$, F′=4 transition by at least a few transitions linewidths (2 to 3 × ~5.7 MHz). Where the atoms in the chamber (which have been previously released from an evaporable getter), are at room temperature, they have an average velocity of around 250 ms^{-1} and so the Doppler effect dictates that only those atoms moving towards an oncoming laser effectively sees a resonant laser, resulting in the scattering of an oncoming photon. Because the emission of the absorbed photon occurs in a random direction, there is a net force on the atom acting against the component of velocity. This is a process known as Doppler cooling [11] and for two counter-propagating beams this effect is 1 dimensional. The presence of all 6 beams therefore cools in all 3 orthogonal dimensions. This does not trap the atoms however, hence the addition of a magnetic field is required. The magnetic field is provided by two coils, with mutually counter-rotating currents, and the trap site is formed at the magnetic field minimum provided the lasers all overlap at this position. This field splits the Zeeman sub-levels of the hyperfine transition by an amount proportional to the field strength so as to provide a spatial dependence to the magnitude of the positional restoring force.

With a cloud of ultracold Rubidium atoms present in the chamber, the next aspect of the atomic physics experiments conducted involves the stimulation of Raman transition between the two $5S_{1/2}$ hyperfine ground states, F=2 and F=3, for the purpose of velocity-dependent atom interferometry. The goal here is to use this transition to impart momentum to the atoms for the purpose of atom interferometry [12, 13]. It is required that the two lasers involved in the Raman transition are detuned from the single photon transition, while still maintaining a fixed RF beat frequency between them. In other words, the two lasers must still be resonant with the same virtual excited energy level. As described above, the ability to shift this virtual state to many tens, possibly even a hundred, GHz away from the single photon resonance is desirable, and so to stabilise these lasers both relative to each other and the real excited state is of great importance.

1.1.1 Synopsis

This thesis adopts the following structure. For the remainder of this introductory chapter, we briefly review the various methods for generating optical frequency combs from diode lasers and highlight why active mode-locking is the appropriate method to employ in this research. This review focuses on gain switching, the so called 'frequency comb generators' and the various methods by which diode lasers may be mode-locked.

Constituting chapter 2 is a review of some popular spectroscopy methods and a demonstration of CW laser stabilisation to the hyperfine structure of the Rubidium D_2 line via polarisation spectroscopy. Stabilised CW External Cavity Diode Lasers (ECDLs) are used as frequency references and fixed wavelength coherent optical sources in chapters 5 and 8. Further, in the context of a Rubidium referenced frequency comb, the ability to demonstrate locking a laser to a spectroscopic feature of Rubidium is crucial. Chapter 2 is therefore dedicated to laser frequency stabilisation.

Chapters 3 and 4 respectively consider the modulation characteristics and the mode-locking performance of the laser. In the former, the mode-locked laser construction and experimental arrangement is described initially, and is followed by a characterisation of the laser diode (which is to be mode-locked later) in CW operation. The latter parts of chapter 3 are devoted to the modulation characterisation of the laser diodes and, intrinsic to this, we make an attempt at RF impedance-matching the modulation signal transmission line to the laser diode. The aim here is to maximise the coupling efficiency of the RF modulation signal to the laser diode active volume. In the following chapter we present a comprehensive characterisation of the diode laser mode-locking performance over the various parameter spaces that we have experimental access to. Included in this is a characterisation of the laser operating at both 785 nm (its free running wavelength) and 780.2 nm (the desired wavelength), in the time, optical frequency and RF domains for the purpose of determining the optimum operating conditions for these specific commercial devices.

Chapter 5 complements the results of the previous two chapters by proving the frequency comb structure of the mode-locked laser emission. Highlighted is the design and implementation of a custom, in-house made, dual moving arm Michelson interferometer based on an air bearing design. This is an entirely passive device with data taken on a shot to shot basis, so an accurate method for velocity linearisation of the moving mirrors by using the simultaneously monitored beat frequency interferogram of a Rb stabilised CW ECDL is described. This chapter is concluded with data showing the frequency comb structure of the mode-locked laser as well as future design additions and recommendations.

A key milestone for this work is the demonstration that the frequency comb can fulfil it's intended role as a frequency reference for Rubidium. As such chapter 6 is devoted to demonstrating proof of the principle that CW injection locking of an oscillating mode of the frequency comb is capable of anchoring the chosen mode to a fixed spectral position. We take this experimental opportunity to also investigate the 'mode-locking in clusters' regime of laser operation, and use CW injection locking to try and improve the mode-locked laser emission properties by way of improving the time-bandwidth product[1].

---

[1] The time-bandwidth product is simply the product of the mode-locked laser emission bandwidth in units of hertz and the temporal pulse width in units of seconds.

Bringing the frequency comb investigation to a close, chapter 7 investigates the use of Optical Phase-Locked Loops (OPLL) for stabilising CW lasers to the frequency comb; thereby demonstrating feasibility in the context of the desired use of the frequency comb. As part of this investigation, we attempt to characterise the performance of the OPLL circuits by stabilising one CW laser to another CW laser, as well as measuring the RF beat note between two CW lasers when stabilised to the frequency comb.

The remaining two experimental chapters diverge from the main context of the thesis, by borrowing the principles of laser diode current modulation and stabilisation, and applying them to two different side projects. Chapter 8 demonstrates the stabilisation of a fibre-optic Mach-Zehnder interferometer for use in removing the carrier frequency from the spectrum of a weakly frequency modulated laser[2]. For support and experimental contribution, as well as the writing of the published manuscript, credit belongs to Nathan Cooper. Finally chapter 9 details the second of two side projects which demonstrates initial proof of principle lineshapes for a novel intra-cavity method for trace analyte detection. The data were instrumental in securing a CASE studentship award to fund a PhD place to investigate the method.

The thesis draws to a close with the conclusions and ideas for future work in chapter 10.

1.2 Diode Laser Frequency Combs

At the heart of this thesis lies the humble semiconductor diode laser and how it can be utilised to produce stable optical frequency combs spanning approximately 0.5 THz. Since 1962, when the first coherent emission from a forward biased p-n junction was reported [14], these devices have become the corner stones of countless research efforts. In their early inception, these devices consisted of forward-biased homojunctions. These p-n junction devices left much to be desired by todays standards, as they required cryogenic operating conditions and up to 10^5 amps per square centimetre of current density to operate. Two ground-breaking developments in diode laser technology came

---

[2] This work, for which I am a co-author, was published as ”Stabilized fiber-optic Mach-Zehnder interferometer for carrier-frequency rejection” [1] and in it I contributed the significant majority of the experimental construction, demonstration, and data capture.

about first with the invention of the single heterojunction and then later with the double heterojunction geometry [15]. These structures provide charge confinement by placing a semiconductor of a given bandgap energy next to a semiconductor of higher bandgap energy. It was the double heterojunction laser that first permitted room temperature continuous-wave (CW) operation at current densities well below 10^4 A/cm^2.

Soon after the first demonstrations of the double heterojunction lasers, some of the first reports of ’spiking’ in the laser emission emerged [16], which boasted temporal features below 0.5 ns in duration by way of modulation of the DC injection current. In 1978 the first 20 ps pulses were reported by Ho *et al* using a room temperature, CW, double heterostructure GaAlAs laser at a current modulation frequency of 3 GHz[3] [17]. It was recognised that this current modulation could be used to ’mode-lock’ the emission of the lasers to form short optical pulses in the time domain and a comb-like structure of optical cavity modes in the frequency domain, provided the modulation frequency was well matched to the laser cavity inverse round trip time. This method is successful because the current modulation propagates energy from the CW carrier frequency, ω_0, to optical sidebands which oscillate exactly on the adjacent longitudinal modes - hence the requirement for matching the modulation frequency to the cavity mode spacing. Temporally short, mode-locked pulses which are successfully generated by strong modulation of the laser DC injection current are said to have been generated by Active Mode-Locking, and it is this process which forms the foundation of this thesis. The brevity of the pulses however is not our primary concern. Our fundamental motivation is the generation and characterisation of a stable frequency comb, by way of active mode-locking, which encompasses at the very least least the D_2 transition of Rubidium to act as a broadband frequency reference for the stabilisation of the multiple CW lasers used in the group. A frequency comb is an optical spectrum which consists of a large number of very fine, uniformly spaced optical components which resembles a comb when viewed in the frequency domain. This comb of frequencies is incredibly useful as it essentially acts as an optical ruler, allowing very precise measurement of unknown optical frequencies. Early efforts at generating frequency combs were achieved by electro-optic phase modulation

---

[3] In this context, referring to the laser as a ’CW’ laser simply infers that the laser device was capable of running in CW operation: many devices before this time would not tolerate sustained (and continuous) current injection without damage.

and later by parametric amplification. Currently the best way to generate a frequency comb is by mode-locking a laser. A mode-locked laser emits optical pulses at very regular intervals in the time domain, and the pulse train in the frequency domain consists of a comb-like array of very precisely spaced optical frequency components. The frequency comb of a mode-locked laser has little intrinsic spectroscopic value in of itself until the precise frequency of each comb line is stabilised. In a mode-locked laser there are two degrees of freedom which must be either monitored or stabilised before the comb is of any spectroscopic value. The two degrees of freedom are the comb mode spacing (or, in the time domain, the inverse of the time between each successive pulse) and the 'carrier envelope offset' frequency. The former of the two is typically defined by the dimensions of the laser cavity, while the latter refers to the difference between the mth optical mode from the mth multiple of the free spectral range from zero frequency. Only when the frequency comb mode spacing *and* the carrier offset frequency are stabilised to a known value does the comb become of use. Any given comb line frequency may be written as $f_m = m \times \Delta f + f_{ceo}$, where Δf is the comb mode spacing and f_{ceo} is the carrier envelope offset frequency. In the time domain, f_{ceo} defines the rate of change of carrier envelope phase with respect to the carrier frequency. Figure 1.2 shows the relationship between the carrier envelope and the carrier frequency of a mode-locked laser pulse, wherein 1.2(A) shows a carrier envelope phase of 0 and 1.2(B) shows the carrier envelope phase shifted by $\pi/2$.

A major breakthrough in terms of stabilising the frequency comb of a mode-locked laser was the realisation of a comb whose frequency components span an octave. With this, the carrier envelope offset can be determined by implementing an $f - 2f$ self referencing interferometer [18]. This uses a frequency doubled low frequency component and beats it with an unaltered comb mode one octave higher in frequency; the comb stability is achieved by stabilising this beat frequency. Stabilising the comb mode spacing is achievable by simply stabilising the pulse repetition rate which can be monitored on a fast photodiode. It should be noted that a true frequency comb is one which spans an octave in spectral bandwidth. In this thesis however, we refer to a frequency comb as simply a comb-like optical spectrum, regardless of the bandwidth. This is because while mode-locked diode lasers can produce a comb-like spectrum, they are far from spanning an octave. We can nevertheless generate a useful frequency comb from a mode-locked diode laser by stabilising a constituent mode to a spectroscopic feature and deriving the modulation signal from a highly stable electronic function generator.

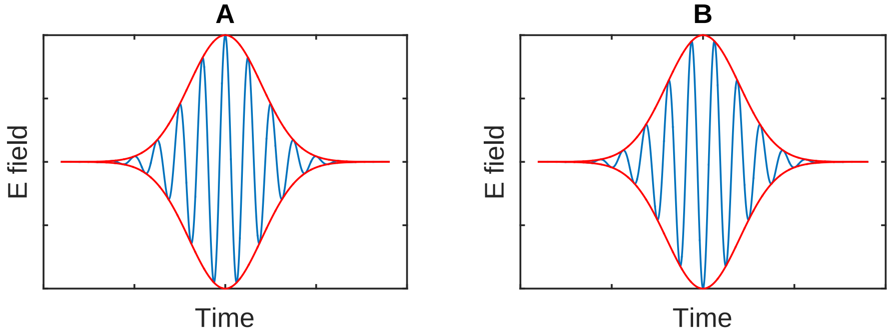

Figure 1.2: Time domain description of the carrier envelope phase evolution. (A) exhibits zero phase difference between the carrier envelope and the carrier frequency electric field, whereas (B) exhibits a $\pi/2$ phase difference between the two.

Generating frequency combs by modulating the injection current of solitary diode lasers and diode lasers in external cavities, as well as external modulation of CW emission, is a vast field of research that was founded in the early 1970s. Today there are multiple different techniques for frequency comb generation in semiconductor lasers and the use of diode lasers is still a very active field due to their size, cost to manufacture, robustness and ease of modulation. With the exception of the Vertical External Cavity Surface Emitting Laser (VECSEL), most semiconductor lasers certainly will not compete with octave spanning comb generation techniques [19]. Through a global desire for system miniaturisation however, their size and hence integrability into existing technology is incredibly attractive. In light of this, below we give a brief review of the salient methods by which to produce frequency combs from semiconductor lasers.

1.2.1 Frequency Comb Generators

The optical frequency comb generator (OFCG), first demonstrated by Kourogi *et al* [20], is a method for generating a broadband coherent set of equally spaced optical modes externally to the laser cavity. Unlike direct modulation of the laser, the optical frequency comb is produced by coupling the light from a stable master laser oscillator into a secondary optical cavity which contains an electro-optic phase modulation device. Phase modulation is achieved through modulation of the refractive index of an optical medium in synchronism with an externally applied electronic RF signal. The result of this modulation is the generation of optical sidebands which are phase coherent with the carrier and removed in frequency by an amount equal to the frequency of modulation. When the RF modulation signal is closely matched to the cavity longitudinal mode spacing the produced sidebands seed the adjacent cavity modes and the process is repeated. For clarity, this method is not the same as mode-locking, as the comb is generated externally to the laser cavity.

In principle any seed laser wavelength can be used provided the cavity maintains the appropriate finesse and a suitable phase modulator is available. For broadband cavity mirror coatings the tuning range is potentially of the order of hundreds of nanometres.

External modulation for frequency comb generation has been demonstrated with injection locked, gain switched Fabry-Perot diode lasers [21], gain switched DFB diode lasers [22] and semiconductor VCSEL's [23] all in the mid-1500 nm region. Also in the 1550 nm region, the emission from an OFCG has been combined with a short length of Tellurium-doped photonic crystal fibre for the generation of an octave-spanning spectra [24]. An excellent example of an OFCG operating at 780 nm, as well as a highlight of the background theory, is given by Kourogi *et al* in reference [25]. Finally, demonstration of a monolithic OFCG can be found in reference [26].

1.2.2 Gain Switching

Gain switching is a method whereby short optical pulses are achieved by rapid modulation of the laser pump energy by either short pump pulses or a sinusoidal pump signal. By applying a modulation to a laser which is operating just under the lasing threshold, the laser may be effectively turned on and off at a rate equal to the modulation frequency, albeit with a small delay relative to the pump energy. Typically with gain-switched diode lasers, there is no external cavity present and so the pulses oscillate inside the semiconductor waveguide between the two facets. Because of this operating principle, the modulation period can be varied over a large bandwidth. With this technique, in general, longer pulses result from longer modulation periods, and in all cases the resulting optical pulse in steady state must be temporally shorter than the round-trip time of the laser cavity.

Due to the pulse generation method, the wavelength regions that gain switching works is essentially limited by the spectral regions for which diode lasers can be fabricated. In 1983, Elliott *et al* generated circa 10 ps pulses [27], while later in 1989, Liu *et al* reported 6.7 ps pulses [28], at 1.3 microns and 863 nm respectively. Later still in 1991, Iwatsuki *et al* achieved sub 6 ps, near-transform-limited optical pulses at 1550 nm [29]. Astonishingly, in 1999 pulses as short as 20 fs were achieved with a system based around the use of gain switched emission from an injection-seeded diode laser [30].

1.2.3 Mode-Locking

As with both of the above techniques, mode-locking is a technique for generating short optical pulses from lasers. Its name is derived from the concept that the oscillating spectral modes acquire a locked relative phase relationship and, at a given position in the cavity, the electric field amplitudes of every mode periodically constructively interfere to give a short optical pulse. In actuality, this position of mutual constructive interference oscillates within the cavity at the photon round trip time and is collectively referred to as the optical pulse. The cavity round trip time is given by the inverse of the cavity FSR, which is the frequency difference between the allowed longitudinal modes of the cavity, given by,

$$\omega_{FSR} = \frac{\pi c}{nL}, \tag{1.1}$$

where c, n and L are, respectively, the speed of light, the cavity refractive index and the cavity mirror separation length. The optical path length of the cavity therefore determines the pulse repetition rate in the time domain and the optical mode separation in the frequency domain.

A laser operating in CW will have an initially oscillating mode which can be assumed to be at the centre of the gain profile. Creating the extra spectral modes requires the addition of a modulation process which affects either the light directly, or a frequency dependent operating parameter such as the rate of charge injection to the active region. The modulation, when operating at $\omega_m = \omega_{FSR}$, acts to transfer energy from the initially oscillating mode, ω_0, into optical sidebands either side of ω_0. With $\omega_0 \pm \omega_m$ now oscillating, the modulator continues to transfer energy from ω_0 into the sidebands, only now it can also transfer energy from $\omega_0 \pm \omega_m$ into $\omega_{+2m,0}$ and $\omega_{-2m,0}$ respectively. This energy transfer is the spectral broadening mechanism, and will continue until an equilibrium state is reached. This state is reached when, for all oscillating modes, the gain per mode equals the loss per mode. Assuming all systematic losses per mode are the same, the main spectral narrowing mechanism is therefore the shape of the gain profile above threshold and so the width of the mode-locked optical spectrum is a balance between the modulation energy transfer and the gain profile. The electric field of the first oscillating mode, in the frequency domain, can be written,

$$E\left(t\right) = E_0 e^{i(\omega_0 t + \phi_0)} \tag{1.2}$$

where E_0 and ϕ_0 are the electric field amplitude and phase of the carrier mode respectively. With modulation applied, and subsequently more spectral modes oscillating, the general expression for the total electric field is,

$$E\left(t\right) = \sum_{p=-m}^{m} E_p e^{i((\omega_0 + p\omega_m)t + \phi_p)}, \tag{1.3}$$

where E_p and ϕ_p represent the amplitude and phase of the p^{th} modes respectively, and $p = 0, 1, 2, 3,$ etc.

If the value of ϕ_p is random and variable in time for each oscillating spectral mode, the transient intensity will tend towards a fixed value and hence the laser is in CW operation, albeit with more than a single oscillating spectral mode. If however the value of ϕ_p is the same for each mode (zero for the sake of ease) and periodically invariant with respect to a fixed position in the cavity, the result is a sharp narrow spike in total field amplitude. This short spike in amplitude corresponds to a short spike in intensity which oscillates inside the cavity as time evolves, given by

$$I\left(t\right)=\left|E\left(t\right)\right|^{2}=E_{0}^{2}\frac{\sin^{2}\left(P\omega_{m}t/2\right)}{\sin^{2}\left(\omega_{m}t/2\right)}, \tag{1.4}$$

where $P = 2p + 1$. Here it has been assumed that all the optical modes have the same amplitude given by E_0. The width of the pulse in the time domain is inversely proportional to the number of modes oscillating in phase by a relationship known as the time-bandwidth product. For a Gaussian intensity profile, a time-bandwidth product of 0.44 signifies that the pulse is Fourier Transform (or "transform") limited, and hence all present optical modes are perfectly phase locked. In all cases the Fourier Transform of the spectrum in the frequency domain reproduces the pulse intensity profile in the time domain, however only a transform limited Gaussian pulse gives a time-bandwidth product of 0.44. A time-bandwidth product greater than 0.44 for a Gaussian pulse can occur for multiple reasons, such as that certain modes are not phase locked due to significant phase noise on the optical modes or that the laser cavity contains a net non-zero dispersion resulting in a frequency chirp within the intensity profile. In any case, these effects will be manifest in a pulse width appearing longer than the inverse measured spectral width.

As far as a mathematical description of mode-locked diode lasers is concerned, various transient behaviours of diode lasers can be explored by starting with a set of coupled rate equations for the oscillating electric field and the charge carrier density. These rate equations, which were born out of a semiclassical approach to modelling diode laser emission originally described by Haken *et al* [31] and Lamb [32], have been used to describe actively mode-locked diode lasers [33, 34], chaotic behaviour and relaxation oscillations [35]. They have also been further modified to account for spontaneous emission and to model the effects of injection locking, where one source of coherent radiation is injected into the cavity of a slave diode laser [36]. In-depth reviews are given by Tartwijk and Lenstra [36], Haken [37] and Agrawal and Dutta [38]. The rate equations themselves, which we derive for reference in appendix A, are given by,

$$\begin{aligned}\frac{dE\left(t\right)}{dt} &= \frac{1}{2}\left[\Gamma\left(1+i\alpha\right)G_N\left(N-N_{th}\right)\right]E\left(t\right)+E_{sp}\left(t\right),\\ \frac{dN\left(t\right)}{dt} &= \frac{J}{ed}-\frac{N}{\tau_{ib}\left(N\right)}-G_N\left[N\left(t\right)-N_{tr}\right].\end{aligned} \tag{1.5}$$

In these equations E and N are the time varying linearly polarised electric field and electron-hole pair number density (otherwise referred to as the carrier density), respectively, and N_{th} is the carrier density at the lasing threshold. Other symbols are defined as Γ, the optical confinement factor of the optical mode field inside the semiconductor waveguide, α, the linewidth enhancement factor and G_N the differential laser gain given by $G_n = \upsilon_{gr}\frac{\partial g}{\partial N}$, where υ_{gr} is the group velocity inside the laser medium and g is the overall gain coefficient. E_{sp} is the field contributed to the oscillating optical mode by spontaneous emission, J is the injected current density which provides the basic framework for current modulation of the laser gain, e and d are the electronic charge and waveguide thickness respectively, τ_{ib} is the carrier density dependent inter-band relaxation time and finally N_{tr} defines the carrier density required for the semiconductor to reach optical transparency.

In essence, light is produced in a semiconductor p-n junction by electron-hole recombination from the conduction to the valence band. If the band edges in the semiconductor are assumed to be flat, transitions between the conduction and valence bands are loosely analogous to those within a 2 level atomic system. The precise band structure of the devices used in this work is both mostly unknown and considerably more complicated than the flat 2 level system approximation used in the semiclassical approach. Accurate determination of the real band structure is however far beyond the scope of this work and also unnecessary within the framework of the semiclassical laser theory. Within this framework the complex electric field inside the laser cavity is adequately described classically using Maxwell's equations and the optical amplifier is described quantum mechanically. A quantum mechanical treatment of the amplifier medium is strictly required for a more complete picture because, where the flat 2 level model is employed, the presence of the electric field polarises the medium by inducing a dipole moment on each atom. Furthermore, in a real laser, a classical treatment of the amplifier medium is not capable of describing the spontaneous emission which is required for laser emission to begin. Conveniently though, we may avoid the quantum mechanics by using a self-consistency procedure [36]. This procedure states that for an electric field vector $\boldsymbol{\mathcal{E}}$ present in a polarisable medium, each atom acquires an electronic-dipole moment which, when averaged over all dipoles, results in a macroscopic polarisation, $\boldsymbol{\mathcal{P}}$. Through Maxwell's equations, this polarisation acts as a field source which results in the field $\boldsymbol{\mathcal{E}'}$. The self-consistency condition is therefore satisfied when $\boldsymbol{\mathcal{E}} = \boldsymbol{\mathcal{E}'}$. For a comprehensive quantum mechanical description of the gain medium, the reader is directed towards reference [39].

Further justification of the 2 level approximation is found through consideration of the timescales for intra-band relaxation within the semiconductor [40]. Intra-band relaxation processes occur on the order of 50 fs [41] which means that on the pulse timescales in the region of 1 - 20 ps, and with inter-band processes occurring on timescales of picoseconds to nanoseconds, the material polarisation can be effectively assumed to adjust instantaneously.

1.2.3.1 Passive Mode-Locking

Passive mode-locking is a process of pulse formation by modulation of the intra-cavity losses. Passive mode-locking is not forcibly synchronised to any form of external signal, instead relying on the inherent mode structure of the passive laser cavity to determine which optical modes may oscillate and the length of the cavity to define the pulse repetition rate. Passive loss modulation can be realised by utilising a nonlinear optical element called a Saturable Absorber. In the case of a saturable absorber mirror (SAM) the reflectivity of the mirror behaves non-linearly with the pulse intensity, preferentially reflecting only parts of the pulse whose intensity is higher than the saturation intensity. This process acts to lock the phases of the modes contributing to the pulse by attenuating the modes whose phase angles are out of alignment with the pulse amplitude maxima. For passive mode-locking to work with slow saturable absorbers, it is required that the saturable losses must saturate faster than the gain saturation, the absorber must recover faster than the gain and that the unsaturated gain just surpasses the unsaturated loss. The first condition insures that a net window of gain opens around the centre of the pulse. The second condition ensures that loss is greater than the gain everywhere other than the pulse centre when in pulsed operation as the gain should be lower than the loss at the point of gain saturation, and the final condition means that laser oscillation can build up when the laser is turned on in the first instance.

Passive mode-locking has been demonstrated using monolithic DFB lasers [42], quantum well lasers [43], quantum dot [44, 45] and dash lasers [46], as well as external cavity lasers [45, 47], and with external [48] and internal [49] pulse compression. Passive mode locking has also been demonstrated with diode lasers near our target wavelength [43, 50], and indeed further towards the blue/purple wavelengths [51, 52]. Repetition rates have also exceeded hundreds of GHz [53,54], and even THz [55,56] in a bid towards high optical communication data rates. Generally these ultrahigh repetition rates are achieved with colliding pulse mode-locking [57] and compound-cavity mode-locking [58]. Despite not being a diode laser, the Vertical External Cavity Surface Emitting Laser (VECSEL) [59] is also worthy of mentioning on account of the impressively short pulses that can be achieved [60].

1.2.3.2 Active Mode-Locking

Active mode-locking is achieved through modulation of the laser gain, cavity length (or refractive index), polarisation or losses at a rate which is derived from an external clock or oscillator. For any implementation of active mode-locking, the modulator frequency should be closely matched to the cavity FSR. In the case of diode lasers where strong RF sinusoidal modulation of the laser injection current is employed, the gain of the laser is modulated so as to selectively amplify the circulating pulse near the positive peak of the modulation amplitude. Where diode lasers have very short cavity lengths, modulation at the fundamental cavity mode spacing can be problematic most fundamentally in terms of modulation response at these frequencies, but also in terms of available modulation sources. In order to achieve active mode-locking in diode lasers, an external cavity may be used so as to lower the fundamental mode spacing into the 1-10 GHz region where high power electronic signal generators / amplifiers are readily available and also where the diode modulation response is typically superior. The important properties of the laser devices themselves is discussed in chapter 3. In terms of general operating conditions, it is common for the laser to be temperature stabilised, biased around threshold and modulated with signal powers of +25 dBm.

Active mode-locking has some significant advantages over passive mode-locking. Firstly, because the modulation signal is electronically generated, it is easy to synchronise with other equipment, as well as electronically stabilise using phase locked loops. A further related advantage is that multiple actively mode-locked lasers may be electronically synchronised, potentially paving the way towards cost effective forms of dual optical frequency comb spectroscopy with diode lasers. Secondly, as the magnitude of the gain seen by the pulse is defined by this external signal, pulse timing jitter can be very low compared with passive mode-locking [61]; the noise per mode originating from timing jitter is proportional to the mode number, compared with the square of the mode number for passive mode-locking [61].

One of the main appeals of using semiconductor lasers for mode-locking is the broad gain bandwidth, which is of the order of 10 to 20 nm. If emission over this bandwidth could be successfully mode-locked, the resulting pulse widths would have a conservative temporal width of 100 fs. Invariably however, pulses are limited to approximately five times this limit by various limitations including the modulation bandwidth limit, device parasitics and maximum modulation power handling. Due then to the relative flatness of the gain over the centremost nanometre of the total gain bandwidth, care should be taken to artificially narrow the optical spectrum, if necessary, so as to avoid mode-locking in clusters. These are discussed in more detail in chapters 3 and 6, but for now it may be understood as the monolithic diode laser cavity supporting isolated clusters of external cavity modes which are incoherent with one another, and therefore give rise to the emission of pulses which are not transform limited and likely contain noisy substructure.

A different form of active mode-locking occurs if the laser is operated well above threshold and phase-modulated rather than amplitude modulated. This 'FM mode-locking' is achieved either by modulation of the laser injection current or by an optical phase modulator such as an EOM [62, 63]. The principle of operation is almost identical; optical sidebands are generated by the phase modulation which must reside on a cavity resonance. The phase modulation propagates energy into successive sidebands and the constant inter-mode phase relationship gives rise to intensity pulses in the time domain.

Active mode locking has been achieved using many different types of laser diode, including a standard ridge-waveguide laser [64], Semi-Insulating Planar Burried Heterostructure (SIPBH) [65], free-space travelling-wave amplifier [66, 67] and Tapered Amplifers [68]. Where an external cavity has been used, feedback methods include reflection gratings [69–71], planar mirrors [64] and fibre ring cavities [72]. To date, the shortest known pulses from an actively mode-locked laser diode are 560 fs and were generated using a harmonically driven, actively mode-locked SIPBH structure [73]. An excellent review on active mode-locking in diode lasers can be found in reference [74].

1.2.3.3 Hybrid Mode-Locking

Hybrid mode-locking is the amalgamation of active and passive mode-locking. It combines the advantages of an electronically derived gain modulation at considerably lower RF signal powers with the relative experimental simplicity of passive pulse shaping. Hybrid mode-locking of a diode laser is possible using either free space optical elements [75–77] or where the saturable absorber, gain section and gain modulation section are formed in a single monolithic semiconductor waveguide and then integrated into an external cavity [51, 78–81].

Free-space optical elements can be used in various configurations. Using a ring cavity and active modulation of a semiconductor amplifier to promote the initial generation of optical pulses, a SAM can be placed after the amplifier to provide pulse shaping. It is also possible to use an external active loss modulator such as an Acousto-Optical Modulator (AOM) to provide amplitude modulation which a saturable absorber can then further shape into a short pulse. In the case of the monolithic devices, typically these consist of a large central section under DC forward bias to provide the bulk gain to the system, a small section for RF modulation at the front, an anti-reflection coated front facet (the facet which faces the external cavity) and a small section at the uncoated facet which is DC reverse biased. The actively modulated section therefore provides the electronic synchronisation and promotes pulse formation while the reverse biased section acts as a saturable absorber to provide passive pulse shaping. It is not uncommon for the active section to require 15-20 dBm less power than in a purely active system as it is the saturable absorber which performs the bulk of the pulse shaping. This in turn provides two advantages; the first being the need for much lower power RF electronics, and the second being that, through an electronically addressable absorber section, the DC reverse bias may be precisely tailored to generate the optimum pulse widths.

While this method routinely produces high quality (low time-bandwidth product) optical pulses in the low picosecond regime, it also requires specific fabrication of the devices if adopting the monolithic approach. To the author's knowledge, no commercially available devices at 780 nm are available, which means any hybrid approach to frequency comb generation would require a separate saturable absorber.

An interesting approach to hybrid mode-locking was reported in 2000 by Lee *et al*, whereby in a nominally actively mode-locked laser, the gain region is modulated at the first sub-harmonic of the cavity FSR such that the pulse traverses the cavity twice per modulation period [82]. By doing so, if the DC injection current is positioned such that the modulation current drops the carrier concentration below the transparency concentration during the negative portion of the modulation sine wave, the pulse experiences saturable absorption, and hence extra pulse shaping.

Chapter 2

Diode Laser Stabilisation and Rubidium Spectroscopy

In this chapter we introduce the diode laser, how it may be integrated to form an External Cavity Diode Laser (ECDL) and highlight its importance in the work to follow. We then continue to discuss the issues with diode lasers in terms of their optical emission, specifically linewidth and frequency stability, and then go on to describe how these issues may be overcome by way of wavelength stabilisation. In this thesis we employ a Rubidium stabilised ECDL as the CW reference laser for the air track Michelson interferometer in chapter 5 and as the experimental laser in chapter 8. As such, after briefly highlighting some of the common laser stabilisation methods, we go on to demonstrate and characterise the stabilisation of a CW ECDL to the laser cooling transition in ^{85}Rb.

Throughout this work, we make use of two distinct configurations of ECDL, and so it is worth setting in stone the distinction between the two early on. Unless otherwise stated, when addressing the use of a 'CW' laser, we are referring to the geometry highlighted in the following section of this chapter. When addressing the mode-locked laser, we are referring to the specific laser geometry introduced in section 3.2.

2.1 The Diode laser and the External Cavity Diode Laser

The light emitting part of the diode laser is formed when two specifically doped layers of semiconductor are formed together creating a p-n junction. The p-doped semiconductor has an excess of electron holes while the n-doped semiconductor has an excess of electrons. Upon formation the Fermi levels are misaligned and electrons from the n-doped region recombine with holes in the p-doped region leaving fixed positively (negatively) charged donor (acceptor) sites in the n (p) region respectively. Because of this growing charge gradient, a corresponding electric field grows across the semiconductor junction which opposes the respective charge diffusion, creating a region devoid of free carriers known as the depletion region. In other words, the electric field creates an energy barrier (known as the "Barrier voltage") which eventually becomes too great and prohibits further electron-hole recombination. At this point the Fermi levels are now aligned and the band edges are distorted.

In order to promote further recombination, a bias voltage must be applied to overcome the static electric field. The applied voltage creates an electric field that partially offsets the static field and therefore allows electrons and holes to flow into the depletion region and recombine radiatively. If the bias voltage is applied in the opposite polarity, the static field is enhanced thereby prohibiting any flow of charge; this is the device acting as a diode. The correct polarity for laser action to occur is to have the negative contact connected to the p-doped semiconductor, otherwise known as a forward bias. Emission wavelengths are defined by the semiconductor bandgap energy and can range between approximately 400 nm to a few tens of μm, with typical gain bandwidths of the order of 10 nm. The more precise operating wavelength then depends upon the laser cavity itself.

To achieve lasing, the gain in the laser resonator must overcome the total losses. These losses include mirror losses due to light coupling out of the cavity, mirror absorption, and all other non-useful optical losses. In a diode laser, as the injection current is increased, the point where lasing occurs is called the threshold current and signifies the transition from complete spontaneous emission to coherent output. After threshold the laser output power is approximately linear with injection current and the efficiency of the device is proportional to the power-current gradient.

With the mechanism for light generation in place, attention should now be paid to how the light is confined within the device. The semiconductor cleaved facets form a Fabry-Perot cavity, where the refractive index gradient between the semiconductor and the surrounding air of approximately 3.6:1 is sufficient to provide a normal incidence Fresnel reflectivity of ∼30%. The mirror separation distance, L, typically lies between 200-1300 nm. Light confinement in the spatial directions parallel and perpendicular to the plane of the substrate is achieved through refractive index gradients. The former is achieved through different semiconductor layers within the structure while the latter is achieved through either lower index semiconductor barriers or through 'gain guiding', which is where the higher carrier concentration in the depletion region raises the effective refractive index. Typical spatial dimensions are 100-300 nm and 1-2 μm for the thickness and width respectively. Light leaving the laser is subject to strong aperture diffraction where the rectangular shaped aperture gives rise to an elliptically shaped beam. A short focal length lens should be used to collimate the beam, and an anamorphic prism pair can be used to correct the beams elliptical spatial intensity profile if desired.

An External Cavity Diode Laser (ECDL) is formed when a standard laser diode is incorporated into a setup whereby light is fed back to the laser monolithic cavity via an external feedback element. The external cavity itself is formed by the front facet of the laser diode and the additional feedback element. Together, the diode laser monolithic cavity and the external cavity form a *composite* cavity. The spectral properties of this new configuration can have beneficial influences on the overall laser emission. In the first instance, if the linewidth of the external cavity is less than the linewidth of the isolated diode laser, the overall laser emission linewidth may be reduced [83]. Secondly, if a dispersive element such as a diffraction grating is used, this provides additional functionality in terms of wavelength tuning and hence stabilisation, and also has the ability to both narrow the linewidth yet further and force the oscillation of only a single monolithic cavity mode. Figure 2.1 shows the cavity configuration for the CW lasers used in this work.

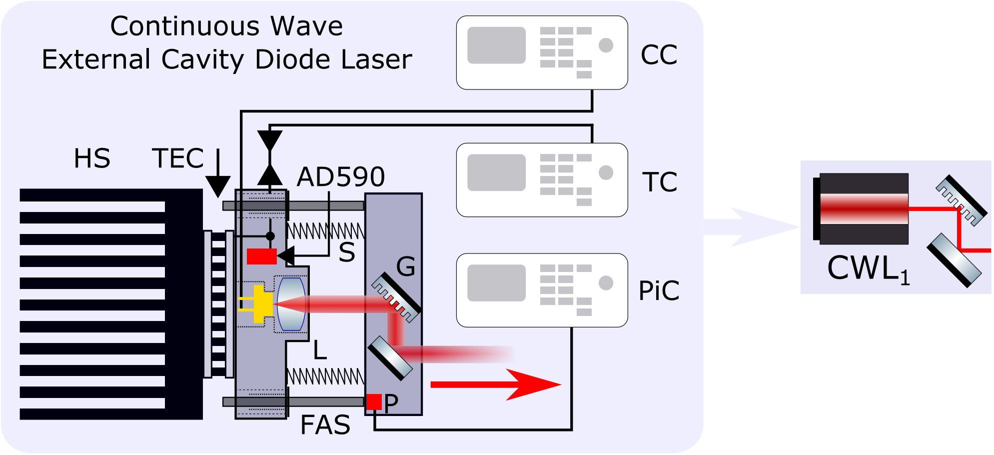

Figure 2.1: Schematic diagram showing the CW External Cavity Diode Laser and the reduced schematic used throughout the rest of the thesis to denote this optical arrangement. HS; Heat Sink, TEC; Thermo-Electric Cooler, S; Spring, L; Lens, FAS; Fine Adjustment Screw, G; Grating, P; Piezo, CC; Current Controller, TC; Temperature Controller, PiC; Piezo Controller. The AD590 is the temperature monitoring integrated circuit whose output is read by the thermal controller.

The external cavity is formed by the front laser facet and a diffraction grating which is mounted in such a way that the first order diffracted beam is reflected back to the diode, providing wavelength selectivity. The laser diode (Thorlabs L785P090) is mounted in a monolithic Aluminium housing and held in place by a threaded retaining ring. An aspheric lens (Thorlabs TME240-B) is mounted in the housing to provide collimation of the laser emission. A further housing containing a diffraction grating (Thorlabs G13-18V) mounted in the Littrow configuration [84–86] with an additional mirror[1] is spring mounted onto the ends of three fine adjustment screws (Newport AJS100-0.5H) which provide fine tuning of the external cavity. A temperature controller (Thorlabs TED200C) monitors the temperature reported by an AD590 integrated circuit and feeds back to the current of the peltier TEC which exchanges heat between the housing and the heatsink. DC Injection current to the laser is supplied by a Thorlabs LDC202 current controller. Scanning of the laser wavelength over approximately 3 - 4 GHz is provided by a piezo stack attached to a piezo driver which outputs an amplitude and frequency adjustable sawtooth or triangular waveform.

---

[1] The additional mirror is to largely eliminate beam pointing variations as the grating angle is changed.

2.2 Diode Laser Frequency Stabilisation

Among virtually all atomic, optical and molecular physics experiments there exist stable, narrow linewidth lasers. Indeed the 'out of the box' performance of the laser tends to be unsatisfactory for the final application, be it in terms of the laser linewidth, centre wavelength, drift stability or some combination thereof. The instantaneous linewidth emitted by a laser will in fact be very narrow; however over any appreciable experimental period of time, noise present in the laser system couples to the optical emission and results in linewidth broadening and drift of the central wavelength. For diode lasers a good general approximation is that the laser linewdith is the emitted power spectral density averaged over a few tens of milliseconds, resulting in a Gaussian lineshape, while drift is understood as the longer term change in position of this lineshape. Controlling the emission of the diode laser is a matter of correcting both of these effects by first comparing the optical frequency against a known stable frequency reference and then feeding back to the laser, in a suitable way, a signal derived from the offset from this known reference.

Diode lasers suffer from both fundamental and environmental noise. The former consists of processes intrinsic to the laser operation; the most notable of which is phase noise caused by spontaneous emission coupling into the oscillating laser spectral mode. The latter is essentially everything that affects the laser whose source exists externally to the gain region. Generally the most significant sources of environmental noise are thermal drifts caused by air currents and mechanical perturbation caused by vibrations generated from surrounding equipment and people. It follows that simple modifications to the lasers' immediate environment, such as blocking air currents and mechanically isolating the laser from the optical bench, can significantly reduce laser instability. A good attitude towards diode laser stabilisation is "One gets out what one puts in".

The basic principle behind laser stabilisation is to attempt to correct the laser frequency noise and drift by comparison of the laser frequency with a stable, fixed frequency reference such as a cavity [87–91], an atomic transition [92, 93] or both [94]. This real-time comparison results in a signal which is proportional to the absolute frequency difference and sensitive to the sign of the offset, and is known collectively as the 'error signal'. The error signal then requires suitable interpretation before being fed back to the laser and completing the feedback loop.

With semiconductor diode lasers there are three very common methods for feeding back to the laser; via the current, temperature and an intra-cavity dispersive element. Feeding back to the current is the most common due to the frequency bandwidth which can be corrected for. Limited typically by the servo gain bandwidth, feeding back to the current has the potential to correct noise Fourier components up to many tens, if not hundreds, of MHz.

Temperature variations tend not to be a path for active stabilisation in terms of the wavelength stabilisation. It is most common for the temperature stabilisation to be on a separate feedback loop where the temperature is monitored and corrected towards a user defined set point irrespective of the current laser wavelength. Further, the bandwidth limit of the temperature stabilisation is generally limited by the thermal capacity of the object being stabilised: Small thermal masses are susceptible to faster temperature changes but are more easily corrected in a timely manner, and vice versa. That is not to say however that the temperature set point cannot be chosen so as to tune the laser as closely as possible to the desired wavelength in the first instance.

Feeding back to an intra-cavity dispersive element, such as the angle of a diffraction grating, is also very common and typically caters for the larger, slower frequency variations up to approximately a few kHz as well as longer term wavelength drift. Adequate stabilisation of the temperature and feeding back to the grating angle can achieve linewidths on the order of 1 MHz. Adding feedback to the current can achieve linewidths of approximately a few hundred kHz [93]. Indeed, with adequate elimination of noise before it reaches the laser, it is possible to achieve passive laser linewidths of a few tens of kHz [95]. Expenditure of a significantly higher degree of effort can produce portable and stationary 1Hz linewidth diode lasers [96, 97], or static mHz linewidth diode lasers [98].

2.3 Review of Techniques

2.3.1 Frequency Modulation Spectroscopy

Frequency modulation (FM) [99,100], first demonstrated by Bjorklund [101], is a process whereby the instantaneous *frequency* of a sinusoidal (carrier) waveform is modulated by an amount proportional to the amplitude of the modulating waveform, thereby encoding the form of the modulation waveform onto the carrier. In the FM regime, as opposed to wavelength modulation, the act of frequency modulation imposes frequency sidebands on the carrier frequency, ω_0, which are separated from ω_0 by the modulation frequency, ω_m. The frequency triplet is then scanned over the optical resonance of interest and the resulting beam is detected by a photodetector. The photocurrent generated by the detector is mixed with a reference signal which, in this case, is a copy of the electronic modulation signal in a phase sensitive way known as demodulation. This demodulation may be conducted in two regimes; where the reference signal is in phase or in quadrature with the photocurrent (or 'experimental') signal, which, respectively, provides information about the absorption and dispersion properties of the optical resonance and hence the spectroscopic application is achieved.

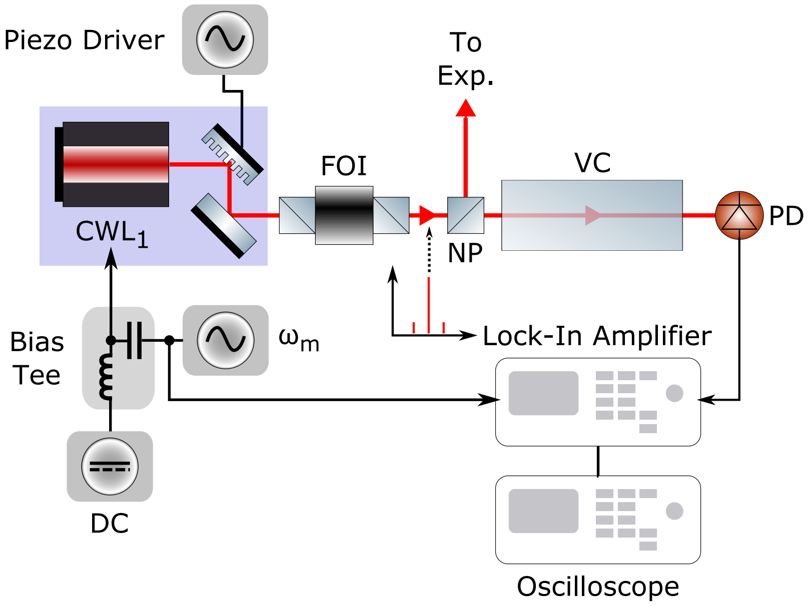

Figure 2.2: Diagram showing the schematic layout of a frequency modulation spectroscopy experiment. DC; Direct Current drive, FOI: Faraday Optical Isolator, NP; Non-Polarising beam splitter cube, PD; Photodiode, VC; Vapour Cell.

While we leave the mathematical description of this process to chapter 9, the experimental schematic required is given in figure 2.2.

Wavelength modulation (WM) is a very similar technique and the distinction between the two can be understood in terms of the unitless quantity called the modulation depth, β, which is given as the ratio of the peak frequency deviation experianced by the carrier and the frequency of modulation such that,

$$\beta = \frac{\Delta\omega}{\omega_m}. \tag{2.1}$$

In the FM regime, β is usually less than unity because ω_m is typically a fast, low amplitude signal resulting in first order sidebands only. Furthermore, for the sidebands to be discernible, ω_m should generally be at least twice the value for the laser linewidth FWHM. In the case of WM, the modulation signal more accurately takes on the form of a shallow gradient current ramp where instead of frequency sidebands being produced, the carrier frequency is swept over the resonance. This implies that β is very large as a result of $\Delta\omega$ and ω_m (the current ramp repetition frequency in this case) being of the order of the resonance linewidth (potentially MHz - GHz) and hundreds of kHz, respectively.

The FM regime is usually favourable for two reasons. Firstly, information about the amplitude absorption *and* dispersion lineshapes of an optical resonance can determined through phase sensitive demodulation of the FM beam after interaction with an analyte, and secondly, because ω_m can be placed in a region where very little spectral noise exists on the free running laser, ultrasensitive measurements of even the weakest resonances can be achieved.

Since its initial demonstration, this technique has also been extended with the use of higher order harmonic detection [102] and multiple simultaneous modulation signals [103].

2.3.2 Saturated Absorption Spectroscopy

Saturated Absorption spectroscopy is a sub-Doppler technique which uses a single photodiode to monitor the transmission of a weak probe beam through an absorbing analyte, whose optical properties are determined by a strong pump beam capable of saturating a resonant transition. For this technique to be most effective, the pump and probe beams should be derived from the same source and be counter propagating at the point of interaction with the analyte. Because the pump beam is capable of altering the population density of the transition ground state, the dependence of the magnitude of the absorbed optical power on the magnitude of the incident optical power is nonlinear. Nonlinear spectroscopy is a broad field which includes saturated absorption spectroscopy, as well as polarisation spectroscopy and techniques which rely on multi-photon absorption [104].

The linewidth of an electronic transition is most fundamentally limited by the lifetime of the excited state whereby the longer the spontaneous lifetime the narrower the transition linewidth. Any and all electronic transition linewdiths are therefore broadened homogeneously according to their spontaneous lifetime; this is referred to as Natural Broadening and has a Lorentzian lineshape. For the cooling transition in ^{85}Rb this natural linewidth is approximately 6 MHz.

It is experimentally convenient to perform spectroscopy on Rb when in the vapour phase. This however gives rise to a further broadening mechanism; that of Doppler broadening. Doppler broadening of the transition linewidth is an inhomogeneous effect, meaning that it does not affect all atoms equally. It manifests as a red or blue shift of the absorption frequency as governed by the atoms' speed and direction with respect to the direction from which the light field is incident. In other words, if the atom has a component of velocity along the laser propagation axis, the resonance frequency is blue (red) shifted if the component of the atoms' velocity is counter- (co-) propagating to the optical field. At room temperature, the atoms have sufficient velocity such that the Doppler broadened D2 line of ^{85}Rb is approximately 500 MHz and hence completely obscures the hyperfine structure.

Sub-Doppler spectroscopy is achieved not through slowing the motion of the atoms, but instead by addressing only the atoms whose velocity is zero along the laser propagation axes of the pump *and* probe beams simultaneously. This technique is commonly referred to as Lamb Dip spectroscopy [104] and characteristically shows a dip in the absorption of the probe beam at the central frequency of a Doppler broadened lineshape. To understand the Lamb Dip, let us consider the effects of the pump and probe beams as they are scanned in frequency across a resonance. Far from any hyperfine resonance, the ground state population observed by the probe beam is mostly unperturbed by the pump beam, as the two beams are absorbed by atoms of differing velocities. As such the absorption profile of the (monitored) probe beam depicts that of the Doppler broadened lineshape. As the laser is tuned through resonance, the strong pump beam is capable of saturating the hyperfine transition and reducing the population of the ground state of the atoms which are also seen by the probe beam, thereby yielding a peak in the probe beam transmission. The width of this peak is defined by the natural linewidth of the hyperfine transition.

A standard optical setup to achieve this kind of spectroscopy is depicted in figure 2.3 and an example of a saturated absorption spectrum achieved using a Rubidium vapour cell is given in figure 2.5.

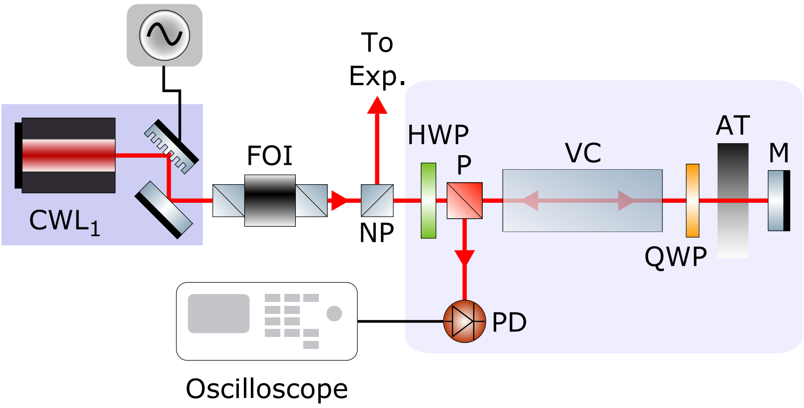

Figure 2.3: Schematic diagram of Saturated Absorption spectroscopy. FOI; Faraday Optical Isolator, NP; Non-Polarising beam splitter cube, HWP; Half Wave Plate, P; Polarising beam splitter cube, VC; Vapour Cell, PD; Photodiode, QWP; Quarter Wave Plate, AT; Attenuator, M; Mirror.

It is possible to use this spectrum directly as a frequency reference by using a technique called 'side of fringe' locking [105]. Side of fringe locking works by artificially offsetting the entire spectrum vertically such that the side of the resonance lineshape crosses zero at roughly half the height of the feature and using this zero position as the lock point. Clearly however, this means that the lock point is not at the centre of the hyperfine transition. By applying a weak modulation to the laser to generate optical sidebands and then demodulating as described in section 2.3.1 allows for the generation of an error signal for each transition which crosses zero at the transition centre.

2.3.3 Polarisation Spectroscopy

Polarisation spectroscopy [106, 107] is a sub-Doppler, pump-probe based spectroscopic technique using two beams originating from the same laser. In a pump-probe setup similar in layout to a variant of saturated absorption spectroscopy, a weak probe beam and a strong pump beam are sent near counter propagating through a vapour cell containing an analyte. The former beam is linearly polarised at 45 degrees to an analysing polarising beam splitter while the latter is circularly polarised. Far from resonance the pump beam observes no interaction with the analyte and hence the probe beam polarisation is unaltered yielding a net zero signal from dual balanced detectors placed after the analysing polarising beam splitter. Around resonance however the pump beam induces a birefringence in the complex refractive index of the analyte causing the probe beam polarisation to become elliptical, disrupting the complete signal cancellation during balanced detection. Polarisation spectroscopy provides an experimental error signal in the form of a dispersion lineshape that is both background free and suitable for use in active laser wavelength stabilisation. A schematic diagram of the optical configuration is shown in figure 2.4.

Linearly polarised light may be decomposed into left and right circularly polarised light (σ^- and σ^+ respectively) in equal measure. Optical pumping of a hyperfine transition with linearly polarised light will result in equal absorption of both σ^- and σ^+ components by the degenerate m_F states. The linearly polarised probe beam will therefore observe no birefringence as its polarisation components are also affected equally. By using a σ^+ circularly polarised pump beam, for example, it is possible to shift the population towards positive m_F states until equilibrium (saturation) is reached. At this point, the relative absorption coefficients for the two circular polarisation states of the probe beam differ from each other and, therefore, through the relationship between absorption and dispersion described by the Kramers-Kronig relation, the refractive index observed by each polarisation state is also different. This birefringence causes the probe beam to become elliptically polarised either side of resonance and hence an imbalanced intensity on the balanced detectors.

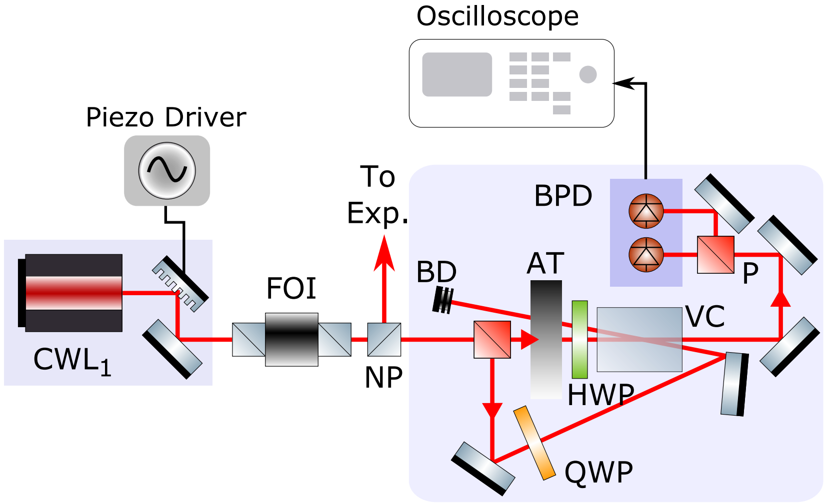

Figure 2.4: Diagram showing the schematic layout of polarisation spectroscopy. BPD; Balanced Photodiode, FOI; Faraday Optical Isolator, NP; Non-Polarising beam splitter cube, BD; Beam Dump, HWP; Half Wave Plate, QWP; Quarter Wave Plate, VC; Vapour Cell, P; Polarising beam splitter cube, AT; Attenuator.

2.3.4 Discussion

The above is a brief look into the many different techniques that can be employed in laser stabilisation. One further method commonly used in atomic physics is the Dichroic Atomic Vapour Laser Lock (DAVLL) [108, 109]. This method uses a magnetic field to separate the Zeeman sublevels so that the σ_+ transition is shifted to a higher transition frequency and the σ_- transition is shifted to a lower transition frequency. The polarisation content of a linearly polarised laser is then analysed by a linear polariser at 45 degrees to the laser polarisation axis and two photodiodes whose signals are subtracted from each other to generate an error signal.

A significant feature of polarisation spectroscopy over FMS and Saturated Absorption is the ability to derive a dispersion shaped error signal, which crosses zero at resonance, without the need to modulate the laser. Indeed, it is possible to frequency modulate the beam for FMS or saturated absorption after the beam has been split, however this requires the use of external phase modulators which are far more costly than the apparatus required for direct modulation of the laser bias current. It is for this reason that polarisation spectroscopy is implemented to stabilise the laser which is later used for injection locking the slave mode locked diode laser. DAVLL, while also not requiring modulation of the laser, is not preferable as it generates an error signal with a very shallow gradient, resulting in poor laser linewidth compared to the above techniques.

2.4 Rubidium Spectroscopy and Laser Stabilisation

As part of this demonstration, both a Saturated Absorption and Polarisation Spectroscopy setup were constructed for the purpose of calibration and comparison. In figure 2.5 we show an example Saturated Absorption spectrum, the corresponding two demodulated spectra when the laser in the saturated absorption configuration is frequency modulated and the spectra achieved by Polarisation Spectroscopy. All spectra are taken at a room temperature of 291 K and the wavelength scan is achieved by applying a sawtooth waveform to the piezo stack which controls the angle of the grating feedback element. The pump beam power for all four spectra was 250 μW and the Rb vapour cell is approximately 7 cm long and whose flat external faces are AR coated.

In the Saturated Absorption spectrum we can observe 12 peaks in the probe beam transmission. Each of these peaks is the Lamb dip of a hyperfine transition, however only six of these twelve peaks are real transitions. Peaks 1, 4 and 6, and 7, 10 and 12 correspond to real transitions ^{85}Rb F=3 - F$'$=4, 3, 2 and ^{87}Rb F=2 - F$'$=3, 2, 1 respectively, while 2, 3, 5, 8, 9 and 11 correspond to crossover peaks and appear exactly in the middle of their two corresponding constituent real transitions. The Doppler background has not been subtracted and the overall curve has been normalised so as to give an indication as to the relative peak sizes only. In reality, if the probe transmission far from resonance is normalised to unity, the trough of the Doppler broadened background typically drops to approximately ∼0.65 [2].

In order to achieve the two FMS spectra shown in figure 2.5, the saturated absorption setup is used and a -20 dBm, 1 MHz sine wave is superimposed upon the laser bias current via a bias tee so that very weak sidebands are generated in the laser emission. Using such a weak modulation signal ensures that only very weak first order only sidebands are generated. The detected probe beam transmission signal from the detecting photodiode is now demodulated against the laser modulation reference signal using a lock-in amplifier (SRS model 844). The phase angle of the reference signal with respect to the experimental signal is altered manually until the appropriate demodulated signal is achieved on the oscilloscope. The signals in the two FMS spectra have been manually offset so that the middle of the gradient for zero detuning corresponds to zero signal amplitude. The peak trace amplitude is then normalised to unity. This is perfectly acceptable as an arbitrary experimental signal input sensitivity may be chosen on the lock-in amplifier, hence only the comparison between features is important. The 1 MHz modulation signal was chosen such that the total 2 MHz separation between the sidebands was appreciably less than the 6 MHz FWHM natural linewidth of the hyperfine transitions.

The Polarisation Spectroscopy spectra in figure 2.5 shows two dominating polarisation features, corresponding to the two closed transitions in the two isotopes: ^{85}Rb F=3 - F′=4 and ^{87}Rb F=2 - F′=3. The other transitions are considerably smaller due to the high pump and probe power, and is done so that the closed transitions dominate. If a much weaker pump power is used, we would expect to see much more evenly shaped transition strengths [106].

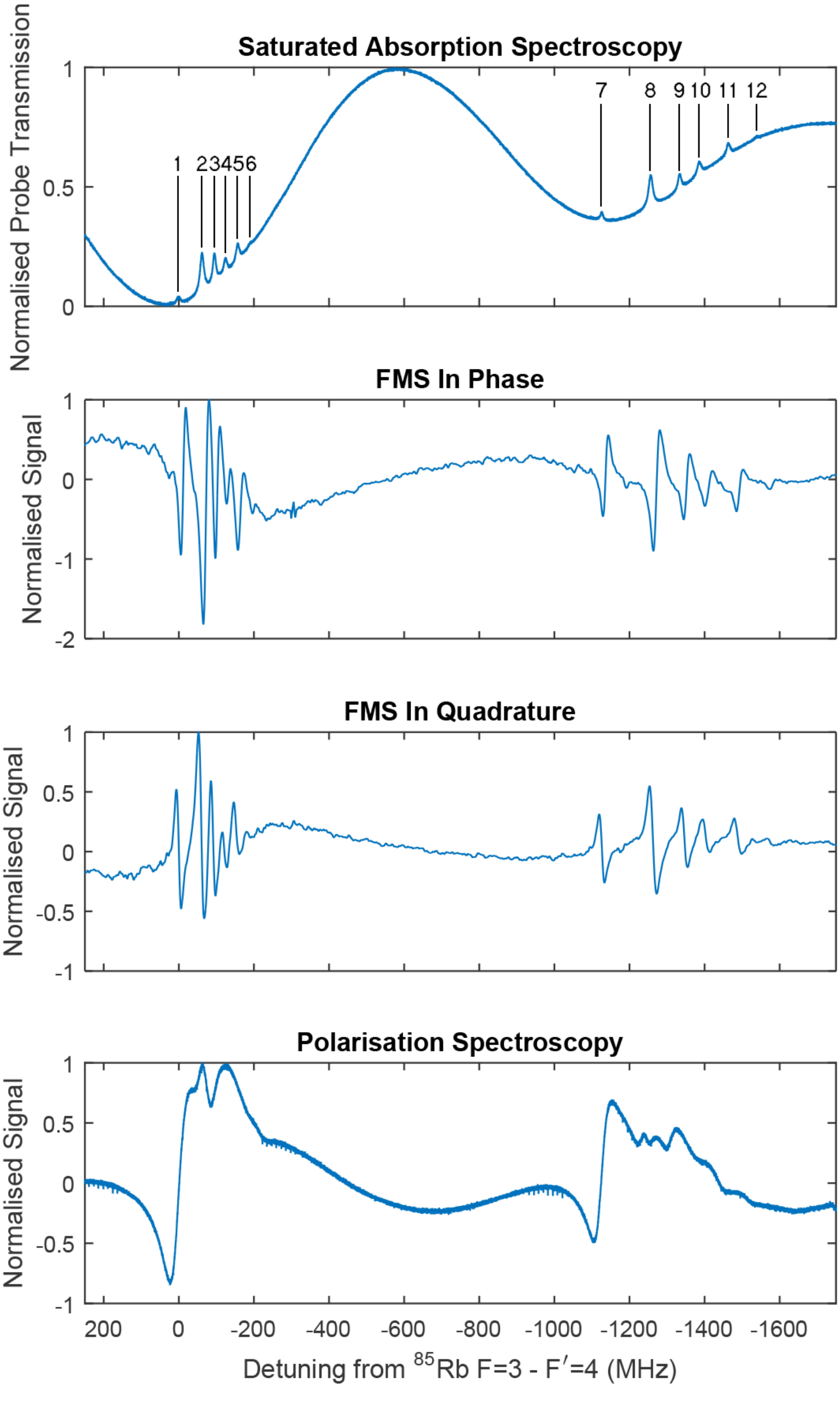

Figure 2.5: Figure showing the hyperfine spectrum of ^{85}Rb (left) and ^{87}Rb (right) D2 line with zero detuning corresponding to the $F = 3 - F' = 4$ transition in ^{85}Rb atom. The figure also shows the derived error signals for Frequency Modulation Spectroscopy (in-phase and in-quadrature signals) as well as the spectrum derived from Polarisation Spectroscopy.

2.4.1 Linewidth Measurement

In order to determine the linewidth of the lasers, a beat note is produced on an RF spectrum analyser between two ECDLs (which are a carbon copy of each other) where each laser is wavelength stabilised via its own separate (identical where possible) polarisation spectroscopy experiment. In order to measure the beat note between two lasers, there are a number of conditions which should be satisfied. Firstly, the two beams incident on the photodiode should have a component of their polarisations parallel to each other. The maximum signal will be achieved when the laser polarisations are as close to parallel as possible. Secondly, the beams should be as close to perfectly co-propagating as possible. If the beams are convergent on the photodiode, this will give rise to a spatial intensity profile. In this case the surface area of the photodetector must be smaller than a single spatial fringe in order to observe a signal. Thirdly, in terms of the laser linewidth, the beat frequency should be placed at least a single laser linewidth from zero frequency. Finally, no part of the detecting equipment should have a frequency bandwidth less than the beat note frequency.

Directly after the Faraday isolators of each laser, a beam splitter divides the beam powers equally, where one portion of each beam is sent to its respective polarisation spectroscopy setup, and the other is used in finding the beat note. These two beams are aligned to each other over a distance of at least 4 meters using mirror pairs and a single non-polarising beam splitter cube. Their polarisations are then aligned by a single polarising beam splitter cube before being focused on a fast photodiode (EOT Model ET-4000). The photodiode is connected to a RF spectrum analyser (Advantest R3273) where the beat note is observed directly.

The two lasers are locked, respectively, to the ^{85}Rb F=3 - F$'$=4 and ^{87}Rb F=2 - F$'$=3 transitions, giving a beat note at 1126.5 MHz. It is expected that the laser linewidths are Gaussian and hence the individual linewidths are equal to the measured beat note linewidth divided by 1.44. Figure 2.6 shows the measured beat note linewidths for when the two lasers are locked, (A) and (B), and when they are free running, (C) and (D), where (B) and (D) represent the linear, normalised conversions of (A) and (C) respectively. From the Gaussian fit, we extract a FWHM of 792±9 kHz for the locked lasers and a FWHM of 1.188±0.039 MHz for the unlocked lasers. We therefore arrive at individual laser linewidths of 550±6 kHz when stabilised, and 825±27 kHz when free running. With regards to the linewidth requirements set out in the previous chapter for the cooling and trapping of Rubidium, the locked laser linewidth is acceptably narrow over the 100 ms sweep time of the measurement.

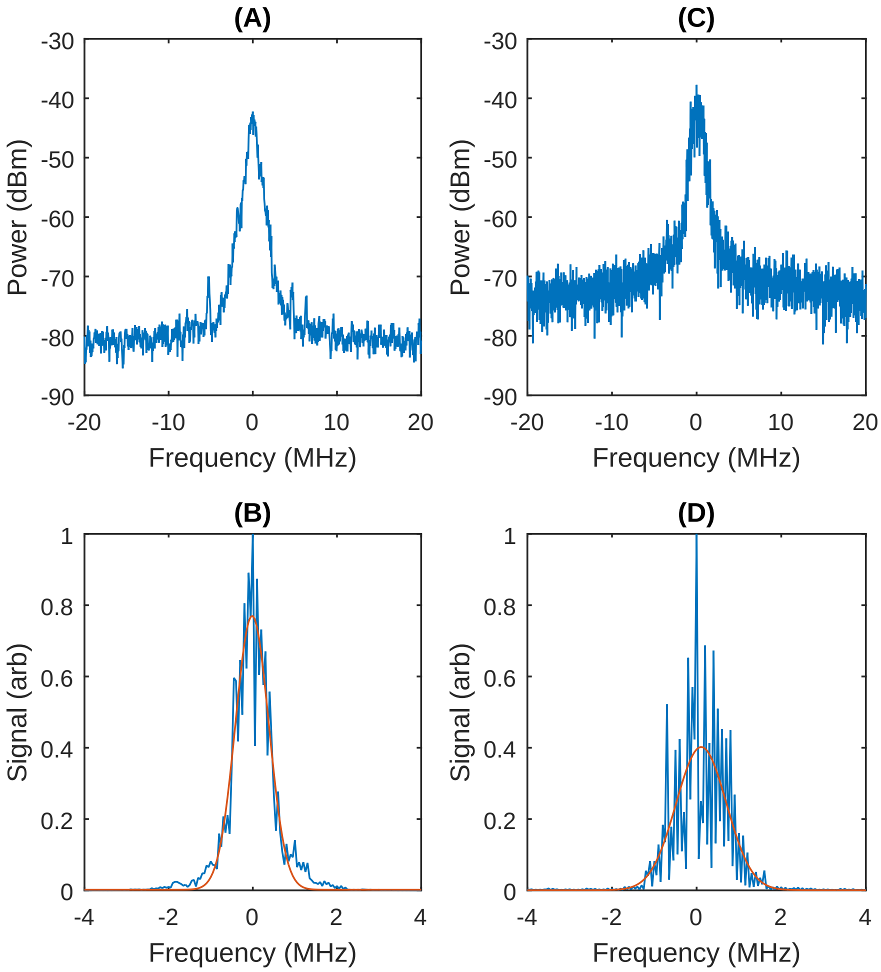

Figure 2.6: Comparison of the beat note between two CW ECDLs when stabilised to Rubidium, A and B, and free running, C and D. For this comparison, two polarisation spectroscopy experiments were constructed, one for each ECDL. For the locked beat note, the two lasers were respectively locked to the ^{85}Rb F=3 – F$'$=4 and ^{87}Rb F=2 – F$'$=3 transitions, providing a beat note at 1126.5 MHz on the RF spectrum. (A); RBW=1.1 kHz, VBW=1.0 kHz, 100 ms sweep time. (C); RBW=5.6 kHz, VBW=4.3 kHz, 100 ms sweep time. Figures B and D are the linear conversion of A and C respectively, where the maximum amplitudes are normalised to unity and then fit with a non-linear least squares Gaussian fit (Red curves).

Chapter 3

Continuous Wave and Current Modulation Characterisation

The focus of the thesis now returns to the diode laser mode-locking for the following five chapters. This chapter and the next present the bulk of the device characterisation in terms of the modulation response and mode-locking performance. It is important however to first understand the ideal device physical characteristics in order to provide context and initial direction for the investigation. Following this the main experimental configuration used throughout the thesis is presented in detail along with a description of the salient analytical equipment employed. Experimental investigation begins with a characterisation of the CW operation of the chosen laser diodes as this provides information regarding the threshold current, wavelength tuning rates [110] and external differential efficiency [111,112], as well as a basic measure of the quality of the AR coating on the diode front facet. We next present a weak modulation signal optical characterisation and finish with a purely electronic characterisation with the aim of developing an impedance matching circuit for enhanced modulation efficiency. The principle reason for the small signal modulation response investigation is that, through consideration of the S_{21} and S_{11} parameters, we may yield information about the optical modulation efficiency and possible electronic parasitics [113–115] associated with the circuit.

3.1 Important Laser Diode Properties

As we are aware, active mode-locking in semiconductor injection lasers can be achieved through strong RF modulation of the laser gain [64, 69, 73] whereby the modulation signal is coupled capacitively to the DC injection current that biases the laser, and is achieved using a bias tee circuit. The modulation signal itself is typically a sinusoidal waveform whose period matches the optical round trip time of the laser cavity. The diode laser is incorporated into an external cavity so as to reduce the fundamental modulation frequency to approximately 3 GHz. The first key property is therefore the efficient optical coupling to the external cavity. This is important because we wish for the spectral influence of the composite cavity to completely dominate over any spectral or temporal effects caused by the monolithic laser cavity. Achieving this optical coupling requires a high quality anti-reflection coating on the diode front facet. To quantify what is meant by 'high quality', an AR coating in this context is referred to as good if it exhibits power reflectivity lower than 0.1%. If the AR coating is either not present, or of poor quality, trailing optical pulses may be observed in the time domain and strong modulation of the optical emission spectrum (at a frequency equal to the semiconductor cavity FSR) may be visible in the spectral domain.

A possible knock-on effect is that this etalon behaviour gives rise to isolated groups, or 'clusters', of optical modes that are in themselves phase coherent and as such form an optical pulse. Each cluster is not necessarily phase coherent with the adjacent cluster, and in the temporal domain the pulses are overlapped. This lack of 'inter-cluster' coherence is governed by the quality of the AR coating and the modulation strength [116].

The second important property is that the combined diode and external cavity configuration provides a high slope efficiency. The slope efficiency is given by the rate of change of optical power with DC bias current and it essentially parameterises how well the laser as a whole converts electrical power to optical power. This is important in the mode-locking process because it helps define how effectively a given modulation signal power modulates the laser gain. Fortunately this measurement is incredibly straightforward to take as it only involves measuring the optical power as a function of DC injection current while the laser is in CW operation. Coincidently, if the external cavity is removed (or simply angled away so as to eliminate any optical feedback) and the optical power is measured over the same current range, an indication of the quality of the AR coating can be achieved.

The third, and possibly the most important aspect however is a large gain modulation bandwidth. The modulation response of a diode laser is generally split into two regions which are separated by the relaxation oscillations. At frequencies lower than the relaxation oscillation frequency, it is generally assumed that the charge carrier density in the conduction band of the laser is able to follow the influence of the applied modulation signal. Above the relaxation oscillation resonance however, the carrier density response to the modulation falls off rapidly. The modulation bandwidth is therefore loosely defined as the -3 dB bandwidth after the observed laser relaxation oscillation frequency, and is governed by device parasitics which prohibit modulation current from reaching the active region. For the purpose of short pulse mode-locking, a large modulation bandwidth is of paramount importance due to the strong pulse shortening effects observed for a high power, high frequency modulation signal [65, 117]. For our intended purpose of demonstrating a narrow-band stable optical frequency comb reference, we do not require necessarily the shortest optical pulses, and so significant modulation response up to only ∼4 GHz is sufficient.

The final requirement is to do with the stability of the modulation source. Excessive phase noise in the RF oscillator will translate to enhanced inter-mode beat note linewidths in the spectral domain and increased pulse to pulse timing jitter in the temporal domain [118].

While active mode-locking of semiconductor diode lasers has been demonstrated many times over the last 3 decades, to our knowledge, attempting to mode-lock the specific devices employed here has not been conducted. Moreover these laser diodes are ’off the shelf’ devices and hence none of the above parameters are known. This is in contrast to much of the previously reported active mode-locking literature in which the devices being explored are fabricated to custom specifications. Therefore three main ’datasheet’ criteria had to be considered when choosing a device which, in approximate order, are:

- Reflectivity of internal semiconductor facet - Diode lasers are exceptionally sensitive to optical feedback due to their very high small signal gain. Sensitivity to reflection coefficients as low as -80 dB have been reported [119]. Further, as described above, the AR coating is critical to the external cavity coupling efficiency and reducing the effect of the monolithic cavity.
- Maximum injection current capability - Active mode-locking through injection current modulation generally requires upwards of +25 dBm of RF modulation power.
- Per unit cost of the laser devices.

The mere requirement of an AR coating on the diode front facet filtered out the vast majority of commercially available devices, and at the time (early 2013) no commercial devices were available which were designed for high power, high frequency current modulation. We outline the chosen device below and discuss its integration into a custom external cavity.

3.2 Experimental Configuration

Figure 3.1 shows a schematic representation of the experimental mode-locked laser configuration. The specific devices settled upon are GaAs ridge waveguide Fabry-Perot semiconductor diode lasers (Eagleyard EYP-RWE-0790-04000-0750-SOT01-000) with an AR coating on the front emission facet. The (stated) maximum operating injection current is 180 mA and the AR coating reflectivity is typically 0.03%. These devices are housed in a standard TO-9 case and therefore are compatible with the custom solid aluminium laser diode mounts previously fabricated for our research group. These mounts are based on a modified design by Arnold *et al* [86, 120]. Emission from the laser is collimated with an 8mm focal length, 0.5 NA aspheric lens (Thorlabs TME240-B) and the external cavity is formed by using a 50±3% output coupler mirror (Layertec GMBH, model 110095). The output coupler is mounted centrally in a bracket which has fine angular adjustment control via three (pitch, yaw and extension) fine adjustment screws (Newport AJS100-1H) and in all cases the external cavity is aligned for minimum lasing threshold. The laser diode is mounted inside the custom housing and held in place by a retaining ring to avoid gradual cavity misalignment. To ensure good electrical contact with the external contacts, the core and cladding of a sliced SMA cable are soldered directly to the laser anode and cathode respectively. At the other end of the short SMA cable is a Bias-Tee (Mini Circuits ZX85-12G+) which allows for the RF modulation signal to be superimposed upon the DC injection current. The DC operating current is provided by a Thorlabs LDC202 laser diode controller. Temperature control of the laser diode is provided by a Thermo-Electric Cooler (TEC) which is placed between the laser mount and an intermediary heat sink, and is controlled by a Thorlabs TED200C temperature controller. The controllable resolution of the current driver and temperature controller are 0.01 mA and 0.01°C respectively.

The temperature controller is attached to an AD590 integrated circuit (IC) which measures absolute changes in the mount temperature. The temperature controller monitors the reported temperature value and compares it to a user defined set point temperature. A built in PID in the temperature controller feeds back to the TEC current so as to nullify any offset between the actual and set point temperatures. The intermediary heatsink is cooled by four TEC's wired in series and connected to a standard lab DC power supply with completely manual voltage set point. This configuration provides a good balance between fine temperature control at the lasing device while maintaining a broad overall temperature tuning range.

Modulation of the laser diode is achieved through a low noise Voltage Controlled Oscillator (VCO, Mini Circuits ZX95-3600+) which generates a low power (+3 dBm) RF modulation signal which is subsequently bandpass filtered (Mini Circuits VBF-2900+) and amplified to approximately +27 dBm (Mini Circuits TVA-11-422). The VCO output frequency is controlled by a custom made voltage source based on a precision voltage reference semiconductor IC (REF01) and the VCO tuning sensitivity is approximately 30 MHz/V.

Multiple items of equipment are used in analysing the laser emission and these are summarised in table 3.1 below.

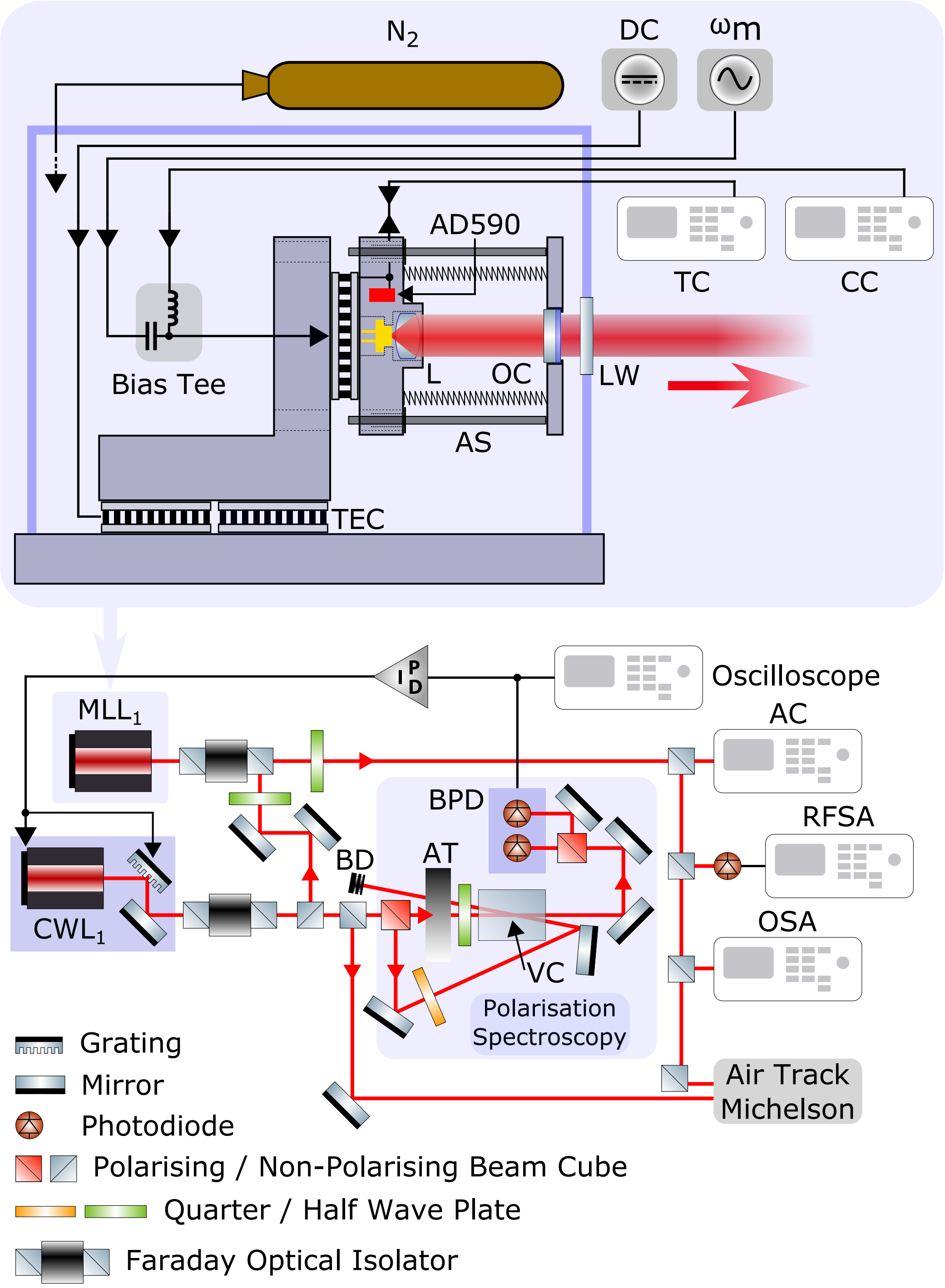

Figure 3.1: Schematic diagram of the experimental arrangement.(Top) Mode-locked diode laser, surrounding housing and operating equipment. TEC; Thermo-Electric Cooler, AS; Fine Adjustment Screw, L; Lens (Aspheric), OC; Output Coupler, LW; Laser Window, TC; Temperature Controller, CC; Current Controller. (Bottom) Mode-locked diode laser integrated into wider experiment. The CW laser 1 can be both spectroscopically locked to Rubidium via polarisation spectroscopy and used as the seed injection source for the mode-locked laser. BD; Beam Dump, AT; Attenuator, BPD; Balanced Photo Detector, AC; Autocorrelator, RFSA; RF Spectrum Analyser, OSA; Optical Spectrum Analyser, DC; Direct Current.

Model	**Technique**	**Notes**
Advantest R3273	RF Spectrum Analyser	26 GHz bandwidth
AndoAQ-6315A	Optical Spectrum Analyser	0.05 nm resolution
Femtochrome FR-103XL	Intensity Autocorrelator	0.1 ps temporal resolution
Advantest TQ-8326	Wavemeter	1 pm / 100 MHz resolution
New Focus 1414	Fast Photodiode	25 GHz bandwidth
EOT model ET-4000	GaAs Fast Photodiode	12.5 GHz bandwidth
Hamamatsu G4176-03	Fast Photodiode	7.5 GHz bandwidth
Mini Circuits ZVA-183+	RF amplifier	18 GHz bandwidth
Tektronics MDO4104B-6	Oscilloscope	1 GHz bandwidth
Agilent 86116A	Fast Oscilloscope	63 GHz bandwidth
Mini Circuits TVA-11-422	RF Instrument Amplifier	4.2 GHz bandwidth
Agilent 8753ES	Vector Network Analyser	30 kHz - 6 GHz bandwidth

Table 3.1: Summary of main light analysis equipment employed.

3.3 Continuous Wave ECDL Characterisation

3.3.1 Injection Current vs Optical Power - The I-P Curve

An external cavity diode laser (ECDL) is formed with the Layertec 50% planer output coupler mirror, and the overall laser composite cavity is formed by this mirror and the rear, uncoated facet of the semiconductor gain chip. Due to the AR coating, the semiconductor monolithic cavity is assumed at this point to contribute negligibly to overall feedback into the gain region. We begin by considering the power-current behaviour of the laser where data for with and without the external cavity feedback are presented in figure 3.2.

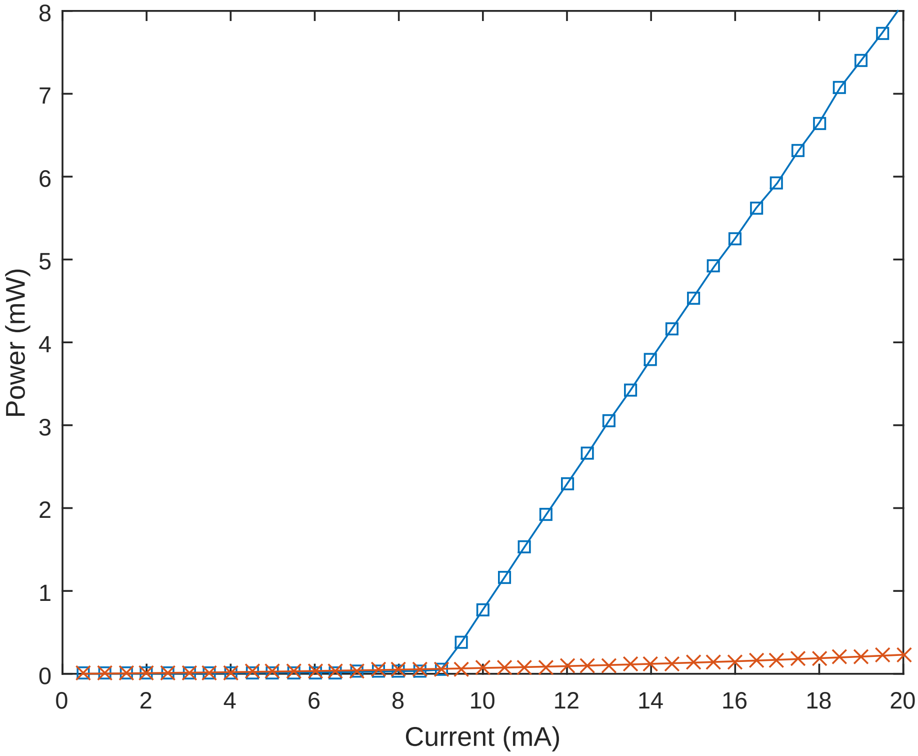

Figure 3.2: Threshold and output power characterisation for CW operation of the mode-locked diode laser with (blue) and without (red) a 50% output coupler. The internal diode facet is AR coated to 0.03%. The threshold current, I_{th}, is calculated to be 8.96 mA± 0.04 mA.

Clearly observable in figure 3.2 are both the threshold current at ∼9 mA and the expected linear region of operation post threshold. Within this linear operation regime the slope efficiency of the compound device can be calculated so as to quantify the pump to optical power conversion. Calculating the slope gradient to be 0.734±0.040 W/A, the external differential quantum efficiency, η_{ext}, is given by [121],

$$\eta_{ext} = \frac{dP_{cw}}{dI}\frac{e\lambda}{hc} = 0.464 \pm 0.040 \tag{3.1}$$

where P_{cw} is the measured optical power for a given DC injection current I, e is the electronic charge, h is the Planck constant, λ is the emission wavelength and c is the vacuum velocity of light. The uncertainty is calculated from figure 3.2 by a linear regression fit and extraction of the RMS uncertainty. The confidence bounds are 95%. Our value for the slope gradient is approximately a factor of 17 better than in reference [73] ∼0.041

W/A, $\lambda = 1.30\mu$m) and 1.3 better than in reference [122] ($\sim 0.56\ W/A, \lambda = 785.5nm$). It is however also considerably lower than in reference [123], which demonstrates a slope gradient of 1.19 W/A at 812.8 nm.

Also shown in figure 3.2 is the power-current data for the same ECDL configuration with the output coupler mirror tilted sufficiently to avoid any feedback to the gain section. The behaviour of the optical output below the threshold current is expectedly similar and no linear region is found indicating that no significant optical cavity exists in this current range. Feedback from the imperfect AR coated facet mirror, while very weak, is still non-zero and so will eventually feedback sufficiently to cause stimulated emission. It is anticipated however that the injection current required to observe this is both considerably above the expected bias current region for mode-locked operation and close to, if not beyond, the current damage threshold for the devices.

3.3.2 Current and Temperature Wavelength Tuning

Figures 3.3 and 3.4 show, respectively, the tuning rates of the Eagleyard laser diodes with respect to injection current and temperature. The data in these figures is acquired using a fibre coupled wavemeter with stated frequency resolution of 100 MHz, whereby the optical frequency reading is logged approximately every three seconds for a period of three minutes for every current and temperature increment. It should be noted here that a significant issue was faced when attempting the following data capture while using the 50% output coupler mirror to form the external cavity. Over the current range of 10 to 25 mA (I_{th} = 8.96 mA± 0.04 mA) the laser exhibited a large range of highly unstable operation and the linewidth broadened to approximately 0.5 nm in a symmetric 9 mA current region centred at 18.5 mA. No useful tuning data was achieved. A reasonable hypothesis is that this was caused by both the lack of a dispersive optical element inside the cavity and possibly weak extra-cavity optical feedback; unwanted optical feedback can be very effective in destabilising the laser emission. In addition to an extra optical isolator outside the cavity, a 20 μm thick, uncoated fused silica etalon was placed inside the cavity and, while the laser stability saw significant improvement, still no useful data was achieved. An unsettling notion is that the laser instability is being caused by feedback from the imperfect AR coating on the semiconductor facet. A possible explanation for the observed linewidth broadening is that if the feedback from the AR coated facet is sufficient, competition exists between two or more internal cavity modes due to the position and magnitude of the gain curve, thereby destabilising the emission. This notion is supported (though not confirmed) by the observed partial emission stabilisation as a result of the large FSR, low finesse etalon being added to the laser cavity.

For the purpose of these measurements only, a new external cavity was formed by temporarily replacing the output coupler mirror with a diffraction grating (1800 lines/mm) in a Littrow configuration identical to the setup described in figure 2.1. The spectral resolution of the grating is given by $\Delta\lambda = \lambda/\mathrm{N}_l \simeq$ 100 GHz, where N_l is the number of grating lines illuminated.

Observable in figure 3.3 are regions of higher point density which are the modes of the external laser cavity. Their separation is approximately 0.007 nm (∼3.4 GHz) which corresponds well to the approximate physical dimensions of the laser cavity. From these data it is calculated that the current tuning rate of the laser is 0.00166±0.00006 nm/mA (-808±29 MHz/mA). Somewhat bafflingly, there exists a non-negligible point density at wavelengths between the external cavity modes. This behaviour is unexpected considering that there is no part of the cavity whose length corresponds to a mode separation of $\simeq$1.7 GHz.

Figure 3.4 demonstrates the tuning characteristics for the laser as a function of changing temperature. Averaged over the plotted data the temperature tuning rate of the oscillating optical frequency is 0.00984±0.00058 nm/K (-4.790±0.281 GHz/K) and so this represents a far coarser wavelength tuning method.

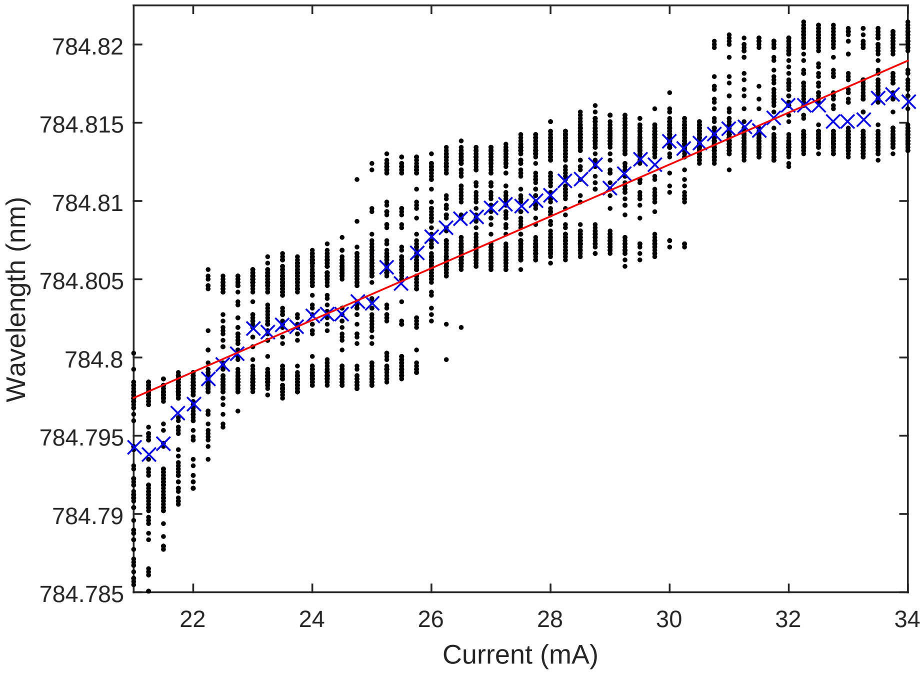

Figure 3.3: Wavelength tuning characteristics for varying DC injection current. Black points represent the individual wavelength measurement data points, the average of these measurements per current setting is given by the blue crosses and the red line represents the (linear regression) fit to the average.

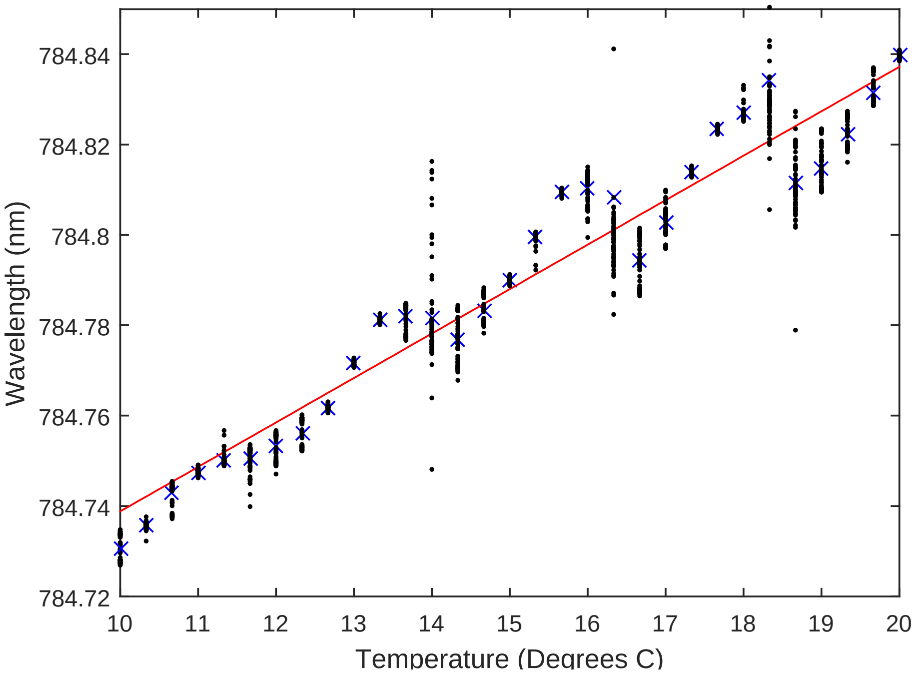

Figure 3.4: Wavelength tuning characteristics for varying mount temperature. Black points represent the individual wavelength measurement data points, the average of these measurements per temperature setting is given by the blue crosses and the red line represents the (linear regression) fit to the average.

3.4 Diode Laser RF Modulation Response

We begin the analysis of the current modulated diode laser by considering the optical response to a weak RF modulation signal over a large frequency span without the external cavity. In order to obtain meaningful results for the modulation response, we require a calibrated system capable of determining the magnitude and phase of a measured signal with respect to the supplied modulation signal. The Vector Network Analyser is such a system and the meaningful parameterised data is provided in the form of the Scattering parameters, or 'S-Parameters'. The S-Parameters are directionally sensitive coefficients which describe the magnitude and phase of a signal at a chosen port with respect to the origin of the signal (see figure 3.5(A)). For our purpose the S-parameters of interest are the forward scattered, S_{21}, and back scattered, S_{11} parameters, which represent the signal received at port 2 and port 1 respectively, given a modulation signal originating from port 1. Under this convention the S_{21} and S_{11} parameters provide information for the electrical to optical conversion and back reflected modulation signal respectively.

Mathematically the S-parameters are represented in matrix form by the following relationship,

$$\begin{pmatrix} b_1 \\ b_2 \end{pmatrix} = \begin{pmatrix} S_{11} & S_{12} \\ S_{21} & S_{22} \end{pmatrix} \begin{pmatrix} a_1 \\ a_2 \end{pmatrix}, \tag{3.2}$$

where, after expansion, we find the two relationships given by,

$$b_1 = S_{11}a_1 + S_{12}a_2, \tag{3.3a}$$

$$b_2 = S_{21}a_1 + S_{22}a_2. \tag{3.3b}$$

In this description the subscripted numbers on each lower case letter define the port number on the VNA, and so it follows, perhaps in a somewhat unintuitive way, that a_1 and b_1 are in fact physically connected to the same VNA port. Each port on the VNA is terminated with a characteristic impedance, Z_0, which in most instances is 50 Ohms.

Solving for each S-parameter, where $a_1 = \mathcal{V}_1^+$, $a_2 = \mathcal{V}_2^+$, $b_1 = \mathcal{V}_1^-$ and $b_2 = \mathcal{V}_2^-$, we find,

$$S_{11} = \frac{\mathcal{V}_1^-}{\mathcal{V}_1^+}, \quad S_{21} = \frac{\mathcal{V}_2^-}{\mathcal{V}_1^+}, \quad S_{12} = \frac{\mathcal{V}_1^-}{\mathcal{V}_2^+}, \quad S_{22} = \frac{\mathcal{V}_2^-}{\mathcal{V}_2^+}, \tag{3.4}$$

where $\mathcal{V}$ is a voltage and the superscript sign defines the direction of the signal with respect to the subscripted port number i.e. negative and positive refer to a reflection and transmission of signal respectively. Experimentally, we are usually interested in the magnitude of the S-parameters on a log scale, which is given mathematically as $-20\log_{10}|S_{xx}|$ in dB.

Figure 3.5(B) gives a schematic representation of how the VNA is connected to the laser diode. The Device Under Test (DUT) is a combination of the Bias Tee, laser diode and fast photodiode

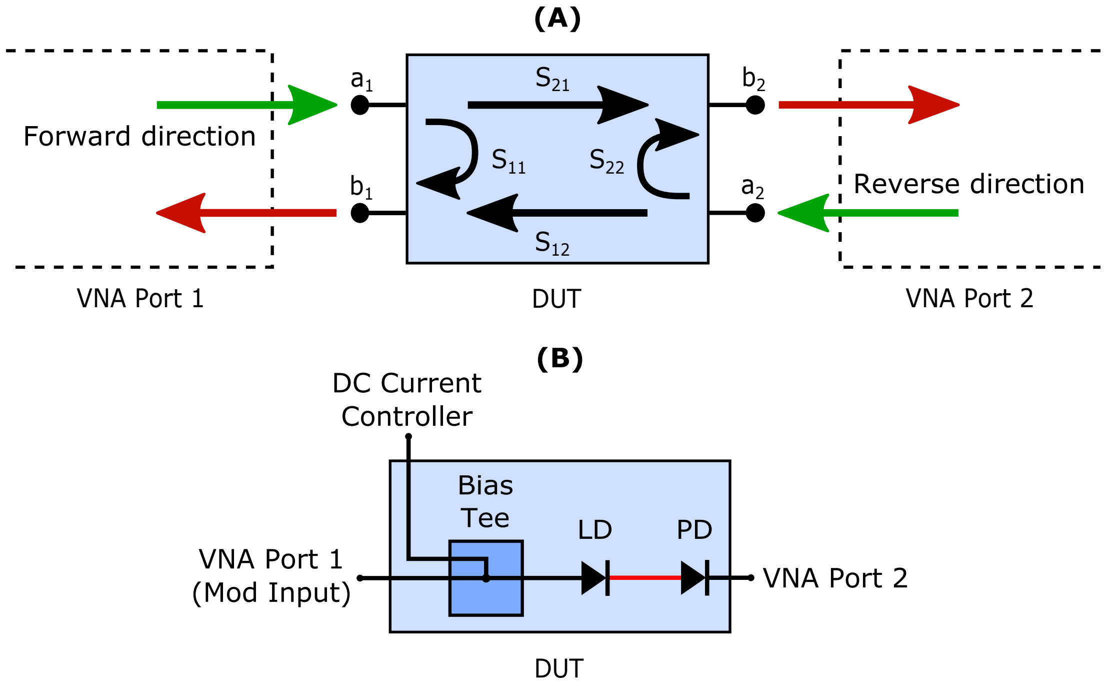

Figure 3.5: Schematic diagram of the S-Parameters and their respective relationship in a 2 port VNA. (A); The VNA connects to the Device Under Test (DUT) so as to measure the desired scattering parameter. (B); the DUT is a composite device consisting of a Bias Tee, a laser diode and a fast photodiode. Port 1 of the VNA is connected to the modulation port of the bias Tee and the DC current controller is used to bias the laser diode (LD), while port 2 is connected to the fast photodiode (PD).

3.4.1 RF Modulation S_{21} Response

Initially a weak +0 dBm modulation signal is applied to the diode with no external cavity and the log magnitude S_{21} parameter is recorded as a function of injection current and junction temperature (figure 3.6). It is worthy of noting first of all that, because there is no optical cavity (either in the form of the semiconductor gain chip or an external cavity), these curves essentially demonstrate the ability for the power in the laser spontaneous emission to follow the form of the sinusoidal modulation waveform.

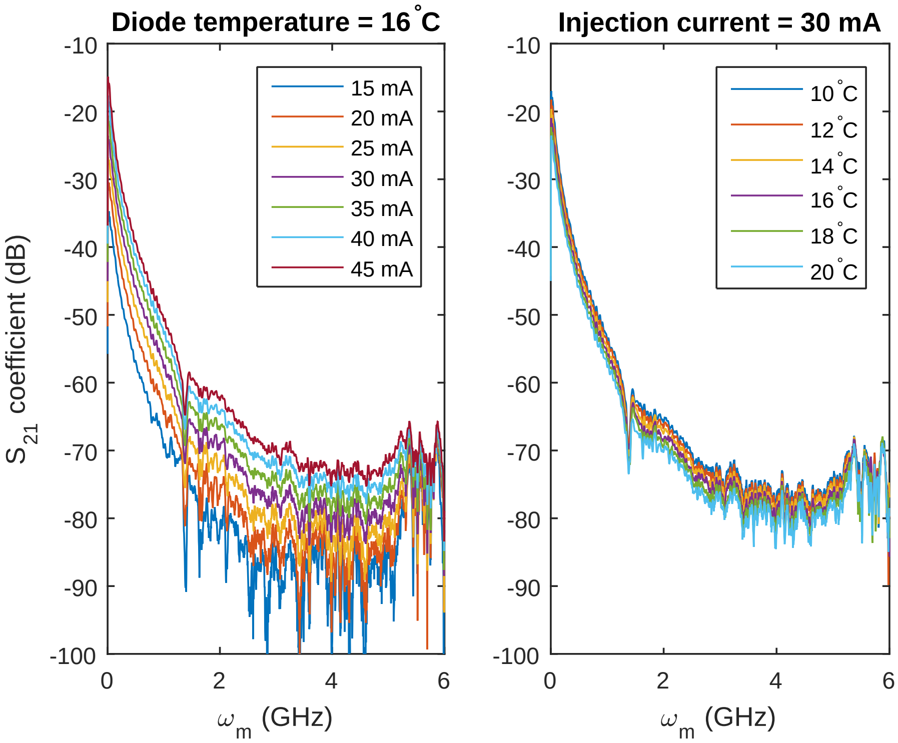

Figure 3.6: Measurement of the log magnitude S_{21} scattering parameter of the mode-locked diode over a 6 GHz spectral window showing the forward scattered response of the diode for varying DC injection currents (left) and junction temperatures (right). All traces are averages of 8 sweeps.

As expected, the AM response falls off rapidly as ω_m increases. At $\omega_m \approx 5.5$ GHz a significant increase of nearly 10 dB as compared with the response at 4 GHz is observed which, at first glance, is believed to be the relaxation oscillation frequency for the specific device. Relaxation oscillations are the result of the resonant relationship between charge carrier density and photon density due to a perturbation to the steady state system, and can be understood as the carrier density being unable to follow the photon decay rate.

Following the perturbation (a small positive step-like change in injection current, say), the photon density spikes due to the initial carrier density spike which rapidly depletes the carrier density. This depletion causes a sharp fall in the photon density which allows the carrier density to recover via the injection current. The process repeats albeit with an amplitude damping factor which acts to return the system back to a steady state. According to [124] the relaxation oscillation frequency is defined in terms of the threshold injection current and intra-cavity photon lifetime and is given by:

$$\omega_{RO} = \left[\frac{\gamma_c}{\tau_1} \left(\frac{I}{I_{th}} - 1 \right) - \left(\frac{1}{2\tau_1} \frac{I}{I_{th}} \right)^2 \right]^{\frac{1}{2}} \tag{3.5}$$

where γ_c is the cavity loss rate given by $1/\tau_p$, the inverse photon lifetime [125],

$$\tau_p^{-1} = \left[\upsilon_{gr} \left(\alpha_i + \frac{1}{2L} \ln \left(\frac{1}{R_b} \right) + \frac{1 - R_{AR}}{2LT_{eff}} \ln \left(\frac{1}{R_{eff}} \right) \right) \right], \tag{3.6}$$

where,

$$R_{eff} = \left[\sqrt{R_{AR}} + \frac{\sqrt{\alpha_{il} R_{ext}}\,(1 - R_{AR})}{1 + \sqrt{R_{ext} R_{AR}}} \right]^2 \quad \text{and,} \quad T_{eff} = 1 - R_{eff}. \tag{3.7}$$

τ_1 is the upper laser level spontaneous lifetime, I is the DC injection current and I_{th} is the laser threshold current, υ_{gr} is the group velocity, α_i is the internal losses experienced by the laser, α_{il} is the insertion loss given as a unitless coefficient which defines the coupling efficiency of the two cavities, L is the optical cavity length and R_b, R_{AR} and R_{ext} are the uncoated rear diode facet, front anti-reflection coated facet and planar output coupler mirror power reflectivities respectively. This expression indicates that the relaxation frequency should increase with increasing DC injection current, and that there should be a defined threshold current. As has been shown in figure 3.2 however, no defined threshold current exists while the output coupler is turned away. Further, without the presence of an optical cavity and hence stimulated emission beyond that of single pass gain, there can be no resonant effect between photon and charge carrier numbers because no transient photon decay rate can be quantified. In conjunction with this, at approximately 5.5 GHz the data exhibits a very small red shift of the peak modulation response with increasing DC injection current, not the predicted blue shift. It is therefore reasonable to conclude that this near factor of 10 improvement in the modulation response is the result of a purely electronic resonance in the circuit path before the recombination region and not relaxation oscillations.

Analysis of the temperature dependence of the diode laser optical modulation response appears to further support the above conclusion. Generally speaking, through a concomitant decrease in the threshold current and increase in external efficiency with decreasing junction temperature, it would be expected that any relaxation oscillation frequency would increase with increasing junction temperature and that the magnitude of the optical response would increase with increasing external efficiency. The data in figure 3.6 however exhibits no apparent shift in frequency while supporting an increased external efficiency.

The very low overall response of the diode to current modulation may seem alarmingly small. This is expected however and can be easily explained by the lack of an optical cavity which enforces a very small external quantum efficiency. Over a small enough injection current region (2 mA) where the gradient can be approximated as linear, the efficiency is measured to be η_{ext}=0.006. This value is approximately 115 times smaller than when the laser is operated above threshold.

The external cavity is now formed by realigning the 50% output coupler mirror and optimising for minimum threshold. The external cavity length is adjusted to approximately match a 3 GHz FSR and the VNA frequency sweep is conducted for DC injection currents below and above threshold. The data for this situation is shown in figure 3.7. Immediately visible is the strong enhancement of the modulation response around the external cavity fundamental frequency by approximately 50 dB as well as the overall improvement of the modulation response. Due to the presence of the cavity, between 200 kHz and the build up to the cavity resonance at 2.6 GHz, the modulation is enhanced by 40 - 20 dB respectively. The overall decay in the modulation response is caused by the decreased ability for the carrier concentration to follow the modulation signal as frequency increases. While the observed improvement in the modulation response of 50 dB at the cavity resonance is both significant and expected, the peak response is still at -26.67 dB; well below the level expected for a device with low parasitic losses [65, 73].

With the external cavity now restored, in order to make an estimation of the relaxation frequency of laser configuration, we must first make some assumptions for the values of variables in equation 3.5. Firstly τ_1, the upper lasing level spontaneous lifetime varies considerably between devices and structures and so we shall use a trial figure of 1 ns. Calculation of the total group velocity for the composite cavity is not straightforward. We do not know the dispersion properties of the semiconductor cavity or the glass aspheric collimation lens, so a reasonable guess of the effective index of refraction over the whole composite cavity of 1.1 is used. A summary of the values used and their uncertainty is summarised in table 3.2. From these values we arrive at a relaxation oscillation frequency of 1.107 ± 0.176 GHz which is plotted in figure 3.7. The features observed in the modulation response below and above threshold align well with the initial estimates of the experimental parameters. Curiously though, the behaviour of the above threshold response around this calculated frequency does not portray the usual peak in modulation response observed for true relaxation oscillations, see figure 4.10 in reference [113].

Variable	**Value**	**Uncertainty**
τ_1	1 ns	±0.5 ns
υ_{gr}	$c/1.1$	N/A
R_b	0.32	±0.02
R_{ext}	0.5	±0.03
R_{AR}	0.0003	+0.0003
I	11 mA	±0.005mA
I_{th}	8.96 mA	±0.04 mA
α_{il}	20 cm^{-1}	±10 cm^{-1}

Table 3.2: Summary of parameters used to calculate the relaxation oscillation frequency and their respective errors.

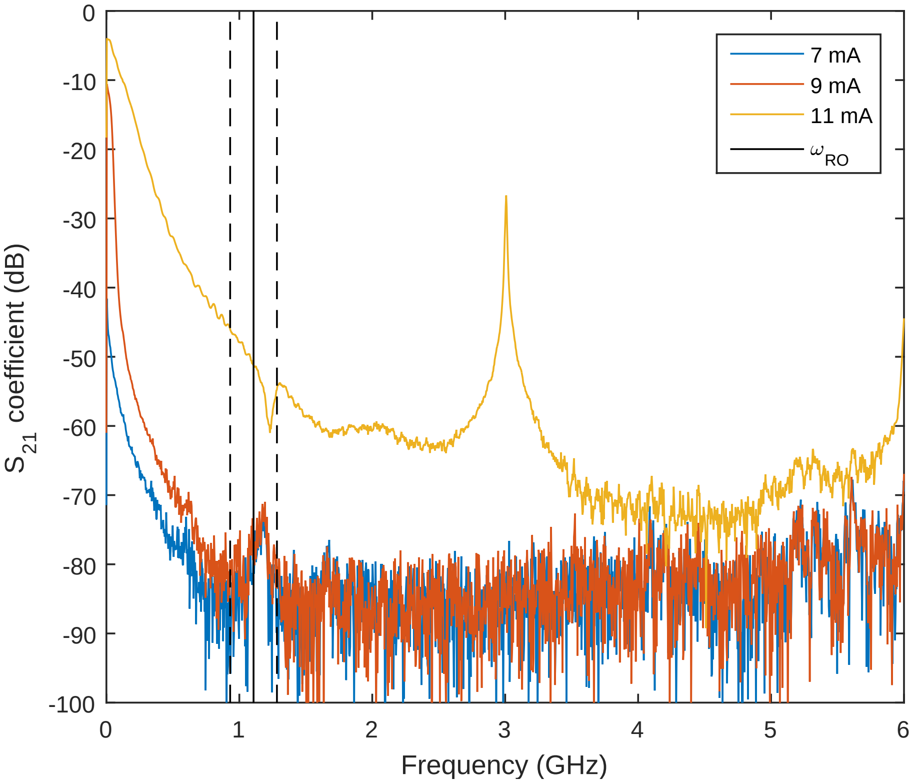

Figure 3.7: Comparison of the measured log magnitude S_{21} scattering parameter for a diode in an external cavity for DC injection currents below and above threshold. Approximately 50 dB of improvement in the modulation response is observed at the external cavity fundamental resonance. The Intermediate Frequency bandwidth was 100 Hz. The solid black line represents the calculated relaxation oscillation frequency and the dashed lines represent the uncertainty limits of this value.

3.4.1.1 Modulation Average Power

Subdivided from the coarse topic of mode-locked diode lasers, there exists a field of reasearch which aims to explain observed optical effects by modelling the diode laser as a collection of lumped circuit components [126–128]. This approach allows for modelling of both the optical emission and electrical circuit properties, such as input impedance, bond wire inductance, contact pad and semiconductor layer capacitance and other parasitic effects. While an in depth analysis of the laser emission via the circuit modelling approach is beyond the scope of this project, we can nevertheless hybridly adopt this tactic, in conjunction with an optical analysis method, to gain a ’first order’ insight into the apparent bottleneck in the modulation response of these specific laser diode devices.

To conduct this analysis, we first make the assumption that, on top of the DC injection current, the average optical power emitted under current modulation scales linearly with the average current injected by the modulation signal. This is a reasonable assumption given that the frequency dependent differential optical gain of the laser scales linearly with the injected charge carrier number if we assume a narrow emission linewidth with respect to the overall gain bandwidth. Provided that an indication of the average injected carrier number can be acquired through inspection of the measured average optical power, with and without current modulation, it is possible to gain insight into the degree of attenuation of the modulation signal.

With the external cavity in place, the laser is sinusoidally modulated at the cavity fundamental frequency with a +27 dBm signal. Measurements of the average emitted optical power are then made as a function of the DC injection current and detuning about the position where the shortest optical pulses are observed for a DC injection current of 15 mA. Figure 3.8 shows the current-power curve for the unmodulated laser and the residual power between the modulated and unmodulated laser as a function of DC injection current and modulator detuning. The residual is simply the difference between the average optical power when the laser is in DC operation and the average optical power when the laser is modulated. A positive value indicates a higher average emitted power was observed when the laser current was modulated. For the zero detuning data the maximum residual optical power is +406.1 μW which corresponds to 539±66 μA RMS. By measurement of the S_{11} parameter, the total real impedance at 3 GHz is approximately 10 ohms (figure 3.11). Because the laser diode is effectively in parallel to ground with a 50 ohm termination, the calculated diode impedance is 12.5 ohms. Using these impedance and current values the RMS voltage across the diode is $\sim$6.7 mV which, given the +27 dBm input signal, corresponds to 0.30±0.04% of the modulation signal reaching the active region. Accounting now for the power lost due to reflection (figure 3.9) and approximate insertion loss into the bias tee, it is estimated that 5 dB is lost giving a best estimate RF power after the bias tee of +22 dBm. As a result the RMS voltage across the diode improves very slightly to 0.53±0.04%.

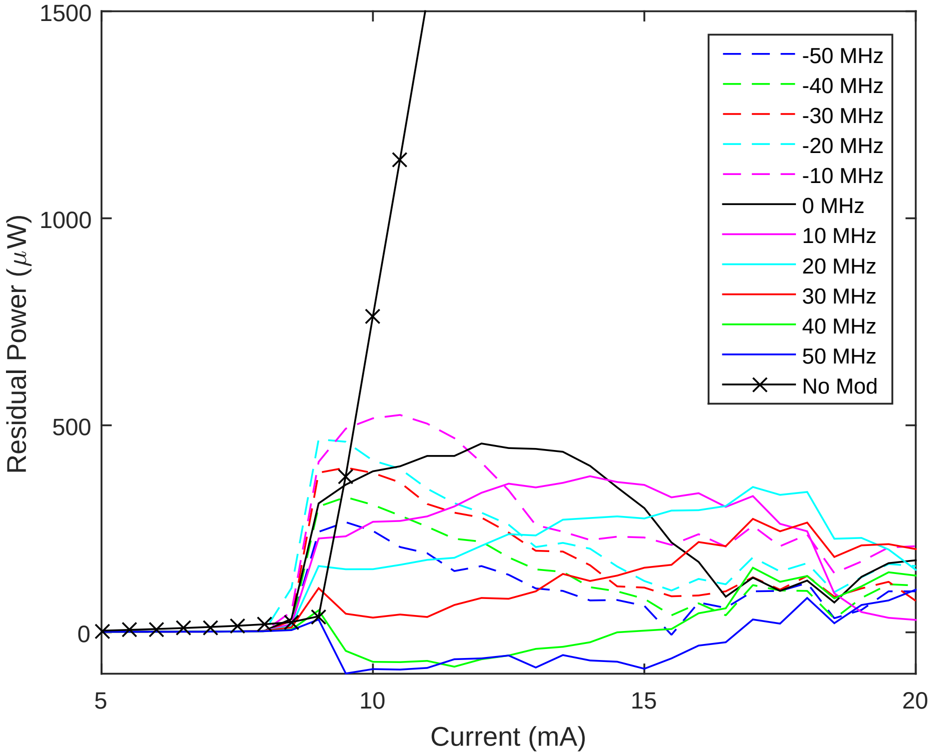

Figure 3.8: Plots of the residual average output power between the CW and mode-locked operation of the laser diode as a function of modulation frequency and DC injection current. The unmodulated curve (crossed points) is a segment of the data shown in figure 3.2 for reference. The legend frequencies are the detuning values of the modulation frequency from the frequency corresponding to the shortest measured optical pulse on an intensity auto-correlator. A positive residual power represents an increased average power output as compared with the unmodulated laser for a specific DC injection current.

3.4.2 RF Modulation S_{11} Response

The S_{11} scattering parameter is sensitive to the magnitude and phase of the modulation signal which is back reflected by the load to the same port from which the modulation signal originated. The magnitude of the S_{11} signal is therefore sensitive to all forms of loss, including that of the signal which is lost to useful output, *i.e.* optical modulation. It is however insensitive to the magnitude of each loss mechanism separately, and gives only the total magnitude detected as a ratio of the power in the emitted signal. Figure 3.9 shows the S_{11} coefficient for three identical model number devices, in which 'Diode 3' refers to the same device used for the previous S_{21} data.

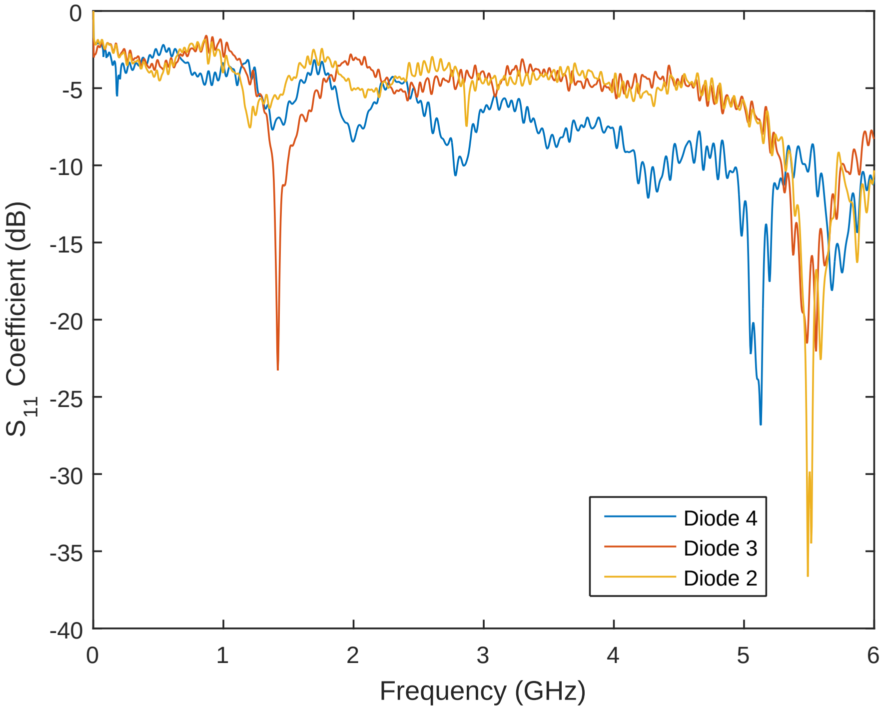

Figure 3.9: Comparison of the measured log magnitude S_{11} scattering parameter for three identical part numbered laser diodes. A larger negative value signifies a favourable ratio of incident to reflected RF modulation power.

Despite the preceding electronics being identical for all three diodes under test, there exist significant differences in their respective electronic characteristics. The features for Diode 3 which signify a severe drop in the magnitude of the back reflected RF signal correspond well with the highlighted features in the S_{21} data. From this one can infer that the RF power at these frequencies is resonant with the device and is acting to improve the RF coupling into the laser recombination region. While the data is not included, during testing all three of the apparent resonances around 5 - 6 GHz for the respective laser diodes all corresponded to an increase in the S_{21} parameter response of a comparable magnitude.

Thus far, no consideration has been extended to matching the impedance of the transmission line (50 Ohm) to the impedance of the diode itself. The DC impedance of a laser diode is of the order of 12 ohms [73, 129], however this is subject to change at RF modulation frequencies as lumped circuit elements (such as resistors, diodes and capacitors) have an associated phase response to an applied modulation signal, and so the circuit impedance becomes complex.

It has been shown that edge emitting semiconductor laser devices exhibit multiple parasitic effects. These effects include;

- Series resistance caused by the semiconductor cladding layer(s) between the metal pad contact and the recombination region,
- inductance caused by the bond wires to the pad contacts,
- shunt resistance from leakage current not entering the recombination region,
- capacitance between the metallic pad contacts and any semi-insulating layers in the device [128].

Though it is beyond the scope of this work to account for the specific parasitic effects of every component in the circuit, an attempt to match the complex diode impedance to that of the transmission line can be made by measuring the total device impedance via the Smith chart functionality of the S_{11} parameter. In radio communications this process is identical to matching an antenna impedance to the transmission line impedance so as to maximise signal coupling to the antenna.

3.4.3 Impedance Matching

It is difficult to imagine a scenario in modern technology where one does not wish to transmit information from one place to another, be that over a short distance between specific devices, or long distances on a geological scale. Common to the vast majority of scenarios and applications is the underlying desire to achieve the required transmission of information with the greatest efficiency and, when integrated over time, the least overall cost. Typically a given application will consist of the initial formation of the signal to be transmitted, possibly followed by an amplification of this signal and finally the transmission of this signal to either a intermediate device, such as an antenna, or the recipient device which performs an appropriate analysis of the signal. The concept of impedance is therefore incredibly important, especially so in RF applications. Typically, equipment used in either RF signal generation, transmission and/or analysis have a standardised input, output or line impedance. For most scientific equipment this tends to be $Z_0 = 50$ Ohms, and indeed for radio communications it tends to be 75 Ohms. This standardisation is born from a desire to maximise the signal coupling from one device or component to another. In a way that is completely analogous to optical reflections that occur at boundaries of unequal refractive index, electronic signals experience reflections at boundaries of unequal impedance.

One of the core motivations for the historical development of the GaAs laser diode has been through a desire to mass produce compact laser sources for reading compact disks. Due to the data surface density and frequency of rotation, the pulsed operating regimes of these lasers is generally no more than a few tens of MHz, where the modulation response is sufficient without the need for impedance matching. In the GHz regime however, as has been observed in figure 3.9, significant power reflection can occur. The role of the impedance matching stub is therefore to bridge the impedance mismatch between transmission line and load device.

The 'open' stub is a small section of transmission line that extends normal to the main transmission line which in effect forms a fixed path length Michelson interferometer. As such, manufacturing the RF stub is easily accomplished using the microstrip transmission line architecture and any suitable method for circuit board printing. Figure 3.10 shows a schematic diagram of the RF stub circuit layout and highlights how the laser diode is connected to the circuit. The term 'open' refers to the operating principle whereby the stub does not short to ground, as opposed by the 'short' stub which is shorted to the ground plane.

RF stub matching has been demonstrated with laser diode modulation applications in the 0.5 - 5 GHz range [130] as well as for modulation frequencies up to 40 GHz [79,131]. Stub matching has also been attempted under the desire to improve the magnitude of sideband generation for atomic physics experiments [132].

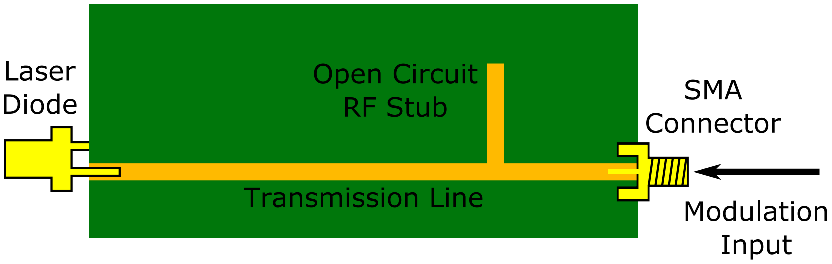

Figure 3.10: Schematic diagram of the RF impedance matching stub. The impedance of the transmission line is determined by the copper track width, thickness, ground plane separation and dielectric material properties, and should be designed to match that of the connecting transmission line entering from the right. The ground plane is the formed by the copper on the opposite side of the copper board.

Figure 3.11 shows the real (top) and imaginary (bottom) parts of the complex impedance of the circuit and transmission line circuit as a function of ω_m. To be able to interpret this data appropriately, a perfect match is where the complex impedance of the load equals that of the preceding transmission line resulting in zero signal reflection. This is represented, in terms of the complex impedance, as the real part tending towards the characteristic impedance of the transmission line (in this case 50 ohms) and the imaginary part tending towards zero, and is written as $Z = R + jX$ Ohms. The latter condition can be understood as a lack of phase lead or lag between the transmission line and the load, while the former is analogous to the magnitude difference in a step-like refractive index change between two media. It is clear that the frequencies where the complex impedance matching is superior corresponds well to both the significant features of reduced reflected modulation signal in figure 3.9 and the improved optical modulation response in figure 3.6.

The noticeable periodicity in the complex impedance data was somewhat unexpected. Analysis of the data for the real impedance reveals a peak spacing of 77 MHz. By assuming a signal propagation velocity in the coaxial cable of $\frac{c}{1.5}$, plugging this index of refraction into the equation for the mode separation in a Fabry-Perot resonator A.27 where m=1 and solving for the cavity length, the result is a length corresponding almost exactly to the length of SMA coaxial cable between the VNA port and the Bias-T used to couple the AC signal onto the DC laser injection current.

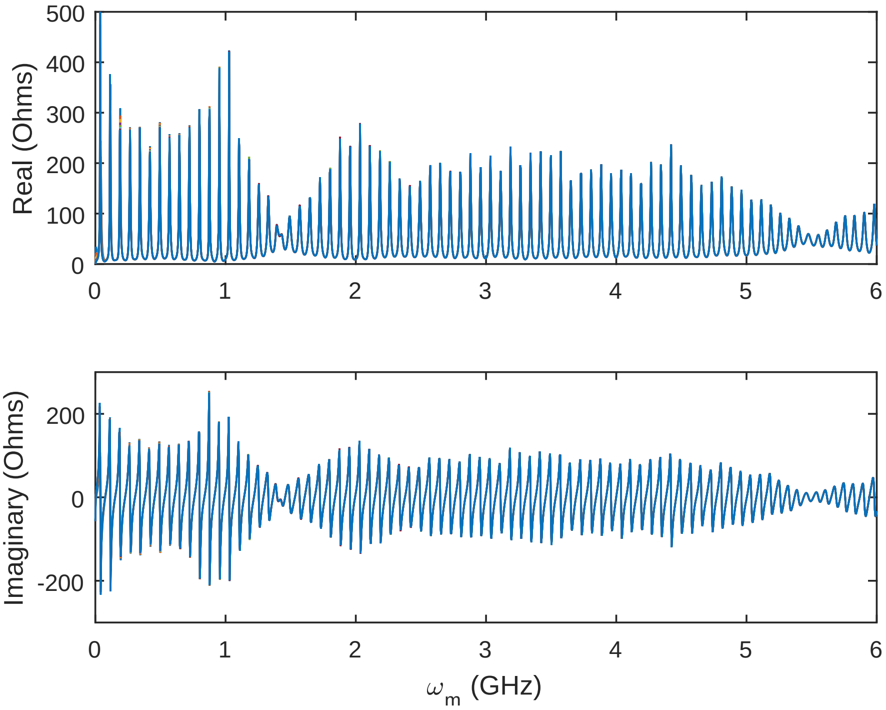

Figure 3.11: Measurement of the diode laser complex impedance derived from the measured S_{11} parameter. For a 50 ohm transmission line, a load complex impedance, $Z = 50 + i0$ ohms represents a perfect impedance match. The sharp drops in reflected magnitude in figure 3.9 correspond with the impedance matching of circuit at those frequencies. The measurement is taken using diode 3.

The RF impedance matching stub can be designed for our specific circuit using the above data for the complex impedance in the more useful form of the Smith chart [133]. A detailed description of how to match a load to a transmission line is given in the reference [134]. The basic operating principle of the RF stub is to act as an interferometer, where the path lengths are given by the load to stub distance and the length of the stub itself. The basic design procedure is as follows. On the Smith chart, all impedance values are normalised against the characteristic impedance of the system which in most cases is 50 Ohms i.e. (50 Ohms = 1, 100 Ohms = 2, etc). One full rotation around the Smith chart corresponds to a physical distance moved of $\frac{c}{2\eta\omega_m}$, i.e. half of the refractive index corrected wavelength corresponding to ω_m. The complex impedance coordinate of the load at the desired modulation frequency, which is read directly from figure 3.11, is plotted on the Smith chart. The linear displacement of the coordinate from the Smith chart centre (1 on the purely real axis) is used as a radius to draw a circle around this central point. This circle (when followed clockwise from the load) will intersect the 50 Ohm circle twice. These intersection positions each correspond to a distance in wavelengths from the load where the stub may be positioned. These distances may be read off directly from the perimeter of the Smith chart. Each intersection corresponds to a certain reactance, and the symmetry about the real impedance axis dictates that the symmetric intersections have the same magnitude of reactance but are opposite in sign. The length of the stub itself is given by the distance (in wavelengths) from the "open circuit" point to the *opposite* chosen reactance value. Therefore, for the load to be matched, the stub should contribute a reactance to the circuit which is equal in magnitude and opposite in sign to the reactance corresponding to the first point intersection with the 50 Ohm circle;

$$Z = 1 + jX - jX = 1 + j0\ \Omega, \tag{3.8}$$

hence the stub cancels the reactance of the load and only the real 50 Ohm impedance remains. The circuit is now matched. The stub is most easily fabricated using the microstrip transmission line technology whereby the dielectric constant, track thickness, width and separation are easily chosen to give a transmission line with a 50 Ohm impedance.

Figure 3.12 shows plots of the log magnitude S_{11} parameter taken for the final stub (bottom) and Standing Wave Ratio (SWR) (top right). The top left plot is a crop of the stub resonance shown in the bottom plot. This data reveals a greater than 47 dB improvement in the suppression of the back reflected modulation power at 3.26 GHz with a 3 dB full width of 2 MHz. Correspondingly the value of the SWR at resonance is 1.006, signifying a near perfect match. The resonance full width is also well within the cavity length adjustment accuracy as defined by the fine adjustment screws. The adjustment screws employed here have a thread pitch of 100 turns per inch of linear adjustment, which corresponds to approximately 18 MHz change in FSR per single rotation.

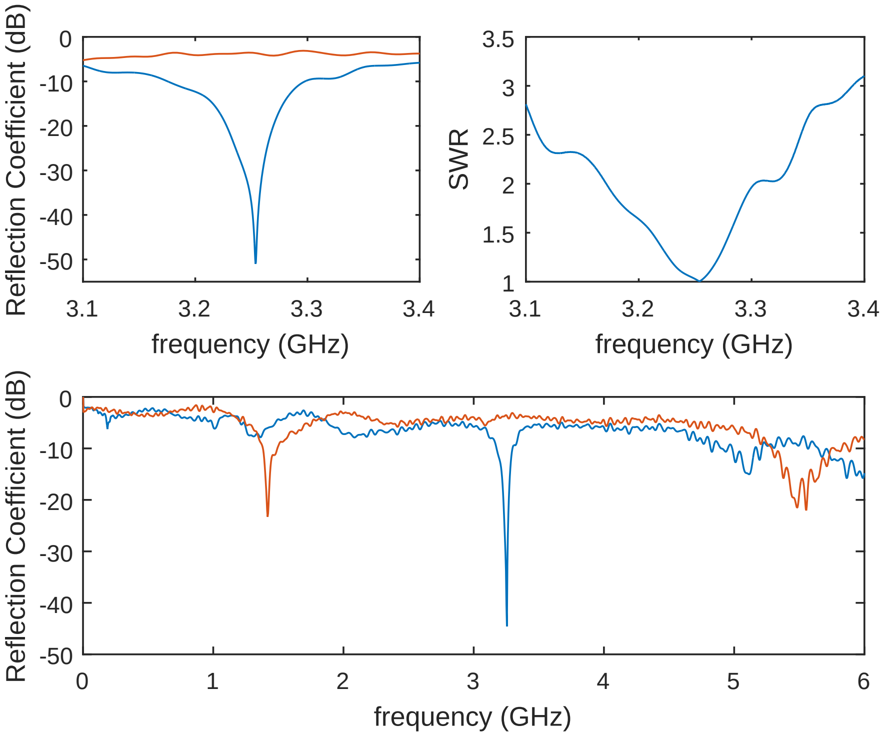

Figure 3.12: Measurement of the RF stub matching circuit log magnitude and SWR S_{11} scattering parameter (top) and comparison to the un-matched load (bottom). A standing wave ratio equal to unity describes a perfect impedance match to the transmission line.

Despite the clear evidence of the matching circuit working as desired in terms of the modulation signal reflection, we observed < 4 dB of improvement in the S_{21} modulation response when used without an external cavity and no improvement in the optical pulse width when later analysed by intensity autocorrelation. This result is both disappointing and puzzling, especially given the previous analysis where significant drops in the magnitude of the S_{11} data correspond well with the noticeable modulations enhancements visible in the S_{21} data. Given the improvement of the S_{11} parameter from 0.43 to 8×10^{-6} , and a measured complex impedance on resonance of Z = 1.004 - j0.006 (Z = 50.2 - j0.3) Ohms, it was expected that the modulation response would see a marked improvement. This potentially highlights a significant issue with these devices. If absorption or radiative emission by the matching circuit is momentarily neglected, it is possible that the device parasitics are damping or radiating the RF signal; about which little can be done.

Some time after attempting the stub impedance matching, it came to our attention that there was a possibility that the PCB material on which the microstrip RF stub was fabricated might be unsuitable for modulation frequencies above 1 GHz [135]. It is reported that certain PCB dielectric materials suffer from high levels of attenuation of high frequency AC signals, and among them is FR-4 - the material from which our stub was fabricated. With access to a FLIR thermal imaging camera we were able to take thermal images of the stub while a resonant +27 dBm modulation signal was applied. Figure 3.13 shows a tilled time lapse set of images taken approximately every 7 seconds (limited by the single frame acquisition and saving time of the camera) over a 2 minute period. Within this period it can easily be seen that three small sections of the PCB material are acting as heat sources and the front most section rises by 15°C. As heat conduction from this area is limited, this area rises in temperature significantly faster. When the RF power is initially turned on the end of the stub itself appears to rise in temperature the fastest. This is attributed to the strong increase in energy density at this position due to the spectral reflection of the modulation power at the end of the transmission line. The camera was not calibrated for the emissivity of the substrate and so the recorded changes in temperature are relative only.

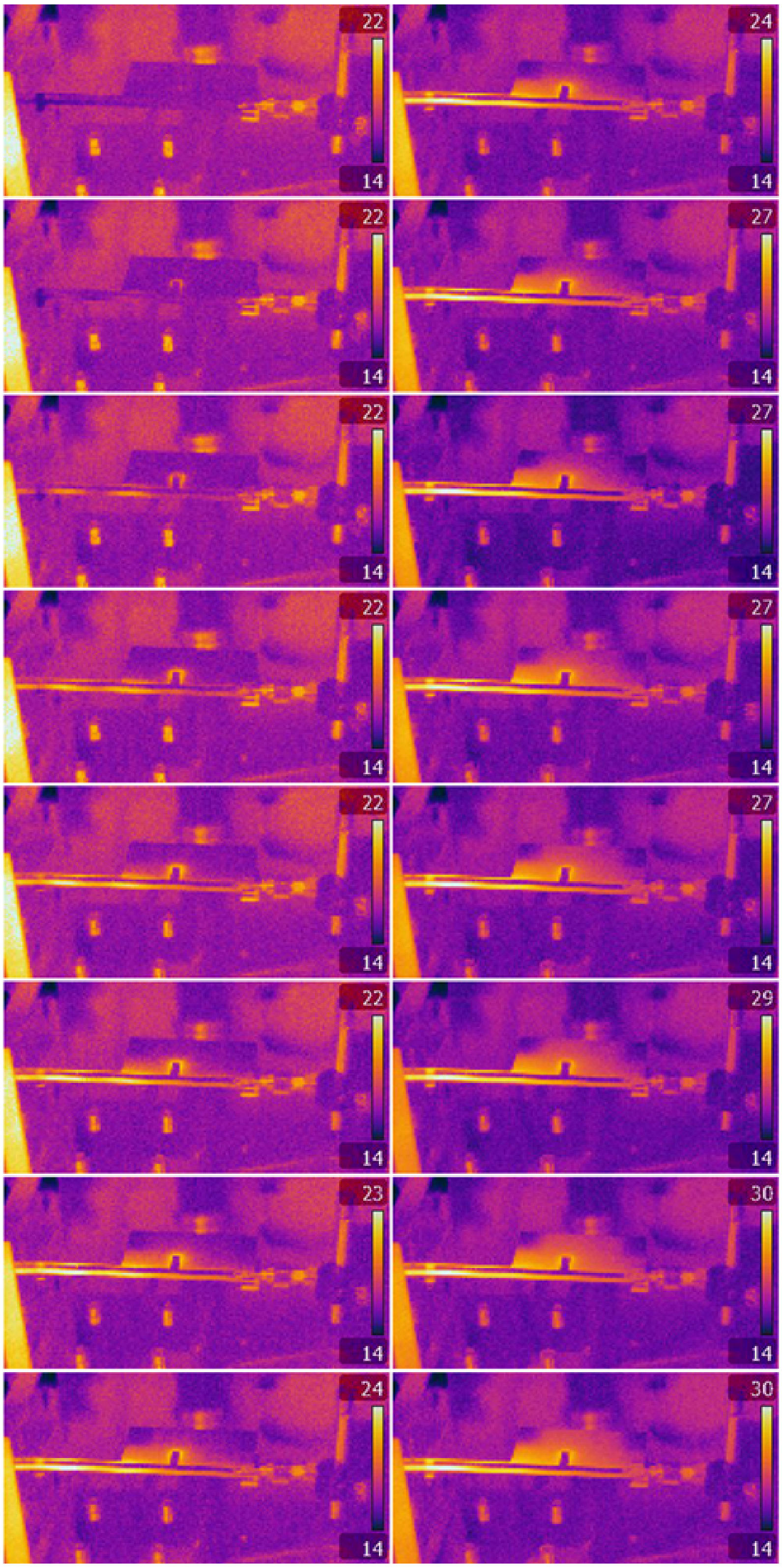

Figure 3.13: Transient heating of the RF stub under strong (+27 dBm) RF modulation measured with an IR camera over a 2 minute window. The stub was allowed equalise with the ambient temperature before the sequence was captured. Image interval is approximately 7 seconds. The RF modulation signal is incident from the right and the diode pins are soldered to the transmission line and ground plane at the far end of the stub.

Chapter 4

Active Mode-Locking Characterisation

This chapter presents the parameter space characterisations of these specific semiconductor devices in order to determine the optimal operating conditions for generating a mini optical frequency comb. The four main experimental parameters we have access to are the DC injection current, diode substrate temperature, RF modulation frequency and RF modulation power. Analysis of the effects of these parameters is conducted using an intensity autocorrelator, optical spectrum analyser and RF spectrum analyser, and therefore experimental results for the temporal pulse width, spectral FWHM, spectral peak wavelength, time-bandwidth product and autocorrelator pedestal characteristics may be achieved. It should be noted that for all surface plots the measured data points are represented by the corners of each surface element and not the centre, and the element colour is determined from the average of the values of the respective four corner z-axis values.

Plotted in figure 4.1 are examples of processed data from the intensity autocorrelator (A) and optical spectrum analyser (B). The former displays the entire recorded trace from the storage oscilloscope and is the averaged result of 64 consecutive, 100k point record length samples over approximately 5 seconds. In the first instance an average of the first ten thousand points are taken and subtracted off the entire record so as to nullify any zero offset voltage outside the scan range of the autocorrelator. Using an appropriate initial best guess for the peak position, a Gaussian lineshape is fit to the autocorrelation via the non-linear least-squares fitting (lsqcurvefit) functionality built into Matlab. From the fit the Gaussian lineshape parameters and their respective standard uncertainties are extracted and used to populate the respective following surface plots for the aforementioned parameter space characterisations. The error in the calculated Gaussian FWHM parameter for each plot of the temporal pulse width is plotted in figures B.1 and B.2 as separate surface plots.

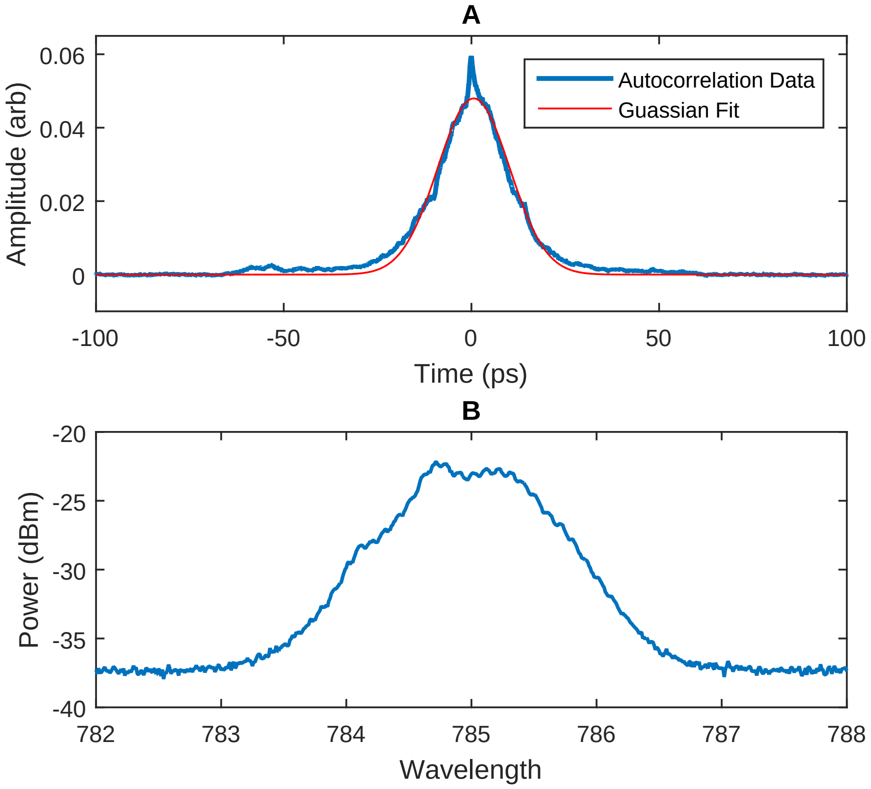

Figure 4.1: Example mode-locked operation data for (A) the pulse intensity autocorrelation, and (B) the optical spectrum. The former shows the full width of the oscilloscope sample. The raised pedestal represents the full temporal scan range of the intensity autocorrelator and is also indicative of the presence of CW optical components. The presence of the coherence spike is indicative of noise in the optical modes and its width is given by the inverse spectral width of the noise content. Asymmetry in the shape of the coherence spike is due to the resolution limit of the autocorrelator.

For the optical spectrum, no specific 'standard' lineshape can be fitted to the data on account of the asymmetry and volatile nature of the shape of the emitted optical spectrum. As a result, the optical spectral width is generally determined by converting from logarithmic to a linear power scale, normalising the peak power to unity, truncating the data to preserve only power values ≥0.5 and extracting the spectral separation by considering the difference between the minimum and maximum wavelength values of the newly truncated power data. This imposes a minimum spectral FWHM uncertainty of twice the wavelength interval between data points, in addition to the spectral resolution of the optical spectrum analyser and is given by, λ_{FWHM} uncertainty = $\pm 2\times(0.05+0.01)$ nm = ±0.12 nm.

4.1 Mode-Locking Characteristics

4.1.1 Temporal Pulse Characteristics

We begin the mode-locking characterisation by considering the temporal characteristics of the optical pulse as a function of the four parameters. Figure 4.2(A) displays the pulse FWHM as a function of DC injection current and housing temperature. The initial starting parameters around which the exploration was conducted were 15 mA and 12.5°C. This starting temperature represents the lowest stable casing temperature for which water condensation did not occur. It was possible to hold the temperature below this for only short periods of time before condensation became problematic. At best the pulse width was 23.60±0.01 ps while the opposite corner of the parameter space exhibits pulse width increases by approximately 60% to 38.58±0.02 ps.

There are two clear trends to the data; increasing the injection current from threshold improves the pulse width and decreasing the temperature for a given injection current also improves the pulse width. The former is attributed to reaching a balance between the magnitude of the gain modulation above threshold and the tendency for the laser to collapse into CW operation at high DC currents. Near threshold, while the window of net gain is at it's narrowest, the magnitude of the gain modulation is also at it's lowest. By increasing the injection current, a region of the modulation signal which would otherwise drop the laser below threshold now provides net positive current. Ideally, due to the charge trapping mechanism in the semiconductor structure, carriers cannot be pulled in the reverse direction back out of the diode. In reality there exists a finite reverse current governed by thermionic emission and is very generally of the order of 1 μA [136]. Simultaneously, increasing the DC injection current also results in a decrease in the proportion of time during each modulation cycle for which the laser is operating below threshold, and hence there will reach a point when the gain modulation is insufficient and the laser will collapse into a CW state. This transition is apparent from an increasing pulse width and the visible pedestal on the autocorrelation trace (figure 4.3(A)).

The latter trend is attributed to the effects of the temperature on the laser threshold current, modulation bandwidth and external differential efficiency [126, 137]. Reduction of the junction temperature reduces the laser threshold current (yielding behaviour as described above) and increases the differential external efficiency. The first effect, within the confines of the above former trend, can exhibit an improvement in the pulse width for a given injection current while the second effect acts to increase the gradient of power-current curve above threshold via an increase in the differential gain coefficient.

A very brief analysis regarding the magnitude of the DC injection current and its dependence on the pulse width is given in [138] and [139]. In the former reference it is stated that the shortest optical pulses are achieved for a DC injection current 20 mA (83%) above threshold which, from reference [73], I_{th} = 24 mA. Equally, in the latter reference, a minimum pulse width of ~12 ps is achieved for a DC injection current 37.5 mA (45%) above threshold. From figure 4.2 the minimum pulse width occurs at 16 mA, or approximately 78% of threshold, which therefore fits into the range set out by the stated literature. Furthermore our presented trend for the relationship between pulse width and DC injection current is also a qualitative match to that described in the stated references.

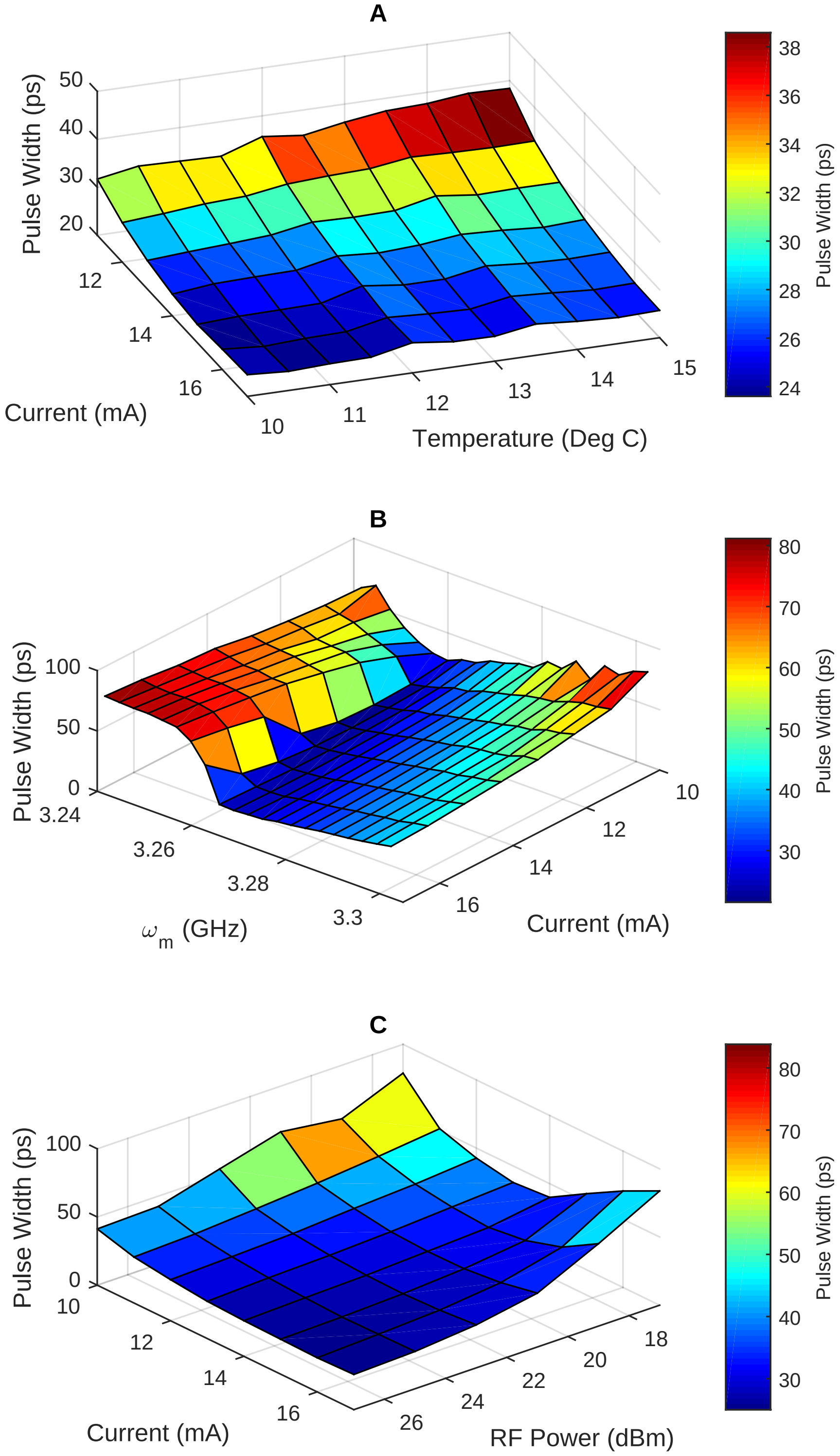

Figure 4.2: Pulse temporal width characteristics for DC injection current, diode case temperature, modulation frequency detuning and RF modulation power parameter spaces

Figure 4.2(B) shows the optical pulse width as a function of DC injection current and

RF modulation frequency. The parameter space is an exploration around an initial 'best guess' position of $I_{DC} = 15$ mA, $T = 12$°C and $\omega_m = 3.266$ GHz, achieving a pulse width of 23.79±0.01(0) ps. The position of the shortest pulse (21.55±0.01(1) ps) corresponds to 12 mA at a modulation frequency of 3.260 GHz.

The salient feature immediately visible in the data is that the change in pulse width about the minimum for a given DC injection current is strongly asymmetric. Morton *et al* [139] have linked this effect to dynamic detuning of the pulse arrival time with respect to the gain modulation waveform, which can be understood as follows. Consider first the pulse build up process when the modulation is initiated. In the first instance the laser is in CW oscillation above threshold with no modulation. As the modulation source is engaged a pulse begins to build up from the centre of the positive region of the modulation waveform while the drop in gain during the negative region aids in dropping the laser out of CW operation. Over multiple round trips the pulse power increases to the point where the gain starts to saturate. This gain saturation occurs due to the strong depletion of charge carriers in the active region via stimulated emission. Upon encountering gain saturation the pulse experiences a spatial gain imbalance whereby the rising edge of the pulse experiences more gain than the falling edge of the pulse, and so the pulse is pulled towards an earlier position on the modulation cycle. According to [139], for steady state pulse operation to be achieved, all positions on the pulse waveform must observe an identical gain per cavity round trip. The pulse therefore must move to a position on the modulation waveform where the time dependent effect of population depletion (by stimulated emission and hence gain saturation) is countered by population recovery (due to the rate of change of charge injection by the modulation signal). It is reported in the same work that this is the only position where the system is stable and that this is also the physical process behind both the minimum achievable pulse width and the eventual appearance of trailing pulses in the time domain as modulation power is increased.

Detuning of the modulation frequency to a lower frequency artificially forces the pulse to arrive at an earlier position on the modulation cycle. At this slightly earlier position the gain gradient is steeper which acts to decrease the pulse width and hence the rate of gain saturation must then also increase . The system is unable to find a steady state position and so the pulse disintegrates rapidly with red detuning of the modulation frequency. Blue detuning of the modulation frequency forces the pulse to arrive at a later position on the modulation cycle where the rate of charge population recovery is reduced. For the identical gain per round trip condition to be met, the pulse width therefore must increase to reduce the gain saturation. The form of the data presented in figure 4.2(B) agrees qualitatively with van der Ziel [138], Morton *et al* [139], Goodwin *et al* [140] and Lowery *et al* [71].

The dependence of the achievable pulse width as a function of the modulation current has been reported by Bowers *et al* [73], whereby their calculations reveal a strongly non-linear relationship between the pulse width as a function of modulation current. It can be deduced from their results that achieving pulse widths below 10 ps requires approximately only 10 mA$_{pp}$ and dropping below 1 ps requires approximately 40 mA$_{pp}$ for a monolithic cavity length of 260 μm. Assuming comparable waveguide thickness and width to the devices used here, these values would need to be almost tripled to achieve comparable current densities which highlights a potential bottleneck with our devices. A marked change in gradient of their (calculated) dependence of pulse width on modulation current to a lower value is attributed to the turn on of laser parasitics which act to block the current from entering the active region. Figure 4.2(C) demonstrates the relationship between modulation power and optical pulse width for our devices. For all DC injection currents tested, the pulse width exhibits a non-linear trend towards a shorter pulse width for increasing modulation power. The low power, high DC injection current region indicates the onset of CW operation. This behaviour is not replicated at the low DC injection current region because near threshold the negative portion of the modulation cycle is likely to still be able to drop the laser below threshold. A concerning trend is the visibly weakening influence the increasing modulation power is having on the resulting pulse widths. Exactly why this is occurring is unconfirmed, however a safe postulate is that the laser parasitics are giving rise to diminishing returns for increasing modulation power.

According to the works of Haus [141] and Schell *et al* [34], the pulse width is inversely proportional to the fourth root of the modulation strength, dJ/dt. This reveals that the pulse width may be reduced not only by increasing the modulation power, but also by increasing the modulation frequency. Due to high frequency limitations of our RF amplifier it was not possible to modulate the laser beyond 4.2 GHz. Results presented in reference [73] and [139] for a semi-insulating planar buried heterostructure (SIPBH) laser diode - a device specifically tailored for high modulation bandwidth and efficient charge channelling into the active layer - the minimum achievable pulse width for 2 GHz , +26 dBm modulation and a 2 GHz composite external cavity was 5 ps. For the same cavity length and modulation at the second cavity harmonic of 6 GHz pulse widths of <1 ps were achieved. Though the shortest optical pulses are not our primary objective, for transform limited pulses, where shorter optical pulses implies a broader optical spectrum, this trend highlights the critical importance of the modulation bandwidth of the device which is to be actively mode-locked.

Results in figure 4.3(A-C) show the measured intensity autocorrelation flat pedestal height as a percentage of the pulse peak height. A flat pedestal is observed when the laser is not completely mode-locked and is therefore a manifestation of CW components being present in the beam. For all three figures we observe a strong correlation between favourable pedestal heights and short optical pulses, which supports the mode-locked nature of the laser under optimal conditions.

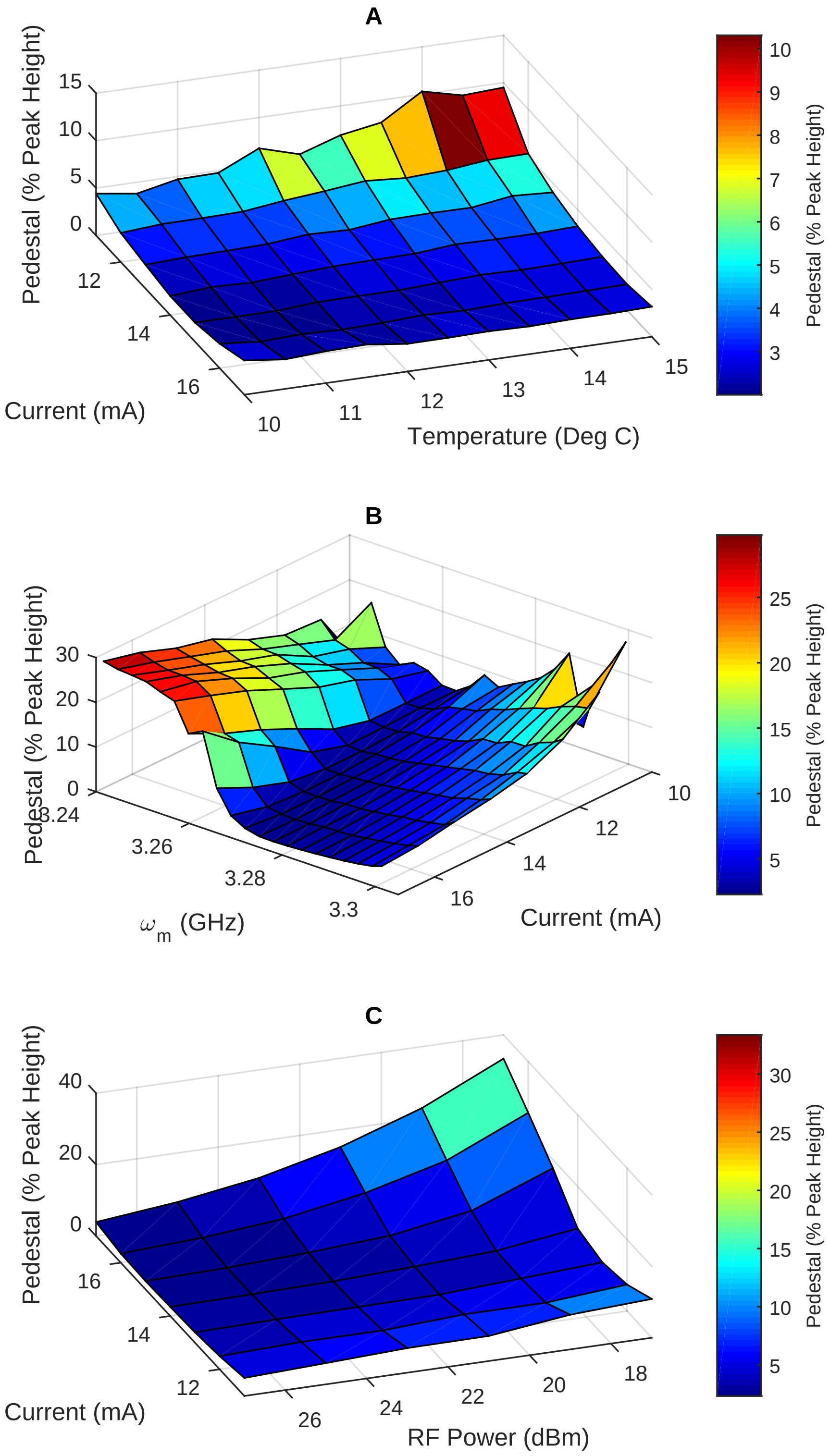

Figure 4.3: Intensity autocorrelation trace pedestal characteristics for DC injection current, diode case temperature, modulation frequency detuning and RF modulation power parameter spaces

4.1.2 Spectral Pulse Characteristics

As a reminder, the core aim of this work is to build and demonstrate a mini frequency comb so as to provide a stable frequency reference around the D2 transition in Rubidium. While the literature has a tendency to concentrate on the generation of the shortest optical pulses, instead the main concern here is the width of the optical coverage and therefore to demonstrate not necessarily a perfectly transform limited optical pulse, but a stable frequency comb spanning approximately 1 nm. Naturally we would prefer to demonstrate both, but a non-transform limited pulse does not automatically define instability. Subsequently we now consider the optical spectral width and peak position in order to determine the optimal operating conditions for the laser diodes.

As a result of manufacturing tolerances and the specific operating environment, laser diodes seldom operate at the desired wavelength for a given experiment 'out of the box'. Temperature tuning and/or a dispersive intra-cavity element is typically employed to shift the wavelength to the desired position[1]. In this section the Eagleyard diodes are characterised under free running mode-locked operation with only a planar, non-dispersive output coupler mirror and so the diode operating wavelength is defined solely by the position of the gain curve and the spectral properties of the cold cavity. For nominal operating conditions (I_{DC} = 15 mA, T=12°C and ω_m = 3.266 GHz), the laser appears to operate at the centre of its gain linewidth at 785 nm. It is intended that a thin, uncoated, fused silica etalon will be employed in conjunction with temperature tuning to reach a central operating wavelength equal to the ^{85}Rb hyperfine 'cooling' transition at 780.244 nm.

Figures 4.4 and 4.5 show the optical spectrum FWHM and spectral peak wavelengths respectively for the same parameter space characterisation as above. With reference back to figure 4.2(A), we observe the expected trend in the spectral FWHM where conditions aiding the shortening of the optical pulse concurrently aid in broadening the optical spectrum.

---

[1] DFB and DBR lasers are an exception because their design is very specific to a desired wavelength.

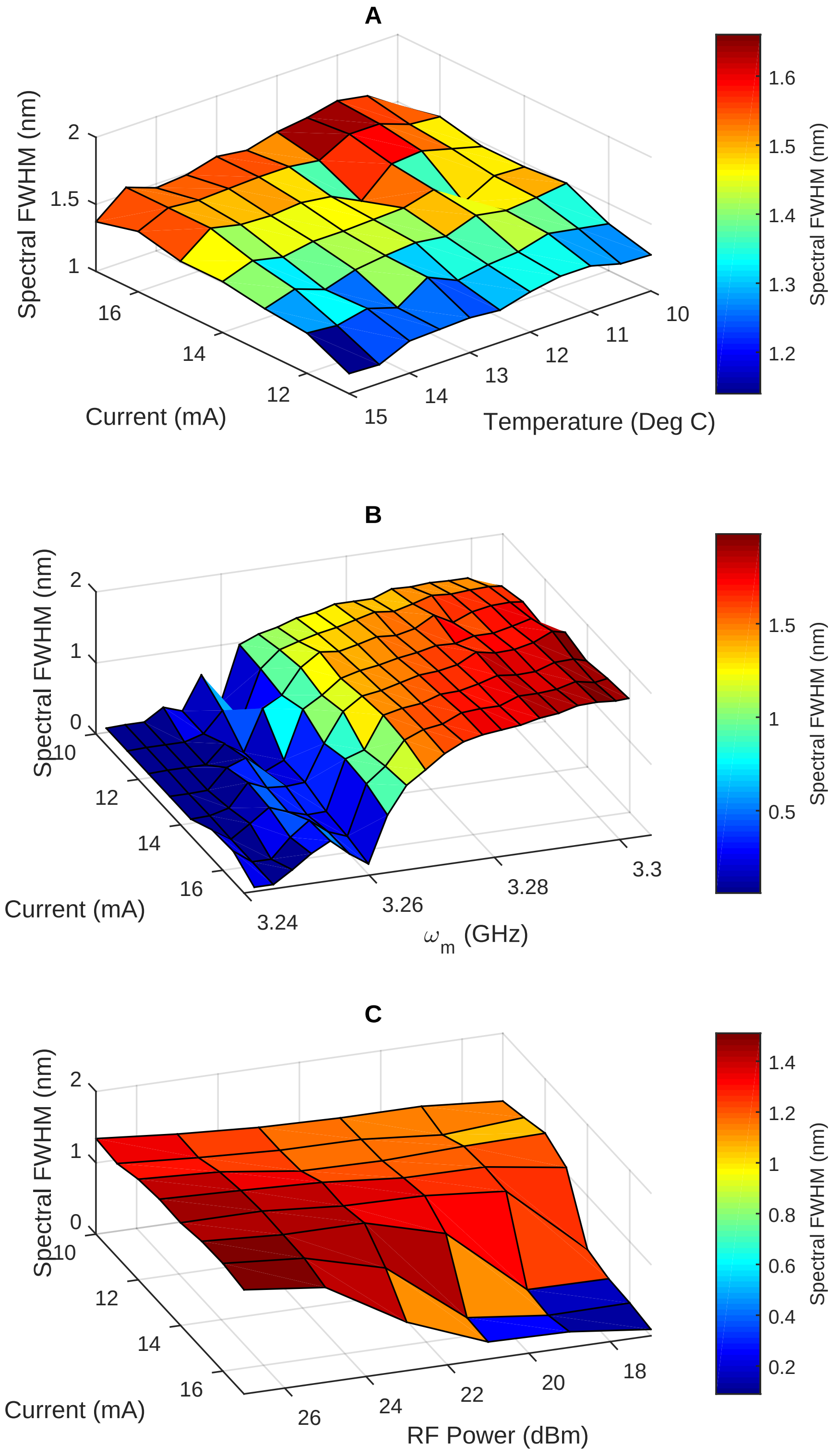

Figure 4.4: Spectral FWHM characteristics for DC injection current, diode case temperature, modulation frequency detuning and RF modulation power parameter spaces.

Likewise the opposite low current, high temperature region observes the narrowest optical spectral width. With respect to the overall requirements of our intended system, a spectral width $\geq$1 nm is sufficient. The spectral width for all plotted data points are greater than 1 nm and so the important temperature effects on the operation of the laser diode may be limited to central wavelength tuning.

The variation of the spectral FWHM as a function of modulation frequency is not entirely obvious. In the low frequency detuning region (3.24 - 3.26 GHz, where in figure 4.2(B) the pulse width sharply increased to beyond 50 ps for all plotted DC injection currents), the spectral FWHM sharply drops to 0.06 nm which corresponds well to the wavelength resolution limit of the optical spectrum analyser. The laser may be assumed to be in CW operation in this region. In the high DC injection current region of this modulation frequency space, there appears to exist some parameter combinations that produce non-resolution limited spectral widths. Where this region corresponds to the highest pulse widths observed in figure 4.2(B), it is perhaps logical to assume that this spectral broadening is highly unstable and certainly unusable as a frequency comb. This spectral behaviour will be revealed in greater detail in chapter 5.

Above 3.26 GHz the optical spectral width sharply increases to above 1 nm and plateaus with an approximate increase in spectral width of only +0.012 nm/MHz. This trend is not immediately intuitive as it would be expected that as the pulse width increases the spectral width would fall, as per the lower modulation frequency region. This observed trend in the high modulation frequency region is however explainable in terms of the same dynamic detuning of the optical pulse framework. By forcing the pulse to arrive at a time closer to the modulation cycle peak than is stable, the modulation can no longer completely counter the effects of gain saturation and hence the pulse broadens. This results in a net population depletion gradient across the pulse and hence gives rise to a refractive index gradient. This in turn causes a frequency chirp across the pulse which broadens the pulse, and the spectral width increases due to the pulse arrival at a position of higher overall gain than in the stable steady state.

Plotted in figure 4.4(C) is the spectral FWHM dependence on DC injection current and modulation power. Good qualitative agreement exists between this figure, figure 4.2(C) and figure 4.3 in terms of the gradual improvement of the mode-locking performance (shorter pulses, lower pedestal and increased spectral width) for increasing modulation power. The reason for this, as described already, is the increase in the rate of change of charge carriers entering the active region for higher modulation powers. Equally the high DC current / low modulation power region where the spectral width drops markedly to approximately the resolution limit of the optical spectrum analyser highlights the region where the laser is likely in CW operation.

Unlike in the earlier test of the current and temperature dependence of the central operating wavelength, the laser cavity no longer contains a frequency dispersive element, nor is the laser emission being forced to operate anywhere other than that defined by the gain linewidth. Calculated from 4.5(A) we arrive at a new set of wavelength tuning rates of +0.053±0.006 nm/mA and +0.275±0.015 nm/K (-25.75±2.92 GHz/mA and -133.66±7.29 GHz/K), as compared with -808±29 MHz/mA and -4.790±0.281 GHz/K from before. The new value for the temperature tuning is in line with values stated in [83,142], however the revised current tuning rate is significantly higher than expected; approximately -1 GHz/mA is expected in accordance with reference [142].

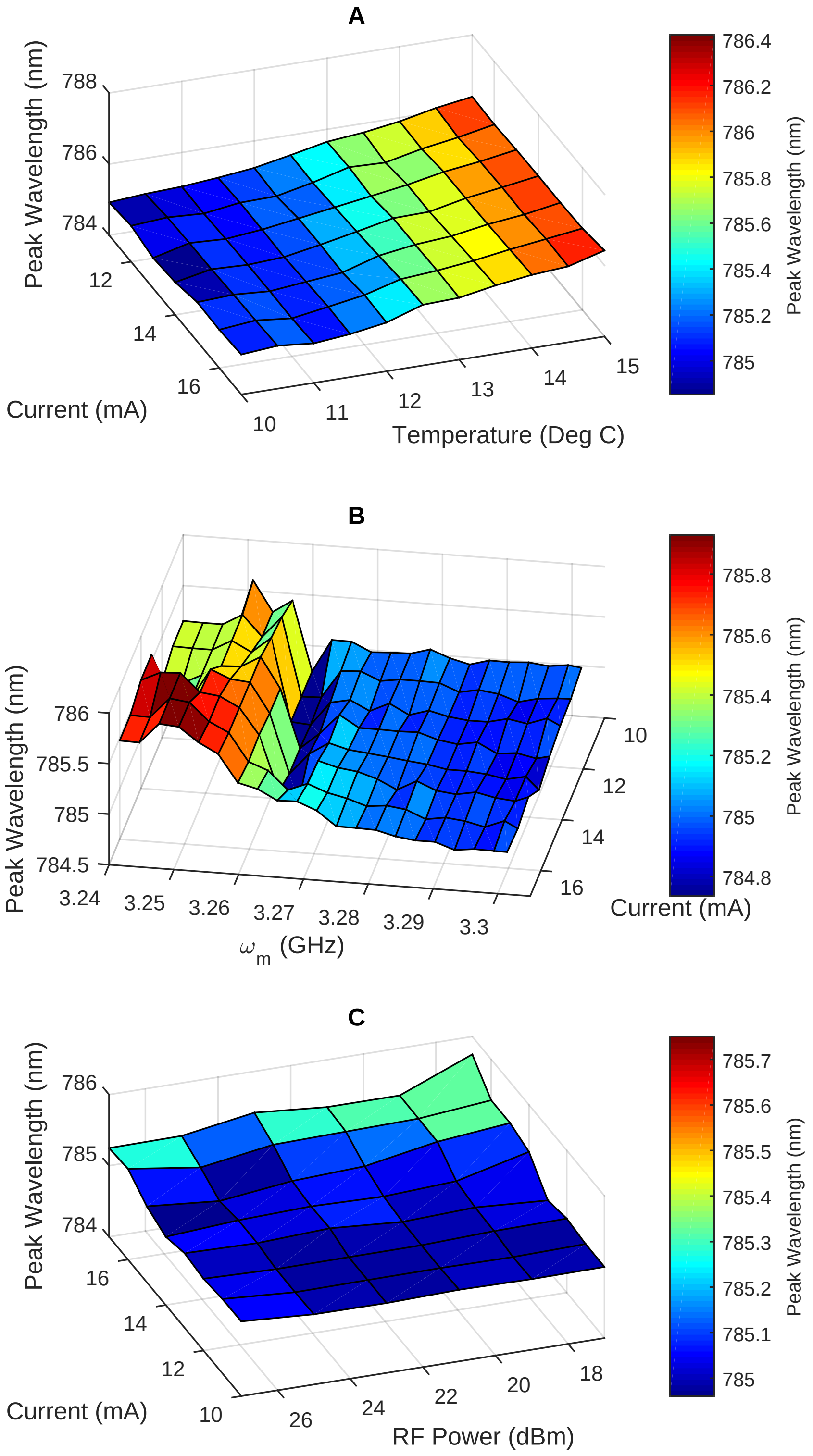

Figure 4.5: Spectral peak (tuning) characteristics for DC injection current, diode case temperature, modulation frequency detuning and RF modulation power parameter spaces.

4.1.3 Time-Bandwidth Product

The Time-Bandwidth Product is the unitless product of the pulse temporal width in seconds and the optical FWHM bandwidth in hertz, and provides a metric for determining the quality of the generated optical pulses. For a Gaussian, sech^2 and Lorentzian pulse, the constant corresponding to a transform-limited pulse is equal to 0.44, 0.315 and 0.142 respectively. A pulse is said to be transform-limited when the temporal width for a specific pulse shape is the narrowest that the corresponding optical spectrum can support. It follows therefore that a pulse of greater temporal width than the transform limit must contain errors in some or all of the phases of the constituent optical modes. The most basic of phase errors is that of noise in the optical phase causing a spatial distribution in the positions of constant phase, and is caused by excessive spontaneous emission coupling into the oscillating optical modes [122]. Other noise sources, such as noise present in the active modulation signal, DC injection current and mechanical perturbation may also contribute to the formation of non-transform limited pulses. Another possible reason is that of significant spectral phase structure in the pulse (which may be linear or non-linear) caused by chromatic dispersion and optical non-linearities. The presence of chromatic dispersion causes the pulse to become either linearly and/or non-linearly chirped. Spectral chirp in semiconductor lasers may be corrected by application of the appropriate opposite chromatic dispersion as demonstrated in references [116, 143–149].

One more possible reason for a non-transform-limited optical pulse is the so called clustered mode-locking regime [125, 141]. In this regime, the output observed by intensity autocorrleation is a broad Gaussian shape, typically with a coherence spike and many times the transform limit, which consists of multiple, temporally overlapped, near transform limited pulses. The effect is the result of bandwidth limiting etalon behaviour within the optical spectrum, and poor optical modulation depth resulting in sub-critical coherence transfer between the modes oscillating in adjacent etalon modes. Specifically with mode-locked diode lasers, the imperfect AR coating on the internal diode facet causes significant spectral filtering at the monolithic cavity mode spacing. For our specific devices, with an effective optical path length given by $2nl$, the monolithic cavity

FSR is ∼56 GHz. Assuming each 56 GHz wide cluster of composite cavity modes forms a Gaussian transform limited pulse, these pulses would be 7.9 ps in duration.

Figure 4.6 shows the calculated values for the time-bandwidth product derived from the above data. These data serve to confirm much of the above analysis regarding the CW and mode-locked operating regimes, while equally highlighting potentially significant issues with the specific laser devices. In the DC injection current / temperature parameter space (figure 4.6(A)), the best time-bandwidth product observed at 14 mA / 11°C is 16.97±1.51, which is approximately 38 times the transform limit.

Figure 4.6(B) demonstrates two clear regions of different behaviour separated by the line of constant modulation frequency equal to ∼3.26 GHz (approximately the optimum for mode-locking performance). Towards higher modulation frequencies, as observed in figures 4.2(B) and 4.4(B), simultaneous temporal and specral broadening occurs, and this manifests in figure 4.6(B) as a steady increase in the time-bandiwdth product. Towards lower modulation frequencies however, where the pulse temporal width is observed to increase sharply and the spectral width is observed to decrease sharply (to approximately the spectrum analyser resolution limit) and become erratic, the laser is assumed to be operating outside the mode-locked region in a fashion more closely resembling CW operation. Recall that in this region, the active modulation is attempting to establish mode-locked operation, however no stable state can be reached and hence we observe the erratic nature of the optical spectrum. It is possible also that any discernible line shape on the intensity autocorrelation may be due to mode beating; The strong RF modulation is giving rise to Bessel function frequency- and amplitude modulation sidebands which are beating to give intensity variations.

Figure 4.6(C) also shows two clear regions where the laser is in mode-locked and CW operation. In the high DC injection current/low RF modulation power region the time bandwidth product has dropped significantly suggesting the laser is operating in CW. As the modulation power is increased, and/or the DC injection current is reduced, mode-locked operation is established.

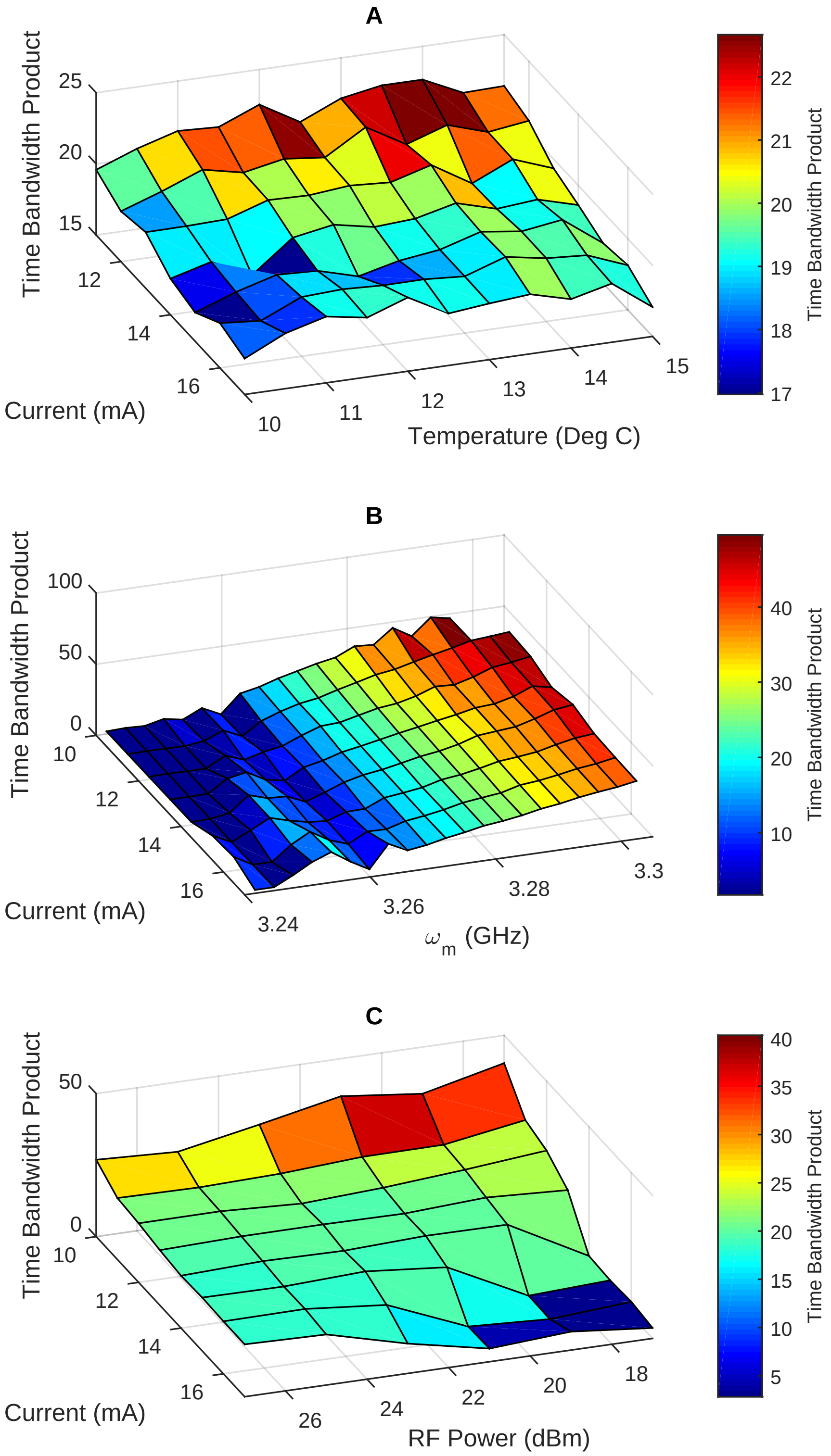

Figure 4.6: Time Bandwidth product characteristics for DC injection current, diode case temperature, modulation frequency detuning and RF modulation power parameter spaces.

This brief consideration of the time bandwidth product has been conducted for two reasons. In the first instance it provides an indication of the quality of the optical pulses, while in the second instance it allows a grasp of the dynamic behaviour between the pulse temporal and spectral width, as a function of the experimental variables, in a single surface plot. In the context of the frequency comb however, around the notionally optimal parameters for optimal mode-locking performance, the precise value of the time bandwidth product is of limited practical importance as by itself it does not define the properties of the optical modes comprising the frequency comb. As stated previously, it is possible to have both a useful frequency comb (in the present context of a frequency reference for Rubidium) in that the modes are phase stable and pulses which are far from the transform limit. Naturally it would be favourable to have transform limited pulses, as this intrinsically implies the phase stability of the comb modes. Indeed, as transform limited pulses have not been achieved, we aim to explore the phase stability of the frequency comb in chapter 7.

4.2 Wavelength Tuning to 780 nm

So far in this thesis the laser emission wavelength has been entirely governed by the free running position of the gain profile and the axial mode structure of the composite laser cavity. No attempt has been made to alter these conditions in a targeted way other than to systematically alter operating conditions such as current, temperature, etc, to determine tuning rates of measurable emission characteristics. Now that the mode-locked laser output characteristics have been achieved, it is prudent to recall that the optical transitions in Rubidium we wish to surround are approximately 5 nm away at 780.244 nm. To aid in tuning the emission, a combination of temperature tuning and the addition of a thin, uncoated, fused silica etalon (20 μm thickness, $\sim$10 nm FSR) is used to achieve the desired emission wavelength. The total change in housing temperature was 17°C from +12 to -5 degrees which placed the diode well outside the manufacturers recommended operating temperature range. Further, because the new case temperature is well below the dew point of the laboratory, a custom acrylic box was machined and constructed to enclose the laser and a Thorlabs laser window (WL11050-C13) was integrated into the housing. Standard dry nitrogen gas was trickled into the housing both to create an atmosphere purged of water vapour and to generate a positive pressure gradient to keep water vapour from diffusing into the housing. A standard 10 m^3 fill volume Nitrogen bottle would last approximately 2 weeks.

Towards the end of the experimental work conducted to characterise the mode-locking performance at its free running wavelength, it became apparent that the laser diode in use may be supporting what appeared to be a higher order spatial mode. In the first instance, by inspecting the rejected light at the first polarising beam splitter cube on the Faraday optical isolator, it became clear that the rejected light had the appearance of a TEM_{10} Hermite-Gaussian (HG) transverse mode, polarised orthogonally to the central TEM_{00} mode[2]. Measurement of the respective powers transmitted and rejected at the isolator revealed a power ratio of 4:1 (00:10). Where the two modes are orthogonally polarised, it is reasonable to investigate the use of a linear polariser inside the laser cavity to reject this higher order mode. We employ an AR coated polarising beam splitter cube (Thorlabs PBS102) which provides $\sim$60 dB of round trip loss and is mounted in the external cavity such that the cube faces are slightly rotated from perfectly normal to the beam axis to avoid back reflection. Figure 4.7 shows two different knife-edge beam profiles and their respective Gaussian fits for the laser operating with and without the intra-cavity polariser. The knife is translated horizontally across the beam so as to obscure one lobe of the 10 mode before the other.

---

[2] By nature of the orthogonal polarisation relationship, we have not invalidated any results thus far on account of the optical isolator; only the 00 mode is transmitted and hence all measurements up to now are of this lowest order component. Conversely however, if indeed this other component is a higher order Hermite-Gaussian spatial mode, it's presence in the laser cavity could have a destabilising effect and potentially go some way towards explaining the significantly longer pulses than expected for the corresponding spectral width.

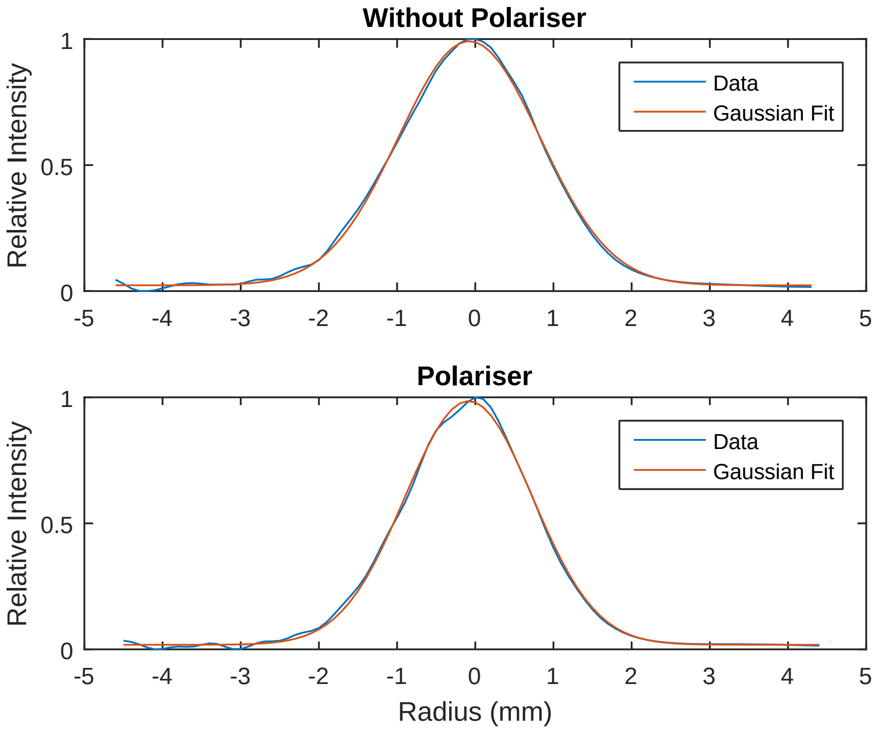

Figure 4.7: Knife-edge beam profiles of the mode-locked laser without and with an intra-cavity linear polariser.

From the data in figure 4.7, no clearly identifiable spatial mode profile of higher order than 00 is visible for when not using the polariser. The presence of a HG TEM$_{10}$ mode on top of the 00 mode would present as visible undulations in the downward slope either side of the peak intensity. Curiously however, the FWHM parameter changes noticeably between the two intensity profiles, whereby without the polariser the beam radius is 1.810±0.009 mm and the radius with the polariser is 1.630±0.008 mm, as determined by the Gaussian fit for each curve. This ∼10% reduction in the beam width is certainly caused by the rejection of the light in the opposite polarisation, however this result is perplexing. The light is linearly polarised which rules out the possibility that its origin is simply that of spontaneous emission, yet without the intra-cavity polariser the beam does not adopt a profile consistent with the addition of a defined higher order spatial mode. This behaviour is not unique to this specific diode as all previously used diodes of the same model number were also confirmed to behave in this way. In any case, initial testing of the laser with and without the intra-cavity polariser revealed no noticeable changes in the best achievable emission characteristics.

Following this brief digression we return now to the re-characterisation of the laser now that the wavelength has been tuned to 780 nm. With the polariser and thin etalon in place the mode-locked laser emission is characterised in the same way as section 4.1 and the salient behaviour is plotted in figures 4.8 and 4.9.

Figure 4.8 shows plots of the temporal (A) and spectral (B) width of the tuned diode laser respectively. While the presence of the linear polariser in the cavity increased the laser threshold current considerably, the counter effect of reducing the threshold current with reduced junction temperature resulted in a threshold current approximately only 1 mA higher than in previous experiments (∼10 mA). Similarly to before the wavelength tuning, the mode-locking performance in terms of the temporal pulse width very near threshold degrades significantly. It is apparent that the temporal pulse width minimum degrades marginally to 22.18±0.01 ps, as compared to 21.55±0.01 ps from figure 4.2, and maintains a pulse width below 25 ps for all tested temperatures at all tested DC injection currents above and including 14 mA (∼140% of threshold).

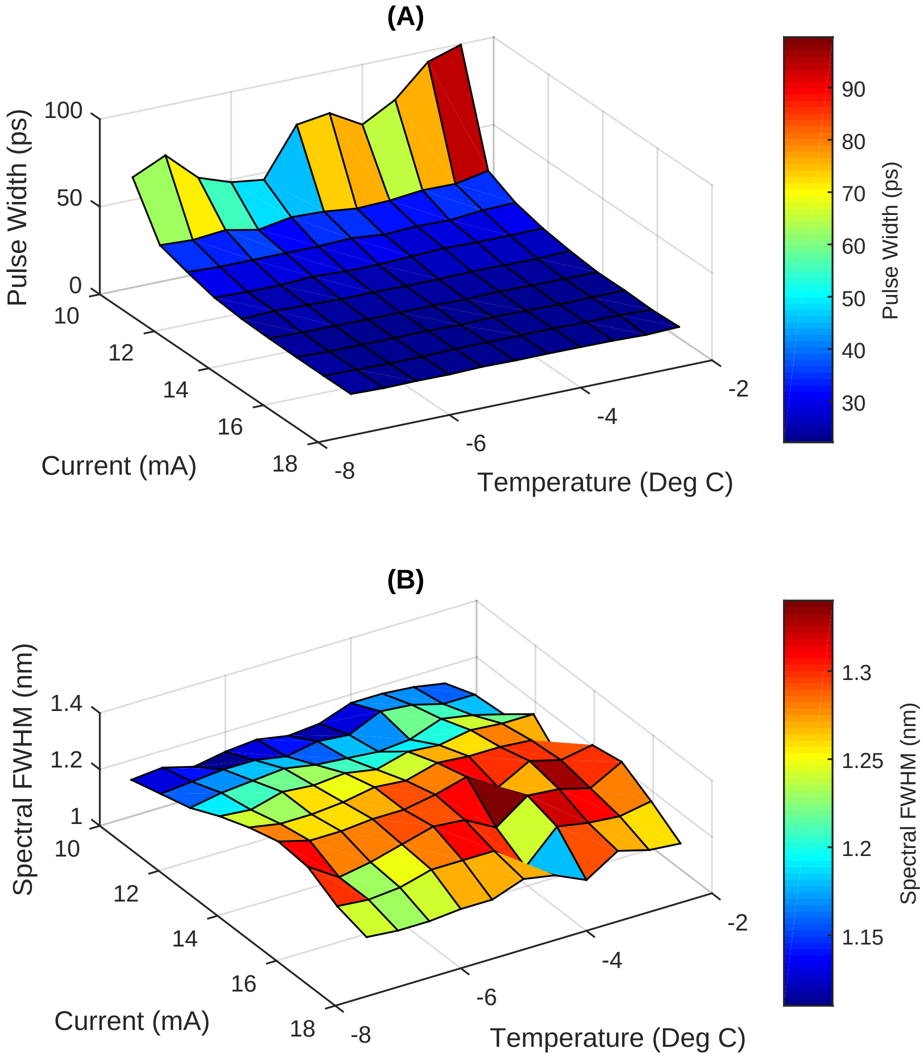

Figure 4.8: Characteristics of the mode-locked diode laser once wavelength tuned to ∼780.2 nm. (A); Temporal pulse width as a function of DC injection current and case temperature, (B); spectral FWHM as a function of DC injection current and case temperature.

In figure 4.9(A) we show the measured spectral peak position as a function of mount temperature and DC injection current. From this plot it is determined that the wavelength tuning rates are +0.117 ± 0.031 nm/K and +0.03 ± 0.06 nm/mA. Observed is almost a factor of 2 drop in the tuning rates when compared with the free running characterisation (+0.275 ± 0.015 nm/K and +0.053 ± 0.006 nm/mA). This change is attributed to the competition between the loss induced by the thin etalon and the actual shift of the gain curve as a function of the altered variables. If the peak of the laser gain profile is shifted away from the transmission peak of the etalon, the spectral position observing the least round trip loss, which exists somewhere between the two peaks, does not necessarily translate in frequency at the same rate as the gain curve when an experimental parameter is changed. From the data in figure 4.9(B) We also observe a slight improvement in the optimum time-bandwidth product for the tuned laser from 16.97±1.51 to 13.41±1.32.

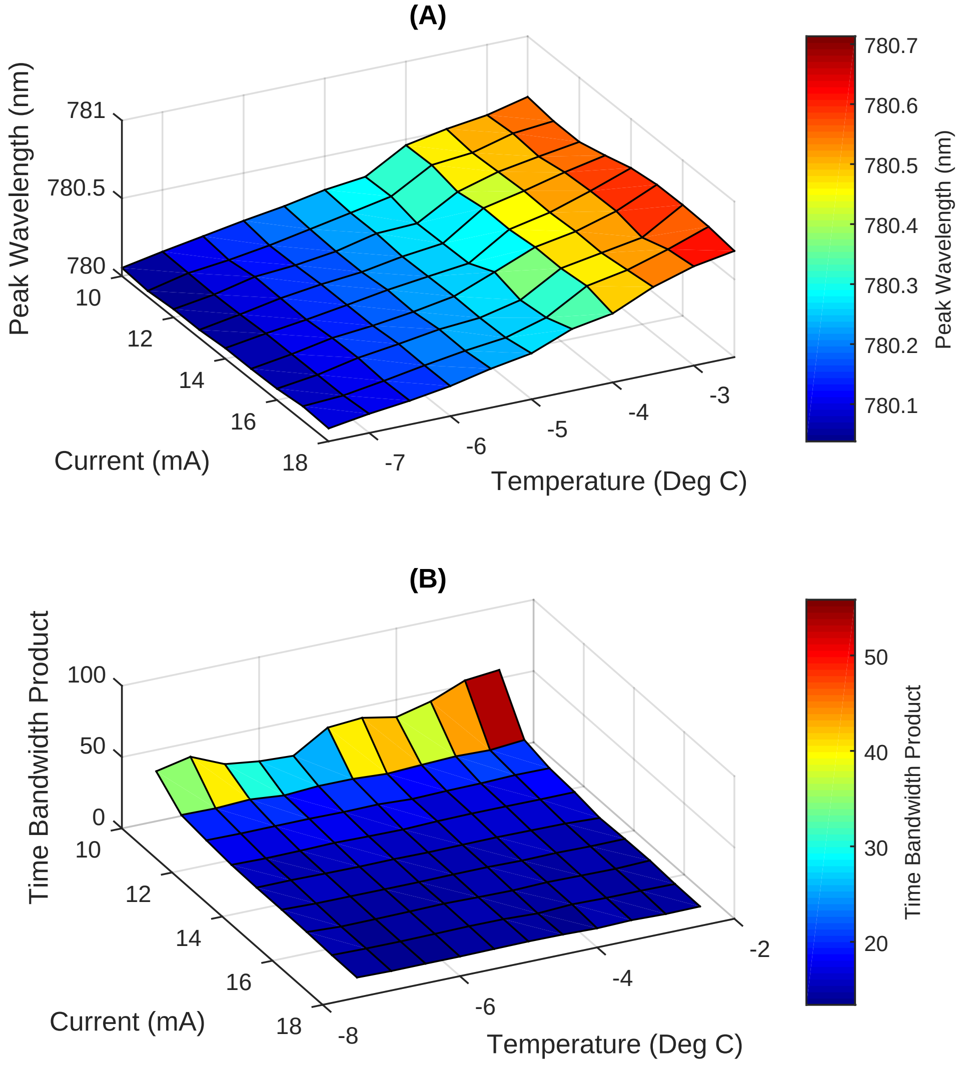

Figure 4.9: Time Bandwidth product characteristics for DC injection current, diode case temperature, modulation frequency detuning and RF modulation power parameter spaces.

Overall the emission characteristics of the laser appear largely unchanged by the tuning of the laser to 780 nm. The higher order spatial mode supported by the laser cavity appears to have little effect on the laser output characteristics, as the parameters of primary interest, i.e., the pulse temporal and spectral width, behave seemingly identically to the characterisation of the laser at ∼785 nm. We tentatively attribute this to the fact that the two spatial modes[3] are of orthogonal polarisations, meaning that any interaction between them must be via the carrier density in the active region. From reference [36], the intra-band carrier diffusion time has been measured to be of the order of 50 fs. Given that the measured pulse temporal width in both this section and the previous is nearly three orders of magnitude longer than this timescale, it is reasonable to conclude that the higher order spatial mode is not having a detrimental (or otherwise) effect on the fundamental mode when considering the mode-locking performance.

4.3 Modulator Characteristics

Of the salient parameters for achieving active mode-locking, the quality of the modulation signal is of great importance. It is widely agreed that low phase noise is critical to stable active mode-locking [118] and so in this section we briefly focus on characterising the modulation signal. In the time domain the modulation signal defines the temporal position of the pulse. If the pulse arrives at a position on the modulation cycle which differs from the steady state position, the modulation signal will act to pull the pulse towards the steady state position through preferential amplification of the leading or trailing edge of the pulse. The detectable manifestation of modulation signal phase noise is jitter in the pulse to pulse temporal separation. In the spectral domain the modulation signal directly defines the optical mode separation and hence noise in the modulation signal will subsequently translate to noise in the optical linewidth of the oscillating modes. The latter effect is easily detectable on the RF spectrum. Figure 4.10 shows the RF spectrum of two separate oscillators, before and after amplification, as well as the corresponding RF spectrum of the mode-locked laser at the external cavity fundamental frequency. Direct measurement of pulse jitter in the time domain was not possible through a lack of a photodiode with suitable frequency response.

Data in the left hand column of figure 4.10 shows a 500 kHz span window of the fundamental modulation signal for the Mini Circuits oscillator, (a), the same modulation signal amplified by 42 dB, (b), and the mode-locked laser fundamental beat note detected

---

[3] While we refer to the extra spatial component in the beam as a higher order mode, its exact classification remains undetermined.

with a fast photodiode, (c). The oscillator is powered by a linear voltage regulator and the frequency tuning voltage is supplied by an Analogue Devices REF01 10 volt precision voltage reference.

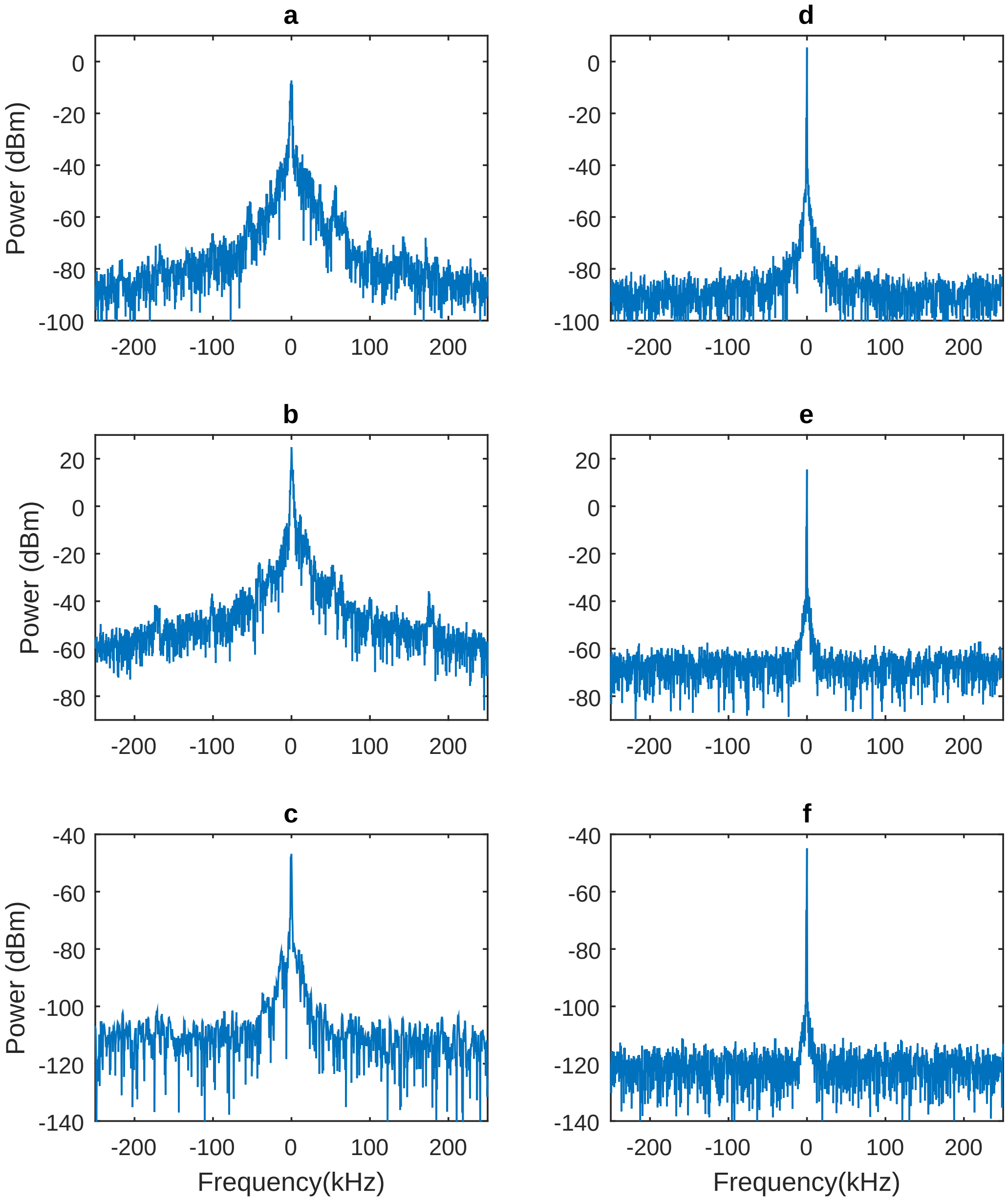

Figure 4.10: Modulator linewidth comparison at the fundamental modulation frequency (3.0 GHz) for the Mini Circuits VCO (left column) and Agilent 8648C arbitrary function generator (right column) over a 500 kHz span, 300 Hz RBW. (a) & (d), direct oscillator output, (b) & (e), amplified (Mini Circuits TVA-11-422) oscillator output, (c) & (f), RF spectrum of mode-locked laser fundamental frequency.

Smoothing capacitors bridge the input and output rails of the linear regulator to ground, and the tuning voltage is adjusted with a 20 turn potential divider. Data shown in the right hand column shows the same respective test conditions for an Agilent 8648C arbitrary function generator. In all cases RBW = VBW = 300 Hz. Due to damage threshold limitations of the RF spectrum analyser, and for the purposes of the data in figure 4.10(b, e) only, in line signal attenuators were used between the amplifier and spectrum analyser. In all cases an 18 GHz bandwidth DC block was used just prior to the RF spectrum analyser. From these data the most important aspect is that the linewidth of the optically derived signal at the fundamental modulation frequency appears to be closely governed by the linewidth - and hence phase noise - of the modulation signal. It is further apparent that the linewidth of the respective modulation sources is not degraded by amplification.

Figure 4.11 shows the RF spectrum over the full 25 GHz bandwidth of the detecting photodiode for a modulation frequency of 2.905 GHz. The resolution bandwidth was 51 kHz and the video bandwidth was 16 kHz. For an ideal mode-locked laser of comparable optical bandwidth, we would expect to see modes of equal height across this frequency span. At the time of acquisition SMA cables of similar bandwidth to the frequency span were not available and the cables used were rated to only 2 GHz. Likewise the DC block has a stated bandwidth of 18 GHz. The fall off of the harmonic amplitudes is therefore reasonably attributed to signal attenuation between the spectrum analyser and the photodiode. In the absence of a suitably fast reference oscillator it was not possible to calibrate the component losses and correct for the harmonic amplitudes in the RF spectrum.

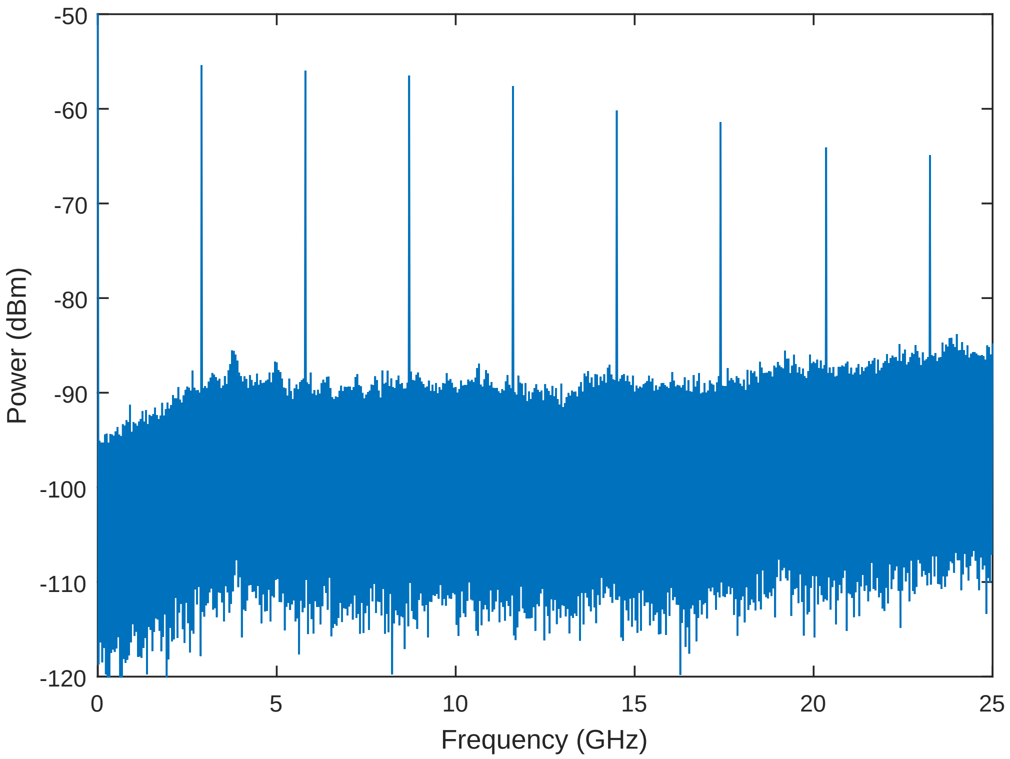

Figure 4.11: Full span RF spectrum of the mode-locked laser. The photodiode frequency response has not been corrected for.

4.3.1 Modulator Detuning Characteristics

While the effects of detuning the modulation frequency from that of the external cavity FSR have been discussed above, we now consider the effects on the RF spectrum in order to determine an accurate modulation frequency detuning range for the system. Figure 4.12 shows a 500 MHz span RF spectrum around the mode-locked laser fundamental frequency for a range of modulation frequencies (A) and the corresponding optical spectra (B) and measured pulse widths (C). According to Ahmed *et al* the locking range for which the mode-locked laser gives stable pulses (amplitude and jitter) is described on the RF spectrum as the detuning region for which the feature at the fundamental modulation frequency remains narrow and surrounded by a low, flat noise floor [150]. Though the noise floor surrounding the fundamental modulation frequency in figure 4.12(A) is not completely featureless, it must nevertheless be assumed that the locking bandwidth extends into the negative region by approximately 5 MHz on account of the pulse width behaviour shown in figure 4.12(C). Towards increasingly positive frequency detuning values, the noise floor indeed becomes almost entirely featureless until approximately +35 MHz where one peak either side of the fundamental begins to appear.

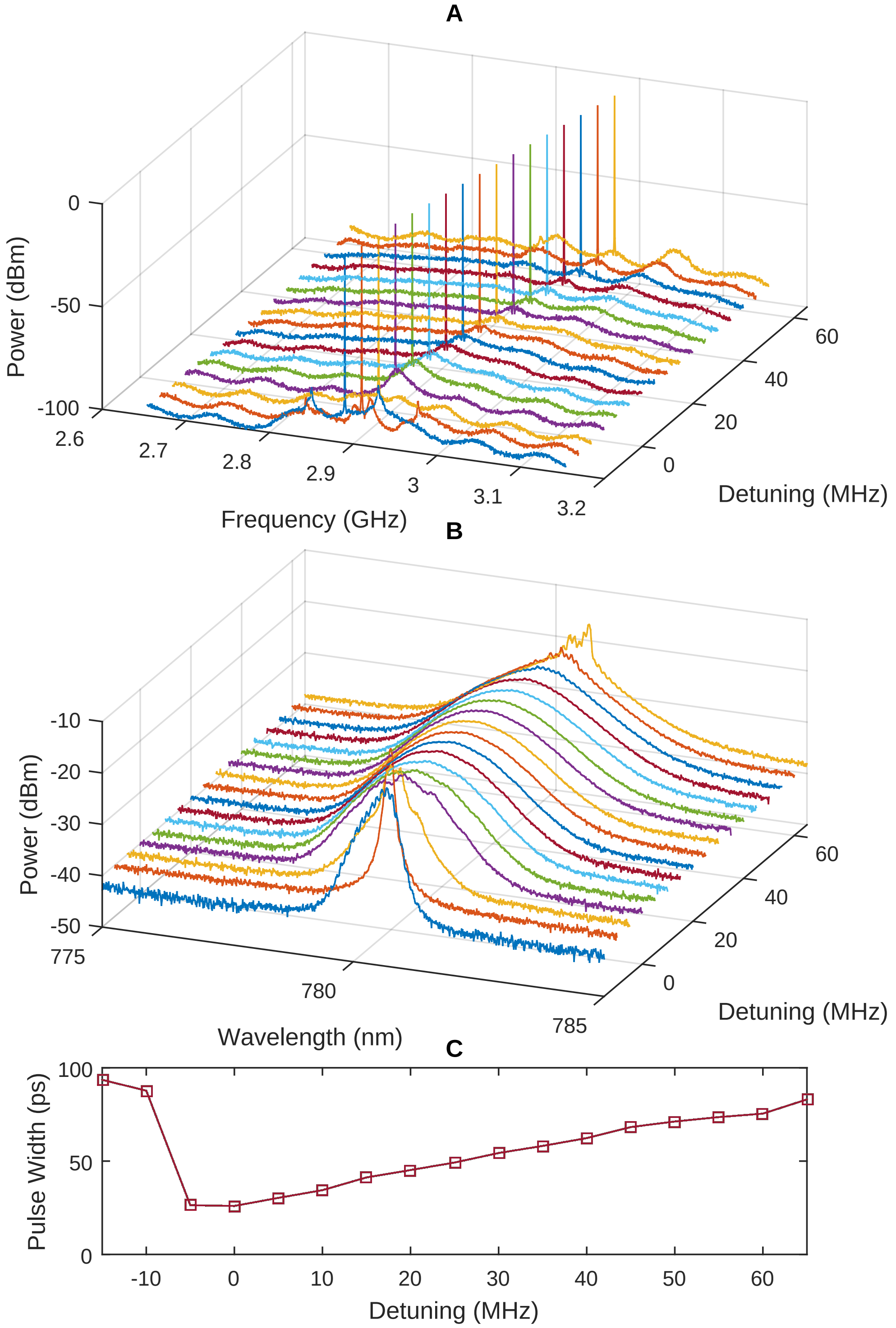

Figure 4.12: Pulse characteristics for detuning of the modulation frequency. Zero detuning corresponds to the frequency for the shortest temporal pulse width. (A); fundamental beat note on the RF spectrum, (B); Optical spectrum, and (C); measured temporal pulse width

This onset of RF spectral broadening therefore defines the positive frequency detuning limit to the locking region. Overall the locking region is ∼40 MHz spread severely asymmetrically about zero detuning, favouring the positive detuning region by 7:1. This result is both corroborated by the smooth optical spectra obtained for the same detuning range and is in qualitative agreement with [150], though they report a locking region of only 25 MHz from -10 to +15 MHz. In the same reference the measured pulse width is also asymmetric, however a steeper average gradient (for the rate of change of pulse width per unit detuning) exists for positive detuning rather than negative. This is at odds with the results presented in this chapter, and also with the work in references [71, 138–140].

4.4 Discussion

In this chapter we first presented a characterisation of the mode-locked lasers temporal and spectral performance over the accessible parameter spaces. In terms of the temporal pulse width, from figure 4.2 we can conclude that the junction temperature is essentially of little importance, inasmuch as over the demonstrated 5 degree tuning range, the pulse width for a given DC injection current changed by less than 10 ps. While the change is small it is nonetheless visible, and the trend of this change - shorter pulses towards cooler junction temperatures - is attributed to the increase in the slope gradient of the power-current curve (figure 3.2) and the slight decrease in threshold current. The junction temperature does however have a large effect on the operating wavelength, where tuning rates of +0.275±0.015 nm/K are observed. In terms of the DC injection current, the effect on the pulse width is considerably stronger. We find that for a temperature of 10°C, the optimum pulse width occurs at approximately 80% of the threshold current, with a symmetric optimum current range of only 2 - 3 mA around this point.

The active mode-locking modulation frequency is the most critical of the experimental parameters in terms of the pulse width. Due to the dynamic detuning effects discussed in section 4.1.1, the detuning range for which the shortest stable pulses exist is approximately 10 MHz. Towards lower modulation frequencies the pulse width increases sharply and the pulse optical spectrum collapses to a state which resembles CW operation. At higher modulation frequencies the pulses remain stable over a considerably larger range, however the pulse width increases monotonically with increasing modulation frequency, reaching approximately double the minimum pulse temporal width for +30 MHz modulation frequency detuning. The spectral width remains inexplicably broad ($\geq$ 1.25 nm) for all positive detuning frequencies. The precise reason for this remains unresolved, however as the temporal pulse width and time-bandwidth product rise steadily with positive modulation frequency detuning, it should be concluded that the acceptable detuning range is within ±5 MHz of the frequency corresponding to the minimum pulse width.

Across all the data presented in section 4.1 it is clear that higher modulation power has a positive impact on the temporal pulse width, spectral width, pedestal height and time-bandwidth product, while having negligible effect on the central emission wavelength.

Following the wavelength tuning of the mode-locked laser to 780.2 nm, plots of the pulse width, spectral peak wavelength, spectral FWHM and time-bandwidth product were given as a function of DC injection current and temperature. In terms of the temporal pulse width, much the same trend is observed as for the laser free running at 785 nm; temperature variations have little effect and the optimum DC injection current around 15 - 16 mA. This optimum DC injection current range is matched also for the spectral FWHM values observed in figure 4.8. It is believed that the presence of the thin etalon is responsible for adversely affecting the central wavelength tuning rate as a function of temperature. With the etalon in place the wavelength tuning rate falls by almost a factor of 2 to $+0.117\pm0.015$ nm/K. The modulation power and modulation detuning, while not shown in section 4.2, demonstrates reassuringly identical behaviour and so the above conclusions, and indeed values, hold for the laser operating at 780.2 nm.

With the mode-locked laser successfully tuned to 780.2 nm, we have identified a set of parameter values and ranges which produce approximately 21 ps mode-locked pulses of spectral width in excess of 1 nm, thereby satisfying our primary aim. A troubling property of the pulses however is their large time-bandwidth product. At approximately 30 times the Fourier transform limit, the pulses are far longer than their inverse spectral width would suggest. It was previously assumed that strong spectral chirp was to blame for the very large time-bandwidth products, and so pulse compression was attempted. Where actively mode-locked diode lasers typically exhibit anomalously, linearly dispersed pulses [144], a dual grating compressor with an integrated telescope [143, 149] capable of generating a net normal dispersion was constructed in an attempt to compress the pulses. Despite considerable effort in the optical alignment of the pulse compressor, no evidence of shorter pulses was observed, supporting (but not confirming) an earlier hypothesis that the mode-locked laser could be operating in a clustered pulse output known as 'mode-locking in clusters'. This is discussed in greater detail in chapter 6.

Chapter 5

Air Track Michelson Interferometer

The purpose of this chapter is to demonstrate an air bearing Michelson interferometer which is capable of adequately resolving the optical spectrum and revealing the structure of the frequency comb. In previous chapters the mode-locked laser diode has been characterised in the time and frequency domain by observing the pulse temporal shape via intensity autocorrelation and by observing the optical and RF spectrum respectively. Through analysis of the RF spectrum (figures 4.11 and 4.12(A)), it would be reasonable to conclude that the mode-locked spectrum consists of discrete optical modes separated by the modulation frequency. The linewidth of the visible beat notes suggests the laser is in stable operation and the marked lack of signal between these modes further suggests the optical emission lacks any significant noise in the form of broad linewidth oscillating optical modes. Despite this positive evidence, the intensity autocorrelation still exhibits both a short pedestal and a small coherence spike, indicative of incomplete mode-locking. This is further supported by the far from transform limited pulses. With the help of the department's mechanical workshop, a dual moving arm Michelson interferometer based on an air bearing design has been designed and fabricated for the purpose of resolving the mode-locked optical spectrum and confirming whether or not the laser emission is in the form of a frequency comb.

Current methods for directly viewing the content of an optically broadband source tend to cater for the two extremes in resolution. On the one hand, spectrum analysers based on dispersive optics provide excellent broadband spectral sensitivity - in some cases, spanning well in excess of 1000 nm - while simultaneously suffering from poor resolution, often being limited to around the order of 0.02 - 0.05 nm and generally reaching this resolution only when viewing a relatively small spectral window. While this is a very useful tool, 0.02 nm corresponds to $\sim$10 GHz, or 3 teeth on our frequency comb. This resolution would need to be improved by nearly a factor of 10 before the comb would begin to be resolvable. On the other hand devices such as the scanning Fabry-Perot optical spectrum analyser (FP-OSA) [151] offer exceptional spectral resolution - of the order of hundreds of MHz to hundreds of kHz - but only over a very small spectral window defined by the scanning range of the moving mirror. Further, a mode-locked laser might generate a spectrum potentially millions of times wider than the spectral window of the FP-OSA. Ultimately these two techniques are unable to resolve the detailed spectral content of the mode-locked laser, and so we are yet to confirm the desired comb-like structure of the laser emission.

The Michelson interferometer does not rely on dispersive optics; instead it derives its frequency resolving capability from the principle of interference. Monochromatic light sent into the interferometer is split and directed down two discrete optical paths before being recombined. At recombination the interference between the two components produces an output power in direct relation to the relative phases of the two beams. If one mirror is scanned so as to continuously alter one path length, the interference conditions change and hence the output power changes also. For a fixed rate of change of relative path length, the output power adopts a pure sinusoidal form. The frequency of this sinusoid is directly related to the moving mirror velocity and the wavelength of the light forming the constituent beams. This sinusoidal waveform is called a *beat* and the recording of this beating on an oscilloscope is referred to as the *interferogram.* The interferogram in the time domain may be Fourier transformed into the frequency domain to give information about the power spectral density of the frequency components comprising the interferogram. The power spectrum will be in terms of the beat frequencies, not the absolute optical frequencies, and so the conversion requires a fixed, known optical frequency to act as a beat frequency marker. To this end we use the spectroscopically stabilised ECDL that was demonstrated in chapter 2.

This chapter is organised into two main sections. The first considers the design characteristics of importance for both the interferometer itself as well as the tertiary equipment for data collection. The second section outlines details of the experimental procedure before continuing to present the results for the frequency comb optical spectrum.

5.1 Air Track Design

This section reviews the requirements of an interferometer for resolving the mini frequency comb and how these requirements translate to specific design characteristics. A collaborative effort was formed by the author and Mark Bampton of the School of Physics and Astronomy mechanical workshop for discussion of the device performance requirements and full credit for the Computer Aided Design and device manufacture belongs to Mark Bampton. All other work and analysis presented in this chapter are the work of the author. While the precise physical design of this system is unique, the concept of the air bearing Michelson interferometer is based on references [152, 153]. Historically many different techniques have been utilised to improve the distance over which the moving mirrors may travel, including a toy train [154] and simple mechanical rail and bearings [155].

5.1.1 Design Considerations and Optical Arrangement

The moving arms of the Michelson interferometer are realised by mounting two retro-reflecting mirrors in a travelling cart which traverses a straight, machined flat, aluminium rail which has a flat top 90° ridge spatial profile; see figure 5.1. Motion of the cart is achieved simply through pushing it by hand, after which its motion is passive. Elastic interaction with mounted springs at each end of the rail are sufficient to maintain long term motion, and the unaided ring-down time is of the order of a few minutes. For the correct interferometric behaviour it is imperative that the back-reflected beams remain perfectly overlapping at the point of interference, so all reasonable measures to ensure that the cart does not drift laterally or vertically as it travels longitudinally should be taken.

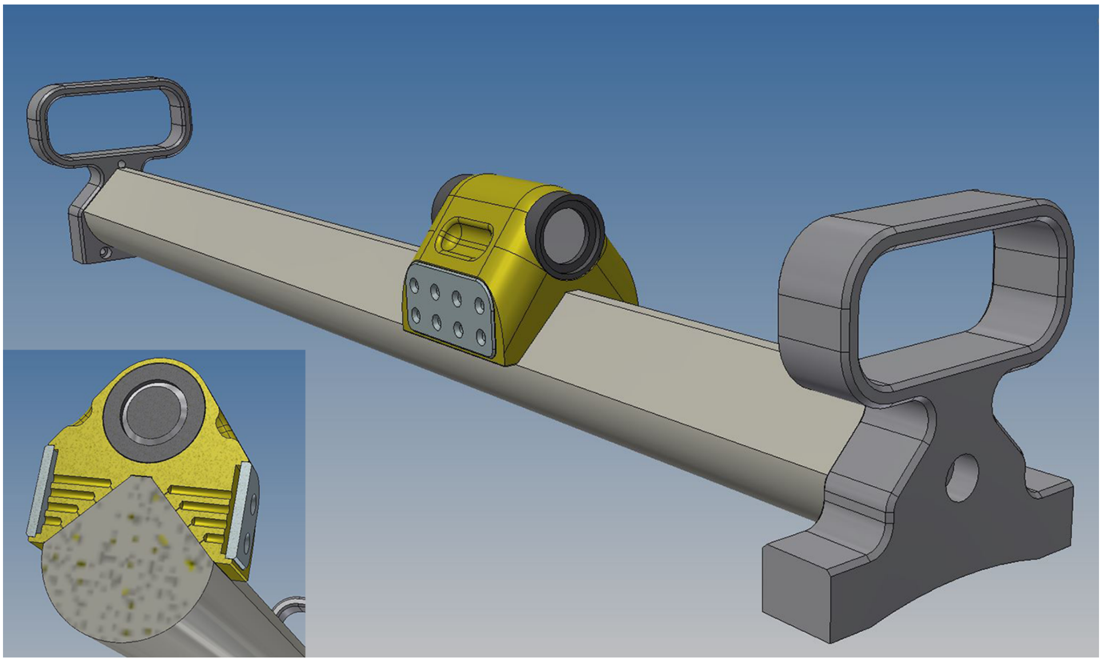

Figure 5.1: Computer Aided Design diagram showing the design layout of the air bearing Michelson interferometer. Inset is a cut view of the internal gas distribution layout. Gas is delivered to the right hand chamber and a pipe drilled to the left chamber (not shown) allows the pressure to equalise between them insuring even pressure over the flat bearing surfaces. Image Credit: Mark Bampton

The first measure is that the gas supply should maintain as close to a constant pressure as possible. Variations in the gas pressure will result in variations in the volume of the gas suspension/lubrication layer. Local pressure variations in this layer may give rise to rotations of the cart around the axes perpendicular to the direction of travel, and an offset in a transverse direction from the axis along which it travels, thereby potentially disturbing the interference when the beams are recombined. A line pressure of only 1 to 2 PSI is used, yielding the lowest possible suspension layer volume while completely avoiding parts of the cart landing on the rail during transit.

The second measure is that the gas should be delivered to the cart as opposed to the rail. The benefit of this delivery method is first and foremost the elimination of local pressure gradients along the direction of travel. It is not unforeseeable that, if the gas were pumped out of the rail, the gas flow rate along the rail may vary leading to variations in transverse displacement, or worse, the periodicity of the gas flow holes may support rotational or displacement resonances in the cart. Gas delivery through the cart also eliminates the necessity of high gas pressures and largely eliminates the possibility of dynamic refractive index variations along the optical path [152]. The one significant drawback of gas delivery through the cart is the effect of the inertia of the gas line on the motion of the cart. It is observed that with only ∼80 cm of light weight rubber tube between the cart and the first solid gas line fixation, the effect of vibrations in this section of the air line (which are caused by the cart changing direction) are sufficient to alter the velocity of the cart by an amount easily visible interferometrically. Velocity corrections of the cart are attempted with varying degrees of success depending on the shot-to-shot velocity profile of the cart, as determined by analysis of the reference laser beat signal. This is discussed further is section 5.2.1.

The final measure is ensuring that the springs used in reflecting the cart at each end of the rail are mounted at the same vertical and horizontal position as the cart's centre of mass so as to reduce unwanted perturbations caused by torque on the cart.

The optical arrangement of the interferometer is shown in figure 5.2. In the real system, the (non-polarising) beam splitter cube is placed such that when the moving cart is placed centrally on the rail, the optical path lengths of the two interferometer arms are equal.

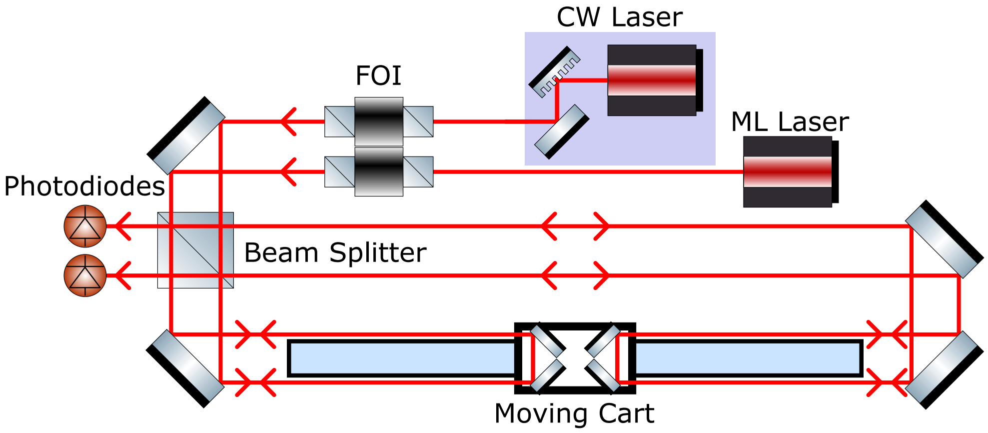

Figure 5.2: Diagram showing the schematic layout of the air bearing Michelson interferometer. FOI; Faraday Optical Isolator.

5.1.2 Spectral Resolution, Photodiode Response and Waveform Sampling

The primary objective is to resolve the spectral content of the frequency comb. The modulation frequency of the mode-locked laser is of the order of 3 GHz and, to confirm the comb like nature of the spectral output, a frequency resolution limit of $\omega_m/10$ would be desirable. The corresponding requirement in resolution of the interferometer is 300 MHz which, for a dual moving arm Michelson interferometer, corresponds to a translation of the retro-reflecting mirrors by a distance $c/2 \times 300$ MHz $= 0.5$ meters. To allow for the decay of residual vibrations caused at the reflection the total rail length is made 20% longer, giving a total traversable distance of 0.6 meters.

It is foreseeable that reasonable cart velocities are of the order of 0.25 - 0.5 meters per second. Furthermore the cart needs only to move 195 nm ($\lambda/4$) to experience one full period of the interferogram. Over a distance of 0.5 meters a total of just over 2.5 million interference fringes can be observed which, in the space of 1 second, requires a detection photodiode whose frequency response exceeds 2.5 MHz. The photodiodes used are Hammamatsu model G4176-03, 50 Ω terminated photodiodes with an applied DC reverse bias of 9V and a stated bandwidth of 7.5 GHz.

With regards to adequate signal sampling, according to signal sampling theory [156] the waveform sampling device is required to satisfy the Nyquist sampling condition. This condition states that, in order to adequately sample an analogue waveform, the sampling rate must be at least twice as fast as the fastest frequency component in the waveform. This is better known as the Nyquist sampling rate, which must at least equal the Nyquist frequency. Below this requirement significant *aliasing* can occur which results in misrepresentation of the input signal. To avoid this, a high sampling rate (up to 5 Gigasamples/sec) digital sampling oscilloscope (Tektronix MDO4104B-6) with a large record length (20 million samples) is used. Over a 1 second recording time at the full record length this yields approximately 16 data samples per fringe. A higher sampling rate could be used to better record the interference fringes, however this would come at the cost of spectral resolution. This will be explored experimentally later in this chapter.

5.2 Experimental Procedure

5.2.1 Mirror Velocity Linearisation

When introducing the concept of the interferogram, it was stated that for a single frequency optical source the rate at which interference fringes are observed (the beat signal frequency) is directly proportional to the velocity of the moving mirror. It follows that, owing to the nonlinear nature of the cart velocity, the spectroscopically stabilised CW laser beat frequency will not be monochromatic. When the CW interferogram is Fourier transformed to achieve the power spectral density, the linewidth will be significantly broadened and therefore not properly represent the linewidth of the laser[1]. This is of course also true for the mode-locked laser and therefore if the cart velocity is left uncorrected, the modes of the frequency comb will not be resolved in the Fourier transform of the recorded interferogram. The solution lies in the realisation that for every recorded fringe in the CW laser interferogram the cart must have moved a distance precisely equal to $\lambda/4$. Further, by counting the total number of fringes for a given interferogram, F_t (which is achieved through finding peaks in the interferogram [157] - or indeed any repeated position of constant phase angle), knowledge of the total distance travelled is acquired. This information is correlated with knowledge of the total acquisition time, τ_{acq}, and the unique time indices for every sampling event according to the scope acquisition. With this information it is possible to determine the magnitude of the lead/lag time of a given peak point in the interferogram from its ideal position described by a constant (average) cart velocity.

The process for velocity correction is as follows. We first find the data points which represent the peaks of the CW laser interferogram sine wave and their respective position indices within the data. We then generate a straight line of length equal to the total number of peaks found, and whose gradient is given by the total number of data points sampled (which is defined by the oscilloscope) divided by the total number of peaks found in the data. In other words we create a data vector of length equal to F_t at equal

---

[1] The interferometer of course does not possess the sub-MHz resolution required to accurately represent the diode laser linewidth, and so a 'properly' represented linewidth in this context would appear as a delta-function-like peak in the power spectrum with width defined by the interferometer resolution limit.

divisions of 20 million/F_t, where 20 million is the total number of discrete data points in the oscilloscope sample of the interferogram. This gives us the peak number within the data and its *ideal* position (index) within the data, and is identical to working out the average velocity. Next, we work out the *difference* in index number between the real peak positions and the ideal peak positions by subtraction of one from the other. At this stage it should be understood that when the cart is moving faster than the average velocity, for example, a given peak occurs earlier in time and vice versa. Because the oscilloscope samples at uniform time intervals, the difference in index number is identical to a time difference when multiplied by the time division per oscilloscope sample. The difference in index number as a function of peak number is plotted in figure 5.3(A) as the 'peak position offset'. By taking the difference, we are stating that the average velocity of the cart is now defined by a line of zero gradient originating from zero in the same figure. The next step is to fit to the difference function with a high order number polynomial. Because the difference function profile is entirely dependent on the motion of the cart at the time of capture and is different each time, a polynomial is the most suitable function to fit to the data. Here we use a 45 order polynomial, limited by computer memory capacity, to fit to the difference function. This is followed by taking the *residual* between the difference function and the fit to the difference function to provide a measure of the quality of the polynomial fit. This residual is plotted in figure 5.3(B). The average number of individual samples per period of the interferogram is given by the total sample length (20 million) divided by the total number of peaks. Typically this ratio is about 20:1 or greater. To have sufficient confidence in the polynomial fit, we require that the residual between the difference function and the polynomial fit is consistently less than 25% of the average number of samples per interferometer period. Thus far we have only calculated the offset of each *peak* in the data from the ideal. Armed with the polynomial fit coefficients we can now calculate the difference in index number for every data point in the interferogram waveform. Finally, to correct the time stamp for each data point, we subtract from each time stamp the calculated difference in index number multiplied by the time between samples. These time corrections are applied to both the CW laser *and* the mode-locked laser interferograms.

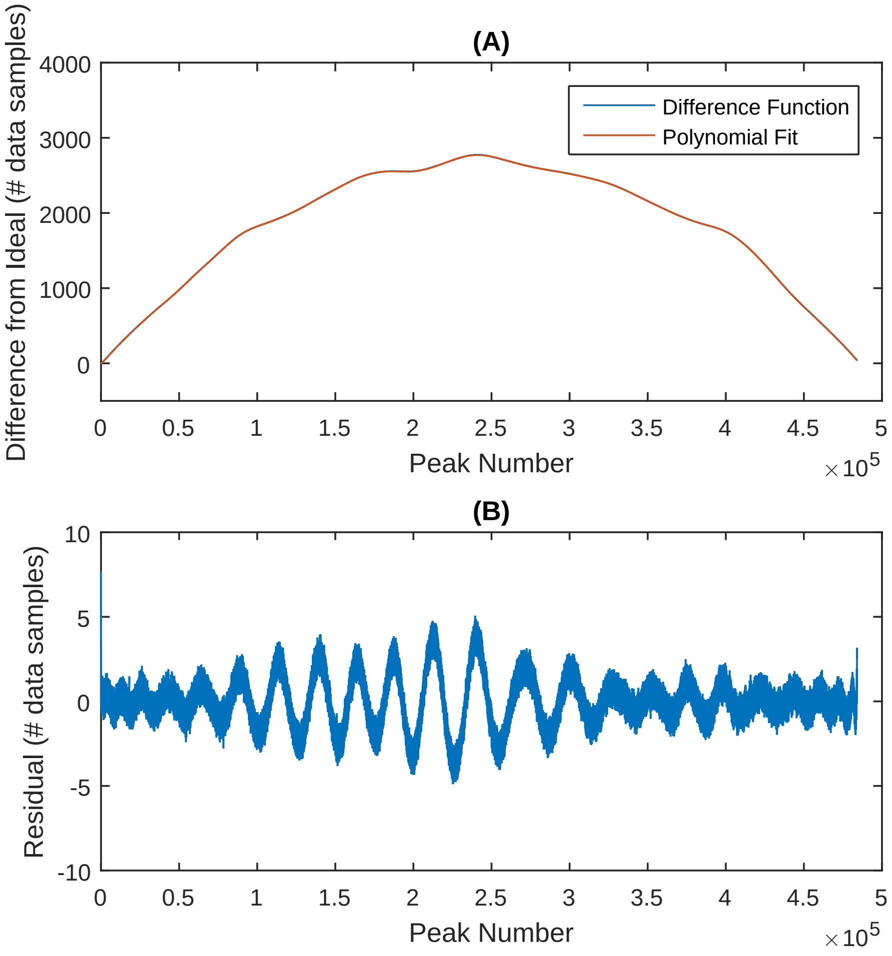

Figure 5.3: (A); Data showing the velocity profile of the moving mirrors, as a difference from the average velocity, in units of peak number against number of data samples. A positive gradient represents the cart moving faster than the average and a negative gradient represents the cart moving slower than the average. Figure also shows a 45 order polynomial fit to the difference data. (B), plotted is the residual between the difference data and the polynomial fit function. The approximate number of samples at the oscilloscope per period of the interferogram for the CW reference laser is 40 for a 20 million data point record length at a sampling rate of 50 MS/s. Using this number of polynomial coefficients, the fit is good enough to achieve our target of the residual being no more than 25% of the number of samples per period on the interferogram.

What we have created is an interferogram data set with a corrected time stamp for each sampling event such that when the CW interferogram is plotted, the data would much more closely represent an ideal, single frequency sine wave. Of course to do this we have forced the time stamps to become irregular. Our aim is to observe the power spectral density of the mode-locked laser, meaning that we need to take the Fourier transform of the time domain interferogram. Calculation of the FFT of a data set requires a uniform time base, which we have destroyed in the data. We therefore perform a spline interpolation of the interferogram data at a uniform time interval and perform the FFT on the interpolation. The quality of the interpolation is highlighted in figure 5.4.

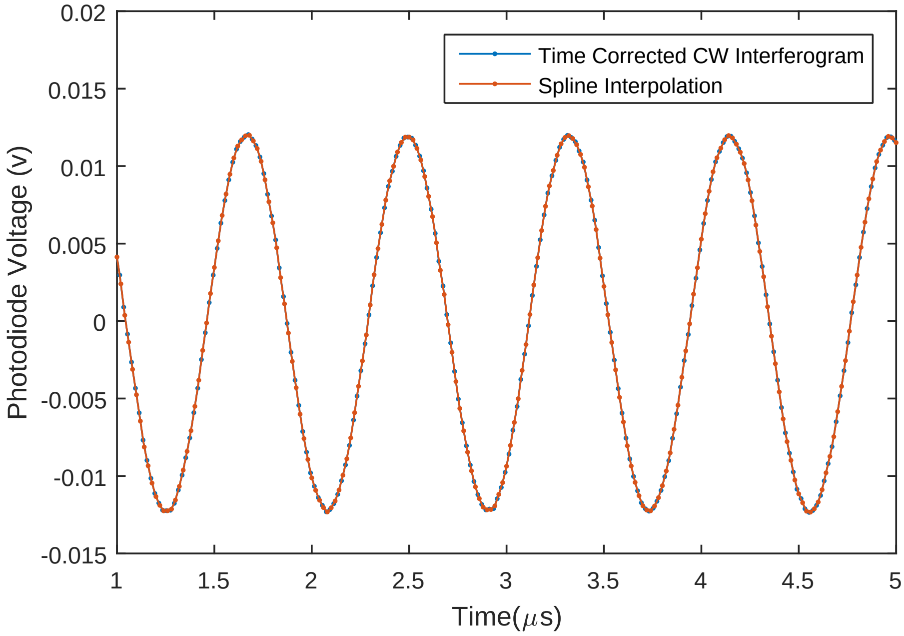

Figure 5.4: Performance of the spline interpolation of the corrected (linearised) time data. Interpolation is conducted to generate a uniform time interval from the corrected time data for the signal amplitude in order to correctly perform the FFT on the amplitude data.

5.2.2 Velocity Linearisation performance: CW laser linewidth

Following correction of the velocity profile for the CW reference laser, it is useful to observe the effectiveness of this correction. This correction is most clearly observed by comparison of the power spectral density of the CW reference laser interferogram before and after correction; see figure 5.5(A). As a result of the data linearisation, the power spectrum of the reference laser is compressed into a stronger, narrower lineshape, centred at 284.229 THz (780.244 nm). Because of the very low point density within the main peak (enlarged in figure 5.5(B)), we estimate the beat note linewidth is 980 MHz, as measured by hand. Given this method, we estimate an uncertainty in this value of ±100 MHz (± 2×10 % of marked division spacing of 500 MHz when magnified further).

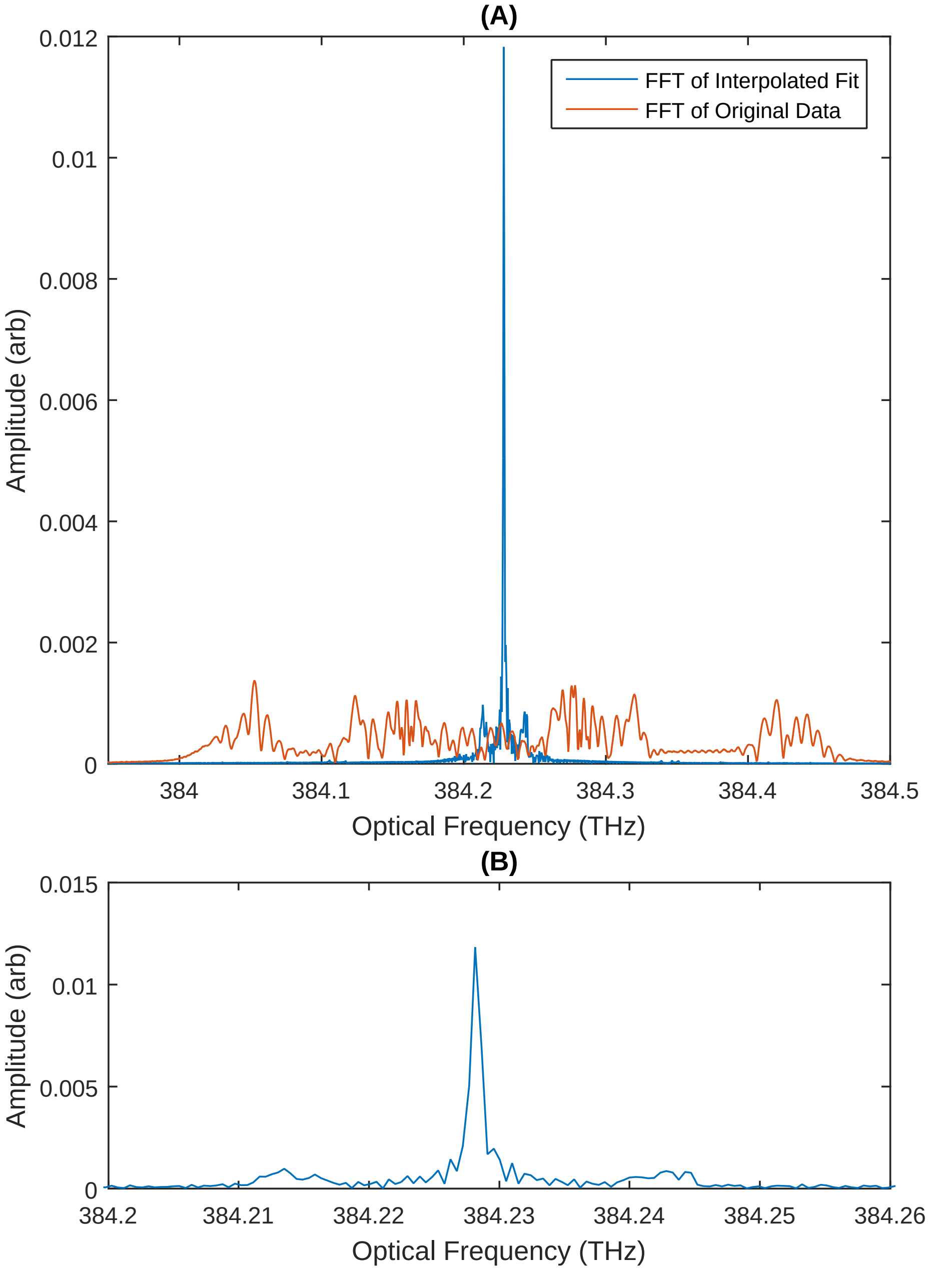

Figure 5.5: (A); Performance of the cart velocity linearisation by comparison of the power spectral density before and after linearisation of the CW laser interferogram, (B); a magnified view of the power spectrum of the corrected data.

As demonstrated in chapter 2, the spectroscopically stabilised CW diode laser we employ here as the reference laser exhibits sub-MHz linewidth. Clearly we are not able to resolve this given the physical constraints of the air track dimensions. Further, as the recording of the interferogram does not start and end at the possible extremes of mirror travel, it becomes clear that the theoretical maximum resolution of each recorded set of interferograms should be calculated in order to compare with the beat note linewidth. Knowing the total number of peaks found and the wavelength of the CW reference laser, the maximum possible resolution is given by,

$$\nu_{res,max} = \frac{c}{F_t \lambda_{cw}}, \tag{5.1}$$

where λ_{cw} is the optical wavelength of the reference laser. For consistency, we calculate the theoretical best resolution for the same interferogram used in plotting figures 5.3, 5.4 and 5.5, and yield a value of $\nu_{res,max}$ = 794 MHz. These results are incredibly pleasing as it highlights the effectiveness of the velocity linearisation procedure and demonstrates that the system possesses a suitable resolution for providing a mark to space ratio of at least 3:1 when considering the frequency comb mode spacing.

It was initially hoped that a mark to space ratio of 9:1 ($\nu_{res,max}$ = 290 MHz) would be achievable. To achieve this, it is required that, for the same given velocity, the interferograms would need to be recorded over a period 3 times longer. Limited by the available oscilloscope sampling rates for a fixed 20 million data point record length, we attempted to capture the interferograms over a 1 second period at 20 MS/s. This is of course at the cost of the number of samples per fringe on the CW laser interferogram. Assuming an identical average velocity as above, this would have yielded $\nu_{res,max}$ =318 MHz; very close to the desired goal. However, a number of issues arose resulting in no usable data or further insight into the mode-locked laser optical spectrum. As expected, the number of data samples per fringe dropped from ∼40 to ∼16. This in itself is still acceptable as a number of samples to unambiguously reproduce the sine wave, hence satisfying the Nyquist condition. The primary drawback is that of the effectiveness of the velocity linearisation. As the cart's motion is recorded for longer, the ripples on the velocity profile are greater in number and potentially in severity. This has a direct impact on the number of polynomial orders required to fit to the difference data in figure 5.3. Even with access to a computer boasting 24 GB of RAM, the 45 order polynomials used above were sufficient to use slightly greater than 100% of this capacity (requiring hard disk based virtual memory). As the number of orders increased, the computation time increased massively, in some cases reaching ∼200 times the computation time of the 45 order polynomial. Indeed, maintaining 45 orders for the polynomial fit resulted in residuals well in excess of the number of samples per fringe, thereby invalidating the linearisation. We therefore arrive at the conclusion that, in order to achieve a better interferometer resolution either significantly more computational resources are required or significant experimental work should be conducted to dampen or eliminate the causes of the variations in the cart velocity.

5.2.3 Mode-Locked Diode Laser Analysis

So far in this chapter the design and layout of the air track interferometer has been presented, as well as an explanation and demonstration of the velocity correction of the moving cart containing the interferometer mirrors. It was shown that, with sufficient computing resources over a short enough record acquisition time, the residual of the peak position difference data and the polynomial fit could be reduced to below 25% of the number of samples per interferogram fringe. It follows that, in doing so, the measured resolution given by the CW lineshape in figure 5.5 could be as low as 123% of the theoretical best resolution. With confidence in the velocity linearisation, attention can now be shifted to consider the mode-locked spectrum. Figure 5.6 shows an example spectrum of the mode-locked diode laser running at 780 nm ($\sim$384 THz) both before and after the velocity linearisation is applied (top), as well as a magnified section of the spectrum centred at 780.244 nm (384.229 THz, bottom).

Due to the correction of the smearing effect that the non-linear velocity has on the spectrum, the peak and trough amplitudes have been increased and decreased respectively. By an identical principle to that shown for the CW laser spectrum, the energies of each frequency comb mode are effectively untangled and appropriately overlapped, reducing the noise level between the modes and increasing the mode amplitude. This is most easily observed in the magnified section of figure 5.6 where obvious frequency components are visible. The active mode-locking modulation frequency is 2.908 GHz, which corresponds almost exactly to the average mode spacing in the same figure.

The final aspect of the experimental results for this chapter consists of an investigation into the effects of modulation frequency detuning around the frequency which gives the shortest optical pulses.

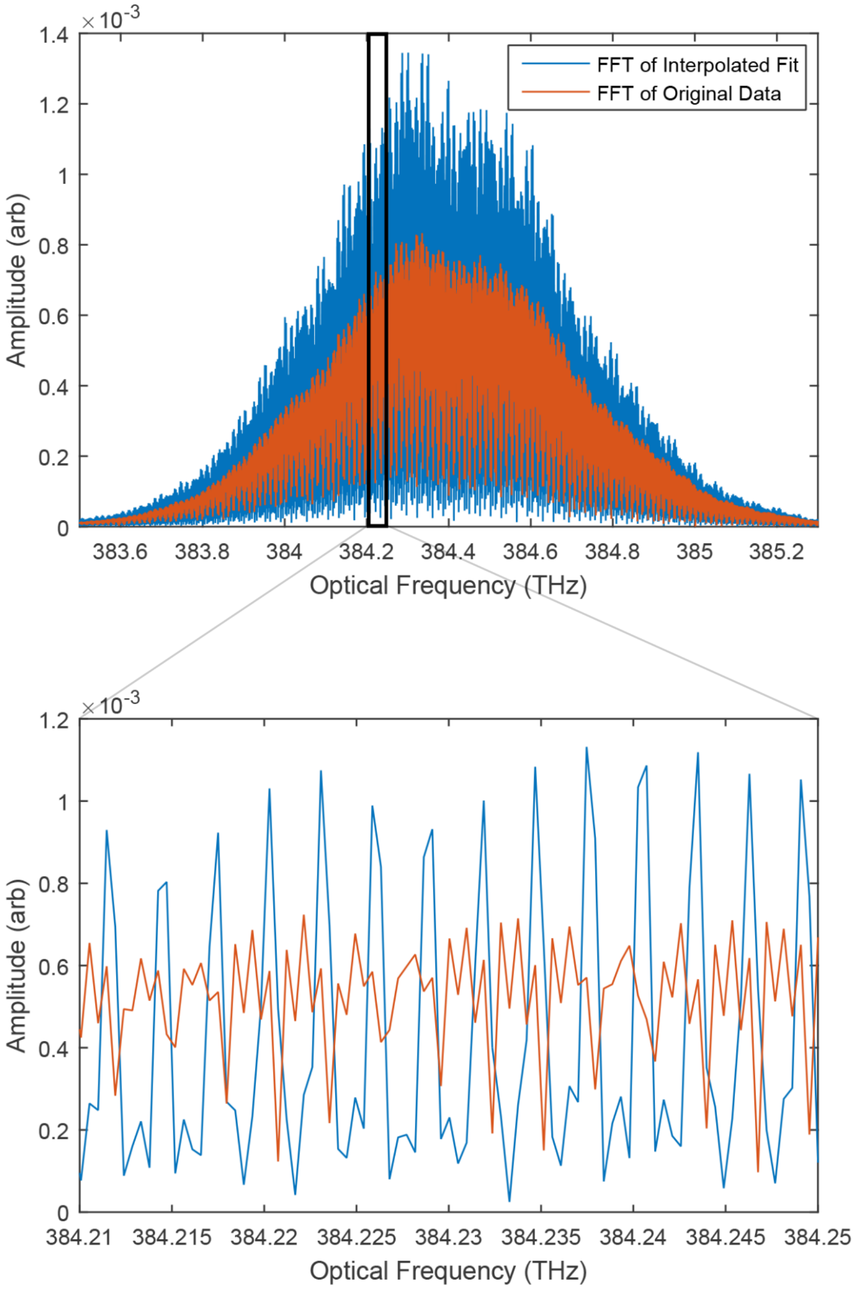

Figure 5.6: Fast Fourier Transform of the mode-locked diode laser interferogram before (red) and after (blue) cart velocity linearisation.

Shown in figure 5.7(A)-(H) are the series of mode-locked laser spectra, each spanning 2 THz and centred at 384.00 THz, while in figure 5.8(A)-(H) are the same spectra only in this case spanning 80 MHz. From (A) to (H) in both figures the detuning changes by 3.33 MHz from -10 MHz to +13.33 MHz respectively. Previously observed in figures 4.2(B) and 4.12(C), the optical pulses exhibited a rapid degradation per unit negative detuning and very gradual degradation per unit positive detuning.

At the largest negative detuning we observe a spectrum which barely resembles that of a frequency comb. At -10 MHz, the pulse has broken up into small clusters of modulated spectrum separated unevenly. At this detuning the spectrum has also narrowed significantly resulting in approximately a factor of 10 increase in amplitude of the tallest mode. If it were not for the irregularity of the clusters, it would be reasonable to conclude that this spectrum more closely resembles a series of CW modes, spaced by the monolithic cavity mode spacing, that are suffering weak frequency and amplitude modulation. This is certainly supported by the sharp rise in pedestal height observed in figure 4.3(B). As the detuning approaches zero (5.7(D), 5.8(D)) the pulse temporal width drops sharply and the system adopts a mode-locked output. No significant substructure between the modes is visible in figure 5.8(D) at this resolution.

The optical spectrum is observed to shift towards higher frequencies as the detuning traverses from negative to positive. This effect is tentatively attributed to the junction temperature dropping as the modulation power is more effectively dissipated optically rather than thermally. Experimentally this could be much more effectively controlled were the semiconductor chip mounted on a TEC and cooled directly, rather than by our method which relies on cooling the laser mount.

From zero towards positive detuning the spectrum is observed to broaden (5.7(E)-(H)) along with a simultaneous drop in amplitude per mode (5.8(E)-(H)). This trend is attributed to the optical pulse being forced to move towards the peak of the current injection waveform where the gain is at it's highest. Non-negligible sub-structure is visible in figure 5.8(H) which is possibly the result of a trailing pulse inside the cavity. It is clear from figure 5.8 that the modulator detuning range for which the mode-locked laser consists of an array of well defined optical modes is between -3.33 MHz and +6.66 MHz, which corresponds very well in magnitude to the previously defined locking range of 10 MHz as defined in section 4.4.

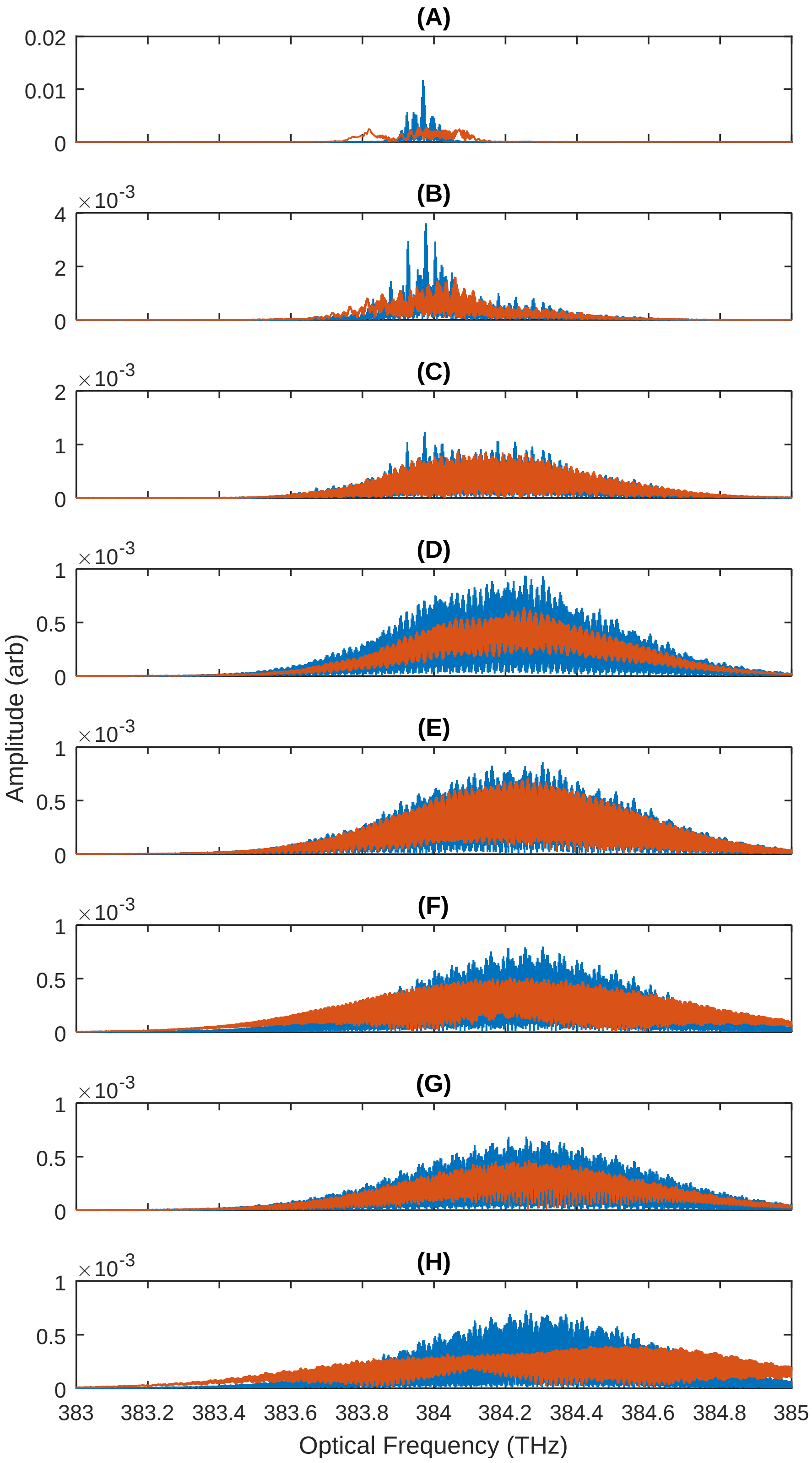

Figure 5.7: Figure showing the optical spectrum of the mode-locked diode laser before (red) and after (blue) cart velocity linearisation. In figures (A) through (H), the detuning of ω_m is swept between -10 MHz and +13.33 MHz in divisions of 3.33 MHz.

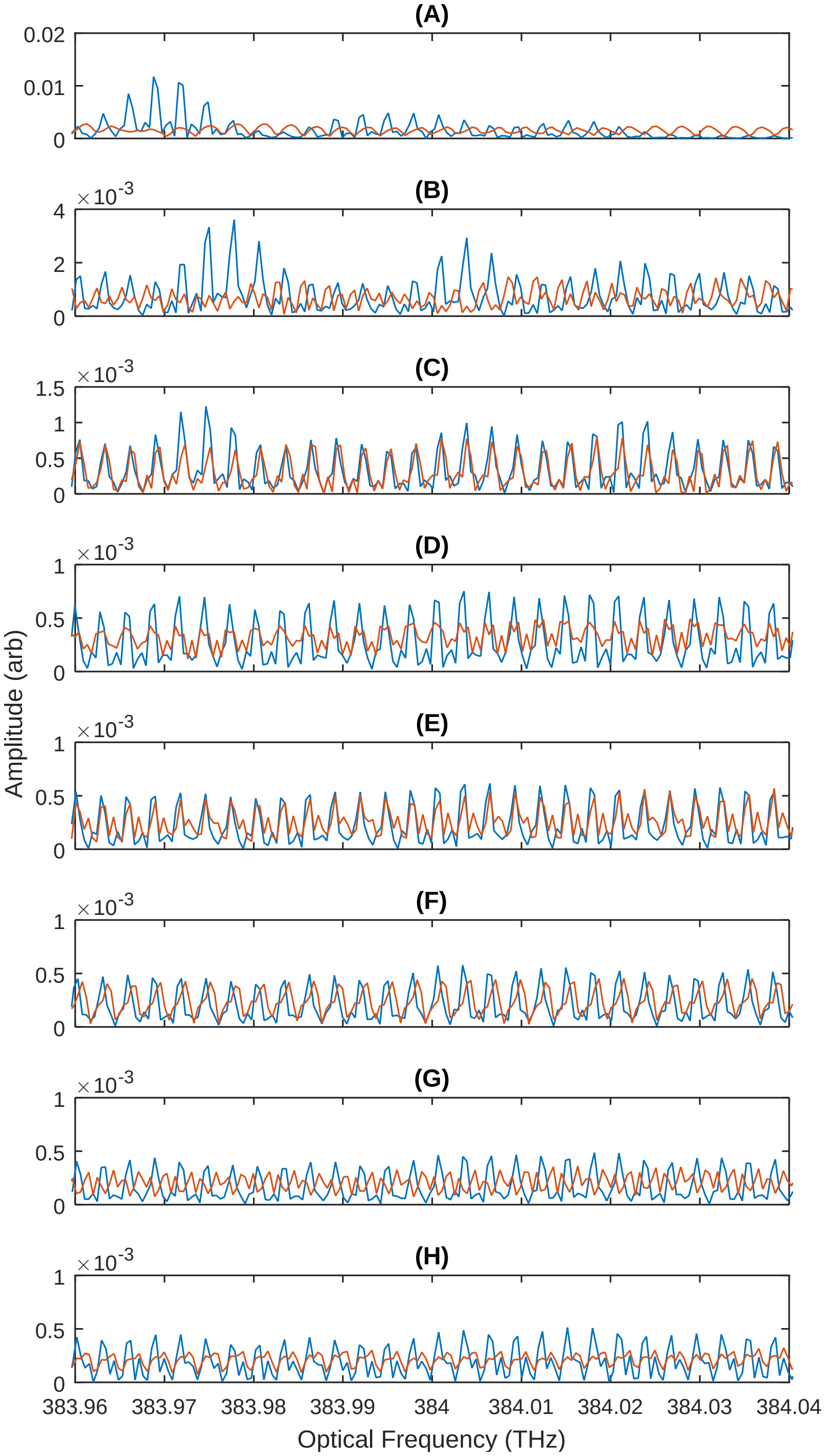

Figure 5.8: Figure showing an 80 GHz segment of the mode-locked diode laser emission spectrum before (red) and after (blue) cart velocity linearisation. In figures (A) through (H), the detuning of ω_m is swept between -10 MHz and +13.33 MHz in divisions of 3.33 MHz.

Using an in-house built, dual moving arm Michelson interferometer based on a low pressure air bearing design, we have demonstrated an optical spectrum analyser capable of resolving the individual frequency comb modes of an actively mode-locked diode laser. By resolving these modes, it has been confirmed that the frequency comb does indeed consist of an array of discrete optical modes. Identified also is a detuning range of approximately 10 MHz for which the frequency comb appears to produce well defined optical modes. Determining the locking range with greater accuracy would simply require more data sets at a smaller detuning increment size.

5.2.4 Improvements

Initially the goal of the interferometer was to be able to resolve frequency components approximately an order of magnitude slower (in frequency) than the frequency of the active mode-locking modulation signal. At approximately 290 MHz, this would have required a travel distance of 0.5 meters. The rail on which the moving mirrors travel was specified to accommodate for this capability, however a computational limitation in the form of available physical memory was revealed to be the bottleneck. Capturing the interferogram at 20 MS/s over 1 second instead of 50 MS/s over 0.4 seconds allows for the maximum cart travel distance to be utilised, however proportionately more polynomial orders are required in the fit to the difference data.

The alternative approach is to eliminate the causes of the cart velocity variations over the course of the data acquisition. The cart weighs approximately 500 grams and yet it is apparent that air currents and the residual vibration in the thin rubber air line[2] are sufficient to cause appreciable velocity changes on an interferometric sensitivity basis. One solution is to increase the mass of the cart to improve inertial properties while suffering a minimal increase in the required gas line pressure to maintain an adequate air bearing. A further solution is to use yet lighter rubber tubing for gas delivery. To put the importance of the gas line weight into context, if the cart is moved to one end of the rail, stabilised and released, the tension in the 80 cm of gas line caused by gravity

---

[2] we estimate that the gas line weighs on the order of a gram per 2 - 3 cm.

is sufficient, when resolved into it's horizontal component, to cause the cart to oscillate along the rail with a period of approximately 40 seconds.

Finally, another simple improvement which could be made would be to employ mechanical actuators to set the cart in motion initially, thereby ensuring greater consistency and reproducibility in the cart starting velocity.

Chapter 6

CW Injection Locking of the Mode-Locked Laser

In this chapter an experimental investigation of the optical injection of a CW laser into an oscillating mode of the mode-locked laser is presented. The aim of this investigation is to determine whether optical injection locking of the mode-locked laser is a viable method for anchoring a chosen oscillating mode to a specific known frequency. Underpinning the technique is the premise that, by injecting optical power from one laser (the 'Master') into a cavity mode of another free-running laser (the 'Slave'), phase coherence is established between the two lasers. This phase coherence occurs because the slave laser predominantly amplifies the injected light to the point where, at sufficiently small detuning between the free running and the injected optical frequencies, the injected light saturates the laser gain, thereby suppressing the free running oscillation frequency [158]. In the case where the master laser light is injected into the slave laser before the slave laser reaches threshold, phase coherence is established because the slave laser predominantly amplifies the master laser signal over it's own spontaneous emission [112]. In a mode-locked laser, by relying on the coherence transfer process, phase coherence between all modes of the mode-locked slave laser and the CW master laser is established. Given this coherence between slave laser modes, and coupled with a stable electronically derived active mode-locking modulation signal, all the frequency comb modes may be accurately determined by their mode number from the injected mode and hence the comb is now useful as an optical frequency reference.

There exist four regimes which injection locking may be categorised by. Case 1 is where a CW master laser is injected into a CW slave laser [159] and was the basis of the first demonstration of laser injection locking by Stover and Steier [160]. Case 2 uses a mode-locked laser pulse from a master laser which is injected into a mode-locked slave laser and is commonly referred to as injection seeding [161]. Case 3 is where a mode-locked pulse from the master laser is injected into a CW slave laser [162]. Finally case 4 is the injection of a CW master laser into a mode-locked slave laser [163]. In this work we concentrate solely on category 4 as it naturally lends itself to the desired result of a spectrally stable optical frequency comb. It is simultaneously possible to investigate a possible property of the frequency comb; the so called 'mode-locking in clusters' regime of operation which, at this stage, is believed to be a manifestation of the weak current modulation depth observed in section 3.4.1.1.

Briefly mentioned in chapter 4, the 'mode-locking in clusters' operating regime is the result of the modulation of the composite external laser cavity axial mode structure by that of the monolithic laser cavity mode structure, i.e., one large FSR etalon imposing its transmission filtering properties onto the mode structure of a smaller FSR etalon by way of interferometric losses. Where an external cavity is employed to reduce the cavity mode frequency separation, the front semiconductor facet must be AR coated. The combination of high small signal gain and difficulty achieving facet reflectivities below 0.1% across the broad gain bandwidth of a semiconductor, usually results in significant spectral modulation of the laser emission. In terms of the emission from the mode-locked laser, the end result in the time domain is a cluster of temporally overlapping pulses which, on the intensity autocorrelation, appears as a broad (with respect to the overall spectral linewidth), noisy optical pulse with a coherence spike. Each monolithic cavity mode (separated by 56 GHz) supports a number of composite cavity modes (of FSR$\simeq$3 GHz) which, in themselves, form a pulse considerably closer to the transform limit.

Overcoming the effects of the monolithic cavity spectral modulation can be achieved in a number of ways. A) Reduction of the AR coating reflectivity reduces the finesse of the etalon and therefore improves the coherent coupling of optical modes between the transmission peaks of the monolithic cavity; B) increasing the modulation depth of the active modulation so as to promote stronger optical coupling between composite cavity modes; C) If the very shortest optical pulses are not necessary, artificially limiting the spectral bandwidth so as to limit the mode-locked emission to a single monolithic mode, thereby concentrating all the active modulation power to a single cluster of modes; D) eliminating the monolithic etalon by cleaving at an angle not parallel to rear facet; and E) harmonic active mode-locking.

Due to the high small signal gain in diode lasers, method A is impractical. Reflectivities down to even 0.001% are calculated in reference [33] to be insufficient for removing the spectral modulation. Method B is typically not an option if one is already at one upper experimental parameter limit. Either the laser parasitics are blocking the modulation power and so substantially increasing the power reaching the active region would require significant investment in a very high power modulation source, or the maximum electrical power handling of the laser is already reached. Method C may be achieved by either; replacing the external cavity mirror with a dispersive element such as a diffraction grating; introducing a thin transmission etalon into the cavity [69]; using a laser with inherent bandwidth limiting infrastructure such as a DBR; or by optical injection locking a single monolithic cavity mode [125]. Method D typically requires bespoke laser designs. Commercial semiconductor devices, such as the laser used in this work, are predominantly aimed at spectroscopic applications which do not require such strict conditions in decoupling the constituent etalons in a composite laser cavity. Lastly method E works by modulating the laser at a higher harmonic of the composite cavity FSR, thereby increasing the axial mode spacing by the same factor as the modulation harmonic number. The associated advantages with this method are twofold. The first is that the higher modulation frequency imposes a steeper charge injection gradient and hence enhances the modulation depth. The second advantage requires careful planning of the composite cavity length with respect to the monolithic cavity length. If the modulation frequency is both a higher harmonic of the composite cavity *and* an appropriate sub-harmonic of the monolithic cavity, it becomes possible to avoid population of the composite cavity modes which see the strongest modulation (attenuation) from the monolithic cavity. Both aspects ultimately act to improve coherence transfer between neighbouring modes.

In this chapter, we concentrate on investigating the use of injection locking as a method for spectroscopic stabilisation and spectral narrowing. The former is a proof of principle for stabilising a frequency comb mode to a spectroscopic feature of Rubidium while the latter is to investigate the suspicion that the laser is mode-locking in clusters. In conducting this investigation, this chapter is subdivided into three salient sections; Heterodyne detection, where we consider whether the comb modes surrounding the injected mode are phase coherent and, if so, up to what mode number from the injected mode; Temporal and spectral analysis, to understand what effect injection locking has on the temporal and spectral width of the laser emission, and; the detuning range between the master and slave laser for which injection locking is maintained. The optical assembly employed in these three investigations is shown in figure 6.1.

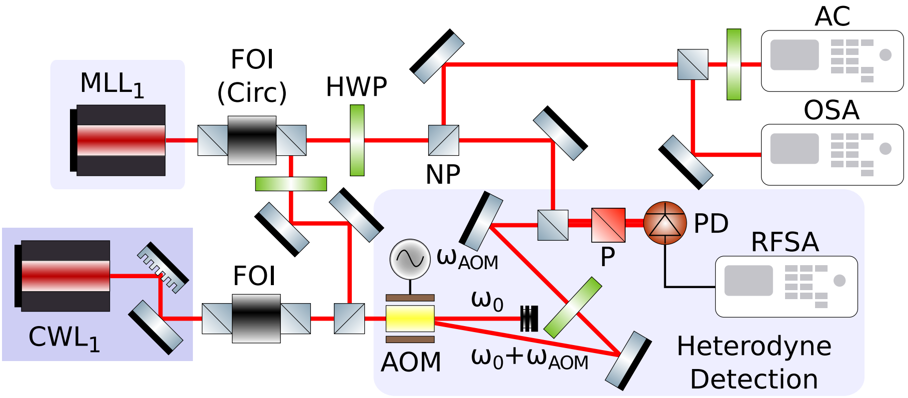

Figure 6.1: Schematic diagram of the system used for the heterodyne beat note detection of master laser AOM sideband against the slave mode-locked laser modes when under optical injection locking conditions. In this configuration the AOM shifted optical frequency beats with the injection locked frequency comb mode on the RF spectrum at the AOM modulation frequency. This effect should also propagate to higher harmonics of the frequency comb mode spacing on the RF spectrum if the adjacent modes are phase coherent *and* the injected mode is suitably locked to the CW master signal. If the beat frequency does not correspond to the AOM modulation frequency, this is evidence for poor or unlocked injection. FOI; Farady Optical Isolator, HWP; Half Wave Plate, AOM; Acousto-Optical Modulator, NP; Non-Polarising beam splitter cube, P; Polarising beam splitter cube, PD; Photodiode.

6.1 Injection Locking Analysis

6.1.1 Heterodyne Detection Analysis

Shown in figure 6.1, the heterodyne detection scheme is used in order to determine the coherence transfer across the comb [163], i.e., to determine how many of the modes adjacent to the injected mode are phase coherent with said mode. Unlike observations of the optical spectrum whereby, assuming one had sub-mode-spacing resolution, the optical power per unit wavelength is measured directly, the heterodyne detection method is sensitive to the RF beating between the optical components. Therefore in order to determine A) whether or not the master laser is successfully injection locking a slave laser mode and B) how far the phase coherence propagates across the comb, we must artificially generate a beat note between the master and slave laser and observe this beating on the RF spectrum. To accomplish this a small proportion of the master laser is separated from the main beam, frequency shifted with an AOM (so as to remain phase coherent with the unshifted beam) and then later beat together with the injection locked mode-locked laser on a fast photodiode. See figure 6.2.

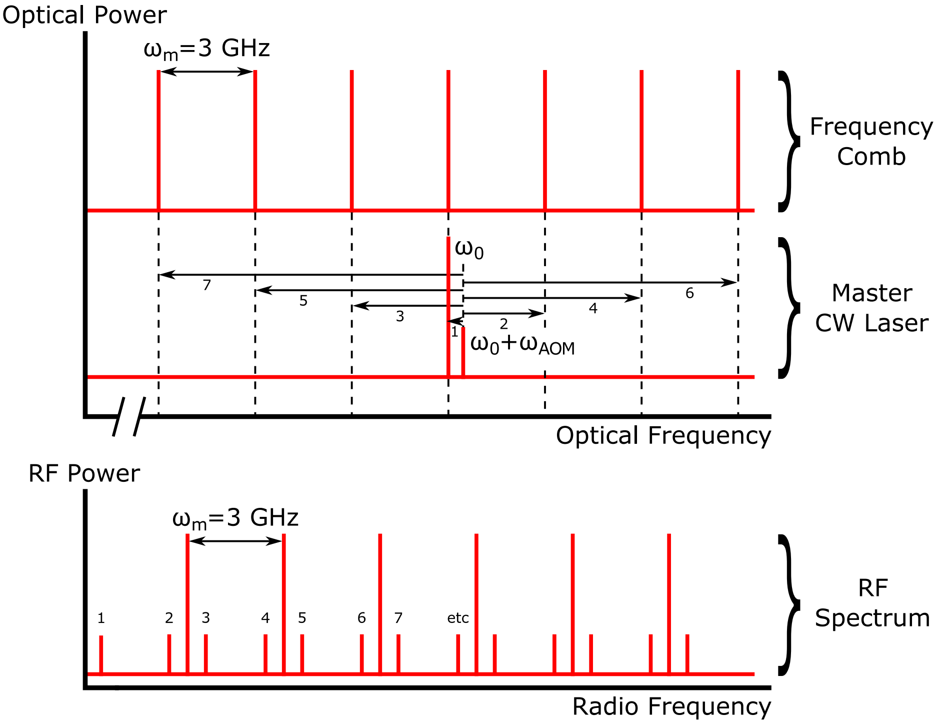

Figure 6.2: Injection locking heterodyne beat note detection principle.

Injection locking is confirmed by the presence of sidebands on the RF spectrum at positions equal to $(p \times \omega_m) \pm \omega_{AOM}$, where p is the harmonic number, $p = 1, 2, 3...$, and ω_m is the frequency of the active mode-locking modulation. If the RF spectrum shows sidebands of unequal distance from a given harmonic, or if the sidebands have significantly larger linewidth, this would be indicative that this mode is not phase coherent with the optically injected mode. Figure 6.3 shows the first 6 harmonics of the mode-locking modulation frequency with visible heterodyne sidebands. The master laser frequency was maintained by DC injection current tweaks to preserve the strongest sidebands around the fundamental (3 GHz) mode.

In this data ω_m = 3.0 GHz and ω_{AOM} = 80 MHz. The marked decrease in harmonic and sideband amplitude after 12 GHz is caused by the falloff in photodiode frequency response due to the stated 12.5 GHz bandiwdth. From figure 6.3 we can confirm that the phase coherence which has been established between the master laser and the injection locked slave laser mode has been transferred across a bandwidth of at least 36 GHz. Due to the photodiode bandwidth limitation it has not been possible to determine whether or not the phase coherence extends to composite cavity modes that reside in adjacent monolithic cavity modes. In an attempt to make this determination, the CW master laser was temperature tuned over a 20 GHz window towards higher optical frequencies and the measurements were repeated. Frustratingly no visible sign of decoherence at the outermost modes on the RF spectrum was observed. At face value this might appear as a positive result, however no further information about the possible mode-locking in clusters regime of operation has been ascertained.

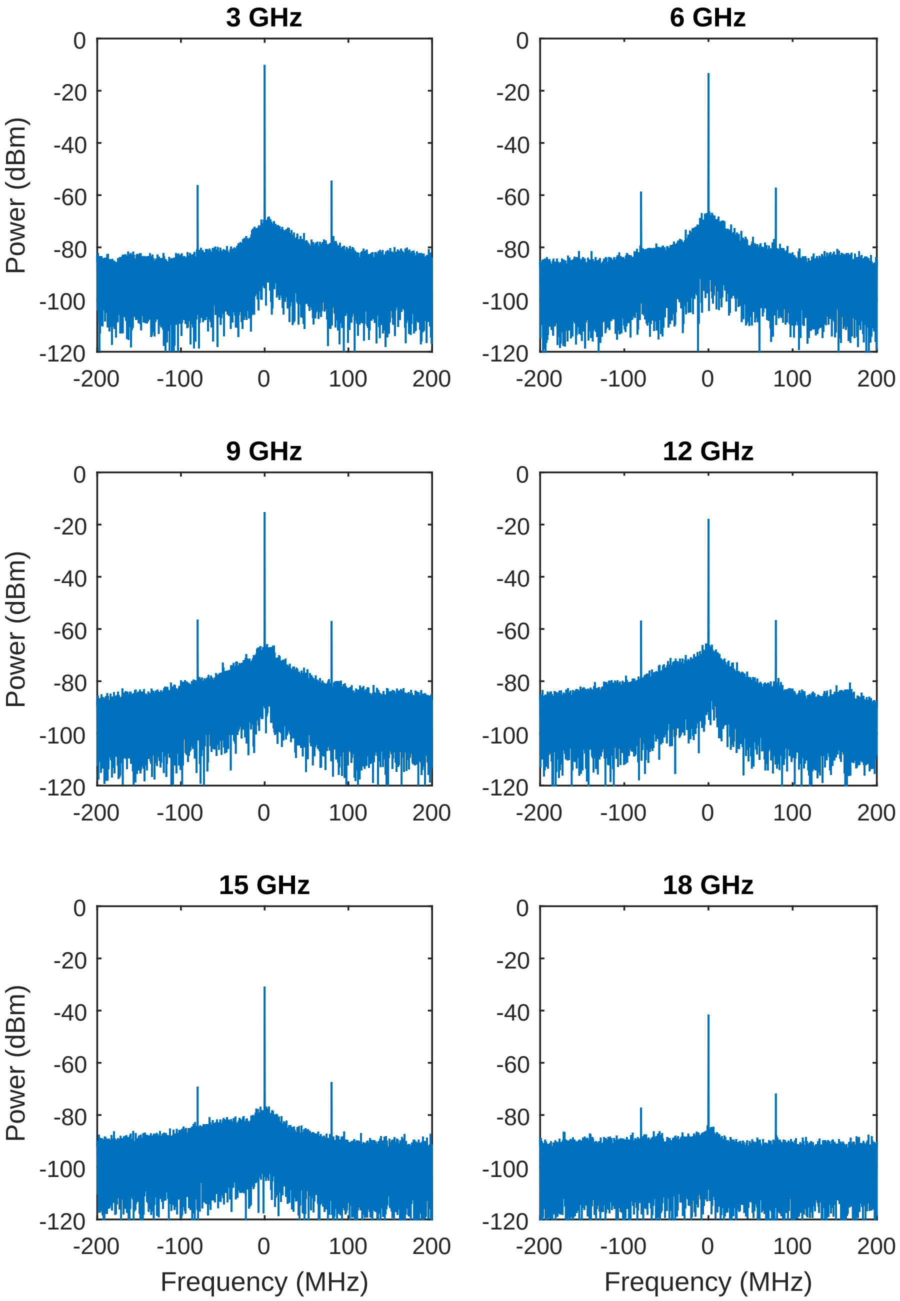

Figure 6.3: Heterodyne beat note detection of master laser AOM sideband against slave mode-locked laser modes when under optical injection locking conditions. The figure shows a 400 MHz spectral window for up to the 6^{th} integer multiple of the frequency comb mode spacing. RBW=VBW=10 kHz.

6.1.2 Temporal and Spectral Analysis

Investigation is now continued to consider the temporal and spectral properties of the pulses under injection locking conditions. Effects of CW injection locking are tested at both ~784 nm, when the laser is operating at 12°C without the linear polariser and thin etalon, and at ~780 nm when the laser is cooled and with the linear polariser and thin etalon in place. It has been reported that the time it takes for the pulse to saturate the gain defines the temporal width [125] of the pulse. Optical pulse broadening occurs in correlation with increasing injected laser power because the injected CW power acts to suppress gain saturation [164]. Figure 6.4(A) shows the residual pulse width between a pulse without injection locking and the pulses at various CW master injection powers. For the case where the linear polariser and etalon are used, the pulses observe a gradual increase in temporal width as the injection power increases, in line with the above reported prediction. The residual pulse width drops unexpectedly for an injection power of -21.6 dBm. This is believed to be either a mistake whereby the mechanical stability, and therefore pointing of the laser, has caused the master laser to shift slightly from the point of most efficient injection, or that the master laser experienced a mode-hop and was injecting less efficiently into a different slave laser mode. The latter is quite unlikely however, as the composite cavity mode spacing of the master laser does not match that of the slave mode-locked laser. This deviation from the near monotonic increase in residual pulse width is far outside the standard error for this data point. At injection powers greater than -21.6 dBm the pulse width appears to rise sharply, indicative that the mode-locked laser is tending towards CW operation, see figure 6.5.

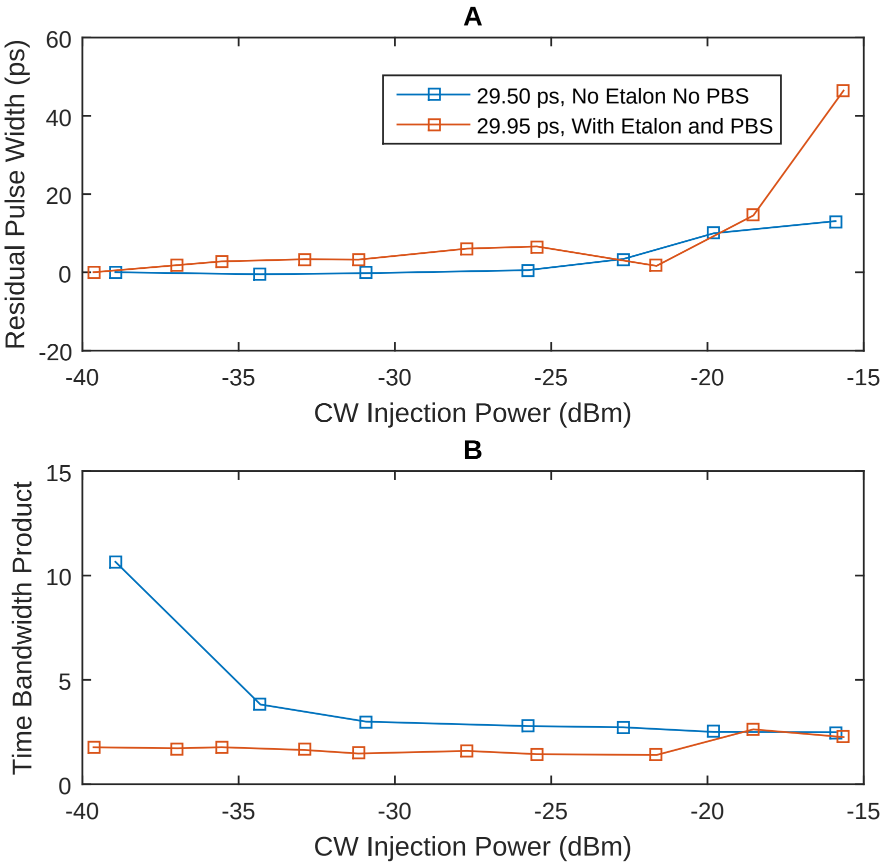

Figure 6.4: Residual of the temporal pulse width for the mode-locked laser between the free running and injection locked states, both when employing the thin etalon and intracavity polariser and when not, (A), and the resulting time-bandwidth products of the injection locked mode locked laser with and without the etalon and polariser. The legend contains the measured pulse width when the injection locking laser is blocked.

Curiously the injection locking behaviour for the same laser without the use of the linear polariser and thin etalon differs noticeably in that the residual pulse width remains largely unchanged until ∼-25.75 dBm. While care was taken to achieve the best optical coupling of the master laser radiation into the slave laser semiconductor waveguide, we attribute this difference in behaviour to a mismatch in the coupling efficiency between the two experiments. It is proposed that, in the case of operation without the etalon and polariser, the injection efficiency is considerably lower. For clarity, the coupling is optimised by running the slave laser in CW and dropping the DC injection current to just below threshold. The pointing of the master laser is then raster scanned across the slave laser until a spike is observed in the slave laser output power. This effect is essentially identical to the grating external cavity optimisation flash test [165], whereby the coupling efficiency is optimal when the slave laser emitted power is maximised.

Calculated from corresponding optical spectra (figure 6.6) taken at the same time as the pulse autocorrelations, figure 6.4(B) shows the respective time-bandwidth products. For the case where the polariser and etalon are employed, the time-bandwidth product sees a vast improvement from ∼13.4, as observed in chapter 4, to between 1.77 and 1.44 for injection powers between -39.6 and -25.5 dBm. This corresponds to approximately 4 to 3.2 times the transform limit respectively. In the case where the polariser and etalon are not employed, the rapid decrease in time-bandwidth product for low optical injection powers possibly supports the above hypothesis regarding the difference in injection efficiency. Given that the thin etalon has a FSR = 10 nm, the spectral filtering has negligible affect over the optical spectral output of the mode-locked laser. For master laser injection powers below -20 dBm the time-bandwidth product for the laser when the polariser and etalon are employed is always at least a factor of 1.5 smaller than for when the polariser and etalon are not employed. This is attributed to the former observing stronger spectral narrowing (due to injection locking) with respect to the concomitant increase in pulse width.

Figure 6.5 shows a very positive sign towards the effect of CW injection locking upon the optical pulses. At injection powers below -35 dBm, the coherence spike is still visible on the pulse autocorrelation. As injection power is increased the coherence spike disappears for all injection powers above -35 dBm. This trend corresponds to the suppression of adjacent monolithic cavity modes and hence the spectral narrowing shown in figure 6.6.

Next we consider the spectral narrowing effects caused by CW injection locking; referred to in the literature as *supermode* or *sidemode* suppression. Figure 6.6 shows example optical spectra of the mode-locked laser spectra under injection locking for a range of injection powers for without the linear polariser and thin etalon (A); and with the linear polariser and thin etalon (B).

Spectral narrowing is caused by suppression of the monolithic cavity modes adjacent to the injection locked mode [125, 166]. Through the combination of weak current modulation and spontaneous emission coupling into more than one monolithic cavity mode, the laser operates in the clustered mode-locking regime. Injection locking provides a stronger signal than that of the coupled spontaneous emission thereby forcing the laser to predominantly amplify this signal. It is clear that in 6.6(A) the injection locking is not limiting the optical bandwidth to a single monolithic cavity mode until the injection power reaches ∼-20 dBm. Furthermore because the monolithic cavity mode separation is relatively small due to the long semiconductor cavity, and also due to the ∼25 GHz OSA resolution, quantifying the degree of sidemode suppression (in dB relative to spectral peak) cannot be conducted in a way that allows direct comparison with published literature. We therefore must adopt a slightly different definition whereby instead of comparing the peak power of the injected mode to the peak of the nearest neighbour sidemode, we consider the third nearest neighbour from the injected mode instead. By this definition, the sidemode suppression for -19.8 dBm is 18.9 dB. This figure improves to 20.1 dB when the injection power is increased to -15.9 dBm. For all weaker injection powers, the mode-locked laser emission appears to operate on multiple sidemodes.

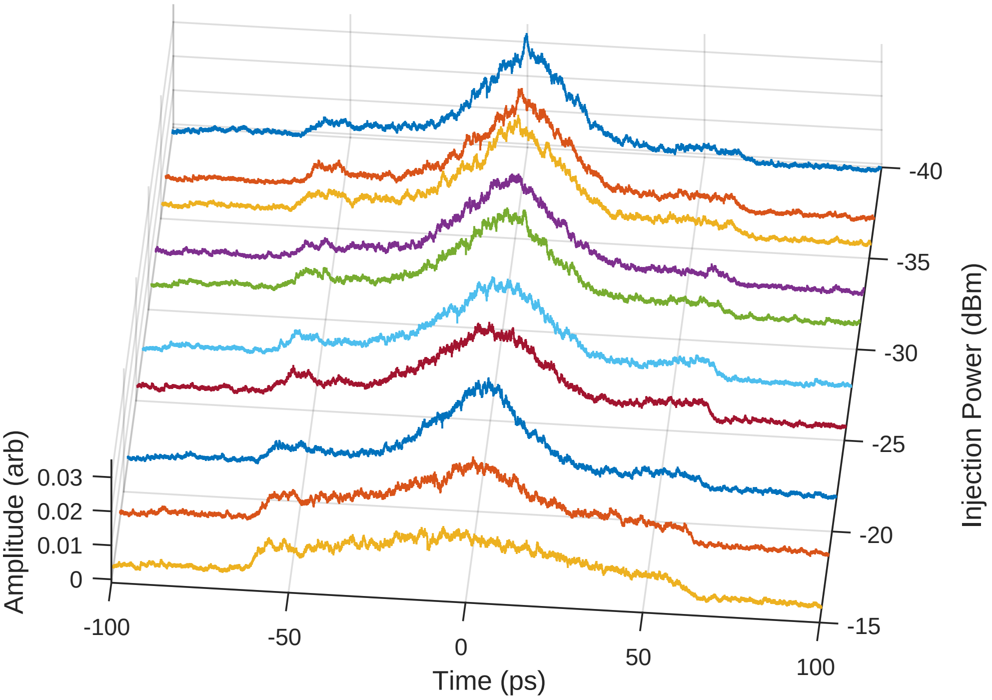

Figure 6.5: Measured intensity autocorrelation of the pulses under injection locking as a function of injection power.

Figure 6.6(B) shows significant improvement in the effectiveness of the injection locking in the presence of the polariser and etalon. For the lowest injected power of -39.6 dBm the sidemode suppression is 9.1 dB, compared with only 2.0 dB for the nearest injection power in figure 6.6(A). Furthermore, by comparison with the same figure, reaching a suppression level of 20.6 dB is achieved with only -25.5 dBm of injected power; nearly an order of magnitude improvement. For comparison, Williams *et al* report sidemode suppression of 18 dB with 9 μW of injected power for a harmonically mode-locked, fibre-based semiconductor laser operating at 1550 nm [167] and Joneckis *et al* report sidemode suppression ratios between 20 and 30 dB depending on the 'injection ratio' [125].

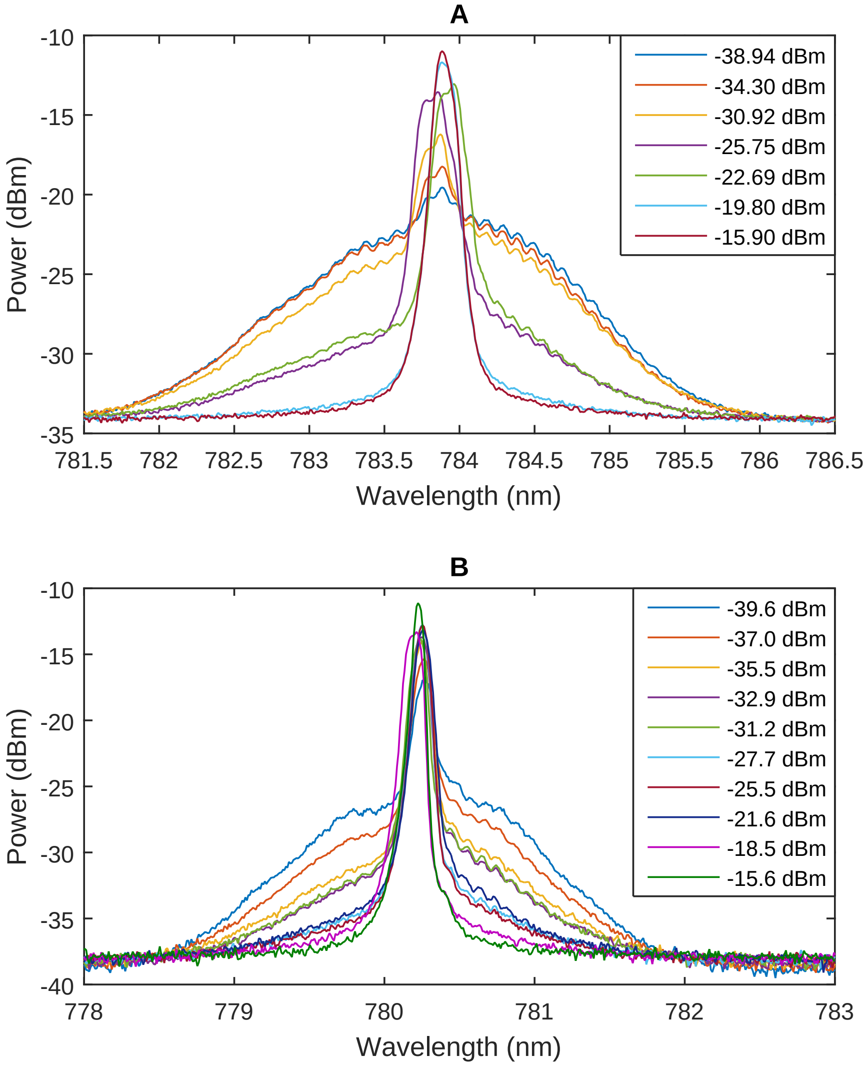

Figure 6.6: Comparison of sidemode supression through CW injection locking of the mode-locked laser without (A) and with (B) the etalon and polariser.

6.1.3 Injection Locking Bandwidth

The final aspect of this chapter is to consider the injection locking range. The locking range is the spectral region within which the slave laser phase is locked to, and coherent with, the master laser. From figures 1.b and 2 in reference [168], it may be observed that there exists the so called beating regions outside the locking region which result from either insufficient injection amplitude at a given detuning, or too large a detuning at a given injection amplitude. As the master laser is scanned by gradual ramping of the DC injection current, it is expected that the slave laser emission will traverse from one beating region to the opposite beating region via the intermediate stable locking region. It is also expected that the locking region will be asymmetric about zero detuning.

In this section we readopt the heterodyne detection scheme used at the beginning of the chapter. The magnitude of the AOM sidebands will provide an indication of the established coherence between the master and slave laser, in that the sideband amplitude will decrease either side of the locking region centre. Figure 6.7 shows a tiled view of an 800 MHz window on the RF spectrum, centred at the mode-locked laser fundamental modulation frequency, for various DC currents applied to the master laser. Alteration of the DC current affects both the optical frequency and the emitted power, so in order to maintain a constant injection power a half-wave plate is placed before the optical isolator.

For increasing DC injection current to the master laser (top to bottom in figure 6.7) the broad beat signal initially visible at $\sim$2.67 GHz shifts to lower detuning values from the mode-locked laser fundamental frequency and the magnitude of the AOM sideband beatnotes increases logarithmically. The reason for the apparent *increase* in the beat note frequency corresponding to *lower* detuning values is because of the symmetry of the optical system.

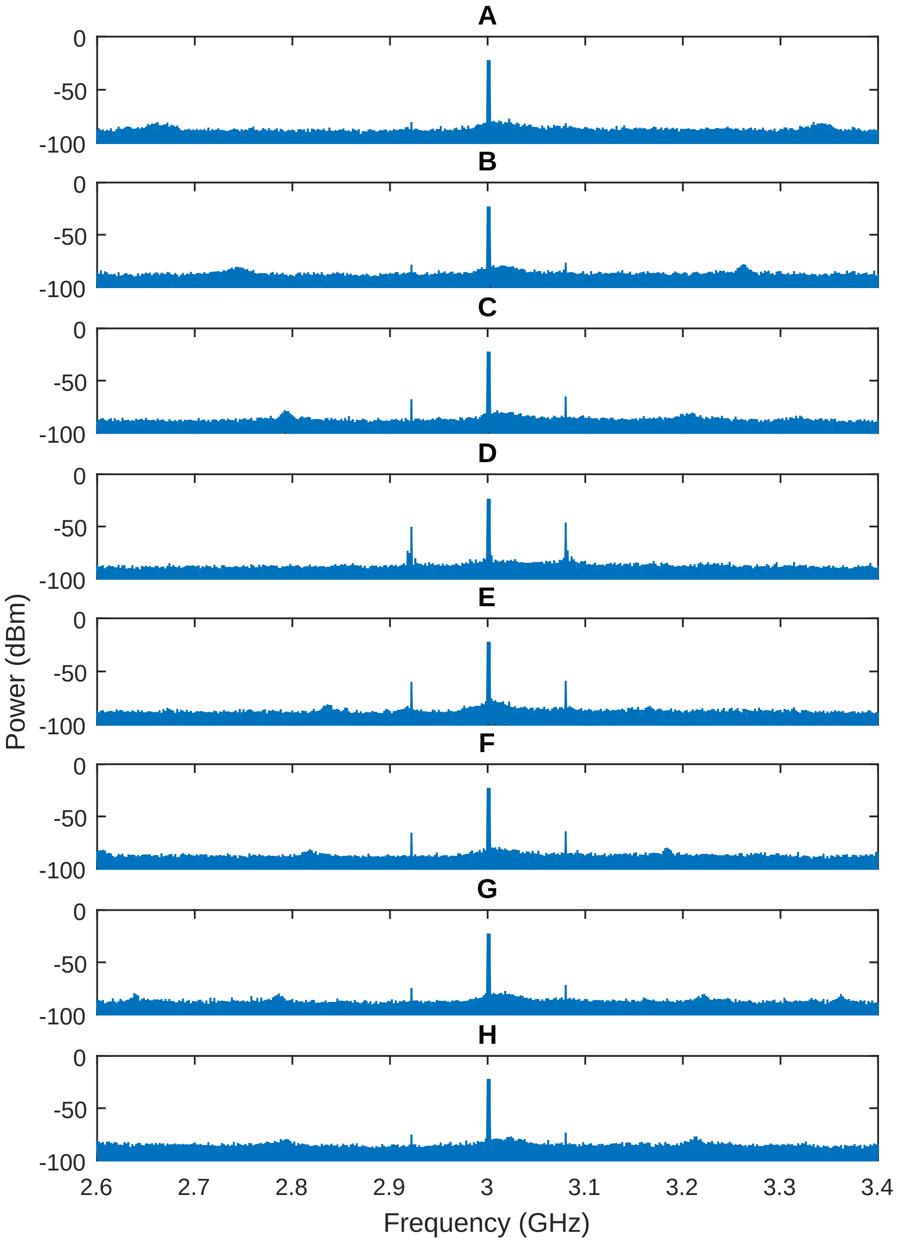

Figure 6.7: Example data series showing the injection locking range for a constant master laser power, as well as the corresponding heterodyne beat with the AOM shifted master laser. The broad peaks which converge on the harmonic at 3 GHz, disappear and then diverge again are caused by the beating of the master laser with the frequency comb. This beat disappears when the mode-locked laser is coherent with the master laser, and the two positions of minimum displacement from 3 GHz mark the points just prior to their disappearance and hence define the locking range. For all plots, RBW=VBW=20 kHz.

The origin of this beat signal is not the same beat as that of the AOM shifted sideband, instead it is caused by the weakly amplified injection signal beating with the nearest frequency comb mode. Even when sufficiently detuned from the nearest frequency comb mode so as to prohibit phase locking, the injected signal from the master laser may still experience amplification [112]. The physical reason for this beating regime is that the master laser light is sufficiently close to a cavity mode so as to observe a net gain but is of insufficient power to saturate the slave laser gain. As the master laser frequency is tuned towards the nearest slave laser mode, phase coherence is established and this beat signal disappears. It follows that by monitoring the two positions (positive a negative detuning) where this beat signal disappears and reappears (with respect to the optical frequency tuning direction), information about the locking range and it's symmetry may be obtained. The RF spectrum analyser is sensitive only to the beat signals present and not the respective absolute optical frequencies of the components causing the beat. Therefore an increase in the beat signal frequency on the RF spectrum (towards the mode-locked laser fundamental frequency) corresponds to the master laser shifting simultaneously towards the nearest slave laser optical mode and away from the nearest neighbour mode of the slave laser. This is also the reason for the beat signal symmetry about the mode-locked laser fundamental frequency (3 GHz).

The locking region is defined as the detuning frequency range where the beat signal disappears, indicative that phase coherence has been established between the master and slave laser. The positions in figure 6.7(C) and (E) represent the positions of minimum detuning where the beat note is still visible and all detuning frequencies within these bounds represent established injection locking.

Data in figure 6.8 shows information extracted from figure 6.7 and three other similar data series, where each data series represents a different master laser power. The information extracted from the series in figure 6.7 is represented in figure 6.8 by the 9.8 μW master laser injection power pane. For increasing injection powers, the measured injection locking ranges are, respectively, 0.242±0.014 GHz, 0.242±0.010 GHz, 0.224±0.008 GHz and 0.370±0.008 GHz. With the errors accounted for, these values do not rule out the possibility of a monotonically increasing locking range for increasing injections powers, as predicted in the literature for CW master and CW slave lasers [169–171]. Jung *et al* also report the same trend of increasing locking range with increasing injection power for a CW master laser injection locking a mode-locked slave diode laser [163], however they present considerably larger locking ranges for injection powers comparable to those investigated here. They demonstrate a locking range in excess of 0.8 GHz for -22 dBm of master laser power. Contrary to both the work presented here and to the wider literature, Jung *et al* go on to state that the locking range is symmetric. It is worthy of noting that the specific semiconductor laser being characterised is a hybridly mode-locked diode laser in an external cavity, where the saturable absorber forms part of the semiconductor waveguide. As such it is unclear what effect, if any, the saturable absorber may have on the symmetry of the injection locking range.

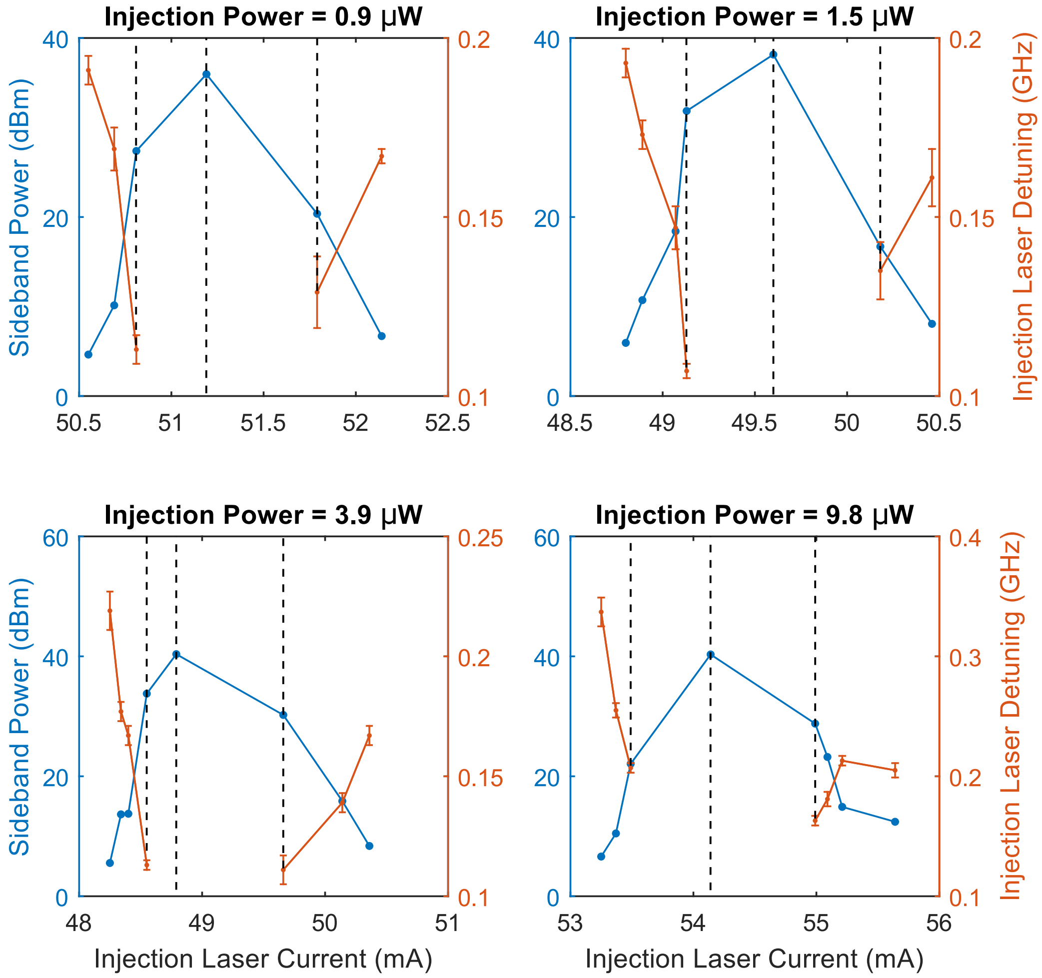

Figure 6.8: Demonstration of the injection locking frequency range and asymmetry about the central lock point for various master laser powers. Data points are extracted from the series in figure 6.7 and three other similar series (not shown).

The physical reason behind the predicted asymmetric locking range about zero detuning is based around the affect of the injected light upon the refractive index of the slave laser gain region. The presence of the master laser radiation acts to deplete the inverted carrier density and hence the complex refractive index is altered in such a way as to increase the wavelength of the slave laser mode [168]. The strength of this effect, which originates from the linewidth enhancement factor for semiconductor lasers, α, is dictated by the power in the master laser and the value of α [172]. It is also these two parameters which define the degree by which the locking region as a whole is red shifted [168, 170].

From the data in figure 6.8, it has been confirmed that the locking range is asymmetric about zero for master laser powers equal to 0.9 μW and 1.5 μW. Further, the relative size of the locking ranges favour a larger locking range for negative detuning, as predicted in the literature. This relationship begins to break down for a master laser power of 3.9 μW, and has reversed by 9.8 μW. At the time of writing, it remains unclear as to why this is observed.

In summary, the work in this chapter has confirmed first and foremost that CW injection locking of the mode-locked diode laser is a suitable method for locking the injected slave laser mode to the master. This in essence is a proof of principle foundation for supporting future work on this system. It has also been shown from the temporal and spectral emission of the injection locked slave laser that, without injection locking, the mode-locked laser is almost certainly operating in the clustered mode-locking regime. Suppression of the side-mode clusters of 20.6 dB has been achieved with -25.5 dBm of master laser power which was sufficient to reduce the time-bandwidth product to 1.44. This reduction clearly came at the cost of spectral bandwidth; a frustrating consequence given the aim of achieving a $\sim$1 nm wide frequency comb. Finally a maximum injection locking bandwidth of 370 MHz has been demonstrated. While the respective locking ranges either side of zero detuning begin to behave in an unexpected way for higher master laser powers, it has been confirmed that the magnitude of the locking range follows the magnitude of the master laser power, as per the literature. The next logical progressions for the work in this chapter would be to use a spectroscopically stabilised master laser and retest the above data for comparison, and also to implement a method for stabilising the slave laser cavity to the master laser frequency to prevent long term mechanical drift and prolong the stable locking time.

Chapter 7

Analysis of the Optical Frequency Comb

In this body of work we have demonstrated so far that actively modulating the laser drive current, and hence the laser gain, produces approximately 20 ps pulses of spectral width greater than 0.5 THz. Close inspection of the fundamental modulation frequency on the RF spectrum revealed a clean beat signal with no discernible substructure above -50 dBc when using a stable reference oscillator. A higher resolution inspection of the mode-locked optical spectrum with the air track Michelson interferometer revealed a comb of uniformly separated modes corresponding to the main laser pulse. Investigation then proceeded to demonstrate injection locking of the frequency comb to a master CW laser frequency. Coherence between the comb and the master CW laser was established over a 36 GHz span. In tune with published literature, it was also shown that spectral narrowing to a single monolithic cavity mode was achieved along with a small degree of temporal broadening. Finally, via detuning of the master injection signal around the free running optical frequency of the nearest slave laser mode, a locking range of greater than 200 MHz was demonstrated for all injection powers, distributed asymmetrically in favour of a slightly greater locking range towards red detuning. The final stage, presented in this chapter, is the inspection of the frequency comb in a manner becoming of its intended final application; stabilising the (now) slave CW lasers to the frequency comb. We wish ultimately to use the frequency comb as a frequency reference system for the wider atomic physics experiments within the group. These experiments require multiple high power, coherent CW light sources close to, and potentially hundreds of GHz away from, the single photon hyperfine transition frequencies within the Rubidium D2 line. In order to have confidence in the optical frequency of a slave laser stabilised to the comb far from the Rubidium lines, the frequency stability of the comb should be investigated and quantified. To achieve this, two CW lasers are stabilised to the comb and the RF beat note between them is observed on the RF spectrum analyser.

Through a desire to maintain versatility within the system, we opt for an electronic feedback method rather than a direct optical method for stabilising the slave CW lasers to the frequency comb. The Optical Phase Locked Loop (OPLL) is a closed loop feedback system where an optically derived electronic beat frequency is stabilised to that of a reference local oscillator (LO) signal [173–179]. A phase/frequency detector (PFD) generates an error signal based on the phase/frequency difference between the two signals which a servo uses to feed back to one of the constituent lasers used to derive the optical beat signal. By choosing a high stability reference TTL modulation source, and with suitable servo bandwidth, the phase of one laser may be stabilised to the phase of the other. The main appeal for using this method in this research is to maintain versatility in the lock point frequency of the CW laser relative to the frequency comb; if a stable arbitrary function generator is used to supply the reference TTL signal to the PFD, the lock point may be positioned anywhere within the PFD input bandwidth.

In this chapter we employ an in-house built circuit based on the ADF4007 frequency synthesizer / PLL integrated circuit (IC) and OP467 quad op-amp chip. The circuit was designed and populated by Dr M. Himsworth, with 'feedback'[1] on the initial designs by (now) Dr J. Rushton, and with design cues from reference [182]. Feedback to the laser(s) is provided by a slow servo output to a piezoelectric transducer that controls the slow frequency variations and a fast servo output that feeds back (for expedience) to the laser bias current via a modulation input on the current controller. The OP467 has a -3 dB gain bandwidth of $\sim$ 200 kHz and a stable unity gain bandwidth of 28 MHz. The laser current controller has a -3 dB modulation bandwidth of 500 kHz. From section 2.4.1, the free running linewidth of the grating stabilised ECDL lasers is 550±6 kHz.

---

[1] Apologies.

The total phase locking frequency bandwidth is 1 - 7 GHz, however the PFD operates at the much lower bandwidth. The ADF4007 IC is capable of dividing down the experimental RF beat note before the PFD by an amount equal to 8, 16, 32 or 64. For our purpose the divider is set to 64. The final consideration is that of the frequency comb mode spacing. To avoid complication the optical beat note generated between the frequency comb and the CW laser we wish to stabilise must be appreciably below half the frequency comb mode spacing. The LO frequency is therefore chosen to be 30 MHz at the oscillator source which is intrinsically divided by 2 by a reference divider to 15 MHz. Therefore the target experimental RF beat note is $15 \times 64 = 960$ MHz. With the mode-locked laser operating without injection locking, we begin by current tuning the CW laser and monitoring the beat on the RF spectrum.

7.1 Beat Sign Analysis

7.1.1 Experimental Setup

For this experiment it is required that the beat note between the two CW slave lasers be measurable while simultaneously being able to measure the discrete beat notes of the CW slave lasers against the comb. To achieve this, the optical arrangement depicted in figure 7.1 was constructed. In the first instance, the two slave CW lasers are linearly polarised orthogonally to each other before being combined at a non-polarising beam splitter cube. One output from the combining beam splitter is directed through a half wave plate in order to rotate the polarisations of both beams by $\pi/4$, before being sent through a polarising beam splitter cube in order to project the parallel components into a given output from the cube. The transmitted beam pair is then incident on a fast photodiode (PD3) while the reflected pair is directed onto a beam dump. The other non-polarising beam splitter output is then combined with the mode-locked laser output at a second non-polarising beam splitter. The mode-locked laser is linearly polarised at 45 degrees to both the CW slave lasers. The beam triplet is now incident on a polarising beam splitter cube whose transmission axis is aligned to completely transmit CW laser 1 and completely reflect CW laser 2.

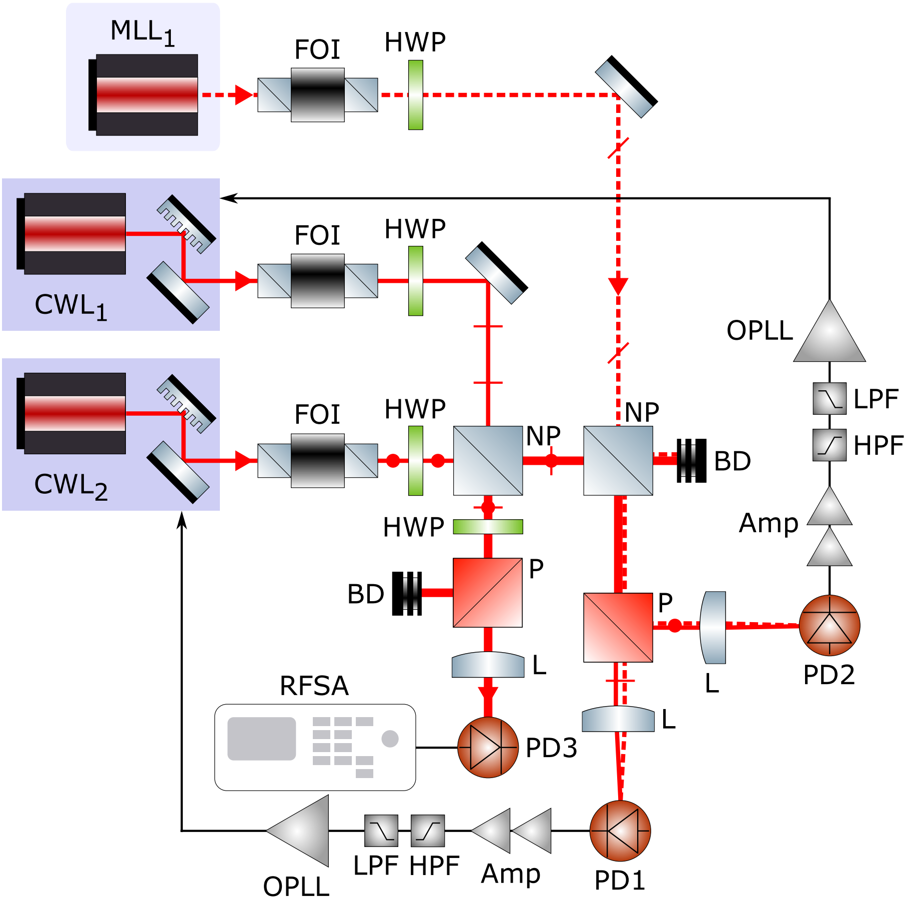

Figure 7.1: Schematic diagram showing how the experimental beat frequencies between the CW lasers and the frequency comb are generated before being utilised by the OPLL circuit. Photodiode (PD) 1 and 2 monitor the beams from CW lasers 1 and 2 respectively, and both photodiodes receive half of the available frequency comb power resolved into the same respective polarisation as the incident CW laser. PD 3 monitors the beat frequency between the two CW lasers. The beat signals at PD 1 and 2 are amplified by approximately 65 dB and bandpass filtered before being sent to the OPLL RF input. The output of the OPLL is fed back to the CW lasers' grating angle via the piezo voltage, and to the current via the modulation input on the DC current controller. In this figure the dots and lines in the optical beams represent their respective linear polarisation states. FOI; Faraday optical isolator, HWP; Half Wave Plate, NP; Non-Polarising Beam splitter cube, P; Polarising beam splitter cube, L; Lens.

Where the mode-locked laser is at 45 degrees to both CW lasers, the mode-locked laser power is split equally between each polarisation axis and superimposed upon each CW laser polarisation. A lens then focuses each beam pair onto a separate fast photodiode. This setup therefore allows for the simultaneous generation of a beat note between the two CW slave lasers, and a unique beat note between the mode-locked master laser and the two individual CW slave lasers. The latter two beat notes are amplified and sent to the OPLL circuits which stabilises the slave lasers to the master by feeding back to their respective DC injection currents and external grating angles by way of the piezo voltage. The former is then monitored on the RF spectrum analyser to determine the comb stability.

7.1.2 The Beat Signal

The RF frequency we wish to stabilise is derived from the beating of the frequency comb and the CW laser on a fast photodiode. The photodiode generates a current proportional to the intensity variations caused by the interference of the optical fields,

$$I_{beat}(t) \propto \left| E_{fc}(t) \times e^{i\left(\omega_{fc}t+\phi_{fc}(t)\right)} + E_{cw}(t) \times e^{i\left(\omega_{cw}t+\phi_{cw}(t)\right)} \right|^2, \tag{7.1}$$

where E_{fc} and E_{cw} represent the field amplitudes of the nearest frequency comb optical mode and the CW laser respectively, and ω_{fc} and ω_{cw} represent their optical frequencies. Expansion of equation 7.1 yields,

$$I_{beat}(t) \propto E_{fc}^2(t) + E_{cw}^2(t) + 2E_{fc}(t)E_{cw}(t)\cos\left(\omega_{beat} + \Delta\phi(t)\right), \tag{7.2}$$

where $\omega_{beat} = \omega_{fc} - \omega_{cw}$ and $\Delta\phi(t)$ is the combined phase difference which includes oscillator phase noise. The first two terms on the right of equation 7.2 are the DC components of the two constituent beams. The RF spectrum analyser will not tolerate DC current at the input so a DC block (Mini Circuits BLK-18) is used to AC couple the photodiode signal. Due to the very low optical power per frequency comb mode, the magnitude of the beat signal will be significantly below the -10 dBm minimum input threshold to the ADF4007. Two in line RF amplifiers are used to amplify the beat signal (2× Mini Circuits ZRL-1150LN+, +34 dB Gain), and bandwidth limiting high- and low-pass filters (Mini Circuits SHP-800+ and VLF-1000+) when not inspecting the beat signal on the RF spectrum.

In all of the frequency comb analysis presented in this chapter, the mode-locked diode laser is operating under cooled conditions and in the presence of the thin etalon and linear polariser so as to achieve wavelength tuning to 780nm.

7.1.3 RF spectrum

The RF spectrum trace in figure 7.2(A) represents the first measurement of the beat spectrum between the CW slave laser and the frequency comb. At this stage no feedback electronics are connected to either laser therefore both should be considered as free running. At frequencies higher than 976 MHz, four additional peaks are visible, while at lower frequencies only a single peak is visible. The frequency separations from peak a are listed in the figure caption, as well as the nearest lower frequency neighbour separations in brackets. It is believed that peak a represents the main optical mode of the frequency comb. Peaks b through f, and their relative separations, correspond to no known distance or frequency of modulation in either system, nor do they correspond to any peaks in the sub structure (for any detuning) in figure 4.12.

In an attempt to determine the origin of these unexpected peaks, the frequency comb mode spacing was altered by 1 MHz divisions via changes in the active modulation frequency over a 10 MHz span centred at 3.0 GHz and the RF spectra are shown in figure 7.2(B). Of most interest under the context of beat signal quality - parametrised by linewidth and isolation from additional neighbouring spectral structure - is the apparent improvement in appearance of the beat signal quality towards larger negative detuning. From 0 to -5 MHz, peaks b through e are observed to translate towards peak a. Peak b merges with peak a causing a higher peak power, narrower peak a, while peak e merges with peak d yielding a similar effect. Peaks e and f also translate to smaller detuning from a as ω_m is decreased. For increasingly positive modulation frequency detuning, initially all peaks appear to spread apart followed by the appearance of a disintegration of peaks a, e and f into multiple, evenly spaced sub-peaks separated by 20 MHz. The origin of this behaviour remains unresolved. It should be noted that, during acquisition of these data, if either the mode-locked laser or the CW laser were blocked, in most cases the entire trace would drop to noise level, but on rare occasions some unknown signal remained. The source of this unknown signal was traced back to the CW laser and will be discussed shortly.

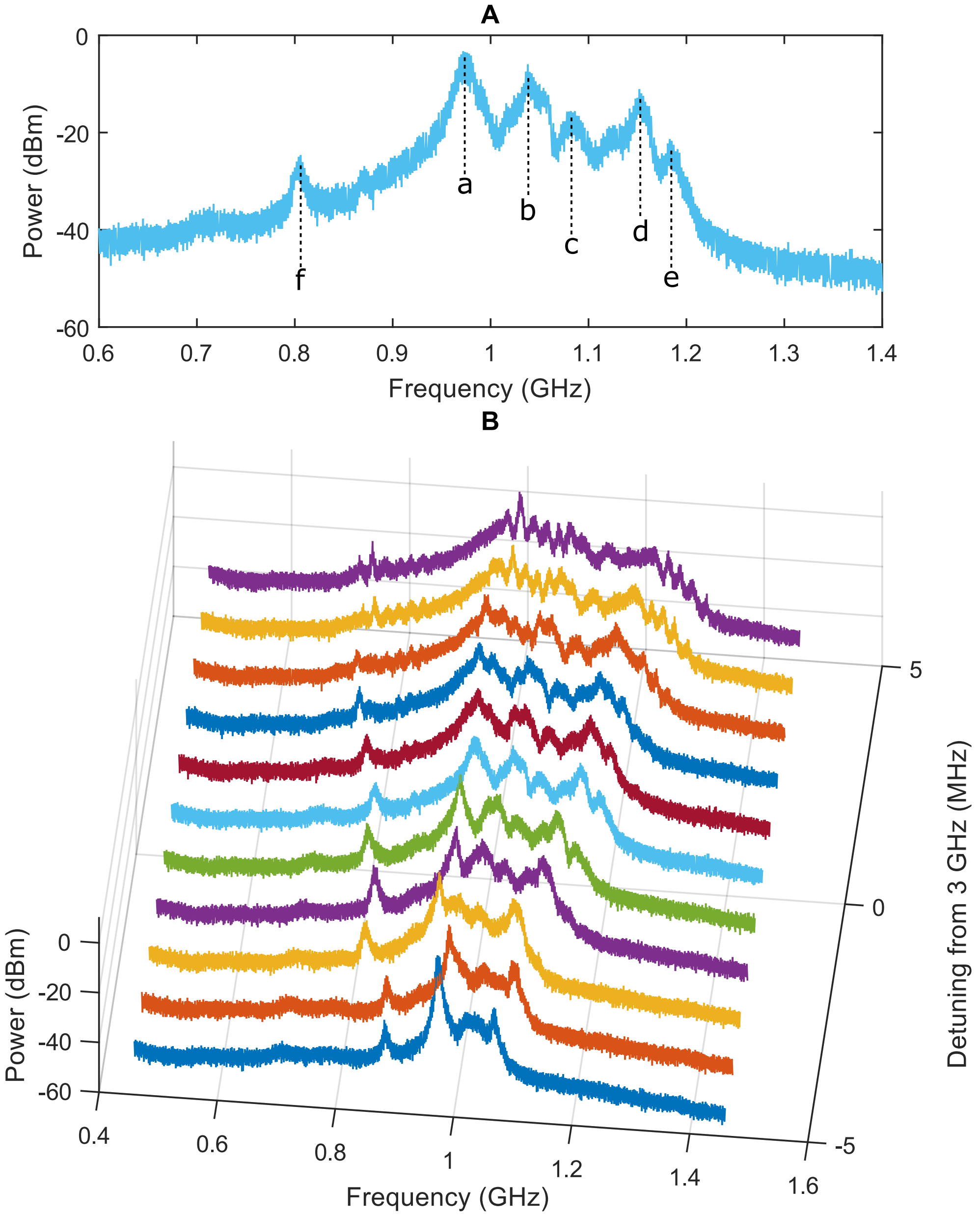

Figure 7.2: (A); An 800 MHz spectral window centred at 1 GHz showing the RF beat signal between a single CW laser and the frequency comb. The peaks are labelled a through f. The frequency separation from a are as follows, where the frequencies in brackets are the separations between that peak and the previous: a=0 MHz, b=54(54) MHz, c=110(56) MHz, d=178(68) MHz, e=209(31) MHz, f=-170 MHz. (B); The same RF beat spectra as (A) except where the mode-locked laser modulation frequency has been explored over a 10 MHz range centred at 3 GHz. The data in (A) is plotted as 0 MHz detuning in (B). For all plots RBW=3 MHz, VBW=100 kHz.

Under no conditions when solely the mode-locked laser was present on the photodiode were unexpected signals observed on the RF spectrum between 0 - 3 GHz, in either mode-locked or CW operation. When the mode-locking modulation signal was turned off and the laser was operating in CW, the beat note between this laser and the slave CW laser consisted of a single peak approximately 10 MHz wide at FWHM with no surrounding sub-structure, which is consistent with the width of peak a in figure 7.2(A). Similar RF spectra were also observed between the frequency comb and the slave cw laser when the slave laser was manually tuned at least 100 GHz away, suggesting that the source of the unknown peaks b through f are not localised to a single comb mode, nor a single monolithic cavity mode of the CW laser.

Returning to the unknown signal originating from the CW slave laser, figure 7.3 shows the evolution of a 4 GHz RF spectral window as a function of DC injection current to the CW laser, where the colour map defines the magnitude of the observed signal above the background noise level. The solid dark blue regions have been intentionally blanked so as to maintain focus only on areas where unusual activity was present.

Of immediate interest is the recurring cluster around 3.6 GHz. Knowing that the laser composite cavity length is approximately 30 mm [183], these clusters are believed to be the inter-mode beat frequency when the laser is operating on multiple composite cavity axial modes. These clusters appear approximately every 2.86 mA, as calculated by the mean current difference between the centre of each cluster. From this we calculate a frequency tuning rate of 1.254±0.005 GHz/mA, in line with the very similar configuration in reference [183]. The symmetric pairs of clusters which appear to converge with increasing DC injection current are of unknown origin, though they appear to converge at constant rate towards 1.80 GHz; the first sub-harmonic of the composite cavity axial mode spacing. The rate of change of frequency with current within these symmetric clusters is of the order of 183±7 MHz/mA, vastly slower than all respective calculations thus far.

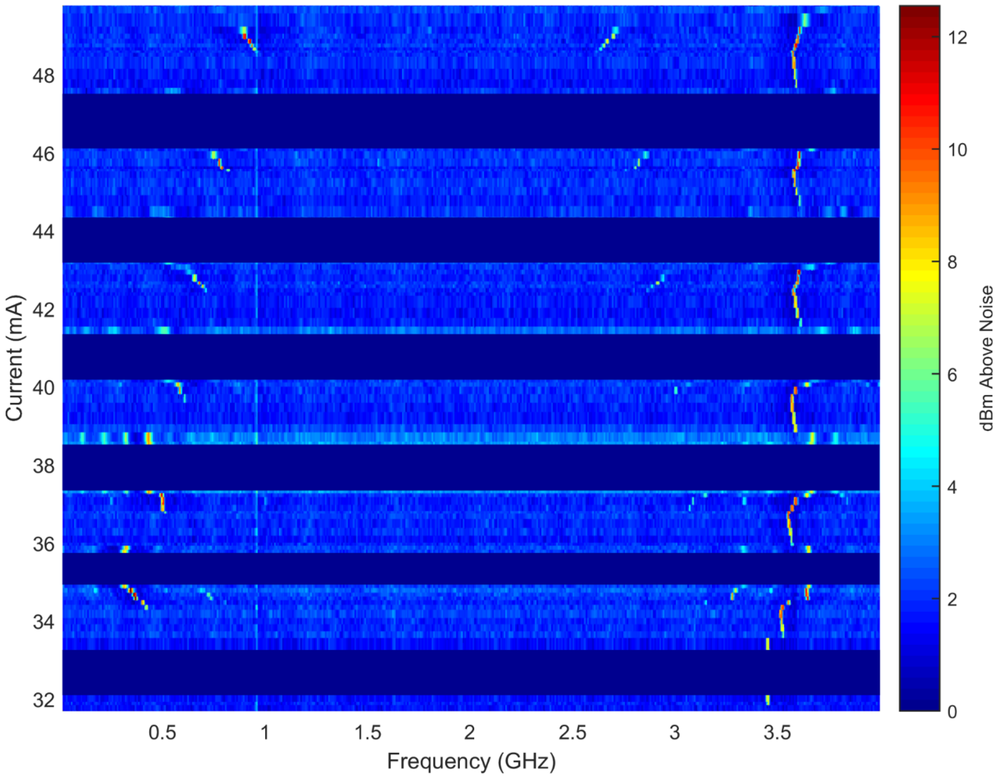

Figure 7.3: Surface plot showing the evolution of noise clusters on the RF spectrum for only the CW slave laser incident on the photodiode as a function of DC injection current to the CW laser. The dark blue blocks are intenionally blanked to highlight only the evolution of the unknown signals. The recurring signals around 3.6 GHz are thought to be the beating of the slave laser external cavity axial modes. RBW=3 MHz, VBW= 30 kHz

The addition of the frequency comb allows for the observation of the evolution of the beat signal between the CW and mode-locked laser as a function of the DC injection current to the CW laser. With the patterns in the data for just the CW laser noted, we are able to identify the evolution of the correct beat signal (green) and the additional signals caused by just the CW laser (red) in figure 7.4. The solid red feature present at 3 GHz is the frequency comb fundamental mode spacing. Signals in the spectrum which are generated by the CW laser only are identified and discounted primarily due to the presence of the cluster at 3.6 GHz, but also through their steeper gradient; c.f. red and green highlighted regions. In this figure, the solid blue regions are now present to mask off the unexpected behaviour observed in figure 7.3. The tuning rate for the CW laser cannot be calculated from any linear trend between data highlighted by the green regions as the laser appears to mode-hop between each highlighted cluster, however an estimate can be made from the gradient within the green regions. The tuning rate is calculated to be 348±2 MHz/mA. This tuning value is the most likely to be correct by nature of the method from which it was derived. The fixed features in the data highlighted by the red arrows below 1 GHz are background pick up noise. The lower frequency was traced to pick up from the nearby OSA, as it disappeared when this device was deactivated. The higher frequency is 957.6 MHz and corresponds, we believe, to pick up from the Universal Mobile Telecommunications Systems (UMTS) Extended-GSM Band 8 downstream channel: a common 3G cellular data carrier frequency found in mobile phones for the European region.

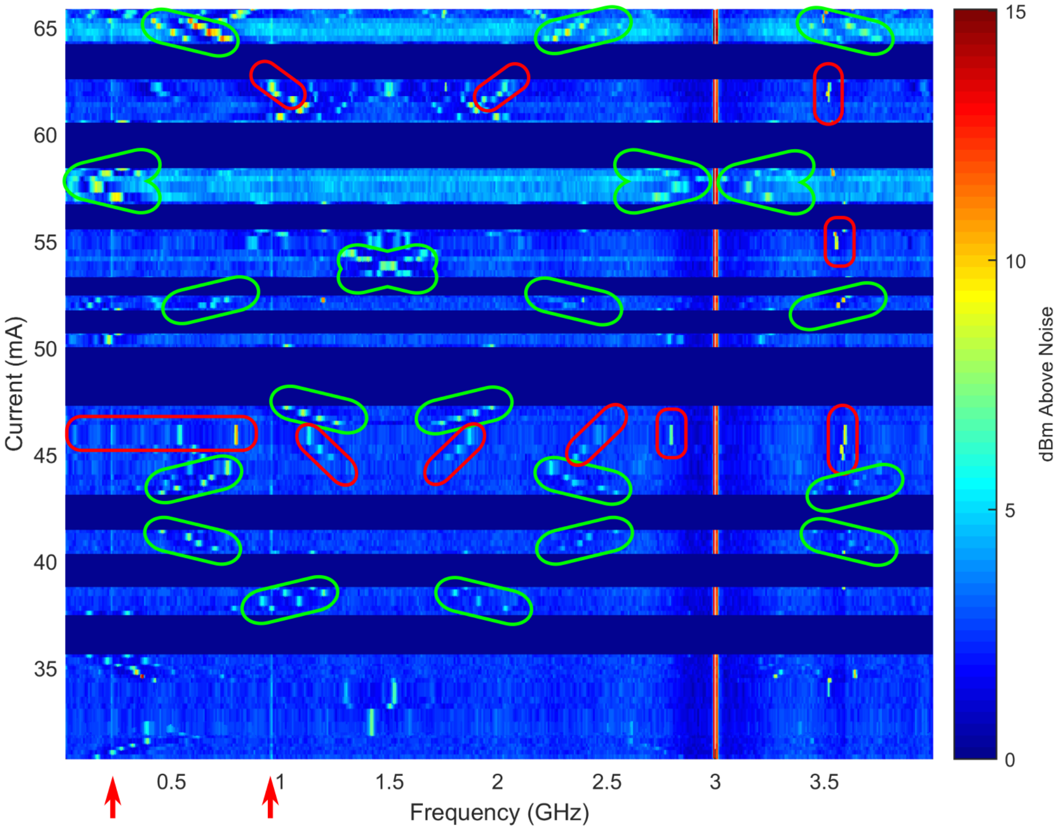

Figure 7.4: Surface plot showing the evolution of the optical beat signals between the CW and mode-locked lasers on the RF spectrum. The solid red vertical line is the mode-locked laser fundamental modulation frequency. The clusters highlighted in red are believed to be the result of just the CW laser, as depicted in figure 7.3, and the highlighted green clusters are believed to be the true beat signal between the CW and mode-locked laser. RBW=3 MHz, VBW= 30 kHz

It is anticipated that, in order to determine the source of the extra peaks *b* - *f* in figure

7.2, both the CW slave laser and the frequency comb will need to be characterised against a source of known spectral properties. A narrow linewidth, single longitudinal mode laser such as a DBR semiconductor laser would be sufficient. We have also not ruled out the possibility that the extra peaks may be electronic in origin, however a number of different electronic amplifiers and filters were tested in various combinations with no visible sign of improvement on the RF spectrum.

7.2 Optical Frequency Lock

In this section we employ the OPLL circuit described at the start of the chapter. To characterise the performance of the lock, we consider the RF beat note signal between two CW lasers for when only the (slow) piezo feedback is used and when both the piezo and (fast) current feedback are utilised. Following this analysis, the same two CW slave lasers will be locked to the frequency comb master laser.

7.2.1 CW-CW Frequency Lock

Initially the two CW lasers are tuned to approximately the same positions by grating angle and temperature tuning using a wavemeter. As stated earlier in the chapter, the lock point, or rather the target frequency difference between the two lasers, is set to be 960 MHz. Once a suitable beat note is located, the piezo feedback is engaged and yields a relative frequency lock, figure 7.5(A, Blue). Due to significant noise over the 67 ms sweep time, the RF spectrum analyser was set to average over 100 samples. Using both piezo and current feedback channels of the system yields the noticeable narrowing of the beat signal visible in figure 7.5(A, Red). The increase in the beat note peak power is due to the higher frequency capability of the current feedback part of the system which forces the slave CW laser to more closely follow the phase variations of the master and hence the beat note power is more effectively concentrated towards the centre of the lock point frequency. To calculate the beat note linewidths the traces in figure 7.5(A) are first converted from the logarithmic scale to linear and then both normalised to the maximum peak height of the more powerful beat note signal before a Gaussian fit is applied to both. Engaging only the piezo frequency lock yields a beat note linewidth of 2.63±0.04 MHz from the fit curve at the FWHM (figure 7.5(B)), whereas engaging both the piezo and current feedback gives a narrower linewidth of 1.40±0.01 MHz (figure 7.5(C)).

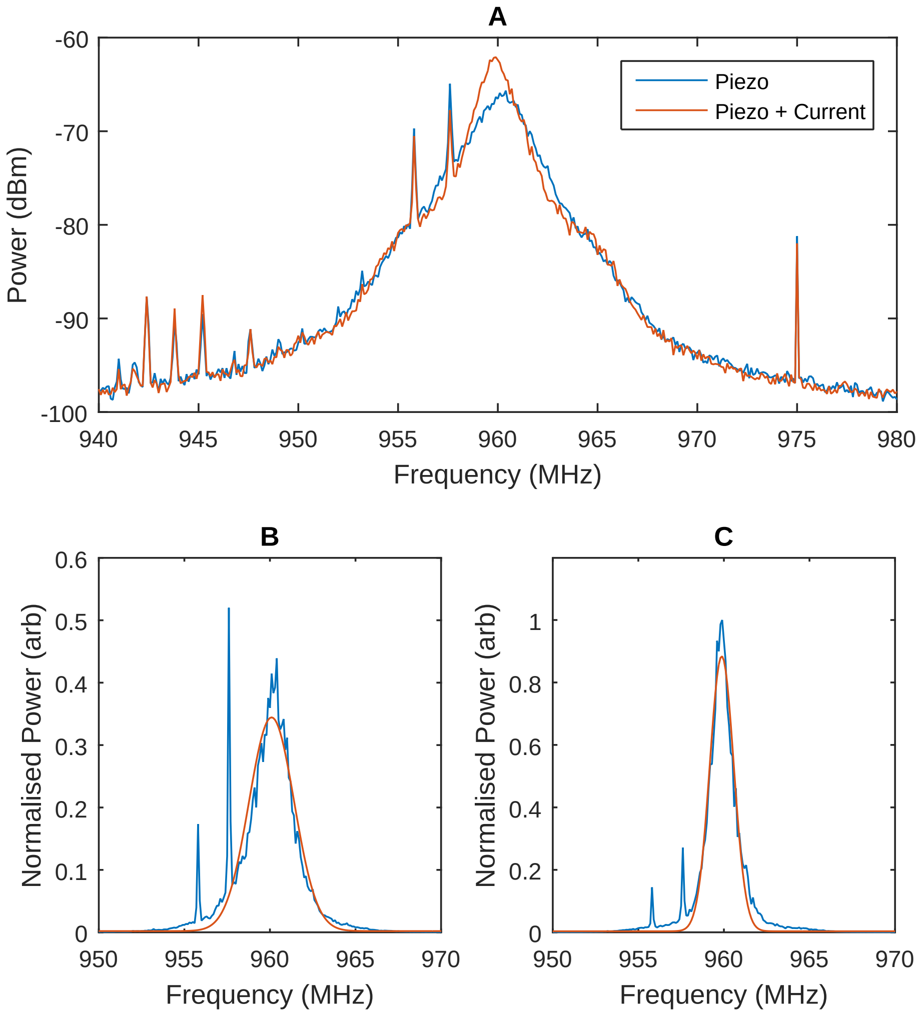

Figure 7.5: Comparison of the beat note linewidths of CW laser (2) stabilised to CW laser (1) via piezo feedback only and combined current and piezo feedback, (A). Subfigures (B) and (C) show the same lineshapes respectively after being converted to a linear scale and where the peak heights of both have been normalised to the peak height of the lineshape in subfigure (C). The red curves in (B) and (C) represent a Gaussian fit to the data. Each trace in (A) is the result of 100 averages at the spectrum analyser. For a singular sweep, RBW=VBW=10 kHz

While observing a narrowing in the beat note linewidth by almost a factor of two, it is clear that the system does not possess the necessary noise bandwidth to stabilise the residual phase error between the two CW lasers. When estimating the bandwidth of a system such as this, typically the RF spectrum will exhibit two pairs of separate peaks, where each pair is symmetric about the central beat note signal. Outwards from the beat note signal centre, the first set of peaks tends to reside nominally at a few hundred Hz, while the second set tends to reside between hundreds of kHz to tens of MHz. These peaks represent the unity gain bandwidth of the piezo and current feedback paths respectively. No noticeable side lobes are visible on either trace in figure 7.5(A) however, making quantification of the system performance difficult. The appearance of the shoulders on the red trace in figure 7.5(A) is possibly an indication of the maximum system bandwidth and is estimated to be 8.0±0.5 MHz. The bandwidth of the system is bottlenecked by the modulation input bandwidth of 500 kHz on the laser current controller. It is assumed that the lock performance would improve if the fast frequency corrections from the PLL servo were coupled into the laser via a high bandwidth bias tee.

7.2.2 CW Lock to the Frequency Comb

Having demonstrated that the OPLL circuit is capable of frequency locking one CW laser to another, the frequency comb is reintroduced along with a second OPLL circuit. The second circuit has a different frequency offset lock point equal to 800 MHz (64×25/2 MHz). The intended result is to have two CW lasers locked to the frequency comb whereby the optical frequency difference between the two CW lasers is much larger than 3 GHz, but still within the maximum (25 GHz) bandwidth of the RF spectrum analyser so that the beat note reveals information about inter-mode stability. With the mode-locked laser free running and not stabilised to any reference, the optical frequency of the two CW slave lasers is expected to drift with the frequency comb, however the inter-mode spacing of the frequency comb modes should be fixed on account of the active modulation. Figure 7.1 shows a schematic of the optical arrangement used to acquire the data in figure 7.6, where the beat signal between the two CW lasers is measured at photodiode 3.

During this part of the experiment the exact beat notes between the frequency comb and the slave CW lasers cannot be viewed on the RF spectrum. An appropriate lock point may be determined by observing the error signal monitor output from the OPLL. When the sign of the detuning between the divided down RF and LO signals flips, so does the sign of the error signal, thereby marking the vicinity of the lock point. The slave CW lasers are tuned to approximately 21 GHz apart, locked to the nearest suitable error signal and the beat note signal is recorded and shown in figure 7.6.

Provided the slave lasers are stabilised to the frequency comb and that there exists negligible breathing of the frequency comb mode separation, a narrow linewidth, frequency stable beat note would be expected. Figure 7.6 displays six beat note signals over five sweep times and six resolution bandwidths, where all spectra are single shot measurements. Over short sweep times (1 - 2 ms), the beat note signal takes the form of a narrow linewidth approximately 250±100 kHz across at -3 dB, which corresponds to individual laser linewidths of 174±69 kHz (figure 7.6(A)-(C)). As the sweep time increases, the beat note signal broadens to approximately 65 MHz (figure 7.6(F)). We propose that the source of this noise is mechanical in nature which originates from multiple sources and manifests as jitter in the external cavity length and grating feedback angle. The optical bench is not pneumatically isolated, hence it is likely that there exists a rich source of background vibration that is coupled to the grating via the laser mount to the bench. It is possible also that the grating feedback corrections from the servo loop suffer over overshoot due to the broad beat note linewidth measured in figure 7.2(A) or through the loop gain being set above optimal. Another possible source of noise is that of electrical noise introduced by the servo loop. The piezo output from the servo loop is fed back to the laser via a piezo amplifier with a flat gain across its input modulation voltage ramp range of 12 dB. The laser optical frequency tuning rate as a function of piezo voltage is 100 MHz/V, which implies that noise amplitude of only 20 $\mathrm{mV_{p\text{-}p}}$ is required from the servo loop output to give ±15 MHz of frequency variation. In reality, this figure is high for solely the background noise intrinsic to the circuit. Effective analysis of the noise sources giving rise to this strong broadening of the beat note linewidth can be achieved through a frequency noise measurement on a FFT spectrum analyser, which would be part of further analysis in continued research. Despite the apparent instability over appreciable fractions of a second, both lasers remained stabilised to the comb for in excess of 10 minutes, during which the lock point defined by the centre of the distribution in figure 7.6(F) remained unchanged.

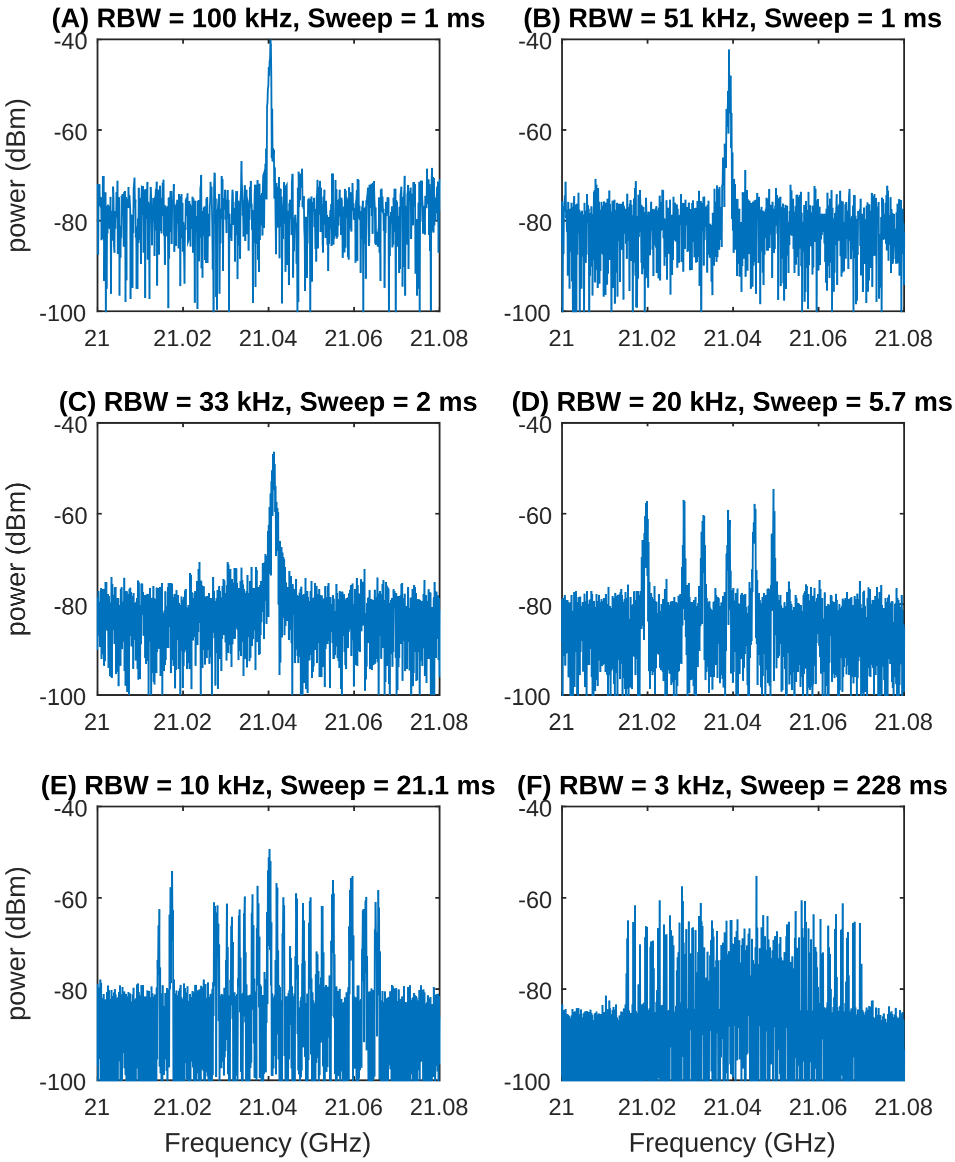

Figure 7.6: Beat note linewidth measurement of two CW lasers stabilised to the frequency comb over various resolution bandwidths and RF spectrum sweep times. In all cases VBW=RBW.

While the work presented in this chapter forms a relatively ’bare bones’ analysis of the frequency comb stability, a number of important investigative steps have been attempted. The substructure present in the beat note between the CW slave laser and the comb is of unresolved origin (figure 7.2). On the one hand, the shape of this sub structure changes as a result of altering the mode-locking modulation frequency, whereas on the other hand this sub structure is not visible on any of the wider span RF spectra of just the frequency comb. Figures 7.3 and 7.4 revealed that the CW slave laser exhibited periodic features on the RF spectrum which also appear in the beat note spectrum between the slave laser and the frequency comb. While the features at ~3.6 GHz are attributed to the slave laser operating on multiple composite cavity modes, the periodic structure that appeared symmetrically about 1.8 GHz remains unidentified. The latter of these figures demonstrated however that the beat note between the slave CW laser and the frequency comb still possessed the same substructure as in figure 7.2.

Figure 7.5 demonstrates that the in-house built OPLL circuit is effective at not only stabilising one CW laser to another, but also that, in itself, it possesses sufficient bandwidth to narrow the beat note linewidth by nearly a factor of 2. It is very likely that this would improve significantly were it not for the bandwidth bottleneck of the laser current controller modulation input. Finally it was demonstrated that the OPLL circuits were effective in broadly stabilising two slave CW lasers to the frequency comb. It is believed that large amplitude, low frequency mechanical noise is the cause of the broad beat note over larger sampling time scales and that with further time to investigate and eliminate this noise, the inter-mode stability of the comb could be fully characterised.

Chapter 8

Light Generation for Atomic Physics Experiments

We now deviate from the frequency comb focus of the thesis to discuss one of two side projects. While the approach is no longer towards the frequency comb generation, many of the underlying principles are preserved thereby maintaining suitable presence in the wider trajectory of the thesis. This chapter has roots in the generation of useful coherent optical sources for use in ultracold atomic physics experiments, while chapter 9 outlines the very early stages of research towards a novel intra-cavity trace water vapour spectroscopy technique based on frequency modulation spectroscopy.

8.1 Stabilised Fiber Mach-Zehnder Interferometer

It is not uncommon for atomic physics experiments to require multiple optical sources that are not only coherent in themselves, but also mutually coherent across all the sources [12, 13, 184]. In order to generate and maintain this coherence between sources, a common approach is to generate frequency sidebands on a monochromatic source through external electro-optical phase modulation or modulation of the DC drive current in laser diodes. In the former case, sidebands may be generated up to a maximum of a few tens of gigahertz away from the carrier frequency, usually with the modulation depth decreasing significantly with increasing modulation frequency. In the latter case, the modulation response is limited to around the carrier relaxation frequency of the specific device. In both cases the generated spectral components propagate coaxially and therefore may require spatial separation to become useful. Acousto-Optical modulation can be used to generate spatially discrete frequency components, however this mechanical standing-wave-based diffractive method is generally limited to only a few gigahertz.

The Mach-Zehnder interferometer may be used as a frequency dependent filter [185] whereby suitable selection of the relative path length imbalance allows for the interferometric spatial separation of specifically frequency separated optical components. Like any optical interferometric device, physical properties such as relative optical path length are susceptible to drift, thereby affecting the optical transmission properties. It is desirable therefore to stabilise the device mechanically to maintain a maximum or minimum in optical transmission at a desired output port.

Perturbation of the interferometer from a given optimal position presents an identical change in optical properties regardless of the direction of the initial perturbation. Monitoring the change in intensity is therefore insufficient for deriving a suitable correction signal to nullify perturbations to the system. While it is possible to dither [186] the interferometer around a peak in transmission, or to 'side of fringe' lock [187], an elegant solution is to generate optical sidebands on both sides of the required optical frequency through phase modulation and observe the differential transmission of these components through the interferometer via phase sensitive detection. At the point where these sidebands are equidistant from a maximum or minimum in transmission, the magnitude of the beat signal between *each* sideband and the carrier is identical and so the relative π phase difference between them results in a zero signal. When the interferometer is perturbed, this perfect beat signal cancellation is disrupted yielding a signal that is both approximately linear through zero and asymmetric in sign. It is this signal which may be used to stabilise the interferometer to the desired maximum or minimum.

The method presented here is a variant of the conventional form of phase modulation [87] where the sidebands are instead generated by Acousto-Optical Modulation and whose transmission through the interferometer are measured alternately. The specific requirement for our intended application is the coherent population transfer between the $F = 2$ and $F = 3$ hyperfine ground states of ^{85}Rb, which have an absolute frequency difference of 3.0357 GHz and is achieved through a Raman transition. Our custom MZI has a splitting frequency equal to 2.7 GHz and the remaining 300 MHz is applied later via an AOM. The splitting frequency of the MZI, ω_{sep}, is the difference in frequency between two optical components that is required for each component to exit the interferometer from diagonally opposite ports. To achieve this, the optical path length beteen the two arms of the interferometer must differ by $\Delta l = \frac{c}{2n\omega_{sep}}$. This splitting effect occurs due to one optical component obtaining a π phase shift compared with the other component over this extra optical path length. Shown in figure 8.1 is a schematic layout of the experiment.

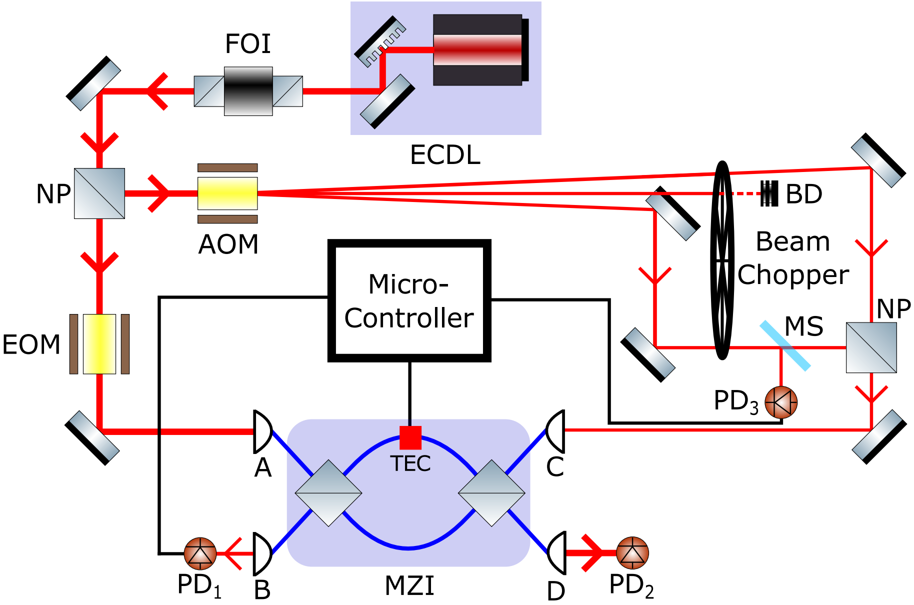

Figure 8.1: Diagram showing the schematic layout of the stabilised Mach-Zehnder interferometer. FOI; Faraday Optical Isolator, NP; Non-polarising Beam splitter Cube, AOM; Acousto-Optical Modulator, EOM; Electro-Optical Modulator, PD; Photodiode, BD; Beam Dump, MS; Microscope Slide,

Optical sidebands of 2.7 GHz are generated on the diode laser output by an EOM before entering the MZI in the forwards direction at port A. Just before the EOM, a beam sampler splits off a small amount of the beam which is then directed through an AOM. This AOM generates spatially discrete sidebands at frequencies of $\omega_0 \pm \omega_{AOM}$ ($\omega_{AOM} =$ 80 MHz) which, after a mechanical beam chopper, are recombined before entering the MZI in the backwards direction at port C. The chopper passes the beams alternately and information about the relative phase of the chopper blade is captured by photodiode 3. The transmission of these AOM sidebands through the interferometer is monitored at output port B by photodiode 1. The error signal is derived by subtraction of the relative magnitudes of the transmitted sidebands. The error signal is processed by a software PID loop programmed into the microcontroller, converted into a Pulse Width Modulation (PWM) signal and finally used to regulate the current to a Thermoelectric Cooler (TEC). The optical path length of one of the interferometer arms is therefore altered through changes in the fibre refractive index as a result of changes in the fibre temperature. Finally, the bulk of the signal at the carrier frequency is transmitted through the MZI from ports A to D and monitored by photodiode 2 for the purpose of measuring the lock performance (during characterisation the EOM is inactive).

8.1.1 Theoretical Lineshape of Error Signal

Our theoretical description of the functional form of the error signal starts with the basic building blocks of frequency modulation, where we consider a sinusoidal perturbation to the phase of an already sinusoidally varying E-field. We may write this field as:

$$E = E_0 e^{i(\omega_0 t - kz + \phi)}, \tag{8.1}$$

where,

$$\phi = \phi_0 + \beta \cos(\omega_m t) \,. \tag{8.2}$$

Here β and ω_m are respectively the modulation index and modulation frequency. Noting that for a monochromatic field the rate of precession of phase angle, ϕ_0, is constant, i.e.:

$$\omega = \frac{d\phi}{dt}, \tag{8.3}$$

it becomes clear that a time dependent perturbation to the phase gives rise to a time dependent shift in optical frequency given by,

$$\Delta\omega = \omega - \omega_0. \tag{8.4}$$

Following some rearrangement it can be shown that

$$\Delta\omega = -\beta\omega_m \sin\left(\omega_m t\right). \tag{8.5}$$

This expression represents the frequency shift imposed on the optical carrier frequency given by a sinusoidal modulation applied to the phase of the carrier signal.

Consider now the magnitude of the transmission of an optical component through the MZI as a function of ψ, the phase difference accumulated by the different path lengths of the MZI. This transmission may be written as:

$$T = \left|1 + e^{i\psi}\right|^2. \tag{8.6}$$

Given the earlier definition of the MZI splitting frequency, it must be the case that if the optical carrier frequency entering the MZI acquires a change in absolute frequency equal to the MZI splitting frequency, the corresponding accumulated phase difference at recombination is $\delta \to \delta + \pi$. Deconstruction of δ into $\delta = \delta_0 + \delta_1$ and rearranging yields $\psi_0 = \psi - \psi_1$, where ψ_0 is the phase shift accumulated for ω_0 and $\psi_1 = \frac{\pi\Delta\omega}{\omega_{sep}}$.

At this point the derivation deviates from that of true phase modulation as we consider that we instead create our frequency sidebands with an AOM at frequencies $\omega_0 \pm \omega_{AOM}$. As such, after substituting for δ, equation 8.6 may be written,

$$S_{err} = \left|1 + e^{i\left(\psi_0 + \frac{\pi\omega_{AOM}}{\omega_{sep}}\right)}\right|^2 - \left|1 + e^{i\left(\psi_0 - \frac{\pi\omega_{AOM}}{\omega_{sep}}\right)}\right|^2. \tag{8.7}$$

Instead of T, we are able to write S_{err} as, unlike with pure phase modulation, we are not required to demodulate the detected transmitted signal against modulation frequency to generate the error signal. Instead, having detected the transmitted intensity of the two sideband beams, the form of the error signal is achieved directly by subtracting the lower sideband signal from the upper. Following expansion of the right hand side and, in the limit of $\omega_{AOM} \ll \omega_{sep}$, the error signal becomes,

$$S_{err} = -\frac{4\pi\omega_{AOM}}{\omega_{sep}} \sin(\psi_0) . \tag{8.8}$$

Equation 8.8 exhibits the same dependence on ψ_0 as for real phase modulation; it equals zero at $\psi_0 = 0$ and is asymmetric in sign either side of zero. It is therefore suitable for locking ψ_0 to zero, or in other words, stabilising the MZI interarm path difference.

8.1.2 Error Signal Characterisation

The interferometer itself was custom made by OzOptics to supplied design specification, while the remaining experiment was setup using standard off the shelf optics. Despite a stated path length difference tolerance of ±0.5 mm, we observed no realistically measurable difference in the positions of maximum sideband transmission or minimum carrier frequency transmission. Characterisation of the error signal is accomplished by perturbing the interferometer and monitoring both the carrier frequency transmission through ports A to D of the MZI, T_{AD}, and the computed residual of the sideband transmission via ports C to B. This perturbation is achieved by simply applying a moderate current to the TEC for a short period of time and allowing the interferometer to drift back towards a state of passive thermal equilibrium. Plotted in figure 8.2 is a short window of the mutual relationship between the two signals. Observed are both a zero value in the error signal as T_{AD} is zero as well as the required sign asymmetry about this point.

It is worthy of noting that, while constructing the MZI setup, care should be taken to ensure equal AOM sideband powers are coupled into the interferometer. Uneven sideband powers will manifest in a narrowing of the locking region and an alteration of the lock point ($S_{err} = 0$). A direct consequence of the latter is the potential for a non-zero value for T_{AD} while the interferometer is locked.

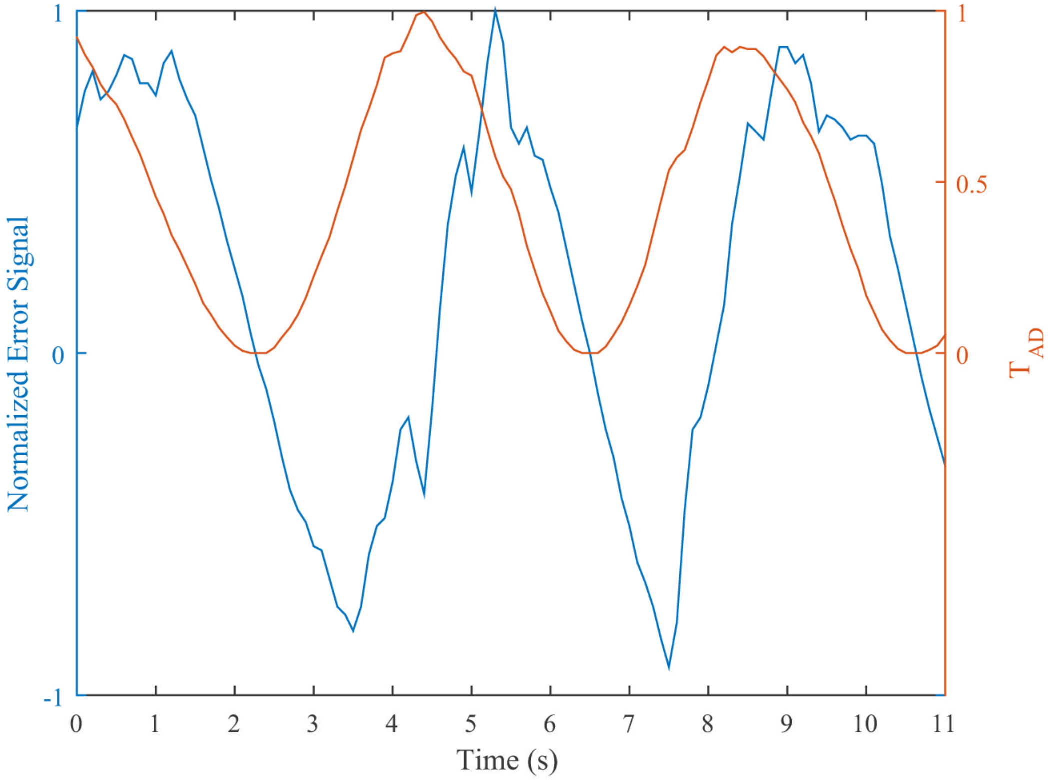

Figure 8.2: Characterisation of the measured error signal and optical carrier signal transmission through the MZI following a small perturbation to the relative path length. The error signal gradient magnitude is proportional to the rate of the change of relative path length.

8.1.3 Carrier Transmission Suppression Analysis

Testing the quality of the lock requires inspection of the carrier transmission over an extended period of time. After an initial time allowed for the interferometer to settle, logging of T_{AD} was started and data was collected over a period in excess of 2 hours while free to drift naturally. The interferometer was then locked to $T_{AD} = 0$ and data for T_{AD} was logged over the same period of time. In figure 8.3 we show the computed FFT of these two signals. Over the period of data acquisition for the locked signal, the average value of T_{AD} was 6.3×10^{-4} corresponding to an extinction of 32.0 dB which is thought to be limited by the response time of the thermal system and the beam alignment to the beam splitter cube. We attribute the lower power spectral density for perturbations faster than 100 mHz to the shallower gradient of the transmission curve for T_{AD} around $T_{AD} = 0$.

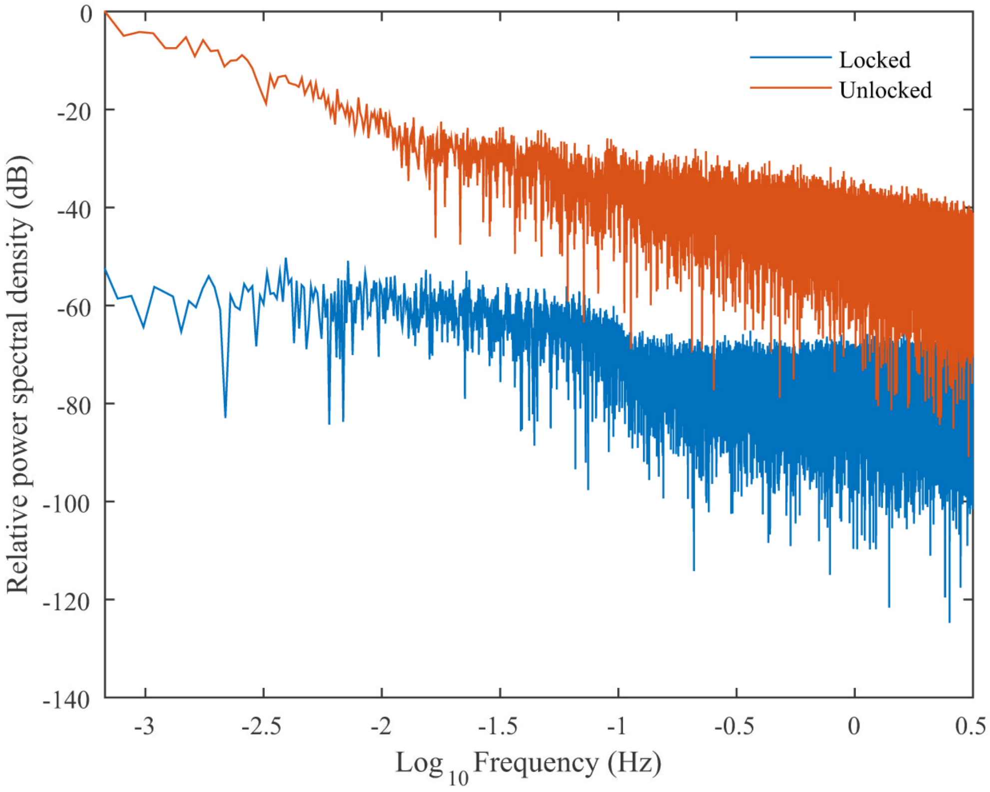

Figure 8.3: Relative power spectral density for T_{AD} around $T_{AD} = 0$ in the locked state and freely drifting in the unlocked state.

In review, while 32 dB of carrier suppression is adequate for our intended purpose, it is possible to improve the interferometric extinction by increasing the top end frequency bandwidth limit of the feedback loop. The microcontroller processing loop time is of the order of 10 ms which is limited by the processing power of the Arduino. In order to reach this upper frequency limit the TEC method of path length adjustment can be replaced by a fiber stretcher [188], though this would necessitate the use of high voltage amplifiers to drive the piezoelectric transducer thereby adding further complexity and cost.

Chapter 9

Intra-Cavity Trace Water Detection

The year 2016 will mark the 350^{th} anniversary since the first demonstration of dispersed sunlight was observed by Newton. With this first optical spectrum, the now immeasurably large field of spectroscopy was born. Over the centuries, spectroscopy has led in one way or another to the discovery of previously unseen parts of the electromagnetic spectrum [189] as well as new matter elements [190]. In terms of precision and accuracy, the field of spectroscopy is rich with techniques for determining the position within the electromagnetic spectrum where a measurable event has occurred. Arguably the latest sub-field of precision spectroscopy to be formed, comes as the result of the invention of the octave spanning frequency comb [191].

The drive towards higher accuracy and precision only forms one half of the story however; the other half is the drive towards high sensitivity [192]. The ability to detect the presence and concentration of some species of interest is of incredible importance in many scientific and technological applications, and it is this principle which forms the basis of this initial work. More specifically, this chapter presents the starting point of a novel, intra-cavity, trace water vapour concentration detection method, which is based on the principles of Frequency Modulation Spectroscopy (FMS). In the context of trace vapour concentration detection, there exists a vast array of highly sensitive spectroscopic techniques to choose from. In the following sections, an abridged review of some of the salient techniques is presented before continuing to outline the principle of this new technique, derive basic cavity reflection lineshape theory and compare against experimental results and finally describe an improved model which forms the essential framework for continuation of this research. It should be noted that this work is far from complete, however the work presented was instrumental in securing a CASE studentship to fund a Ph.D place to continue the research. Between this authors direct involvement and the time of writing this work, a patent application has also been submitted towards securing the intellectual property. Continued research into this project is being conducted with an aim of future miniaturisation and commercialisation of a final product.

In this chapter, the division of work and contribution is as follows. The literature review, experimental setup and acquisition of data and results is solely the work of the author. The theoretical frameworks for the PDH model and the improved transmission based model with AM contribution included is a combined effort by the author and Andrew Chapman. While work towards the FM&AM model was conducted 'by hand' in equal measure by both individuals, the final computerised numerical model was completed by Andrew Chapman. Analysis of the results and their comparisons is the work of the author.

9.1 Review of Literature

9.1.1 Measurement by Direct Absorption

At the most basic level, measuring absorption directly is simply the process of measuring the power of a signal after intereaction with an absorbing sample and comparing it with the known power before the sample. Determination of the absorption coefficient α_{min} (cm^{-1}) in this way is easily understood though the Beer-Lambert law which states that for light traversing a length L through a volume containing an absorbing species, the light intensity will be attenuated by a factor of $e^{-\alpha_{min}L}$, such that,

$$I_l = I_{l0}e^{-\alpha_{min}L}, \tag{9.1}$$

where I_l and I_{l0} are, respectively, the exiting intensity and the incident intensity. The absolute detection limit of direct absorption is that of the shot noise intrinsic to the complete optical and electronic system. This includes effects such as the spontaneous emission in the laser gain medium and the uncertainty in whether an absorption event has actually occurred or not. Assuming that noise associated with the optical signal is reduced to zero, the shot noise limit given in [193] defines the smallest electronically detectable absorption signal as,

$$(\alpha_{min}L) = \left(\frac{2eB}{\eta P_0}\right)^{\frac{1}{2}}, \tag{9.2}$$

where e, B, η and P_0 are the electronic charge, detection bandwidth, detector electronic response (A/W) and incident laser power respectively. In practice failing to achieve, or even approach the shot noise limit is commonplace without extreme care in reducing technical noise in the experimental setup. Noise intrinsic to the detection electronics and radiation source are of primary concern and experimentalists will expend considerable effort to reduce effects such as shot noise in detection electronics and intensity noise in the laser source. One method for accounting for laser intensity noise is to use dual balanced detectors [194] [195]. Initially the laser source will be split into two paths, one containing the sample of interest. The beam traversing the path with no sample contains all noise sources up to the point of detection encoded in it. Dual balanced detectors are therefore used as a common mode noise subtraction method, significantly improving the final SNR and limiting further noise sources to the detection electronics. Care should be taken to ensure that the detectors have suitable bandwidth for detecting the laser intensity noise and that the optical path lengths are equal.

A seemingly obvious improvement to the technique of direct absorption, other than reducing the noise in the system, is to increase the path length over which the incident light field is interacting with the absorbing sample. The use of an optical cavity, as originally proposed by Kastler [193], allows the extension of the optical path length L through the absorbing species by an amount proportional to the cavity finesse, F.

9.1.2 Cavity Enhanced Absorption Spectroscopy

Cavity Enhanced Absorption Spectroscopy (CEAS) [196, 197] is essentially a direct absorption method, where the optical interaction path length is extended by the use of an optical cavity. The presence of the cavity offers two significant advantages. Firstly, the cavity increases the interaction path length by an amount proportional to the cavity finesse and hence alters equation 9.2 by the factor $2F/\pi$, yielding,

$$(\alpha_{min}L) = \left(\frac{2eB}{\eta P_0}\right)^{\frac{1}{2}} \cdot \left(\frac{\pi}{2F}\right). \tag{9.3}$$

The result of the extra factor is an increase in absorption for a given sample density which improves the detection sensitivity. The second aspect is associated with the stored power inside the cavity. The cavity finesse is a function of the mirror reflectivities and of the total intracavity losses. If we assume momentarily that the intracavity absorption is zero, the ratio of circulating intensity inside the cavity and the incident intensity from the laser source may be given as, [112],

$$\frac{I_{circ}}{I_{inc}} \approx \frac{1}{T}, \quad T = t_i^2 \tag{9.4}$$

where t_i is the mirror transmission coefficient and hence T is the mirror power transmission coefficient. If we further assume the mirrors are identical, and transmit only 0.1% of the incident power then the cavity may contain 1 Watt of circulating power for only 1 mW of incident power. This is especially useful for probing very weak absorptions.

Another variation of CEAS is to weakly modulate the laser frequency and employ an electronic servo loop for feeding back to the laser operating current, thus stabilising the laser output and narrowing the laser linewidth. By locking the laser to the cavity resonance via a method such as Pound-Drever-Hall locking [87] and slowly scanning the cavity, one is essentially scanning the laser frequency over the absorbing transition. By ensuring that the cavity scan range far exceeds the absorbing resonance linewidth, the on- and off-resonance absorptions may be determined. Lock-in based demodulation of the detected signal at the cavity modulation frequency yields a dispersion-like signal; the peak-to-peak height of which contains the desired absorption information. A critical aspect of this method however is the gain bandwidth of the locking servo. The laser linewidth must be narrow enough such that the cavity resonance linewidth is at least 2-3 orders of magnitude larger. A high finesse cavity is an excellent frequency discriminating filter and hence if the laser linewidth is of the order of the cavity resonance linewidth, variations in the laser frequency will be efficiently converted to amplitude variations which in turn manifest as intensity noise at the detector.

9.1.3 Frequency Modulation Spectroscopy

Frequency Modulation (FM) is a technique for encoding a sinusoidal waveform onto a stable CW laser which may be recovered later via demodulation. The encoded waveform exhibits an instantaneous frequency difference from that of the carrier frequency which is in direct proportion to the amplitude of the modulation signal. For the purpose of measuring absorption, it is common to assume that the light field one wishes to modulate is purely sinusoidal (ω_0), and that the modulation frequency (ω_m) is also purely sinusoidal, resulting in a relatively simple optical spectrum containing the central carrier frequency and sideband frequencies removed from the carrier frequency by exactly ω_m. The amount of energy from the carrier which is transferred to the sidebands depends on a unitless quantity known as the modulation index (or modulation depth, equation 2.1), $\beta = \Delta\omega/\omega_m$, which theoretically may take any value between 0 and +infinity. In this expression $\Delta\omega$ is the amplitude of the modulation signal, which may be understood as the maximum frequency deviation of the carrier frequency.

The principle advantage of the FM method is that the absorption information from even very weak resonances is encoded into an optical signal at the modulation frequency. In most cases this is a spectral region where little technical noise exists, intrinsically improving the SNR. There exist two generally described domains for modulation of the laser wavelength; Wavelength Modulation (WM) and the aforementioned Frequency Modulation (cf. chapter 2). The former is generally characterised by the modulation index whereby $\beta > 1$ as a result of a large modulation amplitude at low modulation frequencies. Conversely the latter is described by shallow modulation at a high frequency, generating frequency sidebands at greater separations from the carrier frequency than the modulation amplitude. In the WM regime typical values for ω_m are in the tens to a few hundreds of kHz region.

Given in [193], the shot noise limit for sensitivity for FMS is given by,

$$(\alpha_{min}L) = \left(\frac{2eB}{\eta P_0}\right)^{\frac{1}{2}} \cdot \frac{\sqrt{2}}{J_0(\beta)J_1(\beta)}. \tag{9.5}$$

In this equation, $J_i(\beta)$ are, respectively, the zeroth- and first-order Bessel functions of the first kind. The second factor on the right hand side of equation 9.5 actually decreases the theoretical sensitivity of FMS by up to a factor of 4.15 when the denominator, $J_0(\beta)J_1(\beta)$, is maximised (see figure 9.1, $J_0(\beta)J_1(\beta) = 0.34$ when $\beta = 1.08$). While this is the case, it is common to see reported experimental FMS sensitivities superseding those of direct absorption experiments.

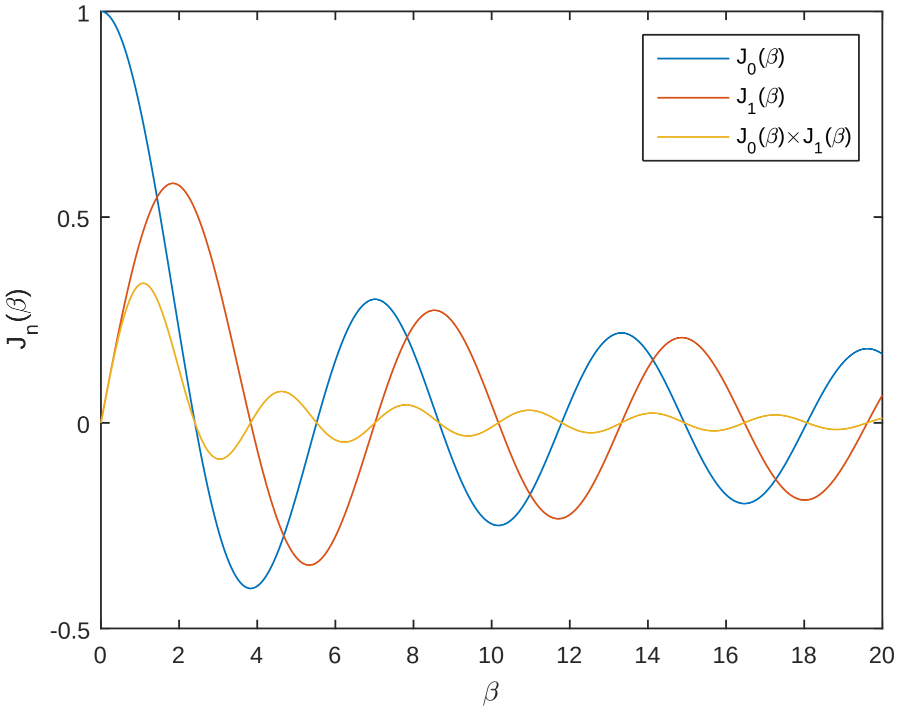

Figure 9.1: Numerical plot showing the magnitude of the first two orders of Bessel functions of the first kind as a function of the modulation depth, β, along with their product over the same range.

9.1.4 Noise-Immune Cavity-Enhanced Optical Heterodyne Molecular Spectroscopy

NICE-OHMS [198] is the amalgamation of two highly successful spectroscopic methods; Cavity Enhanced Absorption Spectroscopy and Frequency Modulation Spectroscopy. NICE-OHMS works by having two modulation tones which are used independently for locking the laser to the high finesse cavity and detection of the absorbing species placed inside the cavity. The 'Noise-Immune' aspect of this technique arises due to the match between the FM modulation frequency and the cavity FSR. By placing the frequency sidebands on the corresponding adjacent axial cavity modes, they are coupled into the cavity in an identical way to the carrier, but also contain identical frequency noise as that of the carrier, and so during phase-sensitive detection the fixed phase relationship between sidebands and carrier allows for the almost complete removal of amplitude modulations caused by the carrier/cavity interaction. In essence, this allows for the presence of the cavity to increase the optical interaction path length while appearing as though the cavity is not present. Where the linewidth of the absorption resonance is typically much broader than the cavity linewidth, the cavity length must be scanned in order to reproduce the entire absorption resonance profile. The detection principle lies in that of the absorbing species altering the intracavity refractive index thereby causing the carrier-frequency axial mode to be phase shifted with respect to the adjacent axial modes. The cavity is monitored to determine the FSR changes due to scanning the cavity length L, and the sideband frequency is tracked to the FSR frequency. Demodulation of the cavity transmission at the FSR frequency generates a dispersion signal due to the beating of the sidebands with the carrier.

Recalling that NICE-OHMS is essentially the combination of two previously discussed methods, for which the shot-noise limited sensitivities in absolute absorption are given by equations 9.3 and 9.5, it is possible to write the shot-noise limited sensitivity for the NICE-OHMS technique as [193],

$$(\alpha_{min}L) = \left(\frac{2eB}{\eta P_0}\right)^{\frac{1}{2}} . \frac{\sqrt{2}}{J_0(\beta)J_1(\beta)} . \left(\frac{\pi}{2F}\right) . \qquad (9.6)$$

9.1.5 Cavity Ring-Down Spectroscopy

Cavity Ring-Down Spectroscopy (CRDS) is a very well established, highly sensitive spectroscopic technique. The founding incarnation of this technique, developed in 1998 by O'Keefe and Deacon [199] utilised a pulsed laser source incident on a high finesse optical cavity, contained within which is the medium of interest. As with other highly sensitive absorption methods, the optical cavity provides an increase in the light-matter interaction path length by an amount proportional to the cavity finesse. Initially a short laser pulse is incident on the cavity, of which an amount enters the cavity in accordance with the reflectivity of the first cavity mirror (typically the mirrors will have reflectivities on the order of 99.99%, resulting in values for the finesse of order 10^5). Upon every round trip of the cavity an amount of light from the pulse is lost to different effects such as Mie and Rayleigh scattering, absorption at the cavity mirrors, absorption from the intracavity media and light coupled out through the mirrors, ultimately leading to an exponential decay in the detected transmitted pulse intensity over time. CRDS is a direct absorption method, however the measurement is performed by determining the rate at which light is absorbed instead of simply the total absorption over a given time. The technique is immune to pulse-to-pulse intensity variations as only the characteristic decay constant is important. The useful absorption information is contained within the ring-down time corresponding to a $1/e$ decay in detected pulse intensity. Comparison of the decay time constants for a cavity with and without an absorbing species present (or more accurately when on and off resonance with the absorbing lineshape) eventually leads to the concentration of the absorber by comparison of the rate of absorption.

Given the plethora of techniques available, table 9.1 aims to give an idea of the achievable values for the measurement of the absorption coefficient across these different techniques.

Author	Technique	Absorption, α_{min} (cm^{-1})
Haller [200]	Balanced Beam Direct Absorption	4.2×10^{-8}
Spence [201]	CRDS	1.0×10^{-12}
Ye [193]	Direct Cavity Transmission	6.4×10^{-13}
Kasyuitch [202]	OFL-FMS	2.1×10^{-11}
Ye [193]	NICE-OHMS	1×10^{-14}
Ma [203]	CE-FMS	1×10^{-14}

Table 9.1: Summary of minimum detectable values for the absorpton coefficient for various ultra-sensitive trace detection techniques.

9.2 Proposed Concept and Relevant Theory

At its foundation, the proposed new spectroscopic method calls upon the principles of intra-cavity FM spectroscopy. The fundamental difference of this method is that where the above methods use the optical cavity as a way of increasing the interaction path length *and* for scanning the central laser frequency over the analyte absorption feature, we instead focus on measuring the properties of the optical cavity itself where we determine the absorption through accurate measurement of the cavity linewidth. From the experimental measurement of the linewidth, the cavity finesse, F, given as,

$$F = \frac{\pi\sqrt{r_1 r_2 e^{-2\alpha_{ic}L}}}{1 - r_1 r_2 e^{-2\alpha_{ic}L}}, \tag{9.7}$$

can be determined and hence the absorption coefficient, α_{ic}, for the intra-cavity losses can be found. Modulation of the DC injection current to a laser diode generates optical sidebands either side of the carrier signal, ω_0, at separations equal to the modulation frequency, ω_m. Information about the optical cavity resonance absorption and dispersion lineshape is encoded onto the frequency modulated beam which may be revealed by subsequent phase sensitive demodulation at ω_m and $2\omega_m$. By sweeping the frequency modulated laser over the cavity resonance and performing the demodulation in-phase (in-quadrature) with ω_m and $2\omega_m$ in real time, absorption (dispersion) lineshapes derived exactly from the cavity resonance can be achieved. It is through this process that we aim to determine the changes in the cavity lineshape - specifically the FWHM linewidth to begin with - and hence determine the analyte absorption.

A crucial advantage intrinsic to the more fully developed system, unlike methods such as NICE-OHMS, is that we intend for the cavity to be stabilised to the line centre of the analyte absorption feature, and for the probing laser to be stabilised to the cavity and on resonance with the analyte absorption. A result of this difference is the reduction is noise originating from the mechanical modulation and tracking of the cavity, and from the constant perturbation of the probing laser.

For the purpose of this initial research, the aim is to derive the basic theory which governs the experimental lineshapes obtained from the interaction of a frequency modulated laser with a Fabry-Perot optical resonator. Through an eventual desire to stabilise the experimental laser to the cavity, we perform the experiment in the cavity reflection regime (rather than transmission) in a manner identical to the Pound-Drever-Hall (PDH) scheme [87, 88]. In the future development of the system, the cavity lineshape measurements will be conducted in the transmission regime while laser stabilisation to the cavity will be derived from the reflection regime. In the following we consider the single frequency emission from a laser which is to be frequency modulated. In actuality, the modulation of the laser drive current imparts the frequency modulation at the source, however the resulting beams are, in the region of small β, identical.

The electric field emitted from a single frequency laser, E_{inc}, oscillating at ω_0 given by,

$$E_{inc}(t) = E_0 e^{i(\omega_0 t + \phi(t))}, \tag{9.8}$$

where E_0 is the field amplitude and $\phi(t)$ is the phase. Because frequency is the rate of change of phase, imparting a sinusoidal modulation to the phase results in modulation of the instantaneous carrier frequency. The form of the modulation signal is given by $\phi(t) = \beta \sin(\omega_m t)$ and hence the incident field becomes,

$$E_{inc}(t) = E_0 e^{i(\omega_0 t + \beta \sin(\omega_m t)))}. \tag{9.9}$$

Where the modulation signal is sinusoidal, using the Jacobi-Anger identity [204] (equation 9.10, where k is any integer) makes possible the expansion of the modulation component of the exponential into a series of Bessel functions of the first kind, $J_k(\beta)$, so that the field becomes (9.11),

$$e^{i\beta\sin(\theta)} = \sum_{k=-\infty}^{\infty} J_k(\beta)e^{ik\theta}, \tag{9.10}$$

$$E_{inc}(t) = E_0 e^{i\omega_0 t} \sum_{k=-\infty}^{\infty} J_k(\beta)e^{ik\omega_m}. \tag{9.11}$$

Under suitably weak frequency modulation of the laser, the infinite sum over the integers k may be reduced to the components pertaining to the carrier frequency and the two first order frequency sidebands, hence $k = -1, 0, 1$ only. With this simplification, and using the Bessel function identity $J_{-k}(\beta) = (-1)^k J_k(\beta)$, the incident field becomes,

$$E_{inc}(t) = E_0\left[-J_1(\beta)e^{i(\omega_0-\omega_m)t} + J_0(\beta)e^{i\omega_0 t} + J_1(\beta)e^{i(\omega_0+\omega_m)t}\right] \tag{9.12}$$

The reflection coefficient of the optical cavity, $R_{cav}(\omega)$, is now introduced such that the total reflected field from the cavity is given by $E_{ref}(t) = R_{cav}(\omega)E_{inc}(t)$. With the spectral properties of the cavity now encoded onto the laser, the beam is directed onto a photodiode. The generated photocurrent is governed by the incident beam intensity, I_{ref}, which is given by $I_{ref} = \frac{1}{2}\epsilon_0 c\,|E_{ref}|^2$. From the expansion of the square modulus of the reflected field we arrive at,

$$\begin{aligned}
I_{ref} = \frac{\epsilon_0 c E_0^2}{2}\Big[& J_0^2(\beta)\big|R_{cav}(\omega_0)\big|^2 + J_1^2(\beta)\big|R_{cav}(\omega_m)\big|^2 + J_1^2(\beta)\big|R_{cav}(-\omega_m)\big|^2 \\
& + 2J_0(\beta)J_1(\beta)\Big[\mathrm{Re}\left(R_{cav}(\omega_0)R^*_{cav}(\omega_m) - R^*_{cav}(\omega_0)R_{cav}(-\omega_m)\right)\cos(\omega_m t) \\
& + \mathrm{Im}\left(R_{cav}(\omega_0)R^*_{cav}(\omega_m) - R^*_{cav}(\omega_0)R_{cav}(-\omega_m)\right)\sin(\omega_m t)\Big] \\
& - 2J_1(\beta)\Big[\mathrm{Re}\left(R_{cav}(-\omega_m)R^*_{cav}(\omega_m)\right)\cos(2\omega_m t) \\
& + \mathrm{Im}\left(R_{cav}(-\omega_m)R^*_{cav}(\omega_m)\right)\sin(2\omega_m t)\Big]\Big].
\end{aligned} \tag{9.13}$$

Inside the large square brackets, the first three terms correspond to the CW carrier, positive sideband and negative sideband optical components respectively. The terms in $\cos(\omega_m t) and \sin(\omega_m t)$ represent the in-phase and in-quadrature beat signals of the individual sidebands against the carrier while the $\cos(2\omega_m t)$ and $\sin(2\omega_m t)$ represent the in-phase and in-quadrature beat signals of one sideband with the other. The superscript asterisk signifies the complex conjugate and R_{cav} is given by [88],

$$R_{cav}(\omega) = \frac{r\left(e^{i\left(\frac{\omega_0}{\omega_{FSR}}\right)-1}\right)}{1 - r^2 e^{i\left(\frac{\omega_0}{\omega_{FSR}}\right)}}, \tag{9.14}$$

where r represents the amplitude reflectivity of the cavity mirrors on the assumption that the two mirrors are identical. The magnitude of the beat signal between each single sideband and the carrier is equal, however there exists a π phase shift between them. If the optical resonance were not present, the resulting beat signal on the photodiode would be zero. As such, the presence of the optical resonance absorption profile acts to alter the magnitude and sign of the beat signals, while the dispersion profile acts to alter the relative phases of the two beat signals, thereby inhibiting the cancellation at the photodiode.

The electronic signal generated at the photodiode, which contains all of the components in equation 9.13, is used as the experimental signal that is to be mixed with the reference signal. The demodulation lineshapes of each beat component in equation 9.13 may be acquired by appropriate choice of the reference signal frequency and phase. Figure 9.2 shows the 4 lineshapes which can be acquired by demodulation, which in order are the ω_m in-phase, ω_m in-quadrature, $2\omega_m$ in-phase and $2\omega_m$ in-quadrature signals. In the literature, these signals are commonly referred to as the '1f in phase', '1f quadrature', '2f in-phase' and '2f quadrature' signals respectively. The reason the modulation signal is chosen as the reference signal is that during demodulation, the lock-in amplifier is sensitive only to frequency components within a very narrow (kHz) band centred at the reference signal and hence it is a very effective way by which to reduce noise on the resulting signal.

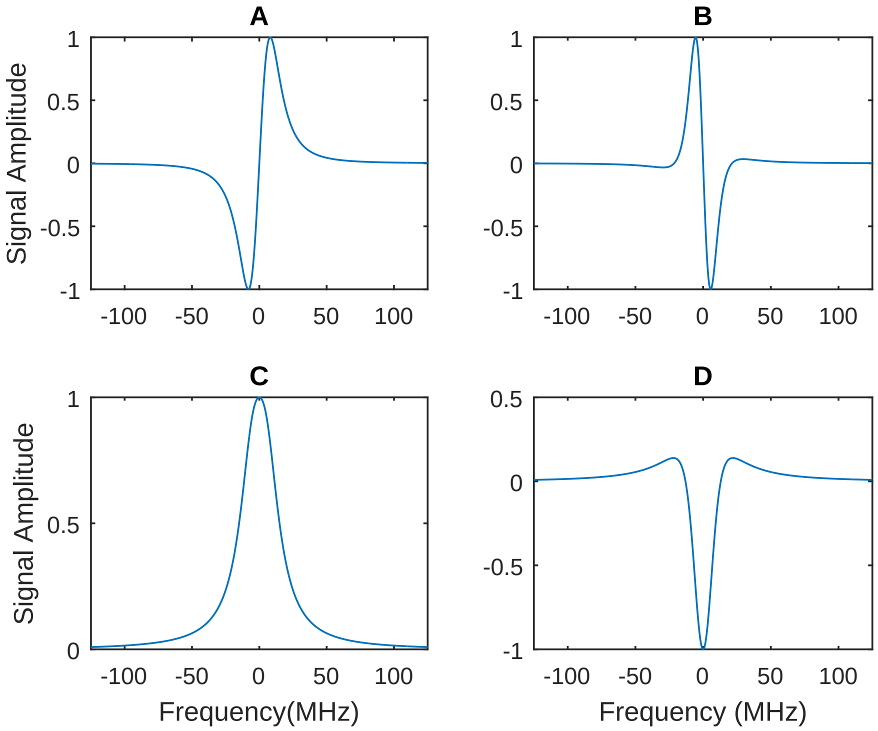

Figure 9.2: Examples of the theoretical demodulation lineshapes given by equation 9.13. For these data, r from equation 9.14 is chosen to be 0.98 which gives an absorption FWHM linewidth of approximately 25 MHz and the value for ω_m is 5 MHz. (A); 1f in-phase, (B); 1f in-quadrature, (C); 2f in-phase, (D); 2f in-quadrature.

The lineshapes given in 9.2(A, B) are the typical lineshapes one requires for laser stabilisation to the optical cavity; between the upper and lower maxima the lineshape is approximately linear, it crosses zero at line centre and has an asymmetric sign about zero. It should be mentioned however that the slope of the absorption signal (A) is modulation frequency dependent and quickly becomes unusable after ω_m is increased about the resonance linewidth FWHM. The dispersion signal however maintains its shape about line centre with the exception of smaller dispersion signals which merge outwards as ω_m is increased. Reference [99] contains an excellent demonstration of the behaviour of the 1f signals as a function of changing modulation frequency. Figures 9.2 C and D show the 2f signals which we ultimately aim to use for determining the shape of the cavity resonance. In the following section the experiment which has been constructed to generate these lineshapes is described and example spectra for the 1f in-phase and 2f-in quadrature signals are presented.

9.3 Experiment and Results

In order to generate the lineshapes predicted by the above theoretical framework, we constructed the experiment depicted schematically in figure 9.3. The laser source is a GaN based, 20 mW diode laser emitting at 405 nm, of which approximately 1.5 mW of laser power is used in total. The diode is integrated into an external cavity identical to that in figure 2.1. Sinusoidal current modulation (TTi TG 2000 function generator) is coupled to the laser through a Bias Tee (Mini-Circuits ZX85-12G+). Spatial filtering of the beam is achieved with a 100 mm plano-convex lens and a 25 μm pinhole before being re-collimated with a 25mm plano-convex lens to achieve a 4 fold reduction in beam diameter to approximately 1 mm. A telescope (not shown) is used to further reduce the beam diameter to approximately 0.5 mm for improved coupling to the FP cavity. The scanning FP cavity has a mirror separation of 5 cm and a Free Spectral Range of 1.5 GHz given by $\frac{c}{4L}$.The measured (FWHM) resonance linewidth is $\sim$ 25.2 MHz thus resulting in a nominal finesse of $\sim$59. By applying a sawtooth modulation signal to a piezo mounted to one cavity mirror, the cavity length may be scanned and hence the resonance frequency is scanned over the laser carrier frequency. The effect is identical to scanning the laser frequency over resonance by current, temperature or grating angle tuning. The cavity reflection is detected with a biased photodiode (Thorlabs DET10A) and amplified by a photodiode amplifier (Femto DHPCA-100, 10^3 V/A gain at 80 MHz bandwidth). Demodulation at ω_m and $2\omega_m$ is achieved using a lock-in amplifier (SRS Model 844). The lock-in amplifier phase locks its own internal stable oscillator to the TTL output of the signal generator from which the laser modulation signal is derived, and it is this phase locked oscillator which provides the reference signal for demodulation. The time constant of the filter applied to the output of the mixers in the lock-in amp are set to 100 μs at 6 dB/Octave. The phase of the reference modulation signal used in the demodulation process is altered manually with respect to the experimental signal to achieve the appropriate waveforms on the oscilloscope. Signal output from the lock-in amplifier is viewed on an oscilloscope which is also the point of data acquisition. It should be noted that in this experiment the contents of the cavity go unaltered. At this very early stage of the research, we simply look to compare the shape and important features of the experimentally obtained signals against the signals generated from the theory. In all of the following numerical and experimental results, the positive peaks for the 1f in-phase, 1f in-quadrature, 2f in-phase, and negative peaks for the 2f in-quadrature have been normalised to unity. While it is not explicitly shown the modulation signal power is that which gives modulation sidebands of approximately 0.1 times the amplitude of the carrier signal, ω_0. A specific power is not given because every laser diode device will have a different modulation response and for the purpose of repeatability, it is only the magnitude of the sidebands that matters rather than the precise modulation power setting used to achieve them.

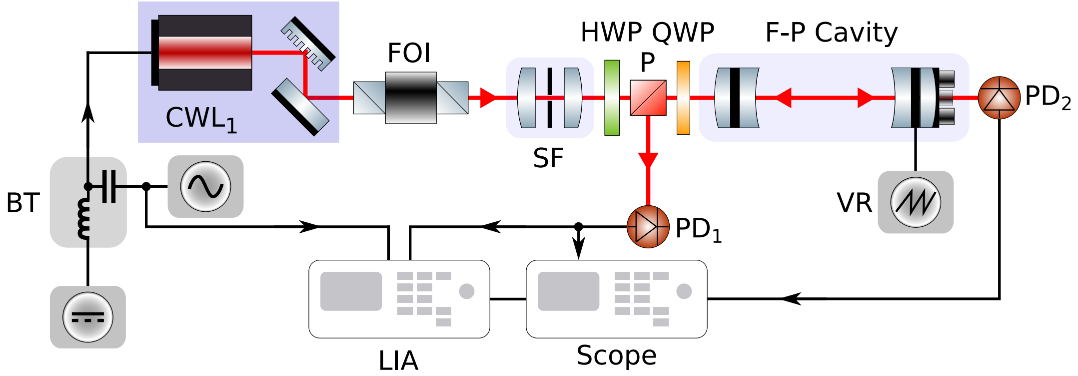

Figure 9.3: Schematic diagram of the optical arrangement for measuring the total back-reflection optical field from the scanning Fabry-Perot cavity. The modulation source to the laser also acts as the demodulation reference for the lock-in amplifier, LIA. The beam is spatially filtered, SF, before the Half Wave Plate, HWP, adjusts the linear polarisation to transmit through the polarising beam splitter cube, P, before being circularly polarised by the Quarter Wave Plate, QWP. The cavity transmission lineshape is measured on Photodiode 2 whereas the cavity reflection is monitored at photodiode 1. The Voltage Ramp generator, VR, scans the piezo attached to the mirror in order to sweep the resonance frequency over apprximatly 3 GHz.

We begin the experimental results by considering the 1f signals. Plotted in figure 9.4 are the in-phase (A) and in-quadrature (B) signals for ω_m= 10 MHz. In each case, the data has been smoothed by a moving gaussian window of width equal to 500 kHz. As predicted from the PDH lineshape theory above, the sign of the gradient changes between the two demodulations and, for the quadrature signal, a very slightly steeper gradient is observed. Something which is not predicted from the PDH theory is the observed unequal relative peak magnitudes. The above PDH theory is based on pure frequency modulation. While this is an acceptable assumption to first order, especially so for very weak current modulation of the laser diode, in actual fact the modulation of the laser diode injection current simultaneously modulates both the instantaneous carrier frequency and the laser output power, the latter of which results in amplitude modulation sidebands which are superimposed upon the FM sidebands. It has been reported that the frequency dependent ratio of AM modulation index to the FM modulation index is as low as 200:1 for modulation frequencies below 20 MHz [205], making the AM contribution essentially negligible. We therefore attribute the significant peak magnitude difference in figure 9.4 to background noise in the measurement. It is possible also that, through the manual process of choosing the optimum phase angle of the reference demodulation signal, the wrong angle was chosen, resulting in quite strong distortion of the experimental lineshape.

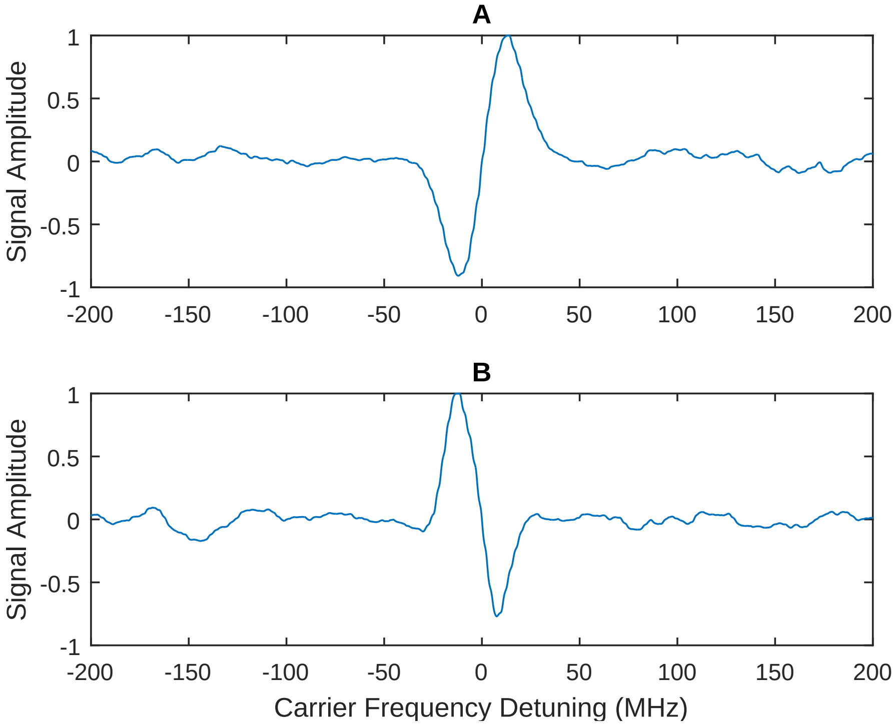

Figure 9.4: Example experimental data for the demodulated cavity reflection signal showing the in-phase (absorption) lineshape, (A), and the in-quadrature (dispersion) lineshape, (B). The detuning refers to the relative position of ω_0 from the centre of the cavity resonance. The value of ω_m is 10 MHz

Plotted in figure 9.5 is a series of 4 1f in-phase demodulation signals. In this figure, plots A-D represent ω_m=5, 10, 15 and 20 MHz respectively, with a cavity FWHM linewidth of 25 MHz.

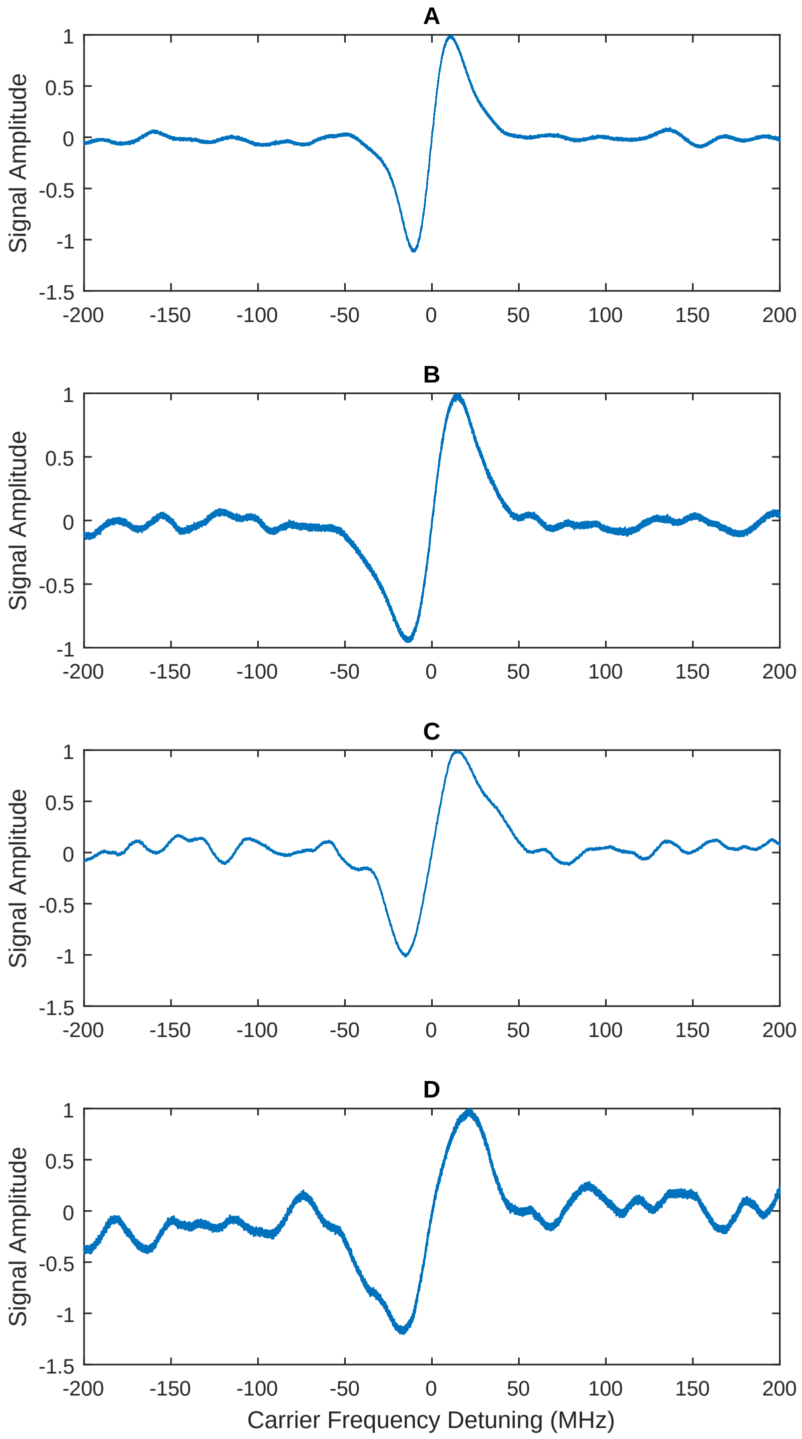

Figure 9.5: Example data for the evolution of the 1f in-phase (absorption) demodulation lineshape as a function of increasing modulation frequency. (A-D) refer to ω_m=5, 10, 15 and 20 MHz respectively. In each case the positive peak amplitude has been normalised to unity.

As predicted by the FM theory derived above and in reference [99], the gradient at the central zero crossing begins to drop as the modulation frequency is increased. This occurs because the frequency sidebands start to interact with the resonance absorption lineshape at larger carrier frequency detunings from the resonance centre. The larger overall frequency range of interaction results in a smearing out of the 1f in-phase lineshape. In any case, provided ω_m does not exceed the resonance FWHM frequency, the slope of the 1f in-quadrature signal essentially approximates a linear slope around zero detuning. A potentially useful aspect of using the in-phase signal for locking the laser to the cavity is that this signal provides a greater locking range than the quadrature signal, albeit at the expense of the quality of the lock, due to the larger frequency spacing between the peaks.

Consider now the 2f quadrature signals for the same modulation frequencies (5, 10, 15 and 20 MHz). Likewise with the 1f signals, at this stage we are not concerned with the precise magnitude of the centre-most feature. Instead we are concerned with the behaviour of the relative magnitudes of the various peaks and the separation of the y-axis equals zero points. The first point to note is the consistent uneven signal amplitude for the two positive peaks. These peaks effectively represent the magnitudes of the positive gradients of the 1f quadrature signal. Their unequal amplitude is attributed, as before, to the presence of the amplitude modulation in the optical signal. The ratio of the two peak heights to the central trough depth also approaches 1:1 as the modulation frequency is increased. This is an unexpected behaviour from an intuitive perspective because, from figure 9.2(B), the dispersion lineshape of the cavity has the greatest magnitude difference at the two Half Width Half Maximum points. As such it would be expected that the magnitude of the central feature would be largest when the modulation frequency approaches the resonance FWHM frequency. The apparent broadening of the 2f lineshape is attributed to the same smearing effect as described for the 1f signals. It is envisaged that, through further research, this effect in combination with the effect observed for the ratio of the maximum peak amplitudes could be precisely characterised for the purpose of determining the precise cavity resonance lineshape, and hence reach our goal of determining the cavity finesse.

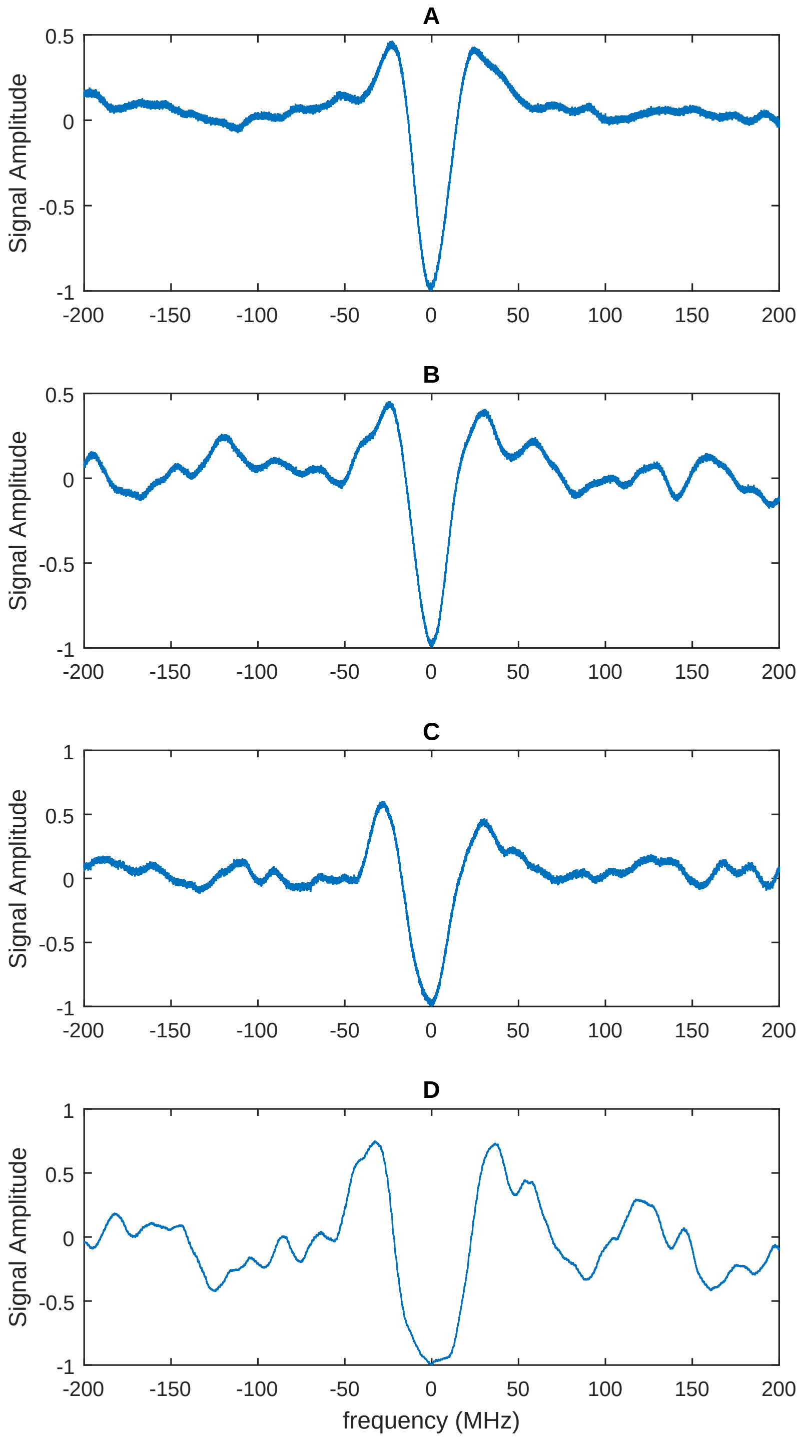

Figure 9.6: Example data for the evolution of the 2f in-quadrature (dispersion) demodulation lineshape as a function of increasing modulation frequency. (A-D) refer to ω_m=5, 10, 15 and 20 MHz respectively. In each case the negative peak amplitude has been normalised to unity.

9.4 Combined FM & AM Model

In light of the above, where we have demonstrated the ability in achieving experimental 1f and 2f signals in the cavity reflection (PDH) regime, and considering that the above numerical model is only capable of predicting the pure FM demodulation lineshapes, this final section is devoted to the derivation of a new model which both incorporates the AM component and aims to predict the cavity lineshapes in the transmission regime. We begin with the transmitted electric field after interaction with the cavity given by,

$$E_{trans}(t) = E_0(1 + M\sin(\omega_m t + \psi)) \sum_{k=-\infty}^{\infty} T(\omega) J_n(\beta) e^{i(\omega_0 + k\omega_m)t}, \tag{9.15}$$

where the Jacobi-Anger identity has already been incorporated. Here, M is the AM index, ψ is the relative phase difference between the AM and FM contributions, and $T(\omega)$ is the transmission function of the cavity. The transmission function provides the mathematical infrastructure for the future addition of the analyte into the cavity. By converting the sinusoidal component of the AM contribution to exponential format and multiplying the entire expression by its complex conjugate, the optical intensity may be written as,

$$\begin{aligned} I_{trans}(t) = \frac{\epsilon_0 c E_0^2}{2} & \left[1 + M\left(\frac{e^{i(\omega_m t+\psi)} - e^{-i(\omega_m t+\psi)}}{2i}\right)\right] \times \\ & \left[1 - M\left(\frac{e^{-i(\omega_m t+\psi)} - e^{i(\omega_m t+\psi)}}{2i}\right)\right] \times \\ & \sum_{k=-\infty}^{\infty} \sum_{l=-\infty}^{\infty} T_k(\omega) T_l^*(\omega) J_k(\beta) J_l(\beta) e^{i(k-l)\omega_m t}. \end{aligned} \tag{9.16}$$

Here, while k and l may represent any integer, we limit their values to $-1, 0, 1$ to indicate that only the first order sidebands are present for small β and small M. By multiplying out the AM terms and summing over all combinations of k and l we arrive at the following intensity,

$$
\begin{aligned}
I_{trans}(t) = \frac{\epsilon_0 c E_0^2}{2}\Bigg[&\left(1+\frac{M^2}{2}\right) + Mi\left(e^{-i(\omega_m t+\psi)} - e^{i(\omega_m t+\psi)}\right) \\
&- \frac{M^2}{4}\left(e^{2i(\omega_m t+\psi)} + e^{-2i(\omega_m t+\psi)}\right)\Bigg]A_{kl},
\end{aligned} \tag{9.17}
$$

where the FM components are given by,

$$
\begin{aligned}
A_{kl} = \Big[&T_0 T_0^* J_0^2(\beta) + T_{-1}T_{-1}^* J_1^2(\beta) + T_1 T_1^* J_1^2(\beta) \\
&- T_0 T_1^* J_0(\beta) J_1(\beta) e^{i\omega_m t} + T_0 T_1^* J_0(\beta) J_1(\beta) e^{-i\omega_m t} - T_{-1} T_0^* J_0(\beta) J_1(\beta) e^{-i\omega_m t} \\
&- T_{-1} T_1^* J_1^2(\beta) e^{-i2\omega_m t} + T_1 T_0^* J_0(\beta) J_1(\beta) e^{i\omega_m t} - T_1 T_{-1}^* J_1^2(\beta) e^{i2\omega_m t}\Big].
\end{aligned} \tag{9.18}
$$

In equation 9.18, the T_k subscript notation refers to the transmission function profile at the frequency, $\omega_0 + k\omega_m$. The first three terms are the DC components of the carrier frequency, and negative and positive sidebands respectively. After some incredibly tiresome rearranging, we arrive at the real and imaginary parts of the 2f signal given, respectively, by,

$$
\begin{aligned}
2f_{IP} = \epsilon_0 c E_0^2 \times \mathrm{Re}\Bigg[& - T_1 T_{-1}^* J_1^2(\beta) - \frac{M^2}{4} T_0 T_0^* J_0(\beta) e^{2i\psi} + \\
& Mie^{i\psi}\Big[T_0 T_{-1}^* J_0(\beta) J_1(\beta) - T_1 T_0^* J_0(\beta) J_1(\beta)\Big]\Bigg] \cos(2\omega_m t),
\end{aligned} \tag{9.19}
$$

$$
\begin{aligned}
2f_{IQ} = \epsilon_0 c E_0^2 \times \mathrm{Im}\Bigg[& - T_1 T_{-1}^* J_1^2(\beta) - \frac{M^2}{4} T_0 T_0^* J_0(\beta) e^{2i\psi} + \\
& Mie^{i\psi}\Big[T_0 T_{-1}^* J_0(\beta) J_1(\beta) - T_1 T_0^* J_0(\beta) J_1(\beta)\Big]\Bigg] \sin(2\omega_m t).
\end{aligned} \tag{9.20}
$$

These expressions represent the in-phase and quadrature beat components at $2\omega_m$, after transmission through the optical cavity, and without loss of generality in terms of the relative modulation indices. The transmission function is given in general terms as $T = e^{-\delta(\omega)+i\phi(\omega)}$, where δ and ϕ are expressions for the frequency dependent resonance absorption and dispersion respectively. The cavity absorption lineshape, for the purposes of the following calculations is assumed to be Lorentzian. Plotted in figure 9.7 are direct comparisons between the theoretical 2f quadrature signal (equation 9.19) and the previously acquired data for the same signal (figure 9.6). While the physical regime for which the signals are derived differ for this experimental and theoretical comparison - the experimental data was acquired in the cavity reflection regime whereas the theoretical data is calculated for the cavity transmission regime - the functional forms of the signals in each case are identical.

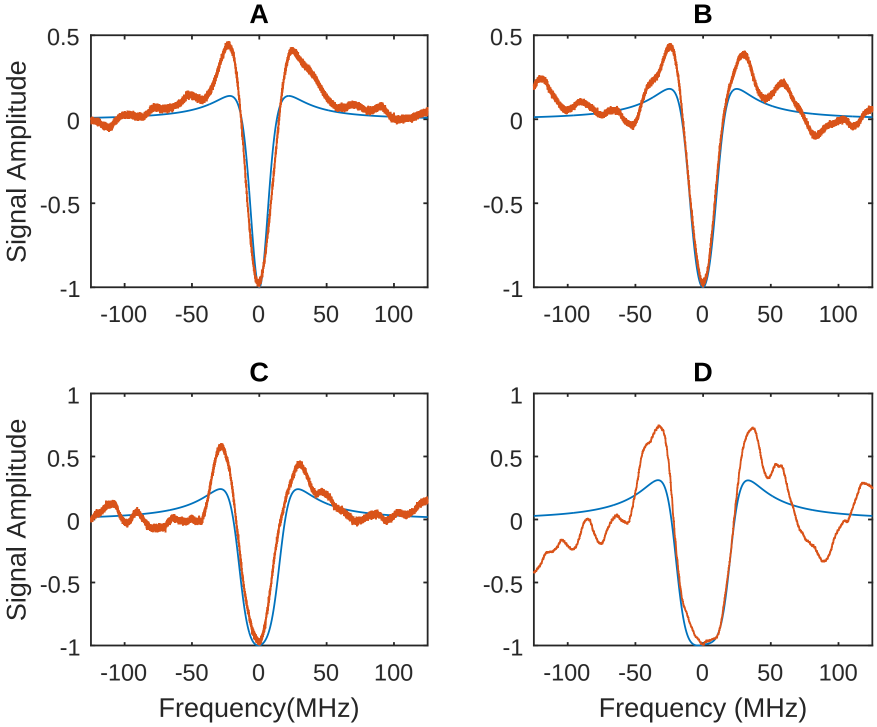

Figure 9.7: Comparison of the theoretical (blue) and experimental (red) 2f quadrature demodulation lineshapes as a function of increasing modulation frequency. The theoretical curves are derived from equation 9.20 in the cavity transmission regime whereas the experimental data is the demodulated reflection signal from the cavity. Figures A - D represent ω_m=5, 10, 15 and 20 MHz respectively.

The first point to note is the mismatch of the peak amplitude between the two positive experimental and theoretical peaks either side of line centre. We acknowledge that while the noise background is not predicted numerically, it's magnitude in the experimental data does not appear significant enough to justify the positive peak amplitude mismatch. The frequency detuning of these peaks from resonance is well predicted by the theory however. Also observed is a good match between the theory and experiment in terms of the zero amplitude crossing point in all 4 cases, notwithstanding the significant increase in the background noise as the modulation frequency increases. Interestingly also, the presence of the AM terms in the 2f quadrature signal appear to predict the noticeable central peak shape distortion around zero detuning in figure 9.7(D). The AM index, while being held constant for all four numerical plots, clearly begins to have a stronger effect as ω_m is increased, acting to shift the position of minimum signal amplitude towards a very small negative detuning and gives rise to the observed asymmetry.

Finally, while the scale of the effect is very small in these numerical plots, the maximum amplitudes of the two positive peaks is predicted by the model to be unequal. For the chosen AM index value of M=0.0005 (cf. β=0.1), the peak amplitude difference for ω_m= 20 MHz is only 0.005%, in favour of a lower amplitude for the positively detuned peak. It is likely therefore that, given the clear imbalance in the experimental data, the FM to AM ratio for this specific laser device is considerably closer to 1:1 than we predict in the numerical model.

The next logical progression for this research would certainly be to reconcile the large mismatch in the positive peaks between the theoretical prediction and the experimental results. Following this, considerable progress could be made towards commercialisation if a comprehensive characterisation of the intra-cavity losses could be conducted, along with complete investigation of the effects observed for varying ω_m for a given cavity resonance lineshape. It is envisaged that under full time research this project could quickly become a working prototype, albeit with optics, cavity mirrors and a laser source tailored towards a wavelength that is much more strongly absorbed by water vapour.

Chapter 10

Conclusions and Future Work

The underlying motivation for the work in this thesis was the development of a coherent, broad bandwidth, stable frequency comb which spans approximately 1 nm and which encompasses the D2 line of Rubidium. The laser sources used for the atomic physics experiments within the group use multiple laser sources which require long term stabilisation near, and far from, single photon resonances. In the current state the MOT lasers are stabilised individually to a Rb vapour cell via separate spectroscopy setups, while the Raman lasers are manually detuned to approximately 10 GHz where they are left free running. It is desirable therefore to provide a stable optical reference for both sets of lasers, onto which the experimental lasers can be stabilised at arbitrary positions up to 100 GHz from the nearest single photon resonance.

To this end, active mode-locking of a commercially available laser diode around a 3 GHz repetition rate was attempted in an external cavity. Initial characterisation shows that the proportion of the modulation current reaching the diode is very small and hence the optical modulation response is considerably weaker than desired. Measurement of the back-reflected modulation power revealed that around 40% of the power is reflected, thereby justifying an attempt at impedance matching the transmission line to the laser diode via a bespoke RF stub based on the microstrip transmission line principle. Thermal characterisation revealed that the stub was heating up through absorption of the incident RF laser modulation signal and no improvement in the laser diode modulation performance was observed. It is highly likely that this is due to the stub's dielectric material. We therefore conclude that using a substrate material which has been specifically designed for RF modulation, such as RT/Duroid 6035HTC from Rogers Corporation [206], may be effective in demonstrating an improvement in the laser diode modulation.

Investigation progressed onto characterisation of the mode-locking performance by way of consideration of the temporal pulse shape via intensity autocorrelation, and spectral content via the RF spectrum and optical spectrum. Approximately 21 ps pulses were observed with a corresponding optical spectrum spanning at least 1 nm. This spectral coverage easily fulfils the comb bandwidth requirements set out by the desired frequency detuning of the above mentioned Raman beams. Characterisation of the optimum mode-locking conditions in terms of the adjustable experimental parameters was also given along with discussion as to their relative importance. We conclude that the temperature has a negligible effect on the pulse width over a 5°C range unless operating close to the threshold current. The operating DC injection current is considerably more important and an optimum value of approximately 80% of the threshold current was determined. The modulation signal power is also important, however data shows that above a certain threshold power (at constant DC current), the pulse width observes only a small degree of temporal shortening as modulation power increases. It is suspected that device parasitic effects are to blame as the increase in modulation power above this apparent threshold does not cause significant improvement in the pulse width. By far the most sensitive parameter is the modulation frequency. Negative detuning by more than approximately 5 MHz causes a sharp increase in the pulse width and a collapse of the broad optical spectrum, whereas positive detuning causes the pulses to broaden vastly slower while broadening the optical spectrum. The time bandwidth product then respectively resembles a laser operating in CW and a very poorly mode-locked laser, where, for large positive detuning, the time bandwidth product reaches nearly 50; approximately 100 times the Fourier transform limit.

At best, the time bandwidth product was 13.41 and hence the pulses are far from the transform limit. Though not documented, optical pulse compression of the pulses was attempted. No evidence of compression was achieved and it was tentatively concluded that mode-locking in clusters was the reason.

Analysis of the RF spectrum for the mode-locked laser revealed a comb of modes up to the bandwidth limit of the RF spectrum analyser. While very encouraging, no solid evidence to suggest the mode-locked laser emission resembled that of a frequency comb was yet acquired. To this end the air track interferometer was constructed. Employing the rubidium stabilised CW ECDL demonstrated in chapter 2 as a reference, the recorded CW and mode-locked laser interferograms were processed to correct for mirror velocity variations and Fourier transformed to give the optical power spectrum. These spectra demonstrated the comb-like nature of the optical spectrum with a resolution limit of 794 MHz. A number of improvements are suggested for this work, including larger computational resources, mechanical actuators for the initial impulse and either lighter gas line tubing or an alternative gas delivery approach. All of these are purely technical limitations and are therefore not insurmountable.

Injection locking was attempted as a way of anchoring an individual frequency comb mode to another laser which could be stabilised to Rb, thereby demonstrating that the stability criteria of the initial objective could be met. For the sake of expedience, the CW (master in this context) laser was free running to allow for quick tunability and for testing the bandwidth over which injection locking could be achieved. Using the heterodyne detection scheme, coherence between the injected mode and the rest of the frequency comb was shown to be successfully transferred by the active modulation process across at least 12 comb modes. This indicates that there is at least 18 GHz of phase coherent spectrum either side of the injected mode. With access to a faster photodiode and, ideally, an RF amplifier of similar bandwidth, a larger bandwidth could be investigated for determining the extent of the phase coherence.

With the mode-locked laser successfully injection locked to the CW master laser, the quality of the resulting pulses improved dramatically. While the pulse width observed a marginal increase of up to 18%, the degree of side-mode suppression on the optical spectrum resulted in the time bandwidth product reducing to as low as 1.44, or 3.27 times the Fourier transform limit. Unfortunately this also resulted in the spectral width of the comb decreasing to below 100 GHz which, while still usable, is below our target comb bandwidth. This investigation does however highlight a possible middle ground for future development of the system. The mode-locking in clusters regime is caused by the combination of weak modulation and imperfect AR coating on the front diode facet. It is not unforeseeable that the etalon used for wavelength tuning could be optically coated to improve its finesse, thereby acting as a bandwidth limiting device as well. If this bandwidth were still broad compared to the monolithic cavity mode spacing, but narrow compared to its FSR, the modulation signal could have its influence limited to perhaps only 3-4 monolithic cavity modes worth of spectral bandwidth. It is suggested therefore that the active modulation perhaps could then couple these clusters of modes together achieving a result much closer to the desired comb bandwidth, but while also maintaining optical pulses far closer to the transform limit. In any case, the evidence provided by the degree of sidemode suppression strongly supports the notion that the laser is operating in a clustered mode-locking regime. Alternatively, and as part of any ongoing investigation, it would be beneficial to attempt to integrate a saturable absorber mirror into the external cavity. This would still maintain the requirement for active modulation so as to have an electronically derived repetition rate and mode spacing, while relinquishing the bulk of the pulse shaping to the saturable absorber.

Returning to the heterodyne detection scheme, the injection locking chapter closed with results indicating that for 9.8 μW of master laser power the bandwidth for which injection locking was established was approximately 370 MHz. It was also shown that the locking range increased with master laser power, as predicted by relevant literature and that for master laser powers below 3.9 μW the injection locking detuning region is shown to be asymmetric in favour of a larger red detuned range.

In the frequency comb analysis chapter the beat note spectrum between the frequency comb and a (now slave) CW ECDL was shown to consist of multiple peaks whose origin, unfortunately, has eluded identification. We propose that the system would need to be calibrated along side a characterised, narrow linewidth laser source. The confusion as to the origin of these additional peaks is enhanced after observation of the RF spectrum of both the CW ECDL and the frequency comb. While the CW laser was shown to exhibit some unusual signals periodically with increasing DC injection current, these did not explain the features observed when beating against the frequency comb. Furthermore, with solely the frequency comb being viewed on the RF spectrum, no features of the magnitude or position observed in figure 7.2 were present.

The in-house made OPLL circuit was shown to be effective at stabilising one CW laser to another and, where electronic feedback was used in conjunction with grating angle feedback (via the piezo drive voltage), the beat note linewidth was reduced by nearly a factor of 2. We propose that the resulting beatnote linewidth would improve were it not for the bandwidth bottleneck imposed by the current controller modulation input. Finally a series of CW-CW beat note RF measurements were taken when two CW slave lasers were phase locked to the frequency comb. Over short sweep times the linewidth of the beatnote appears narrow (approximately 174 kHz for the individual lasers) which broadens significantly as the RF sweep time is increased. While it is proposed that mechanical noise due to lack of isolation is to blame, it would be insightful to fully characterise the OPLL circuit response before any investigation into mechanical noise sources is conducted.

Shifting away from the frequency comb, we have also demonstrated the path length stabilisation of a fibre Mach-Zehnder interferometer for carrier frequency removal from a phase modulated laser source. Remaining stably locked for approximately 2 - 3 hours, the system displayed 32 dB of carrier frequency suppression, limited by the bandwidth of the feedback servo system. We propose that to improve this suppression, the TEC element should be replaced with a fibre stretcher, though this would come at considerably greater cost.

Initial research into a novel intra-cavity trace water vapour detection concept shows definite promise as a successful future technique. The basic starting lineshapes are as predicted by the Pound-Drever-Hall model, and improvements to the theoretical description begin to predict the change in lineshape for the corresponding changes in modulation frequency. Future work on this project would involve complete spectral characterisation of the cavity and incorporation of the analyte absorption and dispersion properties into the transmission function. Further, by switching from a macroscopic cavity to whispering gallery mode resonators (so as to miniaturise the cavity) the door to precisely tailorable and low cost cavities is opened, which would be desirable from a future commercialisation standpoint.

It is regrettable that, due to time constraints, more effort could not be spent investigating the frequency comb Vernier (mode-identification) concept. While that is the case, a second mode-locked laser was constructed to be a carbon copy of the first and a very early results for the RF frequency comb are given in appendix C. We have nevertheless demonstrated in this thesis the building blocks required to investigate this concept further. It is foreseeable that, with two mode-locked lasers a reality, CW injection locking from a Rubidium stabilised master laser could be very effectively used to anchor two common frequency comb modes to the same frequency and hence generate a working prototype of this concept in perhaps only 3 - 6 months. Finally, with the Vernier scale a reality, very little modification could be employed in order to produce the first demonstration of dual frequency comb spectroscopy [207] with mode-locked diode lasers.

Appendix A

Actively Mode-Locked Diode Laser Rate Equations

Here the rate equations which can be used to describe the dynamic operation of semiconductor diode lasers are derived. These coupled rate equations describe the transient behaviour of the laser gain medium and optical emission through the time dependent evolution of the electric field, E, and the charge carrier number, N, and are arrived at through the semiclassical laser theory original described by Haken [31] and Lamb [32]. The presented derivation closely follows those presented by Tartwijk and Lenstra [36], Agrawal and Dutta [38] and Ohtsubo [35].

A.1 Coupled Rate Equations

The derivation of the rate equation for the electric field begins with Maxwell's equations where we derive the basic wave equation for electromagnetic field propagation in a dielectric and the complex dielectric function which provides the framework for the laser gain and loss. From here we continue towards obtaining the complex propagation constant before defining the relationship between example forward and backward travelling electric fields. From these fields the threshold gain and the allowed cavity modes are found which provides the starting condition for reaching the electric field rate equation.

A.1.1 The Field Equation

Maxwell's Equations govern the propagation of an electric field in a dielectric and are given by [208],

$$\boldsymbol{\nabla} \cdot \boldsymbol{\mathcal{D}} = \rho_f \tag{A.1a}$$

$$\boldsymbol{\nabla} \cdot \boldsymbol{\mathcal{B}} = 0 \tag{A.1b}$$

$$\boldsymbol{\nabla} \times \boldsymbol{\mathcal{E}} = -\frac{\partial \boldsymbol{\mathcal{B}}}{\partial t} \tag{A.1c}$$

$$\boldsymbol{\nabla} \times \boldsymbol{\mathcal{H}} = \boldsymbol{\mathcal{J}} + \frac{\partial \boldsymbol{\mathcal{D}}}{\partial t} \tag{A.1d}$$

where, for a dielectric, non-magnetic medium the constitutive equations are given by,

$$\boldsymbol{\mathcal{D}} = \epsilon_0 \boldsymbol{\mathcal{E}} + \boldsymbol{\mathcal{P}} \tag{A.2a}$$

$$\boldsymbol{\mathcal{B}} = \mu_0 \boldsymbol{\mathcal{H}} \tag{A.2b}$$

and from Ohm's law, where σ is the material conductivity,

$$\boldsymbol{\mathcal{J}} = \sigma \boldsymbol{\mathcal{E}}. \tag{A.3}$$

In the above equations, $\boldsymbol{\mathcal{D}}$ is the electric diaplcement vector, $\boldsymbol{\mathcal{B}}$ is the magnetic induction vector, $\boldsymbol{\mathcal{E}}$ is the electric field vector, $\boldsymbol{\mathcal{H}}$ is the magnetic field vector, $\boldsymbol{\mathcal{P}}$ is the density of the induced dipole moments, which, macroscopically, is referred to as the Polarisation vector and $\boldsymbol{\mathcal{J}}$ is the current density vector. In terms of scalar identities, ρ_f, ϵ_0 and μ_0 are the free charge density, the permittivity of free space and the permeability of free space respectively.

From the above, we first take the curl of A.1c, then substitute for equation A.2b, A.1d, A.3 and A.2a, and finally using the vector identity,

$$\boldsymbol{\nabla} \times (\boldsymbol{\nabla} \times \boldsymbol{\mathcal{A}}) = \boldsymbol{\nabla} (\boldsymbol{\nabla} \cdot \boldsymbol{\mathcal{A}}) - \nabla^2 \boldsymbol{\mathcal{A}}, \tag{A.4}$$

where $\boldsymbol{\mathcal{A}}$ is any vector of space, we can achieve the expression,

$$\nabla^2\boldsymbol{\mathcal{E}} - \boldsymbol{\nabla}\left(\boldsymbol{\nabla}\cdot\boldsymbol{\mathcal{E}}\right) - \frac{1}{c^2}\frac{\partial^2\boldsymbol{\mathcal{E}}}{\partial t^2} - \frac{\sigma}{\epsilon_0 c^2}\frac{\partial\boldsymbol{\mathcal{E}}}{\partial t} = \frac{1}{\epsilon_0 c^2}\frac{\partial^2\boldsymbol{\mathcal{P}}}{\partial t^2}. \tag{A.5}$$

The term, $\boldsymbol{\nabla}\left(\boldsymbol{\nabla}\cdot\boldsymbol{\mathcal{E}}\right) = 0$, may be neglected on the assumption that there are no free charges, and using the expression $c = \frac{1}{\sqrt{\mu_0\epsilon_0}}$ results in the following wave equation,

$$\nabla^2\boldsymbol{\mathcal{E}} - \frac{1}{c^2}\frac{\partial^2\boldsymbol{\mathcal{E}}}{\partial t^2} - \frac{\sigma}{\epsilon_0 c^2}\frac{\partial\boldsymbol{\mathcal{E}}}{\partial t} = \frac{1}{\epsilon_0 c^2}\frac{\partial^2\boldsymbol{\mathcal{P}}}{\partial t^2}. \tag{A.6}$$

Following substitution of example sinusoidal fields for $\boldsymbol{\mathcal{E}}$ and $\boldsymbol{\mathcal{P}}$ given by,

$$\boldsymbol{\mathcal{E}}\left(x,y,z,t\right) = \frac{1}{2}\left[\boldsymbol{E}\left(x,y,z\right)e^{i\left(k_0 z+\omega t\right)} + c.c.\right] \equiv \boldsymbol{Re}\left[\boldsymbol{E}\left(x,y,z\right)e^{i\left(k_0 z+\omega t\right)}\right] \tag{A.7a}$$

$$\boldsymbol{\mathcal{P}}\left(x,y,z,t\right) = \frac{1}{2}\left[\boldsymbol{P}\left(x,y,z\right)e^{i\left(k_0 z+\omega t\right)} + c.c.\right] \equiv \boldsymbol{Re}\left[\boldsymbol{P}\left(x,y,z\right)e^{i\left(k_0 z+\omega t\right)}\right] \tag{A.7b}$$

equation A.6 now reads,

$$\nabla^2\boldsymbol{E} + \frac{\omega^2}{c^2}\left[1 - \frac{i\sigma}{\epsilon_0\omega}\right]\boldsymbol{E} = -\frac{\omega^2}{\epsilon_0 c^2}\boldsymbol{P}, \tag{A.8}$$

where $\boldsymbol{E}$ and $\boldsymbol{P}$ are the field amplitudes and *c.c.* represents the complex conjugate. In the context of an electric field inside a dielectric, the degree of the polarisation response of the material to the *total* field is determined by the (complex) frequency dependent electric susceptibility, $\chi(\omega)$. In equation A.9 $\boldsymbol{E}$ is the total field, which must take into account not only the applied field, but also the resulting field from the induced material polarisation. The larger the susceptibility the easier it is for the material to be polarised by the applied field and hence the weaker the penetration of the applied field into the material. The complex susceptibility is related to $\boldsymbol{E}$ and $\boldsymbol{P}$ by the following expression,

$$\boldsymbol{P} = \epsilon_0\chi\left(\omega\right)\boldsymbol{E}, \tag{A.9}$$

where, in the following relationship, single and double primes are the real and imaginary parts, and the subscripts 'bg' and 'p' indicate the background (unpumped) and pumped (by charge injection in the case of the semiconductor laser) components, respectively,

$$\chi\left(\omega\right) = \chi'_{bg}\left(\omega\right) - i\chi''_{bg}\left(\omega\right) + \chi'_{p}\left(\omega\right) - i\chi''_{p}\left(\omega\right). \tag{A.10}$$

Following substitution of equation A.9 into equation A.11, we arrive at the wave equation,

$$\nabla^2 \boldsymbol{E} + \epsilon\left(\omega\right) k_0^2 \boldsymbol{E} = 0. \tag{A.11}$$

where,

$$k_0 = \frac{\omega}{c}, \tag{A.12a}$$

$$\epsilon\left(\omega\right) = \epsilon'\left(\omega\right) + i\epsilon''\left(\omega\right) = \epsilon_{bg}\left(\omega\right) + \chi'_{p}\left(\omega\right) - i\left[\chi''_{bg}\left(\omega\right) + \chi''_{p}\left(\omega\right) + \frac{\sigma}{\epsilon_0\omega}\right], \tag{A.12b}$$

$$\epsilon_{bg}\left(\omega\right) = 1 + \chi'_{bg}\left(\omega\right). \tag{A.12c}$$

In the above, $\epsilon(\omega)$ is the complex dielectric constant and k_0 is the free space propagation constant.

It is worth briefly reflecting on what we have achieved thus far. The wave equation, A.11, is the starting point from which determination of the spatial laser modes can be made. The laser modes are the solutions to the wave equation in steady state and, to reach these solutions as an end user, precise knowledge of the semiconductor structure is required. The reason for this is that the boundary conditions imposed by the structure (essentially refractive index gradients caused by the doped semiconductor layers) define the structure of the optical field. in this thesis the diode we intend to actively mode-lock is a commercial device, meaning that any device parameters on the (sparse) datasheet are for general operation only[1]. We are therefore limited to analysis only in the axial (z) direction along the resonator.

In the axial direction, allowed mode(s) may be altered by changes in the refractive index (and hence optical path length between the resonator mirrors) and the material absorption. An example electric field which has a single linear polarisation parallel to the

---

[1] Attempts were made to acquire information pertaining to the semiconductor structure through direct contact with the brand, but no information beyond the datasheet was provided.

plane of the semiconductor active region, the x direction, and travels in the z direction is given by,

$$E = \hat{\boldsymbol{x}} E_A e^{i(\kappa z + \omega t)} \tag{A.13}$$

where the complex propagation constant, κ, may be found by substitution of equation A.13 into equations A.11, and is given by,

$$\kappa = \tilde{n} k_0. \tag{A.14}$$

Here, $\tilde{n}$ is the complex refractive index, which may be written as,

$$\sqrt{\epsilon\left(\omega\right)} = \tilde{n} = n + i\frac{\alpha_{tot}}{2k_o}. \tag{A.15}$$

The complex propagation constant may now be written as,

$$\kappa = nk_0 + i\frac{\alpha_{tot}}{2}, \tag{A.16}$$

where n is the real component of the refractive index and α_{tot} is the imaginary component which defines the absorption by the laser medium. Related through the complex dielectric function A.12b, n and α_{tot} may be found by relating the real and imaginary parts of equation A.15 [38] which gives,

$$n = \sqrt{\epsilon'\left(\omega\right)} = \sqrt{\epsilon_{bg}\left(\omega\right) + \chi_p'\left(\omega\right)} \tag{A.17a}$$

$$\alpha_{tot} = \frac{k_0 \epsilon''\left(\omega\right)}{n} = \frac{k_0}{n}\left[\chi_{bg}''\left(\omega\right) + \chi_p''\left(\omega\right) + \frac{\sigma}{\epsilon_0 \omega}\right] \tag{A.17b}$$

Typically $\chi_p'\left(\omega\right) \ll \epsilon_{bg}\left(\omega\right)$ and so n may be approximated by $n = n_{bg} + \Delta n_p$ [36], where the latter is the change in background index due to the presence of pump charge carriers. From equation A.17b χ_{bg}'' is the unpumped material absorption and χ_p'' is responsible for the fall in χ_{bg}'' due to pumping of the laser medium, and $\frac{\sigma k_0}{n \epsilon_0 \omega}$ accounts for various internal loss mechanisms.

The total effect of all the loss mechanisms in α_{tot} and their relative changes due to electronics pumping can be expressed as the optical gain, given by [36],

$$g_{opt} = -\frac{k_0}{n_{bg}} \left[\chi''_{bg} + \chi''_p\right] \tag{A.18}$$

The various loss mechanisms may be summarised as follows,

$$\alpha_m = \frac{k_0 \chi''_{bg}}{n} \tag{A.19a}$$

$$\alpha_i = \frac{k_0 \sigma}{n \omega \epsilon_0} \tag{A.19b}$$

$$\alpha_R = \frac{1}{2L} \ln\left(\frac{1}{R_1 R_2}\right) \tag{A.19c}$$

This argument takes into account a laser without an external cavity. We can therefore replace R_2 with R_{eff} given by,

$$R_{eff} = \left[\sqrt{R_{AR}} + \frac{\sqrt{\alpha_{il} R_{ext}}\,(1 - R_{AR})}{1 + \sqrt{R_{ext} R_{AR}}}\right]^2. \tag{A.20}$$

where α_{il} is the coupling factor, or insertion loss factor, into the external cavity. For the purpose of the derivation, we shall stick with $R_1 R_2$ as it stands, because we can account for the external cavity output coupler mirror reflectivity and AR coating when defining the boundary conditions for the E field in the final model. The total absorption coefficient becomes,

$$\alpha_{tot} = -g_{opt} + \alpha_i. \tag{A.21}$$

Due to the fact that the laser is a Fabry-Perot cavity, the oscillating mode must perfectly overlap with itself after one complete cavity round trip. We may therefore write the forward and backward travelling waves as:

$$E_f(z) = E_{A,f}\; e^{\left(-ink_0 z - \frac{\alpha_{tot} z}{2}\right)} \tag{A.22a}$$

$$E_b(z) = E_{A,b}\; e^{\left(-ink_0 (z-L) - \frac{\alpha_{tot}(z-L)}{2}\right)} \tag{A.22b}$$

which are interrelated by,

$$E_{A,f}\left(0\right)=r_1E_{A,b}\left(0\right)\qquad E_{A,b}\left(L\right)=r_2E_{A,f}\left(L\right)\tag{A.23}$$

where, for any integer p,

$$R_p=\left|r_p^2\right|,\tag{A.24}$$

Substitution of these boundary conditions into equations A.22a and A.22b gives,

$$\sqrt{R_1R_2}\;e^{\left[2ink_0L+\alpha_{tot}L\right]}=1.\tag{A.25}$$

Taking the real and imaginary parts give the threshold optical gain and threshold oscillating frequencies, given respectively by,

$$g_{opt,th}=\alpha_i+\alpha_R=\alpha_i+\frac{1}{2L}\ln\left(\frac{1}{R_1R_2}\right)\tag{A.26}$$

and,

$$\omega_m=\frac{m\pi c}{nL}..\tag{A.27}$$

We now make the following definitions regarding the effective refractive index and threshold oscillation frequency such that,

$$n_{eff}=n+\omega\frac{\partial n}{\partial\omega},\tag{A.28a}$$

$$\omega_{th,m}=\frac{m\pi c}{n_{th}L},.\tag{A.28b}$$

The refractive index can be expanded to first order around the threshold oscillation frequency and the threshold carrier density,

$$n=n_{th}+\frac{\partial n}{\partial\omega}\left(\omega-\omega_{th}\right)+\frac{\partial n}{\partial N}\left(N-N_{th}\right),\tag{A.29}$$

whereby equations A.27, A.28a, A.28b and A.29 may be combined to give,

$$(\omega - \omega_{th}) = -\frac{\omega_{th}}{n_{eff}} \frac{\partial n}{\partial N} (N - N_{th}) \, . \tag{A.30}$$

This expression shows how the oscillating laser frequency has a linear dependence on the carrier density, N, and furthermore highlights that the optical frequency decreases for increasing DC injection current.

To derive the field rate equation, we begin from the lasing condition given by equation A.25 and recognise that following a single round trip of the cavity when above threshold, the gain is given by this same condition,

$$\sqrt{R_1 R_2}\; e^{[2ink_0 L + \alpha_{tot} L]} = G \tag{A.31}$$

Central to this condition is the frequency, ω, and carrier density, N, dependence of the wavenumber, k_0. The wavenumber can therefore be expanded to first order around these variables at threshold which, with the help of equation A.29 and A.28a, may be written as,

$$k_0 n = \frac{\omega_{th} n_{th}}{c} + \frac{n_{eff}}{c} (\omega - \omega_{th}) + \frac{\omega_{th}}{c} \frac{\partial n}{N} (N - N_{th}) \, . \tag{A.32}$$

Substitution of equation A.32 into A.31 and separating into components which are independent of and dependent on frequency respectively, we arrive at,

$$G = G_{\omega id} G_{\omega d}, \tag{A.33}$$

where,

$$G_{\omega id} = r_1 r_2 e^{\left[\frac{2i\omega_{th} L}{c} \frac{\partial n}{\partial N} (N - N_{th}) + \alpha_{tot} L\right]} \tag{A.34a}$$

$$G_{\omega d} = e^{\left[\frac{2i\omega_{th} L}{c} \left[n_{th} + \frac{n_{eff}}{\omega_{th}} (\omega - \omega_{th})\right]\right]} . \tag{A.34b}$$

From equation A.25 we exploit the fact that, after one round trip of the cavity, the change of phase must be either 0 or an integer number times 2π, meaning that the first part of the exponential in equation A.34b must be 1:

$$\frac{2i\omega_{th}n_{th}}{c} = 2\pi \;\Rightarrow\; e^{i2\pi} = 1. \tag{A.35}$$

Now using the definition for the round trip time of the cavity, and that $-i\omega$ may be written as the operator $\frac{d}{dt}$, given by

$$\frac{2Ln_{eff}}{c} = \tau_{rt}, \tag{A.36a}$$

$$-i\omega = \frac{d}{dt}, \tag{A.36b}$$

resulting in,

$$G_{\omega d} = e^{-\tau_{rt}\frac{d}{dt}} e^{-i\tau_{rt}\omega_{th}}. \tag{A.37}$$

We must now re-use the condition that, for sustained laser oscillation to occur, the phase of the complex electric field must overlap with itself perfectly following one round trip of the laser cavity. Under this condition, we may state that for a trial forward travelling electric field,

$$E_f\left(t\right) = GE_f\left(t\right), \tag{A.38}$$

and likewise for the backward propagating field. Consider now that the complex field may be separated into terms which vary at different time scales with respect to ω, the optical angular frequency. They are represented respectively as $E_f^*\left(t\right)$ which varies slowly, and $e^{i\omega_{th}t}$ which varies at the optical angular frequency at threshold, and may be written as,

$$E_f\left(t\right) = E_f^*\left(t\right) e^{i\omega_{th}t}. \tag{A.39}$$

Substitution of equation A.39 into equation A.38, further substituting for G from equation A.33 and noting that $e^{-\tau_{rt}\frac{d}{dt}}$ is in effect a delay in τ_{rt}, we arrive at the field under the slowly varying field approximation (SVEA) given by,

$$E^*_{f,b}\left(t\right) = G_{\omega id} E^*_{f,b}\left(t - \tau_{rt}\right). \tag{A.40}$$

The total field may therefore be written in an identical way, where τ_{rt} contains all the frequency independent components of the gain G. For when the alterations to $E(t)$ are small per round trip of the laser cavity, the field may be expanded to first order around the cavity round trip time such that,

$$E\left(t - \tau_{rt}\right) = E\left(t\right) - \tau_{rt}\frac{dE\left(t\right)}{dt}. \tag{A.41}$$

Rearranging to make the differential component the subject and substituting for an expression of identical form as equation A.40 yields,

$$\frac{dE\left(t\right)}{dt} = \tau_{rt}^{-1}\left[1 - G_{\omega id}^{-1}\right]E\left(t\right). \tag{A.42}$$

Employing the following identities,

1. For small x, $e^x \approx 1 + x$,
2. from the rules of logarithms, $e^{\ln(x)} = x$ and $-\ln\left(x\right) = \ln\left(\frac{1}{x}\right)$,
3. from equation A.26, $\frac{1}{2L}\ln\left(\frac{1}{R_1R_2}\right) \equiv \frac{1}{L}\ln\left(\frac{1}{r_1r_2}\right)$, and,
4. the group velocity, υ_{gr}, is given by $\upsilon_{gr} = \frac{c}{n_{eff}} = \frac{2L}{\tau_{rt}}$.

and substituting in for equation A.30, we may write,

$$\frac{dE\left(t\right)}{dt} = \left[-i\left(\omega - \omega_{th}\right) + \frac{1}{2}\left(\upsilon_{gr}\alpha_{tot}\right)\right]E\left(t\right). \tag{A.43}$$

From Tartwijk *et al* [36], where the gain has been expanded to first order, or *linearized*, around the carrier density, N,

$$g_{opt} = \Gamma g = \Gamma g_{th} + \Gamma \frac{\partial g}{\partial N} \left(N - N_{th}\right), \tag{A.44}$$

$$g_{th} = \frac{\partial g}{\partial N} \left(N_{th} - N_{tr}\right), \tag{A.45}$$

$$\left(\omega - \omega_{th}\right) = -\frac{\omega_{th}}{n_{eff}} \left(N - N_{th}\right) = \frac{1}{2} \alpha \Gamma v_{gr} \frac{\partial g}{\partial N} \left(N - N_{th}\right), \tag{A.46}$$

where α is the Henry alpha linewidth enhancement factor [209]. Using the above, we can now write the full rate equation for the electric field as,

$$\boxed{\frac{dE\left(t\right)}{dt} = \frac{1}{2} \left[\Gamma \left(1 + i\alpha\right) G_N \left(N - N_{th}\right)\right] E\left(t\right) + E_{sp}\left(t\right).} \tag{A.47}$$

where,

$$G_n = v_{gr} \frac{\partial g}{\partial N}. \tag{A.48}$$

A.1.2 The Carrier Equation

The carrier equation can be constructed by the simple addition of any effects that cause an increase or decrease in the carrier number. We begin with [36]:

$$\frac{\partial N}{\partial t} = \zeta \nabla^2 N + \frac{J}{e} - R\left(N\right), \tag{A.49}$$

The first term on the right defines the effects of intraband carrier scattering, where ζ is the intraband diffusion coefficient. Where all interband dynamical charge effects occur on a picosecond to nanosecond timescale, and since the spatial effects of the material polarisation equilibrate on a time scale of a few tens of femtoseconds, the spatial intraband scattering term can be neglected entirely. J is the injection current density and R accounts for the losses due to spontaneous and stimulated emission, and can be represented as:

$$R\left(N\right) = R_{st}\left(N, S\right) + \frac{N}{\tau_{ib}\left(N\right)}, \tag{A.50}$$

where $R_{st}\left(N,S\right)$ is the rate of stimulated emission, S is the photon number and $\tau_{ib}\left(N\right)$ is the interband relaxation, or recombination time, which describes the non-radiative upper state population losses, spontaneous emission loss and Auger recombination losses collectively, and is given respectively by,

$$\frac{N}{\tau_{ib}\left(N\right)}=\Lambda N+\beta N^{2}+\Upsilon N^{3}. \tag{A.51}$$

The photon number S is normalised such that $S=\left|E\right|^{2}$. It has been shown in [35] that the rate equation for the charge carrier density is given by,

$$\boxed{\frac{dN\left(t\right)}{dt}=\frac{J}{ed}-\frac{N}{\tau_{ib}\left(N\right)}-G_{N}\left[N\left(t\right)-N_{tr}\right]} \tag{A.52}$$

Appendix B

Mode-Locking Characterisation - Pulse Width Uncertainty

The pulse temporal width characterisation in sections 4.1.1 and 4.2 shows surface plots of the pulse temporal FWHM parameter as determined by the Gaussian fit to the intensity autocorrelation trace captured at the oscilloscope. Associated with these theoretical fits is the uncertainty in the fit which, when using a surface plot to demonstrate the trends in the parameter spaces, does not provide clear infrastructure for showing the uncertainty in the fit value. As such we present the uncertainty in the calculated FWHM parameter in the following surface plots.

The Gaussian fit to the temporal lineshape data is achieved through the non-linear least squares fit functionality in Matlab. The uncertainty presented here is the standard error in the FWHM value calculation.

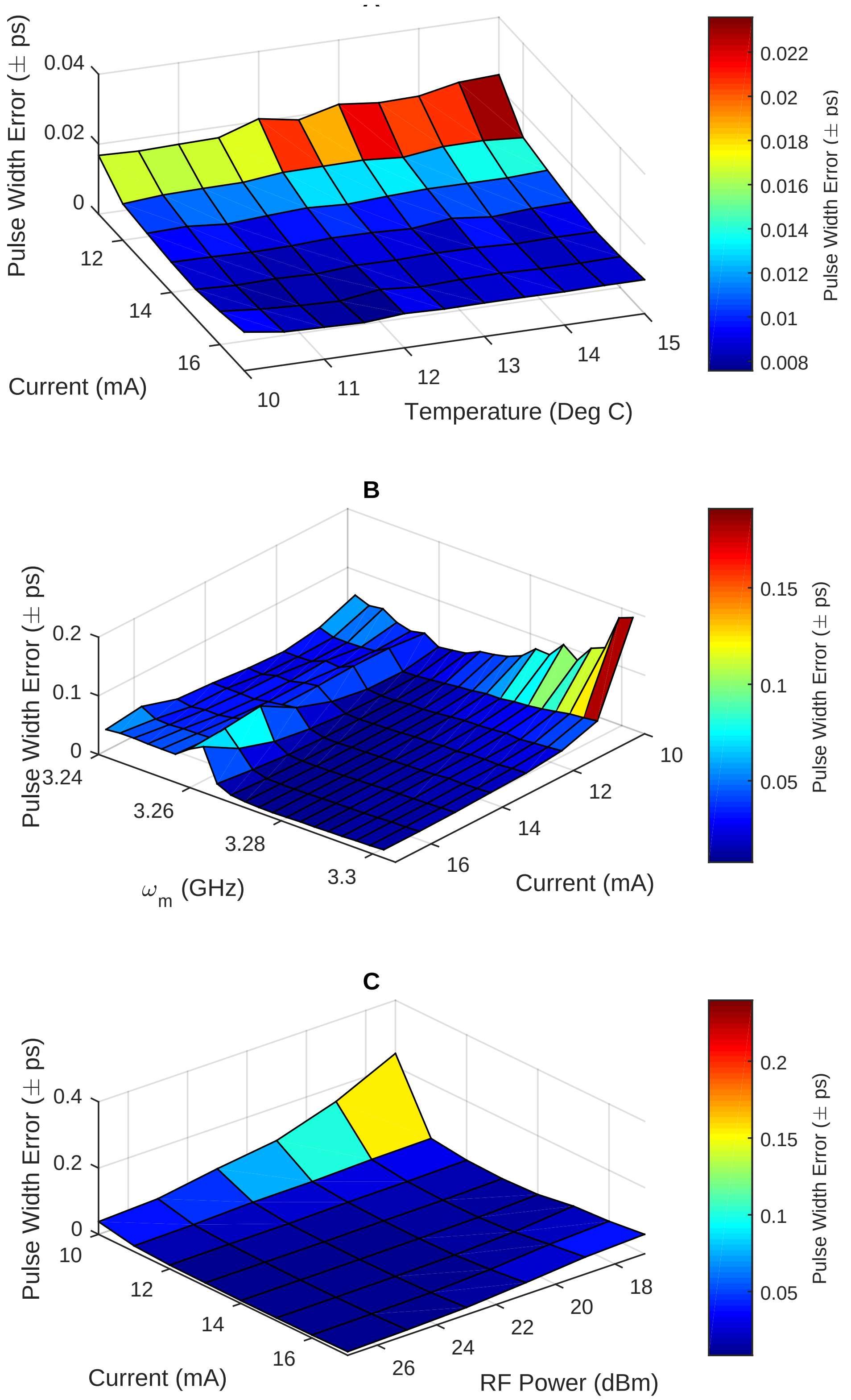

Figure B.1: Uncertainty in the calculated FWHM parameters for the temporal pulse widths. Plots A - C correspond directly to plots A - C in figure 4.2.

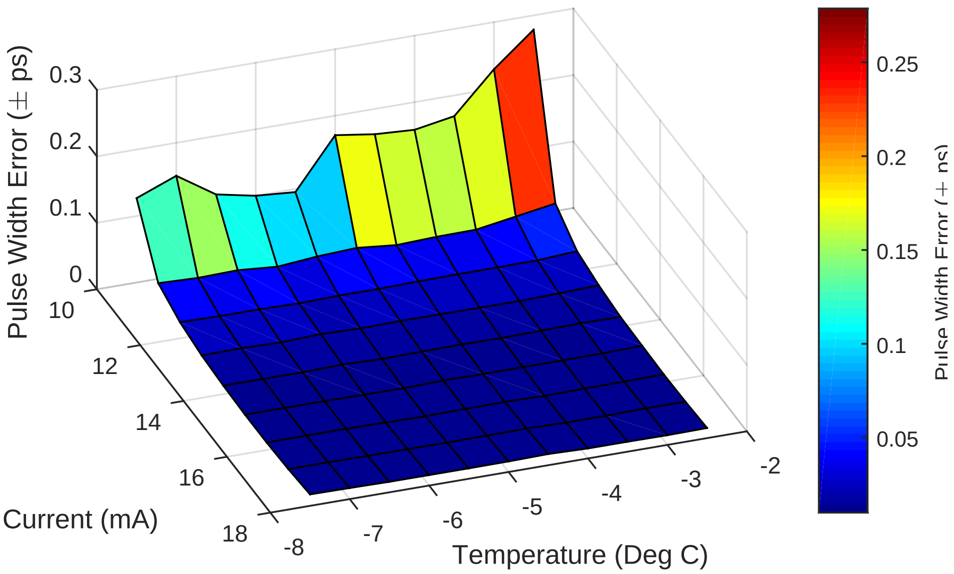

Figure B.2: Uncertainty in the calculated FWHM parameters for the temporal pulse widths. This plot corresponds to plot A in figure 4.8.

Appendix C

Frequency Comb Vernier - The RF Frequency Comb

Here we demonstrate the first results achieved towards the frequency comb vernier. The Vernier is the beating together of two mode-locked diode lasers whose repetition rates are fractionally different. In the frequency domain, this is identical to their mode spacings (and hence active modulation frequencies) being fractionally different. The beating together of these lasers produces a comb of modes on the RF spectrum, where each comb tooth is separated in frequency from its neighbours by the precise active modulation frequency difference between the lasers, and is referred to as the 'RF comb'. In figure C.1 we show the RF comb for the two actively mode-locked diode lasers whose modulation frequencies are 2.995 GHz and 2.998 GHz, and hence the mode spacing of the RF comb is precisely 3 MHz. In this figure, the RBW and VBW were set to 4.7 Hz. The two mode-locked lasers are not stabilised to one another.

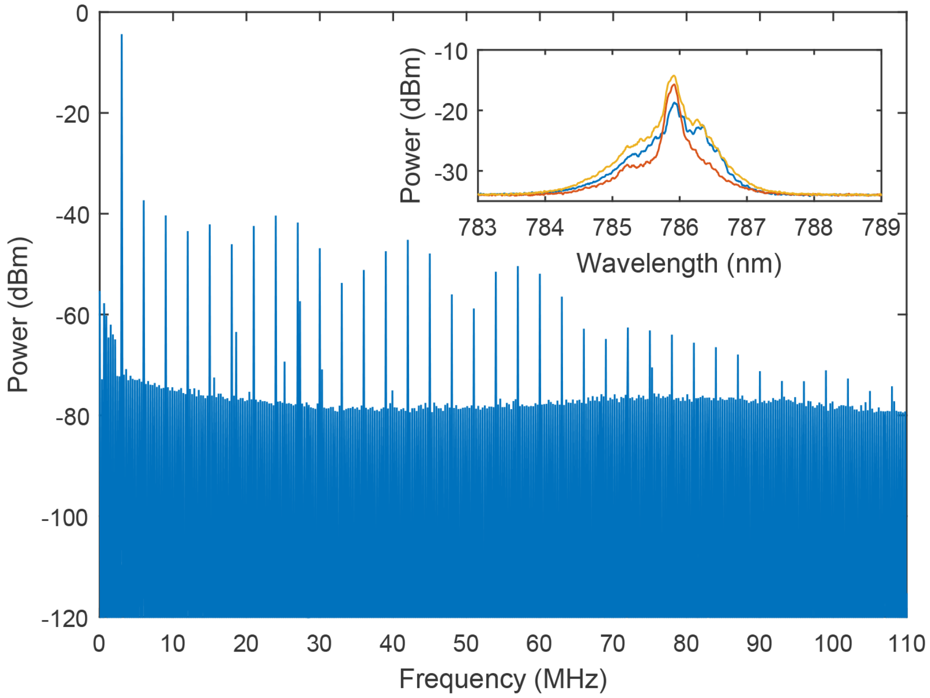

Figure C.1: Radio Frequency comb between two actively mode-locked diode lasers. Inset is the optical spectra for each optical frequency comb (blue and red) and the combined spectra where both mode-locked lasers are incident at the optical spectrum analyser (yellow)

While in the first instance the results appear favourable, i.e., an RF comb of narrow linewidth, evenly spaced frequency components, it soon becomes clear that these results are unfeasible given the experimental conditions. Where the two frequency combs are not phase coherent, and hence free to drift with respect to one another, it is exceptionally unlikely that the optical modes would remain stable enough over the 180 second sweep time of the single shot measurement. Furthermore, where the linewidth of the optical modes is believed to be on the order of at least 1 MHz, the linewidths of the RF comb modes are unfeasibly narrow.

A reasonable conclusion is that the modes are the result of detection nonlinearities in the photodiode. The photodiode will convert the optical pulse train into a corresponding current pulse train; the spectrum of which will contain harmonics of the pulse repetition rate. When both optical pulse trains are incident on the photodiode, and since the pulses from the two combs overlap approximately only once in every one thousand pulses, it is likely that the optical nonlinearity of the photodiode is mixing the harmonics of the two comb repetition rates to generate the above RF comb. Since this depends upon the uniformity of the pulse arrival time(s) and not the linewidth of the optical modes comprising the pulses, the features on the RF comb will be significantly narrower that a conventional optical beat note.

References

[1] N. Cooper, J. Woods, J. Bateman, A. Dunning, and T. Freegarde, "Stabilized fiber-optic MachZehnder interferometer for carrier-frequency rejection," *Applied Optics*, vol. 52, pp. 5713–5717, Aug. 2013.

[2] M. Himsworth, *Coherent Manipulation of Ultracold Rubidium.* PhD thesis, School of Physics and Astronomy, University of Southampton, Sept. 2009.

[3] J. A. Rushton, M. Aldous, and M. D. Himsworth, "Contributed Review: The feasibility of a fully miniaturized magneto-optical trap for portable ultracold quantum technology," *Review of Scientific Instruments*, vol. 85, p. 121501, Dec. 2014.

[4] R. T. Logan, "All-optical heterodyne RF signal generation using a mode-locked-laser frequency comb: theory and experiments," in *Microwave Symposium Digest. 2000 IEEE MTT-S International*, vol. 3, pp. 1741–1744 vol.3, IEEE, June 2000.

[5] F. Nez, M. D. Plimmer, S. Bourzeix, L. Julien, F. Biraben, R. Felder, O. Acef, J. J. Zondy, P. Laurent, A. Clairon, M. Abed, Y. Millerioux, and P. Juncar, "Precise Frequency Measurement of the 2S-8S/8D Transitions in Atomic Hydrogen: New Determination of the Rydberg Constant," *Physical Review Letters*, vol. 69, no. 16, p. 2326, 1992.

[6] F. Nez, M. D. Plimmer, S. Bourzeix, L. Julien, F. Biraben, B. Cagnac, R. Felder, P. Juncar, and Y. Millerioux, "Towards a frequency measurement of the Rydberg constant using the 2S-8S and 2S-8D transitions of hydrogen," *Instrumentation and Measurement, IEEE Transactions on*, vol. 42, pp. 217–221, Apr. 1993.

[7] B. de Beauvoir, F. Nez, L. Julien, B. Cagnac, F. Biraben, D. Touahri, L. Hilico, O. Acef, A. Clairon, and J. J. Zondy, "Absolute Frequency Measurement of the 2S-8S/8D Transitions in Hydrogen and Deuterium:New Determination of the Rydberg Constant," *Physical Review Letters*, vol. 78, no. 3, p. 440, 1997.

[8] F. S. Pavone, F. Marin, P. De Natale, M. Inguscio, and F. Biraben, "First Pure Frequency Measurement of an Optical Transition in Helium: Lamb Shift of the 2^3S_1 Metastable Level," *Physical Review Letters*, vol. 73, pp. 42–45, July 1994.

[9] Y. Millerioux, D. Touahri, L. Hilico, A. Clairon, R. Felder, F. Biraben, and B. de Beauvoir, "Towards an accurate frequency standard at 778 nm using a laser diode stabilized on a hyperfine component of the Doppler-free two-photon transitions in rubidium," *Optics Communications*, vol. 108, pp. 91–96, May 1994.

[10] C. J. Foot, *Atomic Physics.* Oxford University Press, 2005.

[11] T. W. Hänsch and A. L. Schawlow, "Cooling of gases by laser radiation," *Optics Communications*, vol. 13, pp. 68–69, Jan. 1975.

[12] M. Kasevich and S. Chu, "Measurement of the gravitational acceleration of an atom with a light-pulse atom interferometer," *Applied Physics B: Lasers and Optics*, vol. 54, pp. 321–332, May 1992.

[13] A. Dunning, R. Gregory, J. Bateman, N. Cooper, M. Himsworth, J. A. Jones, and T. Freegarde, "Composite pulses for interferometry in a thermal cold atom cloud," *Physical Review A*, vol. 90, no. 3, p. 033608, 2014.

[14] R. N. Hall, G. E. Fenner, J. D. Kingsley, T. J. Soltys, and R. O. Carlson, "Coherent Light Emission From GaAs Junctions," *Physical Review Letters*, vol. 9, pp. 366–368, Nov. 1962.

[15] I. Hayashi, M. B. Panish, P. W. Foy, and S. Sumski, "Junction lasers which operate continuously at room temperature," *Applied Physics Letters*, vol. 17, pp. 109–111, Aug. 1970.

[16] E. P. Harris, "Spiking in Current Modulated cw GaAs External Cavity Lasers," *Journal of Applied Physics*, vol. 42, pp. 892–893, Feb. 1971.

[17] T, L. A. Glasser, E. P. Ippen, and H. A. Haus, “Picosecond pulse generation with a cw GaAlAs laser diode,” *Applied Physics Letters*, vol. 33, pp. 241–242, Aug. 1978.

[18] D. J. Jones, S. A. Diddams, J. K. Ranka, A. Stentz, R. S. Windeler, J. L. Hall, and S. T. Cundiff, “Carrier-envelope phase control of femtosecond mode-locked lasers and direct optical frequency synthesis,” *Science (New York, N.Y.)*, vol. 288, pp. 635–640, Apr. 2000.

[19] M. Rosch, G. Scalari, M. Beck, and J. Faist, “Octave-spanning semiconductor laser,” *Nat Photon*, vol. 9, pp. 42–47, Jan. 2015.

[20] M. Kourogi, K. Nakagawa, and M. Ohtsu, “Wide-span optical frequency comb generator for accurate optical frequency difference measurement,” *Quantum Electronics, IEEE Journal of*, vol. 29, pp. 2693–2701, Oct. 1993.

[21] R. Zhou, S. Latkowski, J. O’Carroll, R. Phelan, L. P. Barry, and P. Anandarajah, “40nm wavelength tunable gain-switched optical comb source,” *Optics Express*, vol. 19, p. B415, Nov. 2011.

[22] P. M. Anandarajah, R. Maher, Y. Q. Xu, X. Latkowski, J. O. Carroll, S. G. Murdoch, R. Phelan, J. O. Gorman, and L. P. Barry, “Generation of Coherent Multicarrier Signals by Gain Switching of Discrete Mode Lasers,” *Photonics Journal, IEEE*, vol. 3, pp. 112–122, Feb. 2011.

[23] E. Prior Cano, C. de Dios Fernandez, A. R. Criado Serrano, M. Ortsiefer, P. L. Meissner, and P. Acedo, “Experimental Study of VCSEL-Based Optical Frequency Comb Generators,” *Photonics Technology Letters, IEEE*, vol. 26, pp. 2118–2121, Nov. 2014.

[24] A. Ishizawa, T. Nishikawa, A. Mizutori, H. Takara, S. Aozasa, A. Mori, H. Nakano, A. Takada, and M. Koga, “Octave-spanning frequency comb generated by 250 fs pulse train emitted from 25 GHz externally phase-modulated laser diode for carrier-envelope-offset-locking,” *Electronics Letters*, vol. 46, no. 19, pp. 1343–1344, 2010.

[25] M. Kourogi, B. Widiyatomoko, Y. Takeuchi, and M. Ohtsu, “Limit of optical-frequency comb generation due to material dispersion,” *Quantum Electronics, IEEE Journal of*, vol. 31, pp. 2120–2126, Dec. 1995.

[26] M. Kourogi, T. Enami, and M. Ohtsu, “A monolithic optical frequency comb generator,” *Photonics Technology Letters, IEEE*, vol. 6, pp. 214–217, Feb. 1994.

[27] R. A. Elliott, H. DeXiu, R. K. DeFreez, J. M. Hunt, and P. G. Rickman, “Picosecond optical pulse generation by impulse train current modulation of a semiconductor laser,” *Applied Physics Letters*, vol. 42, pp. 1012–1014, June 1983.

[28] H.-F. Liu, M. Fukazawa, Y. Kawai, and T. Kamiya, “Gain-switched picosecond pulse (<10 ps) generation from 1.3 m InGaAsP laser diodes,” *Quantum Electronics, IEEE Journal of*, vol. 25, pp. 1417–1425, June 1989.

[29] K. Iwatsuki, K. Suzuki, and S. Nishi, “Generation of transform limited gain-switched DFB-LD pulses <6 ps with linear fibre compression and spectral window,” *Electronics Letters*, vol. 27, pp. 1981–1982, Oct. 1991.

[30] Y. Matsui, M. D. Pelusi, and A. Suzuki, “Generation of 20-fs optical pulses from a gain-switched laser diode by a four-stage soliton compression technique,” *Photonics Technology Letters, IEEE*, vol. 11, pp. 1217–1219, Oct. 1999.

[31] H. Haken and H. Sauermann, “Nonlinear interaction of laser modes,” vol. 173, no. 3, pp. 261–275, 1963.

[32] W. E. Lamb, “Theory of an Optical Maser,” *Physical Review*, vol. 134, pp. A1429–A1450, June 1964.

[33] M. Schell and E. Schöll, “Time-dependent simulation of a semiconductor laser amplifier: pulse compression in a ring configuration and dynamic optical bistability,” *Quantum Electronics, IEEE Journal of*, vol. 26, pp. 1005–1013, June 1990.

[34] M. Schell, A. G. Weber, E. Schöll, and D. Bimberg, “Fundamental limits of sub-ps pulse generation by active mode locking of semiconductor lasers: the spectral gain width and the facet reflectivities,” *Quantum Electronics, IEEE Journal of*, vol. 27, pp. 1661–1668, June 1991.

[35] J. Ohtsubo, *Semiconductor Lasers - Stability, Instability and Chaos.* Springer, 2008.

[36] G. H. M. V. Tartwijk and D. Lenstra, "Semiconductor lasers with optical injection and feedback," *Quantum and Semiclassical Optics: Journal of the European Optical Society Part B*, vol. 7, pp. 87–143, Apr. 1995.

[37] H. Haken, *Light: Volume 2 Laser Light Dynamics.* North Holland Physics Publishing, 1985.

[38] G. P. Agrawal and N. K. Dutta, *Semiconductor Lasers.* Kluwer Academic Publishers, 2 ed., 1993.

[39] W. W. Chow and S. W. Koch, "Semiconductor-Laser Fundamentals - Physics of the Gain Materials," 1999.

[40] J. Ohtsubo, *Chaotic dynamics in semiconductor lasers with optical feedback*, vol. 44, pp. 1–84. Elsevier, 2002.

[41] M. P. Kesler and E. P. Ippen, "Subpicosecond gain dynamics in GaAlAs laser diodes," *Applied Physics Letters*, vol. 51, pp. 1765–1767, Nov. 1987.

[42] N. Kim, J. Shin, E. Sim, C. W. Lee, D.-S. Yee, M. Y. Jeon, Y. Jang, and K. H. Park, "Monolithic dual-mode distributed feedback semiconductor laser for tunable continuous-wave terahertz generation," *Optics Express*, vol. 17, p. 13851, July 2009.

[43] L. Kong, H. L. Wang, D. Bajek, S. E. White, A. F. Forrest, X. L. Wang, B. F. Cui, J. Q. Pan, Y. Ding, and M. A. Cataluna, "Deep-red semiconductor monolithic mode-locked lasers," *Applied Physics Letters*, vol. 105, p. 221115, Dec. 2014.

[44] M. G. Thompson, A. R. Rae, M. Xia, R. V. Penty, and I. H. White, "InGaAs Quantum-Dot Mode-Locked Laser Diodes," *Selected Topics in Quantum Electronics, IEEE Journal of*, vol. 15, pp. 661–672, May 2009.

[45] M. Xia, M. G. Thompson, R. V. Penty, and I. H. White, "External-Cavity Mode-Locked Quantum-Dot Laser Diodes for Low Repetition Rate, Sub-Picosecond

Pulse Generation," *Selected Topics in Quantum Electronics, IEEE Journal of*, vol. 17, no. 5, pp. 1264–1271, 2011.

[46] R. Maldonado-Basilio, S. Latkowski, S. Philippe, and P. Landais, "40 GHz mode-beating with 8 Hz linewidth and 64 fs timing jitter from a synchronized mode-locked quantum-dash laser diode," *Optics Letters*, vol. 36, p. 3142, Aug. 2011.

[47] E. V. Andreeva, N. I. Koroteev, S. A. Magnitskiy, E. Salik, D. S. Starodubov, J. Feinberg, M. V. Shramenko, and S. D. Yakubovich, "Passive mode locking in a multisegment laser diode with an external cavity," *Quantum Electronics*, vol. 29, pp. 103–108, Feb. 1999.

[48] J. C. Balzer, R. H. Pilny, B. Dopke, A. Klehr, G. Erbert, G. Trankle, C. Brenner, and M. R. Hofmann, "Passively Mode-Locked Diode Laser With Optimized Dispersion Management," *Selected Topics in Quantum Electronics, IEEE Journal of*, vol. 21, pp. 1–8, Nov. 2015.

[49] T. Schlauch, J. C. Balzer, A. Klehr, G. Erbert, G. Tränkle, and M. R. Hofmann, "Femtosecond passively modelocked diode laser with intracavity dispersion management," *Optics Express*, vol. 18, p. 24316, Nov. 2010.

[50] H. Wang, L. Kong, A. Forrest, D. Bajek, S. E. Haggett, X. Wang, B. Cui, J. Pan, Y. Ding, and M. A. A. Cataluna, "Ultrashort pulse generation by semiconductor mode-locked lasers at 760 nm.," *Optics Express*, vol. 22, pp. 25940–25946, Oct. 2014.

[51] M. Yoshita, M. Kuramoto, M. Ikeda, and H. Yokoyama, "Mode locking of a GaInN semiconductor laser with an internal saturable absorber," *Applied Physics Letters*, vol. 94, p. 061104, Feb. 2009.

[52] K. Saito, H. Watanabe, T. Miyajima, M. Ikeda, and H. Yokoyama, "Mode locking of an external-cavity bisection GaInN blue-violet laser diode producing 3 ps duration optical pulses," *Applied Physics Letters*, vol. 96, pp. 031112+, Jan. 2010.

[53] D. Bitauld, S. Osborne, and S. O'Brien, "Timing characterization of 100 GHz passively mode-locked discrete mode laser diodes," *Optics Express*, vol. 19, p. 13989,

July 2011.

[54] T. Shimizu, I. Ogura, and H. Yokoyama, “860 GHz rate asymmetric colliding pulse modelocked diode lasers,” *Electronics Letters*, vol. 33, pp. 1868–1869, Oct. 1997.

[55] S. Arahira, Y. Matsui, and Y. Ogawa, “Mode-locking at very high repetition rates more than terahertz in passively mode-locked distributed-Bragg-reflector laser diodes,” *Quantum Electronics, IEEE Journal of*, vol. 32, pp. 1211–1224, July 1996.

[56] D. A. Yanson, M. W. Street, S. D. McDougall, I. G. Thayne, J. H. Marsh, and E. A. Avrutin, “Ultrafast harmonic mode-locking of monolithic compound-cavity laser diodes incorporating photonic-bandgap reflectors,” *Quantum Electronics, IEEE Journal of*, vol. 38, pp. 1–11, Jan. 2002.

[57] Y.-K. Chen and M. C. Wu, “Monolithic colliding-pulse mode-locked quantum-well lasers,” *Quantum Electronics, IEEE Journal of*, vol. 28, pp. 2176–2185, Oct. 1992.

[58] D. A. Yanson, M. W. Street, S. D. McDougall, I. G. Thayne, J. H. Marsh, and E. A. Avrutin, “Terahertz repetition frequencies from harmonic mode-locked monolithic compound-cavity laser diodes,” *Applied Physics Letters*, vol. 78, pp. 3571–3573, June 2001.

[59] S. Calvez, J. E. Hastie, M. Guina, O. G. Okhotnikov, and M. D. Dawson, “Semiconductor disk lasers for the generation of visible and ultraviolet radiation,” *Laser & Photon. Rev.*, vol. 3, pp. 407–434, Sept. 2009.

[60] A. H. Quarterman, K. G. Wilcox, V. Apostolopoulos, Z. Mihoubi, S. P. Elsmere, I. Farrer, D. A. Ritchie, and A. Tropper, “A passively mode-locked external-cavity semiconductor laser emitting 60-fs pulses,” *Nat Photon*, vol. 3, pp. 729–731, Dec. 2009.

[61] D. J. Derickson, P. A. Morton, J. E. Bowers, and R. L. Thornton, “Comparison of timing jitter in external and monolithic cavity modelocked semiconductor lasers,” *Applied Physics Letters*, vol. 59, pp. 3372–3374, Dec. 1991.

[62] P. S. Spencer and D. M. Kane, “FM lasing phenomena in external cavity lasers,” *Journal of Modern Optics*, vol. 47, no. 11, p. 1803, 2000.

[63] R. Nagar, D. Abraham, N. Tessler, A. Fraenkel, G. Eisenstein, E. P. Ippen, U. Koren, and G. Raybon, “Frequency-modulation mode locking of a semiconductor laser,” *Optics Letters*, vol. 16, pp. 1750–1752, Nov. 1991.

[64] H. Nakatsuka, K. M. Abedin, and S. Uemura, “Active mode-locking of conventional diode laser by using external cavity,” *Optics Communications*, vol. 78, pp. 369–372, Sept. 1990.

[65] S. W. Corzine, J. E. Bowers, G. Przybylek, U. Koren, B. I. Miller, and C. E. Soccolich, “Actively modelocked GaInAsP laser with subpicosecond output,” *Applied Physics Letters*, vol. 52, pp. 348–350, Feb. 1988.

[66] P. J. Delfyett, H, G. A. Alphonse, and J. C. Connolly, “High peak power picosecond pulse generation from AlGaAs external cavity mode locked semiconductor laser and traveling wave amplifier,” *Applied Physics Letters*, vol. 57, pp. 971–973, Sept. 1990.

[67] P. J. Delfyett, L. T. Florez, N. Stoffel, T. Gmitter, N. C. Andreadakis, Y. Silberberg, J. P. Heritage, and G. A. Alphonse, “High-power ultrafast laser diodes,” *Quantum Electronics, IEEE Journal of*, vol. 28, pp. 2203–2219, Oct. 1992.

[68] F. C. Cruz, M. C. Stowe, and J. Ye, “Tapered semiconductor amplifiers for optical frequency combs in the near infrared,” *Optics Letters*, vol. 31, no. 9, p. 1337, 2006.

[69] P. P. Vasil’ev, “Ultrashort pulse generation in diode lasers,” *Optical and Quantum Electronics*, vol. 24, no. 8, pp. 801–824, 1992.

[70] L. Goldberg, D. Mehuys, and D. Welch, “High power mode-locked compound laser using a tapered semiconductor amplifier,” *Photonics Technology Letters, IEEE*, vol. 6, no. 9, pp. 1070–1072, 1994.

[71] A. J. Lowery, N. Onodera, and R. S. Tucker, “Stability and spectral behavior of grating-controlled actively mode-locked lasers,” *Quantum Electronics, IEEE Journal of*, vol. 27, pp. 2422–2430, Nov. 1991.

[72] J. Davila-Rodriguez, I. Ozdur, C. Williams, and P. J. Delfyett, "A semiconductor-based, frequency-stabilized mode-locked laser using a phase modulator and an intracavity etalon," *Optics Letters*, vol. 35, p. 4130, Dec. 2010.

[73] J. E. Bowers, P. A. Morton, A. Mar, and S. W. Corzine, "Actively mode-locked semiconductor lasers," *Quantum Electronics, IEEE Journal of*, vol. 25, pp. 1426–1439, June 1989.

[74] E. A. Avrutin, J. H. Marsh, and E. L. Portnoi, "Monolithic and multi-gigahertz mode-locked semiconductor lasers: constructions, experiments, models and applications," *Optoelectronics, IEEE Proceedings*, vol. 147, pp. 251–278, Aug. 2000.

[75] J. McInerney, L. Reekie, and D. J. Bradley, "Bandwidth-limited picosecond pulse generation by hybrid mode-locking in a ring cavity GaAlAs laser," *Electronics Letters*, vol. 21, pp. 117–118, Jan. 1985.

[76] A. Schmitt-Sody, A. Velten, Y. Liu, L. Arissian, and J.-C. Diels, "High-Power Hybrid Mode-Locked External Cavity Semiconductor Laser Using Tapered Amplifier with Large Tunability," *Research Letters in Optics*, vol. 2008, pp. 1–5, 2008.

[77] R. Arkhipov, A. Pimenov, M. Radziunas, D. Rachinskii, A. G. Vladimirov, D. Arsenijevic, H. Schmeckebier, and D. Bimberg, "Hybrid Mode Locking in Semiconductor Lasers: Simulations, Analysis, and Experiments," *Selected Topics in Quantum Electronics, IEEE Journal of*, vol. 19, p. 1100208, July 2013.

[78] D. J. Derickson, R. J. Helkey, A. Mar, J. R. Karin, J. G. Wasserbauer, and J. E. Bowers, "Short pulse generation using multisegment mode-locked semiconductor lasers," *Quantum Electronics, IEEE Journal of*, vol. 28, pp. 2186–2202, Oct. 1992.

[79] S. Arahira, N. Mineo, K. Tachibana, and Y. Ogawa, "40 GHz hybrid modelocked laser diode module operated at ultra-low RF power with impedance-matching circuit," *Electronics Letters*, vol. 39, pp. 287–289, Feb. 2003.

[80] F. R. Ahmad and F. Rana, "Fundamental and Subharmonic Hybrid Mode-Locking of a High-Power (220 mW) Monolithic Semiconductor Laser," *Photonics Technology Letters, IEEE*, vol. 20, pp. 1308–1310, Aug. 2008.

[81] T. Oki, K. Saito, H. Watanabe, T. Miyajima, M. Kuramoto, M. Ikeda, and H. Yokoyama, “Passive and Hybrid Mode-Locking of an External-Cavity GaInN Laser Diode Incorporating a Strong Saturable Absorber,” *Applied Physics Express*, vol. 3, p. 032104, Mar. 2010.

[82] B.-L. Lee and C.-F. Lin, “Novel self-hybrid mode-locking of semiconductor lasers in an external cavity,” *Photonics Technology Letters, IEEE*, vol. 12, no. 9, pp. 1243–1245, 2000.

[83] C. Ye and T. K. Wei, *Tunable External Cavity Diode Lasers.* World Scientific Publishing Co. Pte. Ltd, 2004.

[84] L. Ricci, M. Weidemüller, T. Esslinger, A. Hemmerich, C. Zimmermann, V. Vuletic, W. König, and T. W. Hänsch, “A compact grating-stabilized diode laser system for atomic physics,” *Optics Communications*, vol. 117, pp. 541–549, June 1995.

[85] L. Hildebrandt, R. Knispel, S. Stry, J. R. Sacher, and F. Schael, “Antireflection-coated blue GaN laser diodes in an external cavity and Doppler-free indium absorption spectroscopy.,” *Applied Optics*, vol. 42, pp. 2110–2118, Apr. 2003.

[86] C. J. Hawthorn, K. P. Weber, and R. E. Scholten, “Littrow configuration tunable external cavity diode laser with fixed direction output beam,” *Review of Scientific Instruments*, vol. 72, pp. 4477–4479, Dec. 2001.

[87] R. W. P. Drever, J. L. Hall, F. V. Kowalski, J. Hough, G. M. Ford, A. J. Munley, and H. Ward, “Laser phase and frequency stabilization using an optical resonator,” *Applied Physics B: Lasers and Optics*, vol. 31, pp. 97–105, June 1983.

[88] E. D. Black, “An introduction to Pound-Drever-Hall laser frequency stabilization,” *American Journal of Physics*, vol. 69, pp. 79–87, Jan. 2001.

[89] T. W. Hansch and B. Couillaud, “Laser frequency stabilization by polarization spectroscopy of a reflecting reference cavity,” *Optics Communications*, vol. 35, pp. 441–444, Dec. 1980.

[90] M. G. Tarallo, N. Poli, M. Schioppo, D. Sutyrin, and G. M. Tino, "A high-stability semiconductor laser system for a ^{88}Sr-based optical lattice clock," *Applied Physics B: Lasers and Optics*, vol. 103, pp. 17–25, Sept. 2011.

[91] Y. Zhao, Y. Peng, T. Yang, Y. Li, Q. Wang, F. Meng, J. Cao, Z. Fang, T. Li, and E. Zang, "External cavity diode laser with kilohertz linewidth by a monolithic folded Fabry?Perot cavity optical feedback," *Opt. Lett.*, vol. 36, pp. 34–36, Jan. 2011.

[92] A. A. Madej, L. Marmet, and J. E. Bernard, "Rb atomic absorption line reference for single Sr$^+$ laser cooling systems," *Applied Physics B: Lasers and Optics*, vol. 67, pp. 229–234, Aug. 1998.

[93] K. B. MacAdam, A. Steinbach, and C. Wieman, "A narrow band tunable diode laser system with grating feedback, and a saturated absorption spectrometer for Cs and Rb," *American Journal of Physics*, vol. 60, pp. 1098–1111, Dec. 1992.

[94] Y. Torii, H. Tashiro, N. Ohtsubo, and T. Aoki, "Laser Phase and Frequency Stabilization using Atomic Coherence," Apr. 2012.

[95] E. C. Cook, P. J. Martin, T. L. Brown-Heft, J. C. Garman, and D. A. Steck, "High passive-stability diode-laser design for use in atomic-physics experiments," *Review of Scientific Instruments*, vol. 83, p. 043101, Apr. 2012.

[96] S. Vogt, C. Lisdat, T. Legero, U. Sterr, I. Ernsting, A. Nevsky, and S. Schiller, "Demonstration of a transportable 1 Hz-linewidth laser," *Applied Physics B: Lasers and Optics*, vol. 104, pp. 741–745, July 2011.

[97] H. Stoehr, F. Mensing, J. Helmcke, and U. Sterr, "Diode laser with 1 Hz linewidth," *Optics Letters*, vol. 31, no. 6, pp. 736+, 2006.

[98] S. Hirata, T. Akatsuka, Y. Ohtake, and A. Morinaga, "Sub-hertz-linewidth diode laser stabilized to an ultralow-drift high-finesse optical cavity," *Applied Physics Express*, vol. 7, p. 022705, Feb. 2014.

[99] G. C. Bjorklund, M. D. Levenson, W. Lenth, and C. Ortiz, "Frequency modulation (FM) spectroscopy," *Applied Physics B: Lasers and Optics*, vol. 32, pp. 145–152, Nov. 1983.

[100] W. Lenth, "High frequency heterodyne spectroscopy with current-modulated diode lasers," *Quantum Electronics, IEEE Journal of*, vol. 20, pp. 1045–1050, Sept. 1984.

[101] G. G. Bjorklund, "Frequency-modulation spectroscopy: a new method for measuring weak absorptions and dispersions," *Optics Letters*, vol. 5, p. 15, Jan. 1980.

[102] J. T. Liu, J. B. Jeffries, and R. K. Hanson, "Large-modulation-depth 2f spectroscopy with diode lasers for rapid temperature and species measurements in gases with blended and broadened spectra.," *Applied Optics*, vol. 43, pp. 6500–6509, Dec. 2004.

[103] G. R. Janik, C. B. Carlisle, and T. F. Gallagher, "Two-tone frequency-modulation spectroscopy," *Journal of the Optical Society of America B*, vol. 3, p. 1070, Aug. 1986.

[104] W. Demtröder, *Laser Spectroscopy: Basic Concepts and Instrumentation.* Springer, 3 ed., 2003.

[105] P. Fritschel, A. Jeffries, and T. J. Kane, "Frequency fluctuations of a diode-pumped Nd:YAG ring laser," *Optics Letters*, vol. 14, p. 993, Sept. 1989.

[106] C. P. Pearman, C. S. Adams, S. G. Cox, P. F. Griffin, D. A. Smith, and I. G. Hughes, "Polarization spectroscopy of a closed atomic transition: applications to laser frequency locking," *Journal of Physics B: Atomic, Molecular and Optical Physics*, vol. 35, pp. 5141–5151, Dec. 2002.

[107] G. P. T. Lancaster, R. S. Conroy, M. A. Clifford, J. Arlt, and K. Dholakia, "A polarisation spectrometer locked diode laser for trapping cold atoms," *Optics Communications*, vol. 170, pp. 79–84, Oct. 1999.

[108] K. L. Corwin, Z. T. Lu, C. F. Hand, R. J. Epstein, and C. E. Wieman, "Frequency-stabilized diode laser with the Zeeman shift in an atomic vapor.," *Applied Optics*, vol. 37, pp. 3295–3298, May 1998.

[109] A. Millett-Sikking, I. G. Hughes, P. Tierney, and S. L. Cornish, "DAVLL lineshapes in atomic rubidium," *Journal of Physics B: Atomic, Molecular and Optical Physics*, vol. 40, pp. 187–198, Jan. 2007.

[110] L. A. Coldren, S. W. Corzine, and M. L. Mashanovitch, *Diode Lasers and Photonic Integrated Circuits.* Wiley, 2 ed., 2011.

[111] T. Numai, *Laser Diodes and Their Applications to Communications and Information Processing.* Wiley, 2010.

[112] A. E. Siegman, *Lasers.* University Science Books, 1986.

[113] K. Petermann, *Laser Diode Modulation and Noise.* Springer, 1988.

[114] R. S. Tucker and I. P. Kaminow, "High-frequency characteristics of directly modulated InGaAsP ridge waveguide and buried heterostructure lasers," *Lightwave Technology, Journal of*, vol. 2, pp. 385–393, Aug. 1984.

[115] M. L. Majewski and D. Novak, "Method for characterization of intrinsic and extrinsic components of semiconductor laser diode circuit model," *Microwave and Guided Wave Letters, IEEE*, vol. 1, no. 9, pp. 246–248, 1991.

[116] J. Kuhl, M. Serenyi, and E. O. Göbel, "Bandwidth-limited picosecond pulse generation in an actively mode-locked GaAs laser with intracavity chirp compensation.," *Optics Letters*, vol. 12, pp. 334–336, May 1987.

[117] K. Y. Lau and A. Yariv, "Direct modulation and active mode locking of ultrahigh speed GaAlAs lasers at frequencies up to 18 GHz," *Applied Physics Letters*, vol. 46, pp. 326–328, Feb. 1985.

[118] F. Quinlan, S. Gee, S. Ozharar, and P. J. Delfyett, "Ultralow-jitter and -amplitude-noise semiconductor-based actively mode-locked laser.," *Optics Letters*, vol. 31, pp. 2870–2872, Oct. 2006.

[119] R. W. Tkach and A. R. Chraplyvy, "Regimes of feedback effects in 1.5 m distributed feedback lasers," *Lightwave Technology, Journal of*, vol. 4, pp. 1655–1661, Nov. 1986.

[120] A. S. Arnold, J. S. Wilson, and M. G. Boshier, "A simple extended-cavity diode laser," *Review of Scientific Instruments*, vol. 69, pp. 1236–1239, Mar. 1998.

[121] P. M. Smowton and P. Blood, "The differential efficiency of quantum-well lasers," *Selected Topics in Quantum Electronics, IEEE Journal of*, vol. 3, pp. 491–498, Apr. 1997.

[122] Y. Takushima, H. Sotobayashi, M. E. Grein, E. P. Ippen, and H. A. Haus, "Linewidth of mode combs of passively and actively mode-locked semiconductor laser diodes," in *Active and Passive Optical Components for WDM Communications IV*, vol. 5595 of *Society of Photo-Optical Instrumentation Engineers (SPIE) Conference Series*, pp. 213–227, Oct. 2004.

[123] D. Liang, J. Wang, and D. C. Hall, "High-efficiency native-oxide-passivated high-index-contrast ridge waveguide lasers," *Electronics Letters*, vol. 42, pp. 349–350, Mar. 2006.

[124] J. S. Cohen, R. R. Drenten, and B. H. Verbeeck, "The effect of optical feedback on the relaxation oscillation in semiconductor lasers," *Quantum Electronics, IEEE Journal of*, vol. 24, pp. 1989–1995, Oct. 1988.

[125] L. G. Joneckis, P. T. Ho, and G. L. Burdge, "CW injection seeding of a modelocked semiconductor laser," *Quantum Electronics, IEEE Journal of*, vol. 27, pp. 1854–1858, July 1991.

[126] M. G. Madhan, E. Rekha, and P. RajKumar, "A comprehensive equivalent circuit model for the study of thermal and spectral characteristics in laser diodes," *Optik - International Journal for Light and Electron Optics*, vol. 125, pp. 3030–3036, July 2014.

[127] R. Engelbrecht, J. Groh, C. Stumpf, J. Adametz, and B. Schmauss, "Large-Signal RF Circuit Model for a High-Power Laser Diode Module," *Photonics Technology Letters, IEEE*, vol. 26, pp. 761–764, Apr. 2014.

[128] H. Lv, Z. Li, T. Yang, and C. Huang, "Small-signal circuit modeling for a semiconductor optical amplifier monolithically integrated with a sampled grating distributed Bragg reflector laser," *Optica Applicata*, vol. 42, no. 1, pp. 55–68, 2012.

[129] J. Katz, S. Margalit, C. Harder, D. Wilt, and A. Yariv, "The intrinsic electrical equivalent circuit of a laser diode," *Quantum Electronics, IEEE Journal of*, vol. 17, pp. 4–7, Jan. 1981.

[130] P. Biernacki and A. R. Mickelson, "Impedance matching of laser diodes using packaged microstrip lines: active and passive," in *Lasers and Electro-Optics Society Annual Meeting, 1995. 8th Annual Meeting Conference Proceedings, Volume 1., IEEE*, vol. 1, pp. 238–239 vol.1, IEEE, Oct. 1995.

[131] S. Arahira and Y. Ogawa, "40 GHz Actively Mode-Locked Distributed Bragg Reflector Laser Diode Module with an Impedance-Matching Circuit for Efficient RF Signal Injection," *Japanese Journal of Applied Physics*, vol. 43, p. 1960, Apr. 2004.

[132] M. Vangeleyn, *Atom trapping in non-trivial geometries for micro-fabrication applications.* PhD thesis, 2011. University of Strathclyde.

[133] J. White, "The Smith Chart," pp. 119–160, Sept. 2009.

[134] K. C. Chan and A. Harter, "Impedance matching and the Smith chart The fundamentals.." July 2000.

[135] J. Coonrod, "Understanding When To Use FR-4 Or High Frequency Laminates." Sept. 2011.

[136] S. M. Sze and K. K. Ng, *Physics of Semiconductor Devices, 3rd Edition.* Wiley, 3 ed., Nov. 2006.

[137] M. G. Madhan, P. R. Vaya, and N. Gunasekaran, "A Unified Approach to Study the Thermal Dynamics in Multilongitudinal Mode Semiconductor Lasers," *Fiber And Integrated Optics*, pp. 159–169, Mar. 2001.

[138] J. P. van der Ziel and W. T. Tsang, “Mode locking of semiconductor lasers” in ”Semiconductors and Semimetals,” *Lightwave Communications Technology*, vol. 22B, 1985.

[139] P. Morton, R. J. Helkey, and J. E. Bowers, “Dynamic detuning in actively mode-locked semiconductor lasers,” *Quantum Electronics, IEEE Journal of*, vol. 25, pp. 2621–2633, Dec. 1989.

[140] J. C. Goodwin and B. K. Garside, “Modulation detuning characteristics of actively mode-locked diode lasers,” *Quantum Electronics, IEEE Journal of*, vol. 19, pp. 1068–1073, June 1983.

[141] H. A. Haus, “Theory of modelocking of a laser diode in an external resonator,” *Journal of Applied Physics*, vol. 51, pp. 4042–4049, Aug. 1980.

[142] T. Ikegami, S. Sudo, and Y. Sakai, *Frequency Stabilization of Semiconductor Laser Diodes*. Artech House Inc, 1995.

[143] O. E. Martinez, “3000 times grating compressor with positive group velocity dispersion: Application to fiber compensation in 1.3-1.6 m region,” *Quantum Electronics, IEEE Journal of*, vol. 23, pp. 59–64, Jan. 1987.

[144] M. Kuznetsov, J. M. Wiesenfeld, and L. R. Radzihovsky, “Compression of picosecond pulses from diode lasers using a modified grating-pair compressor,” *Optics Letters*, vol. 15, p. 180, Feb. 1990.

[145] H. F. Liu, Y. Ogawa, and S. Oshiba, “Generation of an extremely short single mode pulse (2 ps) by fiber compression of a gain switched pulse from a 1.3 m distributed feedback laser diode,” *Applied Physics Letters*, vol. 59, pp. 1284–1286, Sept. 1991.

[146] O. E. Martinez, “Grating and prism compressors in the case of finite beam size,” *Journal of the Optical Society of America B Optical Physics*, vol. 3, pp. 929–934, July 1986.

[147] E. B. Treacy, “Optical pulse compression with diffraction gratings,” *Quantum Electronics, IEEE Journal of*, vol. 5, pp. 454–458, Sept. 1969.

[148] A. Consoli and I. Esquivias, "Pulse shortening of gain switched single mode semiconductor lasers using a variable delay interferometer.," *Optics Express*, vol. 20, pp. 22481–22489, Sept. 2012.

[149] J. M. Wiesenfeld, M. Kuznetsov, and A. S. Hou, "Tunable, picosecond pulse generation using a compressed, modelocked laser diode source," *Photonics Technology Letters, IEEE*, vol. 2, pp. 319–321, May 1990.

[150] Z. Ahmed, L. Zhai, A. J. Lowery, N. Onodera, and R. S. Tucker, "Locking bandwidth of actively mode-locked semiconductor lasers," *Quantum Electronics, IEEE Journal of*, vol. 29, pp. 1714–1721, June 1993.

[151] M. Vaughan, *The Fabry-Perot Interferometer: History, Theory, Practice and Applications.* Taylor & Francis Group, 1989.

[152] P. J. Fox, R. E. Scholten, M. R. Walkiewicz, and R. E. Drullinger, "A reliable, compact, and low-cost Michelson wavemeter for laser wavelength measurement," *American Journal of Physics*, vol. 67, pp. 624–630, July 1999.

[153] J. L. Hall and S. A. Lee, "Interferometric realtime display of cw dye laser wavelength with subDoppler accuracy," *Applied Physics Letters*, vol. 29, pp. 367–369, Sept. 1976.

[154] H. R. Xia, S. V. Benson, and T. W. Hänsch, "A 'toy-train' wavemeter," *Laser Focus*, vol. 17, p. 54, 1981.

[155] F. V. Kowalski, R. E. Teets, W. Demtröder, and A. L. Schawlow, "An improved wavemeter for cw lasers," *Journal of the Optical Society of America*, vol. 68, no. 11, pp. 1611–1613, 1978.

[156] J. M. Blackledge, *Digital Signal Sampling.* Horwood Publishing Limited, 2006.

[157] N. Yoder, "PEAKFINDER Noise tolerant fast peak finding algorithm - Matlab Code/Function."

[158] I. Petitbon, P. Gallion, G. Debarge, and C. Chabran, “Locking bandwidth and relaxation oscillations of an injection-locked semiconductor laser,” *Quantum Electronics, IEEE Journal of*, vol. 24, pp. 148–154, Feb. 1988.

[159] J. P. Hohimer, A. Owyoung, and G. R. Hadley, “Singlechannel injection locking of a diodelaser array with a cw dye laser,” *Applied Physics Letters*, vol. 47, pp. 1244–1246, Dec. 1985.

[160] H. L. Stover and W. H. Steier, “Locking of laser oscillators by light injection,” *Applied Physics Letters*, vol. 8, pp. 91–93, Feb. 1966.

[161] M. Margalit, M. Orenstein, G. Eisenstein, and V. Mikhaelshvili, “Injection locking of an actively mode-locked semiconductor laser,” *Optics Letters*, vol. 19, p. 2125, Dec. 1994.

[162] H. Y. Ryu, S. H. Lee, and H. S. Suh, “Widely Tunable External Cavity Laser Diode Injection Locked to an Optical Frequency Comb,” *Photonics Technology Letters, IEEE*, vol. 22, pp. 1066–1068, July 2010.

[163] T. Jung, J.-L. Shen, D. T. K. Tong, S. Murthy, M. C. Wu, T. Tanbun-Ek, W. Wang, R. Lodenkamper, R. Davis, L. J. Lembo, and J. C. Brock, “CW injection locking of a mode-locked semiconductor laser as a local oscillator comb for channelizing broad-band RF signals,” *Microwave Theory and Techniques, IEEE Transactions on*, vol. 47, pp. 1225–1233, July 1999.

[164] S. Arahira, H. Yaegashi, K. Nakamura, and Y. Ogawa, “Chirp control and broadband wavelength-tuning of 40-GHz monolithic actively mode-locked laser diode module with an external CW light injection,” *Selected Topics in Quantum Electronics, IEEE Journal of*, vol. 11, no. 5, pp. 1103–1111, 2005.

[165] K. S. Hardman, S. Bennetts, J. E. Debs, C. C. Kuhn, G. D. McDonald, and N. Robins, “Construction and characterization of external cavity diode lasers for atomic physics.,” *Journal of visualized experiments : JoVE*, no. 86, p. e51184, 2014.

[166] F. Quinlan, S. Gee, S. Ozharar, and P. J. Delfyett, “Greater Than 20-dB Supermode Noise Suppression and Timing Jitter Reduction Via CW Injection of a Harmonically Mode-Locked Laser,” *Photonics Technology Letters, IEEE*, vol. 19, pp. 1221–1223, Aug. 2007.

[167] C. Williams, D. Mandridis, J. Davila-Rodriguez, and P. J. Delfyett, “Injection locked coupled opto-electronic oscillator for optical frequency comb generation,” vol. 8054, pp. 80540C–80540C–10, 2011.

[168] V. Annovazzi-Lodi, A. Sciré, M. Sorel, and S. Donati, “Dynamic behavior and locking of a semiconductor laser subjected to external injection,” *Quantum Electronics, IEEE Journal of*, vol. 34, pp. 2350–2357, Dec. 1998.

[169] O. Lidoyne, P. Gallion, C. Chabran, and G. Debarge, “Locking range, phase noise and power spectrum of an injection-locked semiconductor laser,” *IEE Proceedings J Optoelectronics*, vol. 137, no. 3, p. 147, 1990.

[170] R. Lang, “Injection locking properties of a semiconductor laser,” *Quantum Electronics, IEEE Journal of*, vol. 18, pp. 976–983, June 1982.

[171] F. Mogensen, H. Olesen, and G. Jacobsen, “Locking conditions and stability properties for a semiconductor laser with external light injection,” *Quantum Electronics, IEEE Journal of*, vol. 21, pp. 784–793, July 1985.

[172] K. Vahala, L. C. Chiu, S. Margalit, and A. Yariv, “On the linewidth enhancement factor in semiconductor injection lasers,” *Applied Physics Letters*, vol. 42, pp. 631–633, Apr. 1983.

[173] U. Gliese, T. N. Nielsen, M. Bruun, E. L. Christensen, K. E. Stubkjaer, S. Lindgren, and B. Broberg, “A wideband heterodyne optical phase-locked loop for generation of 3-18 GHz microwave carriers,” *Photonics Technology Letters, IEEE*, vol. 4, pp. 936–938, Aug. 1992.

[174] R. C. Steele, “Optical phase-locked loop using semiconductor laser diodes,” *Electronics Letters*, vol. 19, pp. 69–71, Jan. 1983.

[175] F. Friederich, G. Schuricht, A. Deninger, F. Lison, G. Spickermann, P. Haring Bolívar, and H. G. Roskos, "Phase-locking of the beat signal of two distributed-feedback diode lasers to oscillators working in the MHz to THz range.," *Optics express*, vol. 18, pp. 8621–8629, Apr. 2010.

[176] K. Balakier, M. J. Fice, L. Ponnampalam, A. J. Seeds, and C. C. Renaud, "Monolithically Integrated Optical Phase Lock Loop for Microwave Photonics," *Lightwave Technology, Journal of*, vol. 32, pp. 3893–3900, Oct. 2014.

[177] M. Kourogi, C.-H. Shin, and M. Ohtsu, "A 134 MHz bandwidth homodyne optical phase-locked-loop of semiconductor laser diodes," *Photonics Technology Letters, IEEE*, vol. 3, pp. 270–272, Mar. 1991.

[178] C.-H. Shin and M. Ohtsu, "Heterodyne optical phase-locked loop by confocal Fabry-Periot cavity coupled AlGaAs lasers," *Photonics Technology Letters, IEEE*, vol. 2, pp. 297–300, Apr. 1990.

[179] R. T. Ramos and A. J. Seeds, "Delay, linewidth and bandwidth limitations in optical phase-locked loop design," *Electronics Letters*, vol. 26, pp. 389–391, Mar. 1990.

[180] A. C. Bordonalli, C. Walton, and A. J. Seeds, "High-performance homodyne optical injection phase-lock loop using wide-linewidth semiconductor lasers," *Photonics Technology Letters, IEEE*, vol. 8, no. 9, pp. 1217–1219, 1996.

[181] A. M. Marino and C. R. Stroud, "Phase-locked laser system for use in atomic coherence experiments," *Review of Scientific Instruments*, vol. 79, p. 013104, Jan. 2008.

[182] J. Appel, A. MacRae, and A. I. Lvovsky, "A versatile digital GHz phase lock for external cavity diode lasers," *Measurement Science and Technology*, vol. 20, no. 5, p. 055302, 2009.

[183] S. Patel, *A Chirped, Pulsed Laser System and Magneto-Optical Trap for Rubidium.* PhD thesis, School of Physics and Astronomy, University of Southampton, Jan. 2009.

[184] N. Cooper and T. Freegarde, “Trapping of ^{85}Rb atoms by optical pumping between metastable hyperfine states,” *Journal of Physics B: Atomic, Molecular and Optical Physics*, vol. 46, no. 21, p. 215003, 2013.

[185] D. Haubrich, M. Dornseifer, and R. Wynands, “Lossless beam combiners for nearly equal laser frequencies,” *Review of Scientific Instruments*, vol. 71, pp. 338–340, Feb. 2000.

[186] I. Dotsenko, W. Alt, S. Kuhr, D. Schrader, M. Müller, Y. Miroshnychenko, V. Gomer, A. Rauschenbeutel, and D. Meschede, “Application of electro-optically generated light fields for Raman spectroscopy of trapped cesium atoms,” *Applied Physics B: Lasers and Optics*, vol. 78, pp. 711–717, Apr. 2004.

[187] G. B. Xavier and J. P. von der Weid, “Stable single-photon interference in a 1 km fiber-optic MachZehnder interferometer with continuous phase adjustment,” *Optics Letters*, vol. 36, no. 10, pp. 1764+, 2010.

[188] M. Song, S. Yin, and P. B. Ruffin, “Fiber Bragg grating strain sensor demodulation with quadrature sampling of a MachZehnder interferometer,” *Applied Optics*, vol. 39, no. 7, p. 1106, 2000.

[189] W. Herschel, “Experiments on the Refrangibility of the Invisible Rays of the Sun,” *Philosophical Transactions of the Royal Society of London*, vol. 90, p. 284, 1800.

[190] R. Bunsen and G. Kirchhoff, “Untitled,” *Annalen der Physik und der Chemie*, vol. 189, no. 7, p. 337, 1861.

[191] J. Ye and S. T. Cundiff, *Femtosecond Optical Frequency Comb: Principle, Operation, and Applications.* Kluwer Academic Publishers / Springer, 2004.

[192] J. Hodgkinson and R. P. Tatam, “Optical gas sensing: a review,” *Measurement Science and Technology*, vol. 24, p. 012004, Jan. 2013.

[193] J. Ye, L.-S. Ma, and J. L. Hall, “Ultrasensitive detections in atomic and molecular physics: demonstration in molecular overtone spectroscopy,” *J. Opt. Soc. Am. B*, vol. 15, pp. 6–15, Jan. 1998.

[194] P. C. D. Hobbs, “Ultrasensitive laser measurements without tears,” *Appl. Opt.*, vol. 36, pp. 903–920, Feb. 1997.

[195] G. D. Houser and E. Garmire, “Balanced detection technique to measure small changes in transmission,” *Appl. Opt.*, vol. 33, pp. 1059–1062, Feb. 1994.

[196] L. Gianfrani, R. W. Fox, and L. Hollberg, “Cavity-enhanced absorption spectroscopy of molecular oxygen,” *J. Opt. Soc. Am. B*, vol. 16, pp. 2247–2254, Dec. 1999.

[197] B. Ouyang and R. L. Jones, “Understanding the sensitivity of cavity-enhanced absorption spectroscopy: pathlength enhancement versus noise suppression,” *Applied Physics B: Lasers and Optics*, vol. 109, pp. 581–591, Sept. 2012.

[198] A. Foltynowicz, F. M. Schmidt, W. Ma, and O. Axner, “Noise-immune cavity-enhanced optical heterodyne molecular spectroscopy: Current status and future potential,” vol. 92, no. 3, pp. 313–326, 2008.

[199] A. O’Keefe and D. A. G. Deacon, “Cavity ring-down optical spectrometer for absorption measurements using pulsed laser sources,” *Review of Scientific Instruments*, vol. 59, no. 12, pp. 2544–2551, 1988.

[200] K. L. Haller and P. C. Hobbs, “Double-beam laser absorption spectroscopy: shot noise-limited performance at baseband with a novel electronic noise canceler,” in *Society of Photo-Optical Instrumentation Engineers (SPIE) Conference Series* (B. L. Fearey, ed.), vol. 1435 of *Society of Photo-Optical Instrumentation Engineers (SPIE) Conference Series*, pp. 298–309, July 1991.

[201] T. G. Spence, C. C. Harb, B. A. Paldus, R. N. Zare, B. Willke, and R. L. Byer, “A laser-locked cavity ring-down spectrometer employing an analog detection scheme,” *Review of Scientific Instruments*, vol. 71, pp. 347–353, Feb. 2000.

[202] V. Kasyutich and M. Sigrist, “Characterisation of the potential of frequency modulation and optical feedback locking for cavity-enhanced absorption spectroscopy,” vol. 111, no. 3, pp. 341–349, 2013.

[203] L.-S. Ma, J. Ye, P. Dubé, and J. L. Hall, “Ultrasensitive frequency-modulation spectroscopy enhanced by a high-finesse optical cavity: theory and application to overtone transitions of C_2H_2 and C_2HD,” *Journal of the Optical Society of America B*, vol. 16, pp. 2255+, Dec. 1999.

[204] M. Abramowitz and I. A. Stegun, *Handbook of Mathematical Functions.* National Bureau of Standards, 10 ed., 1972.

[205] R. Schimpe, J. E. Bowers, and T. L. Koch, “Characterisation of frequency response of 1.5 m InGaAsP DFB laser diode and InGaAs pin photodiode by heterodyne measurement technique,” *Electronics Letters*, vol. 22, no. 9, p. 453, 1986.

[206] R. Corporation, “RT/Duroid 6035HTC: High Frequency Laminate,” tech. rep., Rogers Corporation, https://www.rogerscorp.com/documents/1946/acm/RT-duroid-6035HTC-High-Frequency-Laminates.aspx.

[207] I. Coddington, W. Swann, and N. Newbury, “Coherent dual-comb spectroscopy at high signal-to-noise ratio,” *Physical Review A*, vol. 82, p. 043817, Oct. 2010.

[208] D. J. Griffiths, *Introduction to Electrodynamics.* Prentice-Hall International Inc, 3 ed., 1999.

[209] C. H. Henry, R. A. Logan, and K. A. Bertness, “Spectral dependence of the change in refractive index due to carrier injection in GaAs lasers,” *Journal of Applied Physics*, vol. 52, pp. 4457–4461, July 1981.